UNIVERSITÀ DEGLI STUDI DI PADOVA

Sede Amministrativa: Università degli Studi di Padova

Dipartimento di Scienze Chimiche

GRADUATE SCHOOL OF MOLECULAR SCIENCES

CURRICULUM CHEMICAL SCIENCES

XXIX CYCLE

LIGAND AND STRUCTURE DESIGN OF BIO-INSPIRED MULTI-ELECTRON REDOX CATALYSTS

School Director: Prof. Antonino Polimeno

Supervisor: Prof. Marcella Bonchio

PhD Student: Andrea Squarcina

31st January 2017

Abstract

The water-to-oxygen redox couple, H_2O/O_2, powers our aerobic life through the fundamental processes of natural photosynthesis and cellular respiration. Despite its vital role, any failure of this four-electron mechanism turns out to release O_2-derived toxic radicals, inducing a severe oxidative damages of any synthetic and biological materials exposed to the aerobic risk. The aerobic formation of ROS is due to oxygen reduction in-vivo, generating the superoxide anion ($O_2^{\bullet-}$), hydrogen peroxide (H_2O_2), and the hydroxyl radical (HO•). ROS give rise to fast, barrier-less, short-range and non-selective oxidation steps, being responsible for the "oxidative stress", a key factor for cellular death, organ failure and aging diseases. In addition photo-oxidative stress is one key factor limiting plant productivity, i.e. bio-mass and food yield. Noteworthy, ROS-forming mechanisms are also lethal for the stability of bio-inspired materials designed for artificial photosynthesis in vitro. The biological defense against ROS-induced cellular damage stems from the combined action of "anti-oxidant" metallo-enzymes, as superoxide dismutase (SOD), and catalase (CAT). A detoxification cascade occurs via SOD-induced dismutation of $O_2^{\bullet-}$ into O_2 and H_2O_2 which is then converted by CAT into H_2O and O_2 again. In this thesis will be presented the design of a set of novel anti-oxidant catalysts, based on different metal centers, that can emerge by the engineering of a synzyme with integrated SOD/CAT activity able to mimic both the enzymes activities and efficiently perform a complete ROS scavenging also in biological-like solution. The activity of the synzymes will be also tested in water splitting processes to perform both the water oxidation than the proton reduction reactions in water at neutral pH, a key feature to obtain sustainable energy sources from water.

The obtained results will be divided in four main chapters:

- Chapter 2: coupling of a polycationic Mn(III)-porphyrin, with a dinuclear $Mn_2(II,II)L_2$ core (HL = 2-{[[di(2-pyridyl)methyl] (methyl)amino]methyl}phenol) results in a dual Superoxide Dismutase (SOD) and Catalase (CAT) functional analog, $Mn_2L_2P^{n+}$, enabling a detoxification cascade of the superoxide anion and hydrogen peroxide into benign H_2O and O_2. The SOD/CAT artificial manifolds, joined in one asset, exhibit a peak catalytic performance under physiological conditions, with log $k_{cat}(O_2^{\bullet-}) \geq 7$ and $k_{cat}(H_2O_2)/K_M = 1890$. The dual-enzyme (di-zyme) concept allows for a unique, built-in-self-protection, against the irreversible bleaching of the porphyrin unit, (> 75% protection), readily induced by H_2O_2 (200 μM, 20 equivalents, in buffer solution, pH=

7.8). We show herein that incubation of the photosynthetic green algae, *Chlamydomonas reinhardtii,* with the synthetic di-zyme (as low as 0.1 μM), prevents H_2O_2 accumulation under high-light illumination conditions, thus providing an efficient anti-oxidant surveillance and photo-protection.

- Chapter 3: dinuclear $Cu(II)_2L_2$ catalysts were synthesized and studied for their SOD/CAT activity. The goal of this study was to demonstrate that with a proper ligand set, is it possible tune the reactivity of an harmful metal like copper, turns it to a benign anti-oxidant system. The dinuclear copper complexes show SOD activity with $\log k_{cat}$ up to 7.55 and CAT activity with rate of O_2 production up to 4.4 μM/s. Kinetic studies of the process of hydrogen peroxide dismutation show also an evolution of the catalyst during the catalytic turnover. No evidence of oxidation of external substrates was also confirmed as consequence of the sacrificial internal scavenger.
- Chapter 4: novel Fe(III)L, $Fe(III)_2L_2$ and $Co_2(II)L_2$ complexes have also been isolated. Preliminary results indicate that a multi-redox manifold is available for both species, however with scarce activity as ROS scavenger. These complexes show instead an interesting activity in the water oxidation process. In addition the anodic waves observed in reduction are promising for catalytic proton reduction processes performed by using directly water as proton source.
- Chapter 5: application of oxygen evolving catalysts within functional materials has been explored in the field of porous membranes. This novel stimuli-responsive strategy against the irreversible fouling of porous materials and surfaces is based on the molecular design of catalytic pore walls that foster a chemo-mechanical, self-cleaning behaviour under neutral pH and mild conditions of pressure and temperature. To this aim, the catalase-like behaviour of the tetra-ruthenium substituted polyoxometalate, has been exploited for in-pore oxygen evolution so to induce an active fluid mixing and the displacement of foulant particles. The present study includes the fabrication of hybrid polymeric films with porous architecture embedding the tetra-ruthenium catalyst as artificial catalase to guarantee the material self-defence against pore occlusion and oxidative damage with aqueous H_2O_2 as mild chemical effector.

Index

1. Introduction

1.1 Oxygen Paradox and Oxidative Stress

Oxygen is a vital component for cells, being involved in the biological energy production during respiration and photosynthesis. Reduction of molecular oxygen in mitochondria, allows ATP (Adenosine triphosphate) synthesis, the energetic fuel of cell, instead photosynthesis oxidize water to molecular oxygen using light to produce ATP, that is used to reduce carbon dioxide and produce glucose. However at the same time, living cells continuously produce highly Reactive Oxygen Species (ROS).[1] ROS is a generic terms used to group superoxide anion ($O_2^{\bullet-}$), hydroxyl radical (HO•) and hydrogen peroxide (H_2O_2), but often it also includes reactive nitrogen species (RNS) such as peroxynitrite ($ONOO^-$) and nitric oxide ($\cdot NO_2$).[1] The aerobic formation of ROS is due to oxygen reduction in-vivo, generating the superoxide anion, hydrogen peroxide, and the hydroxyl radical (HO•). ROS give rise to fast, barrier-less, short-range and non-selective oxidation steps, being responsible for the "oxidative stress" damages.[1]

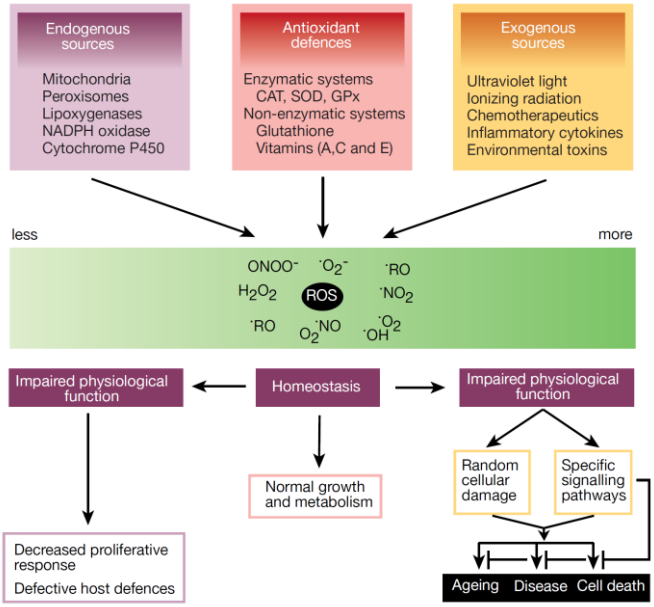

Figure 1. Cellular sources of cellular ROS and effects related to overproduction or deficiency of ROS.

In animals ROS are produced mainly in mitochondria since superoxide anion arises from the first reduction within the respiratory chain, it is called primary ROS and subsequently hydrogen peroxide is produced upon dismutation of superoxide. Then hydroxyl radical, the most reactive and harmful oxygen specie, with a life time of less than 1 ns, is generated from the reaction of H_2O_2 with metal ions, such as Fe^{2+} and Cu^+, through the so called Fenton (1) and Haber-Weiss (2) reactions (Scheme 1).[2]

$$Fe^{3+}/Cu^{2+} + O_2^{\bullet -} \rightarrow Fe^{2+}/Cu^{+} + O_2$$
$$Fe^{2+}/Cu^{+} + H_2O_2 \rightarrow Fe^{3+}/Cu^{2+} + OH^{\bullet} + OH^{-} \quad \textbf{(1)}$$

$$O_2^{\bullet -} + H_2O_2 \rightarrow O_2 + OH^{\bullet} + OH^{-} \quad \textbf{(2)}$$

Scheme 1. Reaction of ROS with metal ions: Fenton (1) and Haber-Wiess (2) reaction.

The crucial issue is that, while a two-electron process would be required to safely reduce H_2O_2 to water, these metals react via one-electron pathways leading to partially reduced reactive species. With respect to hydroxyl radical, hydrogen peroxide present a higher diffusion capability, which extends the potential damage beyond mitochondria, also targeting other cell functionalities.[3] In particular ROS can damage important cellular components like membrane lipids, proteins, DNA, leading to toxic secondary products and also causing cell death. Mitochondrial DNA mutation due to ROS has been implicated in cancer, cardiac disease and type II diabetes.[4] In particular, due to high oxygen consumption, central nervous system is vulnerable to oxidative injury, the accumulation damages during life cycle on DNA, lipid and protein have been proposed to play a key role in neurodegenerative disease.[4–8]

However, despite their dangerous effects ROS, at low concentration, are also implicated in other physiological functions, including cell signaling, which can be impaired at high concentration (Figure 1).

Oxidative damage is also one crucial risk-factor for photo-oxidative stress in the oxygen-rich environment of photosynthetic organisms, readily induced under intense illumination, extreme temperatures and water deficit. Under these conditions, the photo-induced electron-flow in the PSII generally exceeds the transport-chain capacity, so oxygen undergoes one-electron reduction forming the superoxide anion ($O_2^{\bullet -}$, the Mehler reaction). H_2O_2 is eventually generated by its spontaneous or SOD-induced decay, or by a failure of the four electron water oxidation mechanism, collapsing to a bi-electronic peroxide-forming process and subsequently hydrogen peroxide could be reduced to the hydroxyl radical (HO•) via the Fenton reaction (Scheme 2).[9]

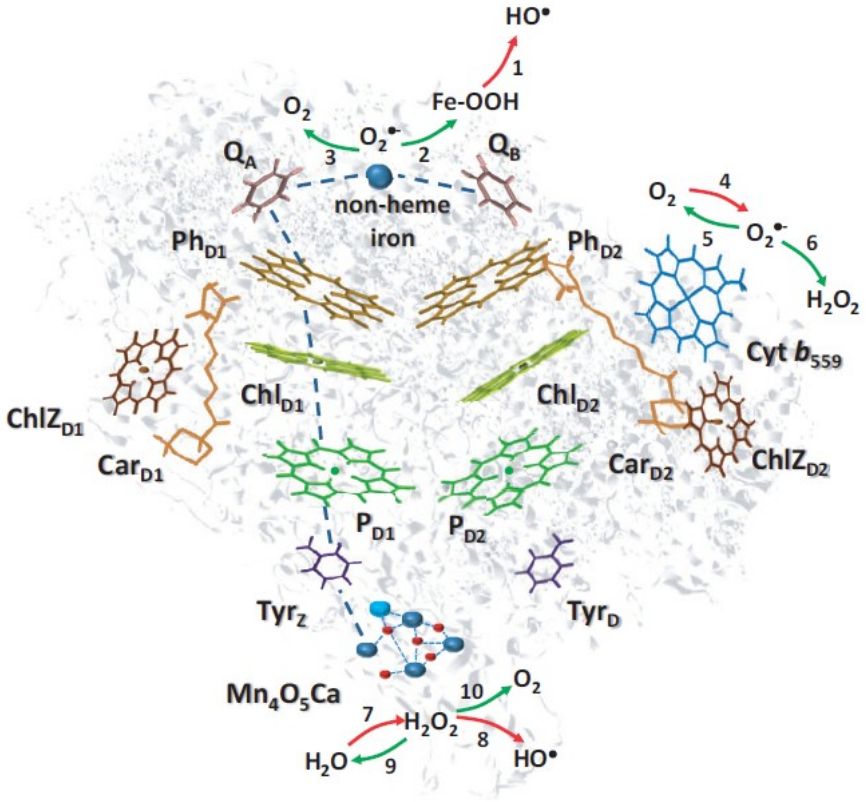

Scheme 2. The arrangement of the metal center in PSII involved in the production (red arrow) and scavenging (green arrow) of ROS. One-electron reduction of the non-heme ferric-hydroperoxo species to HO• (reaction 1). One-electron reduction of $O_2^{\bullet-}$ by ferrous non-heme iron to the non-heme ferric-hydroperoxo species (Fe–OOH) (superoxide reductase) (reaction 2). One-electron oxidation of $O_2^{\bullet-}$ by ferric non-heme iron to molecular oxygen (superoxide oxidase) (reaction 3). One-electron reduction of molecular oxygen by the ferrous iron (II) of Cyt b_{559} to $O_2^{\bullet-}$ (oxygen reductase) (reaction 4). One-electron oxidation of $O_2^{\bullet-}$ by the ferric iron (III) of Cyt b_{559} to molecular oxygen (superoxide oxidase) (reaction 5). One-electron reduction of $O_2^{\bullet-}$ by the ferrous iron of the HP form of Cyt b_{559} to H_2O_2 (superoxide reductase) (reaction 6). Two-electron oxidation of water to H_2O_2 (water oxidase) (reaction 7). One-electron reduction of H_2O_2 to HO• by a manganese ion (Fenton reaction) (reaction 8). Two-electron reduction of H_2O_2 to water (reaction 9) and two-electron oxidation of H_2O_2 to molecular oxygen (reaction 10) (catalase activity).

It has been shown that the rate of $O_2^{\bullet-}$ production in PSI is 15 mmol (mg Chl)$^{-1}$ h^{-1}.[10] The rate of $O_2^{\bullet-}$ production, in PSII has not been determined yet, however it is generally considered that it is less significant compared to PSI.[11,12] ROS production in PSII is mainly associated to one electron reduction of O_2 occurring in the non-heme iron site and heme site of the Cyt b_{559} and to the bi-electronic reduction of H_2O occurring in the oxygen evolving center (OEC) Mn_4O_5Ca (Figure 2). To prevent the oxidative effect of ROS on proteins and lipids, ROS have to diffuse rapidly from the site of formation to the antioxidant catalytic center along specific channels.[13] These channels are proposed to direct dangerous ROS towards the antioxidant catalytic center located either within or outside of the thylakoid membrane.

1.2 Anti-oxidants Enzymes

The biological ROS surveillance, both in animals than in plants, stems from the combined action of key metallo-enzymes, including superoxide dismutase (SOD), and catalase (CAT).[14,15] Also glutathione, a simple molecule containing sulphur, act as defence against ROS thanks to the enzymes glutathione peroxidase (GSP) and reductase (GSR), needed to re-generate the reduced form of glutathione. However, the effective detoxification cascade occurs via SOD-induced dismutation of $O_2^{\bullet-}$ into O_2 and H_2O_2 which is further converted by CAT into H_2O and O_2 again. The SOD/CAT cascade prevents H_2O_2 accumulation and its radical-chain decomposition, thus ruling out reaction branching and exponential radical growth.[1,16] Moreover, oxygen is released in both SOD and CAT mediated reactions, thus mitigating any possible O_2-depletion within the cellular environment (Scheme 3).[14,15]

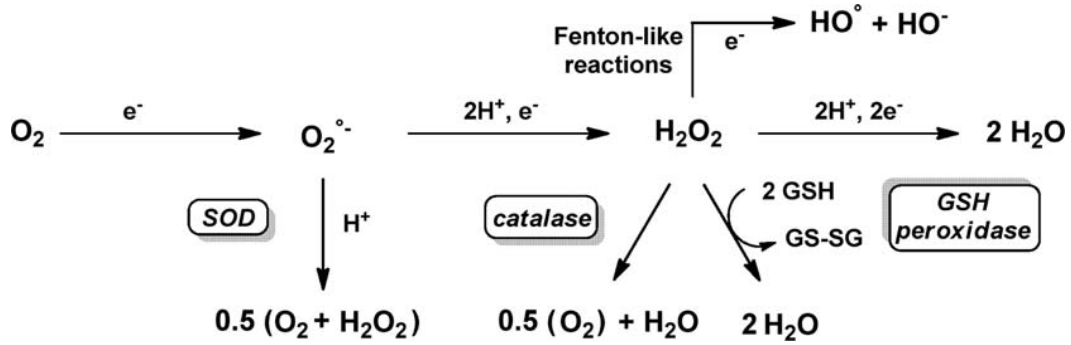

Scheme 3. Single electron transfer pathways of oxygen reduction leading to ROS formation and defence mechanisms by anti-oxidant enzymes.

These enzymes usually contain one or more metal center that catalyze multi electronic reactions. The most common superoxide dismutase are mononuclear, containing only one manganese atom, or dinuclear containing both copper and zinc (Figure 2). From a structural point of view, they are both characterized by a metal core coordinated with histidine residues and other oxygen ligands like aspartate and water molecules that complete the coordination sphere. These protein environments tune the Cu^{II}/Cu^{I} and Mn^{III}/Mn^{II} couple redox potentials obtaining an $E_{1/2} \approx +300$ mV vs NHE. This is a potential intermediate between the potential for the $O_2^{\bullet-}$ reduction (+890 mV vs NHE) and oxidation (−160 mV vs NHE) (Scheme 4). Thus, an equal thermodynamic facilitation is afforded for each step of the dismutation process required to catalyze the net SOD reaction.[17–19]

$$O_2^{\bullet -} + H^+ + \text{SOD-M(III)(OH)} \longrightarrow O_2 + \text{SOD-M(II)(OH}_2\text{)}$$

$$O_2^{\bullet -} + H^+ + \text{SOD-M(II)(OH}_2\text{)} \longrightarrow H_2O_2 + \text{SOD-M(III)(OH)}$$

Scheme 4. Redox processes catalyzed by MnSOD superoxide dismutase.

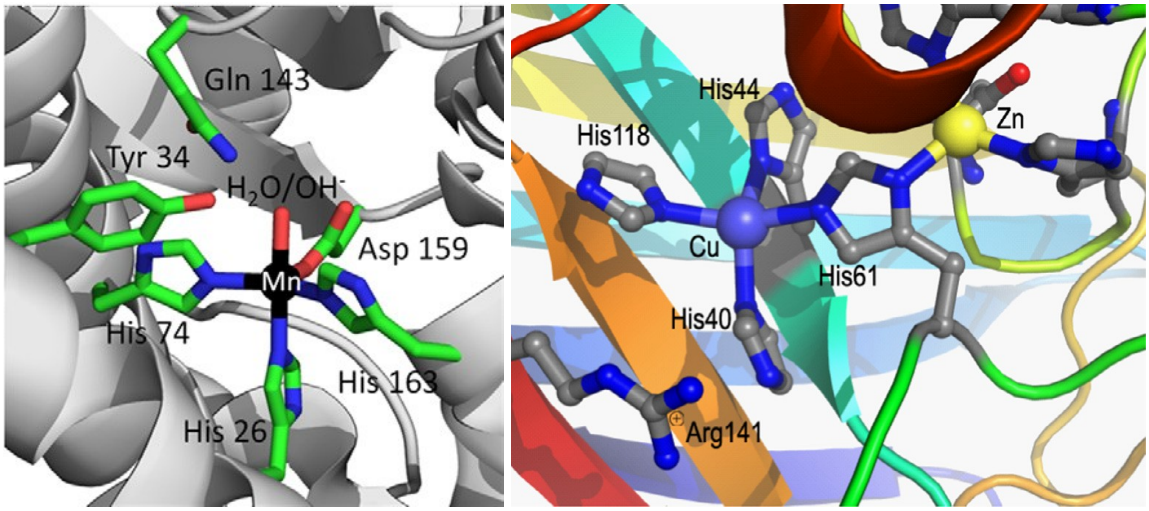

Figure 2. The structure of active site and nearby amino acid residue in Human mitochondrial MnSOD (left) and in Cu, Zn-SOD (right).

Mammals possess two different classes of SODs to control the level of superoxide radicals: the Cu,ZnSOD which is present in the cytoplasm, nuclear compartments and in the inter membrane space of the mitochondria or in extracellular space, and the MnSOD, that is located in mitochondrial matrix.[20–23] In prokaryotes and in the chloroplast of some plants FeSOD metalloenzymes was found to share a high degree of sequence and structural homology with the Mn-SOD enzymes. More recently also a NiSOD enzyme, bearing to a different class of SOD, was discovered in *Streptomyces coelicolor* as an hexameric structure built from right-handed 4-helix bundles, each containing N-terminal binding sites that chelate a Ni ion.[24]

Two families of natural catalases are known, one based on an iron-heme cofactor, and the other, containing a non-heme di-nuclear manganese core (MnCAT) (Figure 3). The most frequent species is a tetramer containing a Fe-protoporphyrin cofactor (Figure 3) in each identical subunits. Below the porphyrin plan there are a tyrosine coordinates to the metal center and an arginine residues, while over it there are a histidine and an asparagine, that play a crucial role in hydrogen peroxide dismutation. There is also a channel, with 30 Å length and 15 Å width, for the access of active site.[25] One defect of these type of catalases is the easy inhibition operated by cyanide and azide anion, like in hemoglobin.

Instead di-manganese catalase is less sensitive to inhibitors; its active core is based on two manganese ions bridged by two μ- oxo oxygen and a $\mu_{1,3}$–carboxylate group from a glutamate residue, the coordination sphere is completed by other glutamates and histidines residues (Figure 3). Terminally bound water molecules are easily displaced from the metal complexes and this apical site likely serves as the initial substrate binding site during catalysis.[26]

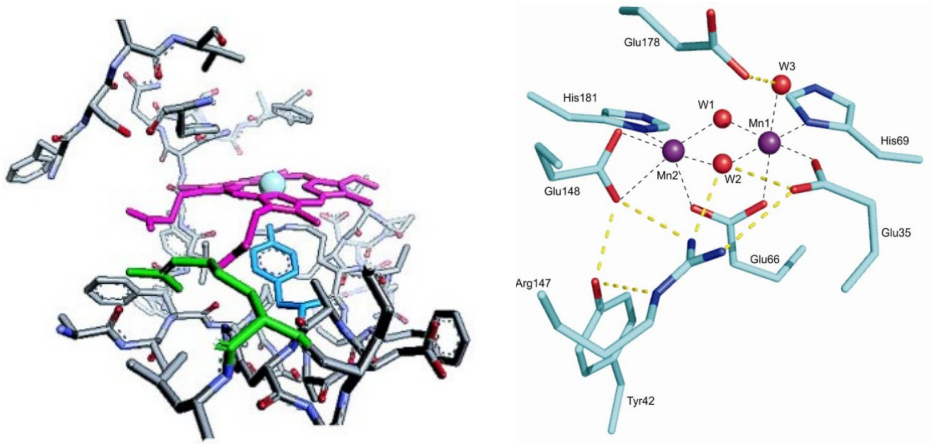

Figure 3. Active site of Fe-heme catalase (left) and active site of MnCAT of *L.plantarum* (right).

MnCATs have been isolated in four oxidation states ranging from Mn_2^{II} to $Mn_2^{III,IV}$; biochemical and spectroscopic studies have shown that these enzymes disproportionate H_2O_2 by cycling between the Mn_2^{II} and Mn_2^{III} oxidation states.[27,28] The electrochemical potentials (vs. NHE, pH = 7) for the two-electron O_2/H_2O_2 and H_2O_2/H_2O couples are respectively 0.28 and 1.35 V. To efficiently catalyze the H_2O_2 dismutation, the protein environment have to control the reduction potential of the di-Mn active site to a value lower than that of the free Mn^{III}/Mn^{II} couple (1.54 V). The two Mn ions of the active site of MnCAT possess the same NO_5 coordination sphere provides a symmetrical environment that stabilizes the homovalent di-Mn core and facilitates the observed redox cycle between Mn_2^{III}/Mn_2^{II} states during H_2O_2 dismutation. Also the bridging carboxylate electronically shield the di-Mn center, facilitating the two-electron Mn_2^{III}/Mn_2^{II} process despite of one-electron $Mn_2^{II}/Mn_2^{II,III}/Mn_2^{III}$ processes.[15] Due to the fast kinetics of this enzymatic reaction, each independent step of the catalytic cycle of MnCATs has not yet been characterized although it has been proposed that during the catalytic cycle, manganese change its oxidation state from Mn^{III} to Mn^{II} and vice versa, although a Mn^{IV} intermediate is not completely excluded. Furthermore, H_2O_2 binding is followed by a reduction of di-manganese center with parallel oxidation of peroxide species and oxygen release. Then

another H_2O_2 molecule binds with a subsequent reduction to water and re-oxidation of the two manganese atoms (Scheme 5).[15,29,30]

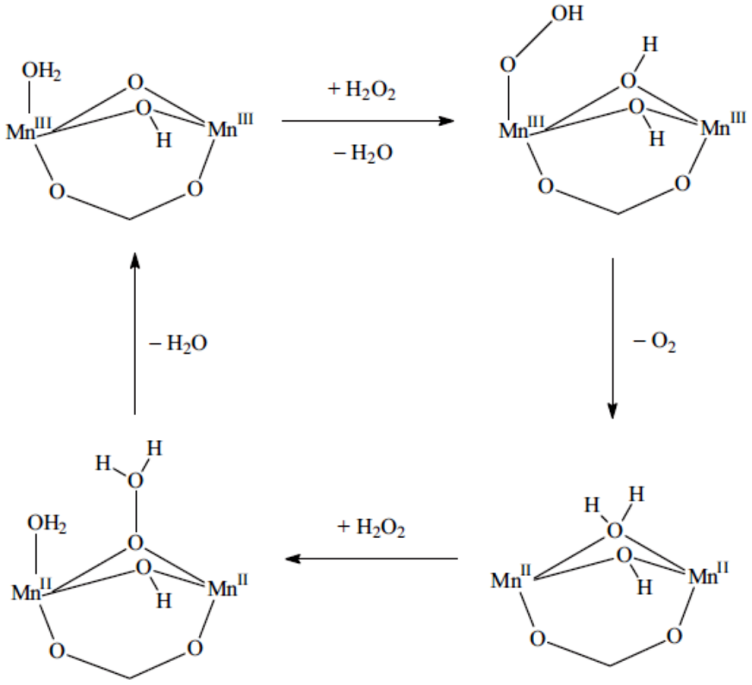

Scheme 5. Mechanism of catalytic disproportionation of H_2O_2 by MnCAT.

In MnCAT, a web of hydrogen bonds contributes to stabilize the di-Mn core with the pair of solvent bridges, making MnCAT active over a wide pH range of 5–12. The loss of catalytic activity at pH< 5 was attributed to protonation of the bridges and formation of an open form of the enzyme.[26]

Thus the proper functioning of CAT and SOD enzymes, present in most aerobic forms of life, allow the correct progress of the catalytic cascade of events involved in ROS scavenging. The lack of this mechanism of defense linked to ROS overproduction are related to many degenerative pathologies. Among these, neurodegenerative disease are the most invalidating and with dramatic social consequences. Alzheimer's disease (AD), Parkinson's disease (PD), Huntington's disease (HD), amyloidosis, but also stroke, atherosclerosis, some forms of cancer, can be connected to oxidative stress. In plants ROS damage all cell bio-polymers, resulting in their dysfunction. They activate plasma membrane Ca^{2+}-permeable and K^+-permeable cation channels, catalyzing Ca^{2+} signaling events, K^+ leakage and triggering programmed cell death.[31]

As will be shown in these chapters the study of catalytic antioxidants, like catalase and superoxide dismutase able to regulate the ROS imbalance generated by several

physiological dysfunction, seem fundamental for the design of more efficient drugs for therapy, additives for crops and also in the engineering of new functional materials.

1.3 Enzymes Analogs

One possible solution to limit ROS damages is to use natural antioxidants such as vitamins or polyphenols, but also artificial molecules like fullerene, peptide derivatives. One of the major problems is the high concentration needed of these molecules, in fact they are able to eliminate ROS according to a direct scavenging process.[32] The use of artificial enzymes, that mimic native enzymes, however with a much simpler formulation, retain a twofold advantage: (i) the multi-turnover catalytic mechanism of action, which is crucial for a sustainable loading/efficiency balance, (ii) the synthetic strategy that allows to tune structure according to expected reactivity. This bio-inspired strategy is generally conceived via the synthesis of transition metal co-factors that are shaped according to their proximal co-ordination sphere and of the outer-environment. The resulting bio-mimetic catalysts generally contain one or more metal centers, that are typically chosen to be manganese, copper and iron or other essential metals, due to their biological relevance.[33] The ligand set structure is also design along bio-inspired guidelines providing the stereo-electronic features that are expected to leverage the catalytic mechanism. At the nano-scale, secondary and tertiary structural elements can also be conceived for the assembly of enzyme analogs, which include the modification of biological proteins and the use of organic-inorganic nanoparticles, as platforms to host multi-valent functional sites dedicated to recognition, signaling, binding, and catalysis.

1.3.1 Artificial Enzymes

Semi-synthetic artificial enzymes have been designed and synthesised by the insertion of a catalytic cofactor into a natural protein scaffold. The protein, mimics the active site of an enzyme by enhancing binding and providing a chiral environment (Figure 4).[34]

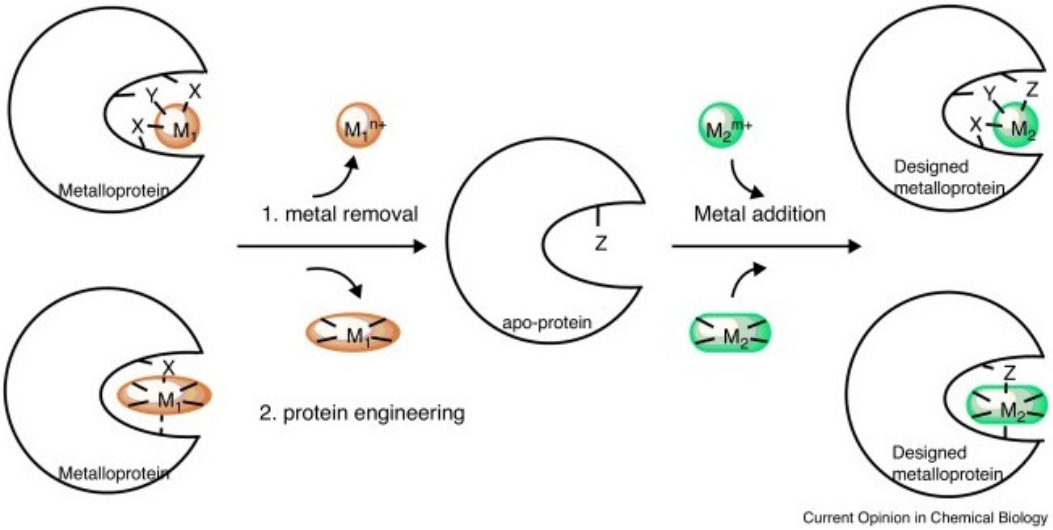

Figure 4. Summary of the main methods of using metal-binding promiscuity to construct artificial metalloenzymes. Top: substitution of metal ions bound directly to amino acid side-chains. Bottom: substitution of metals in cofactors. To incorporate alternative metals into a binding site, the apo-protein (devoid of native metal) must be synthesized first. This can be realized either by direct expression of the apo-protein, or by post-expression removal of the metal by treatment with a chelator or by denaturation. Insertion of the desired metal is then accomplished *in vitro*, by treatment with a metal ion or complex.

In proteins, metal-binding sites consist of either amino acid side-chains or ancillary ligands. These can accommodate non-native metals with similar coordination geometries and electronic properties, a property called "metal-binding promiscuity". To improve binding and function, the side-chain can be varied by protein engineering, with the incorporation of natural or unnatural amino acids, while the ancillary ligands can be chemically modified. In addition to the use of existing metal-binding scaffolds, non-native binding sites can be designed and introduced into proteins, to create artificial metalloenzymes. Some example of this synthetic strategies are reported in literature for the design of different artificial enzymes able to perform a wide a range of catalytic reaction from superoxide dismutation to cross-coupling reactions.[34–36]

Figure 5. Replacement of Cu^{2+} with Fe^{2+} in azurin leading to promiscuous superoxide reduction activity (a) and incorporation of non-native metal complexes at the place of heme in nitrobindin leads to artificial metalloenzymes (b).

A recent strategy for the incorporation of an artificial cofactor in specific locations within a protein scaffold, has been realized by taking advantage of the strong non covalent interaction between biotin and streptavidin ($K_b > 10^{14}$ M^{-1}).[37–39]

Another approach applied in the synthesis of artificial enzymes consist in recreating the enzymatic environment around the cofactor by using not the whole protein but only small biological molecules like short peptides and DNA fragments. This approach called *De novo* protein design seeks to generate a protein scaffolds whose primary sequence bears no relation to native proteins, thus identifying the basic, minimal features for function. This approach permits to evaluate the extent to which the primary and secondary coordination spheres of a metal affect a metalloprotein's activity and function. Recent papers have shown that reproducing the primary coordination sphere alone leads to valuable catalytic models.[40] Actually the most established *de novo* designed protein scaffolds consist of a helical secondary structures, which either self-assemble to form coiled coils or fold as helix-loop-helix motifs into a helical bundle, although catalytic metalloenzymes have recently been reported using β-sheet filaments (Figure 6).[41,42]

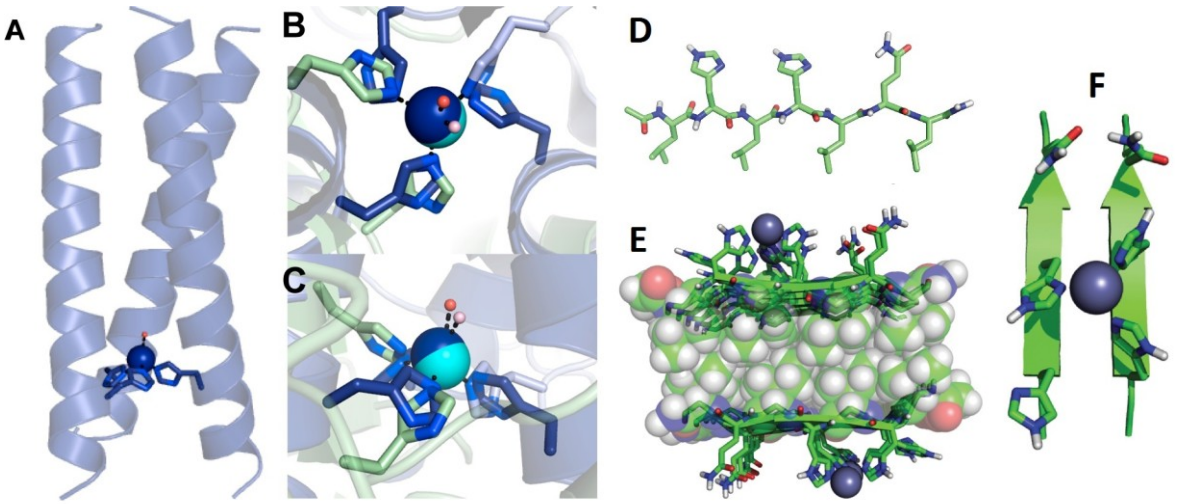

Figure 6. A model of $Cu(TRIL23H)_3^{2+/+}$ based on the helical bundle crystal structure of $Hg(II)_S Zn(II)_N(CSL19PenL23H)_3^+$ (a), top view (b), side view (c), model for one of the designed peptides (11, Ac-IHIHIQI-CONH2) in the extended β-strand configuration showing positions of the residues in the sequence, packing of the hydrophobic core (e) and zinc primary coordination sphere (f).

Artificial enzymes can also be obtained starting from DNA sequences, the chiral nano-environment and the second coordination sphere interactions provided by the DNA are key to achieve high enantioselectivities and, sometimes additional rate accelerations in catalysis.

DNA-based hybrid catalysis was introduced 10 years ago, placing a catalytically active transition metal complex in close proximity to DNA using either supra-molecular or covalent anchoring approaches (Figure 7).[43–45]

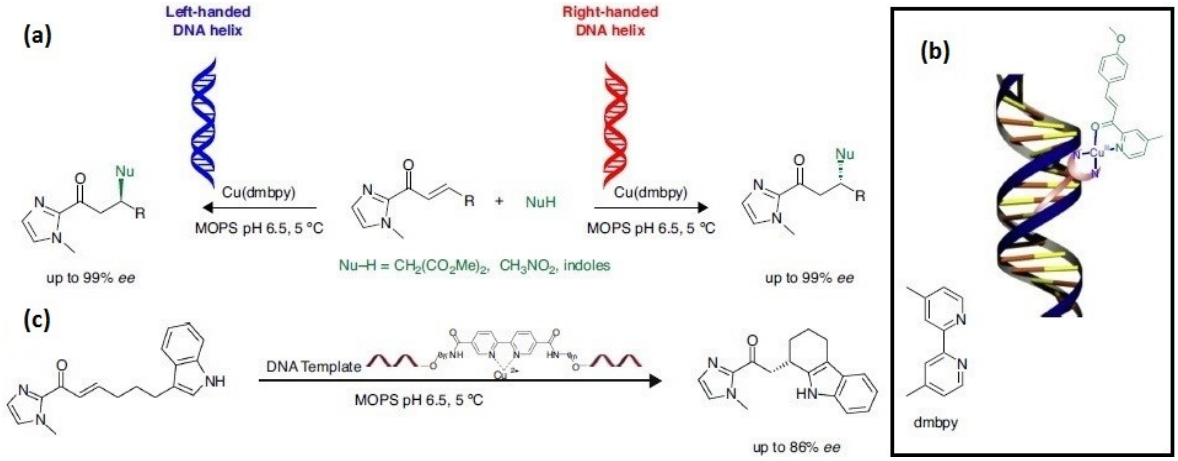

Figure 7. Asymmetric L and D-DNA-based copper catalyzed Michael reactions (a),binding of substrates to Cu(II)-dmbpy in DNA-based catalysis and DNA-based intramolecular Friedel-Crafts alkylation catalyzed by a DNA-based hybrid catalyst with intrastand ligand (c).

DNA-based hybrid catalysis concept has proven to be very powerful in combination with Lewis acid catalysis, there are still not many functional examples.

1.3.2 Synzymes

Synthetic enzymes "synzymes" are coordination complexes, consisting in a proper set of ligand having the function to tune the properties of the metals centers. The architecture of this complexes, simpler if compared with the biological scaffold of the artificial enzymes, have the function to mimic the first coordination sphere of the cofactor of the natural born enzymes recreating in this way their active core without the need to reproduce the complexity of the whole structure. It was already demonstrated for several compounds that the reconstruction of the first coordination sphere around a metal center, is sufficient to obtain a relevant biomimetic activity.

This approach has been successfully accomplished in the mimicry of antioxidant enzyme, like SOD (see paragraph 1.4.2).[40,46] This modular ligand/metal approach, due to its high versatility, has been already exploited within almost every area involving catalytic processes and applied medicinal chemistry, organic synthesis and green energy production.[47–49]

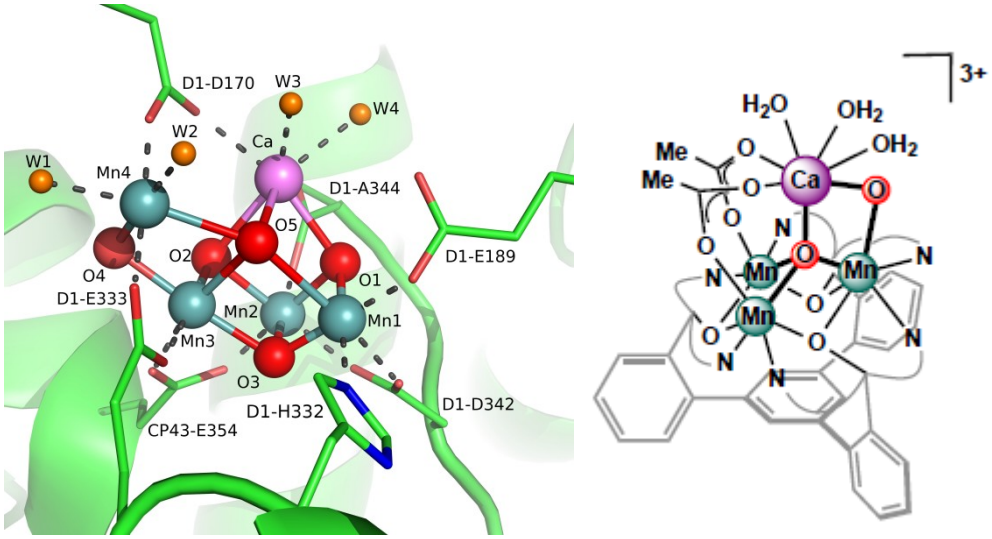

Figure 8. Structure of OEC from single crystal X-ray (left) and correspondence synzyme (right).[50,51]

Small change on the ligand structure permit also a fine tuning of catalyst properties and a deep study of the parameters that influence its reactivity like geometry , redox potential, hydrogen bonding properties etc.

These molecular systems can be also supported and reorganized on/in other nano-scaffold like protein (as already shown), polymers, micelles, dendrimers, nanoparticles and other inorganic substrates.[52–54] In this way it is possible not only to exploit various strategies useful for the localization and delivery of the catalyst but it is also a strategy to permit the assemble multiple catalytic unit in order to obtain multifunctional system to mitigate possible denaturation or degradation side-effects.[55]

The nano-environment generated by supporting the synzyme is also able to modulate its activity by changing the local polarity of the media, facilitating the approach of substrate and increasing the selectivity and stability of the system.[52,56]

Synzymes could emerge by the combination of organic and inorganic units yielding a hybrid functional system, but example of synzymes are known arising from a totally inorganic scaffold that incorporate a bio-inspired metal core. Inorganic synzymes are mainly based on oxoclusters, a class of compounds characterized by the presence of a multimetallic structure in which metals are linked by oxygen bridge and coordinated by organic polydentate ligands. Early transition metals clusters (e.g. Zr, Hf, Ti), mixed clusters (e.g. Ti-Zr, Ag-Zr, Ti-Y Cu-Y), lanthanide (e.g. La-Zn, Ba-Ce, Sm-Ti) and also middle transition metals clusters (Fe, Cr, Mn) have been synthesized during last years.[57,58] They are usually discrete and globally neutral species, featuring different nuclearities and connectivity modes like corner, edge or face sharing of the polyhedral.[59]

Another class of inorganic/hybrid synzymes is based on polyoxometalates (POMs) an interesting class of polynuclear multicharged oxyanionic compounds of variable size (from Ångstrom to tens of nanometers) that are easily synthesized in aqueous solution using early transition metals (e.g V, Mo, W) in high oxidation state (d^0-d^1) under controlled pH, concentration and temperature conditions (see Chapter 4)(Figure 9).[60]

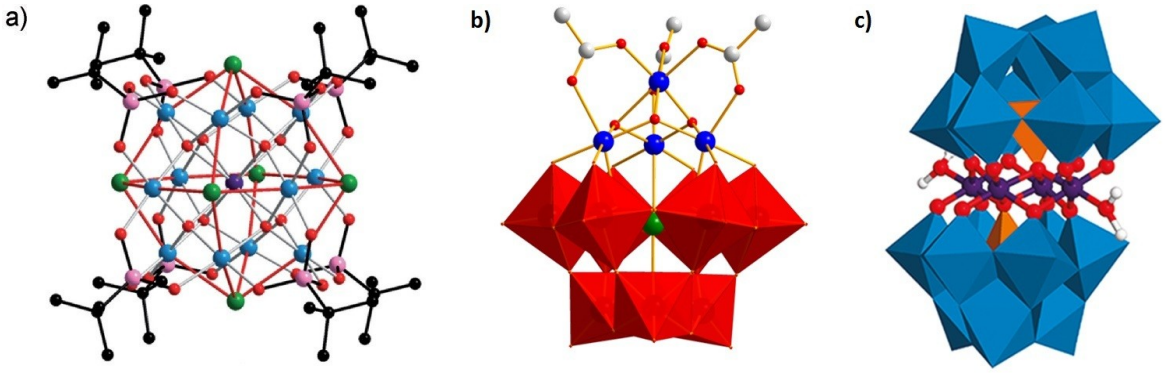

Figure 9. Crystal structure of the Mn_{12}-oxocluster (a), the hybrid Mn_4POM (b) and the totally inorganic Co_4POM (c).[61–63]

These system, in particular the totally inorganic ones, present an high robustness in oxidative condition and their anionic nature make possible the support on charged substrate and the interaction with charged domain of proteins and enzymes.[64,65]

1.3.3 Nanozymes

The artificial enzymes based on functional material (nanozymes) such as fullerene derivatives, gold nanoparticles, rare earth nanoparticles and ferromagnetic nanoparticles, have been found to exhibit unexpected enzyme-like activity.[66–72] These nanozymes have already found wide applications in numerous fields, including biosensing, immunoassays, cancer diagnostics and therapy, neuroprotection, stem cell growth, and pollutant removal. These systems, differently from synzymes, are not atomically uniform due to size and shape variations and do not try to imitate the natural enzymes although their size, shape and surface charge, enable a functional behaviour that mimic the natural enzymes.[73]

These nanomaterials are manly transition metal-oxides based (e.g. CeO_2, Fe_3O_4) or totally metal based (e.g. Pt, Au, Ag) (Figure 10). Nano-ceria is emerging as an excellent antioxidant exhibiting catalase and SOD-like activity, due to its oxygen vacancy and the presence of the mixed valence specie $Ce^{4+/3+}$. On the other hand magnetite (Fe_3O_4) is an efficient oxidant showing high peroxidise-like activity.[68,69,74] Metal based Au, Ag, Pt

nanocluster are efficient in the glucose oxidation while Pt/Au alloy nanoparticles mainly show SOD-like activity.[66,67,75]

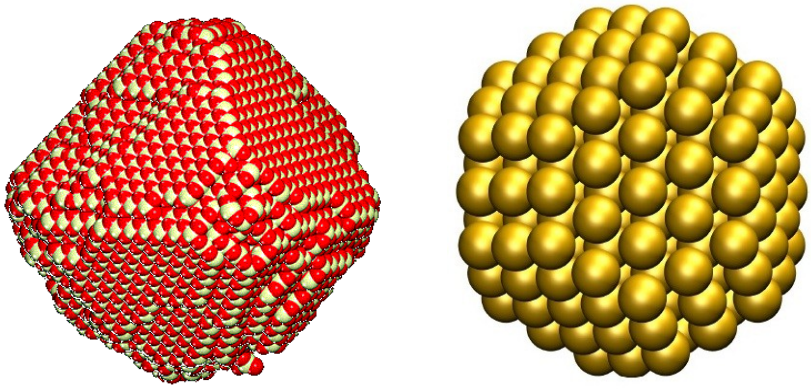

Figure 10. Model structure of ceria (CeO_2) nanoparticle (left) and gold nanoparticle (right).

Catalytic properties of nanomaterials are size-dependent. In most cases, smaller nanoparticles show a superior performance, due to a higher surface to volume ratio, but also tuning the selectivity or the reactions.[69,76,77] Shape and morphology, play also an important role in the tuning of the activity of a nanomaterials for example spheres, rods and plates of the same materials show different activity due to mainly to the different specific surface area.[78,79] The presence of a coating layer improves the nanozyme while tuning the catalytic activity. Surface coating shields the nanozyme functional core from poisoning, but at the same time may prevent the substrate access, which in turn lowers its activity. In this respect, the thickness and size of the coating layer and the packing density of the capping groups are important parameters impacting the catalytic efficiency.[69] Obviously the activity of nanozyme is dependent on the surface composition whereby alloying and doping have a key role in tuning the stereo-electronic features of the functional sites.[80,81]

Most of the nanozymes' catalytic reactions are based only on redox type reactions except for a few cases which are based on hydrolytic reactions. However, compared to the natural enzymes or to the molecular catalysts, the efficiency of most nanozymes lags behind. The up-grade of the nanozymes concept is still awaiting for a major breakthrough and their application to new types of reactions will be an hot topic in this field.[72,82] As a corollary, the toxicity of nanomaterials is a current concern and it is the object of intense investigation. Although ultra-small iron oxide nanoparticles, have been approved for clinical use, in vitro studies on related materials open a major issue on nano-material

toxicity, that in some cases have been found to induce oxidative stress, apoptosis, production of cytokines, and cell death.[83,84]

1.4 Artificial SOD and CAT mimic cofactors

Artificial SOD and CAT enzymes are receiving considerable attention, as they can establish the first "avant-garde" against oxidative stress at the biological level or under a-biotic conditions for materials protection against the aerobic risk.

In particular, mono-nuclear Mn(III) or Cu (II) species have been found to dismutate the superoxide anion while mono or dinuclear manganese complexes have been used for hydrogen peroxide dismutation. There are only few compounds reported in literature that are able to perform both reactions, and only an handful that preserve their activity in water. In the next paragraph, the design of artificial SOD and CAT cofactor will be described showing the state of the art catalysts focusing the attention on manganese complexes.

1.4.1 Mimicry of Superoxide Dismutase (SOD)

Superoxide dismutase (SOD) is a first line of defence against oxidative stress under physiological and pathological conditions. Therefore, the development of therapeutics aimed at mimicking SOD enzymes is a fundamental goal. Moreover, SOD analogues will have suitable thermodynamic and electrostatic properties for the reduction of other toxic species such as peroxynitrite, $CO_3^{\bullet-}$, peroxyl radical, and even H_2O_2 albeit with a lower efficiency. In SOD enzymes (FeSOD, MnSOD, NiSOD, Cu,ZnSOD), the catalysis occurs at the redox active metal site, which is able to easily accept and donate electrons and thus oxidize and reduce $O_2^{\bullet-}$.

The challenge of SOD design lies in the ligand set, which should form stable metal complexes and, while at the same time, facilitating the redox cycle of the metal co-factor. In particular, the following parameters should be taken in account for SOD design: (1) the metal ion redox potential has to lie between the redox potential for oxidation (-0.16 V vs. NHE) and reduction (+0.89 V vs. NHE) of the superoxide radical (Figure 11); (2) the metal ion must be able to cycle between two redox states, that differ by one electron ($M^{III/II}$ for Mn and Fe, $M^{II/I}$ for Cu), faster than the rate of the spontaneous disproportionation of superoxide radical; (3) the ligand environment must have high affinity for both the reduced and oxidized state of the metal to obtain complexes that are stable also under physiological

conditions avoiding the release of the metal during the redox turnover; (4) a minimum of one coordination site must be available for binding of the superoxide radical.[18]

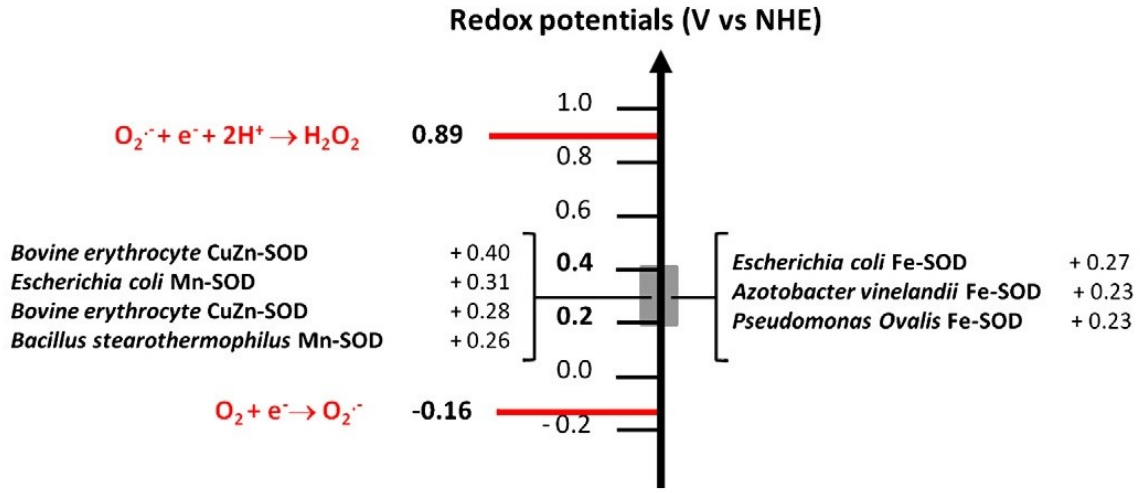

Figure 11. Redox potentials for the reduction and oxidation of superoxide radical and for several SOD in aqueous solution at pH 7.0.

The first SOD mimetics were Fe(III) porphyrin, as iron is the active site of numerous enzymes whose functions are redox based; Mn porphyrin were also investigated at a later stage. Artificial SOD include Mn salen derivatives, Mn cyclic polyamines, metal corroles but also metal salts, metal oxides and Pt nanoparticles.[46]

The activity of SOD-like synzyme can be determined by direct methods like pulse radiolysis and stopped flow analysis, in which superoxide anion is formed in *situ* and the kinetic of superoxide dismutation is followed by UV-Vis measurements. Considering indirect methods, the IC_{50} is usually measured, that is the concentration at which the SOD mimetic inhibits 50% of superoxide production, according to a nitro blue tetrazolium (NBT) or cythocrome C (cyt c) tests. From the IC_{50} is than possible calculate the catalytic rate constant k_{cat} with McCord-Friedovich method.[85]

$$k_{cat} = k_{indicator}[indicator]/IC_{50}$$

Metallo porphyrins (Mn and Fe) are among the most potent catalysts for $O_2^{\bullet-}$ dismutation, with k_{cat} analogous to SOD enzymes.[86] The reduction potential of the metal co-factor is the key factor for performance. More positive is the potential, easier is the metal reduction and better is the ability to disproportionate the superoxide radical. Decorating the porphyrins periphery with electron-withdrawing groups, in particular cationic ones, as close to the metal site as possible is the best strategy to decrease the metal electron density, which make metal more prone to accept electrons. *O*-N-alkylpyridiniumyl porphyrins are

in fact more potent SOD mimics compared with para and meta derivatives, reflecting their superior electron withdrawing power. In particular $MnBr_8$-TM-3- PyP^{4+} and $MnCl_5$-TE-2-PyP^{4+} have the highest $E_{1/2}$ = +480 and +560 mV (vs NHE) although they readily undergo metal leaching under physiological pH conditions (Figure 12). Porphyrins with very negative redox potentials ($E_{1/2}$< –190 mV vs. NHE) indeed show very low or none SOD activity.[87,88]

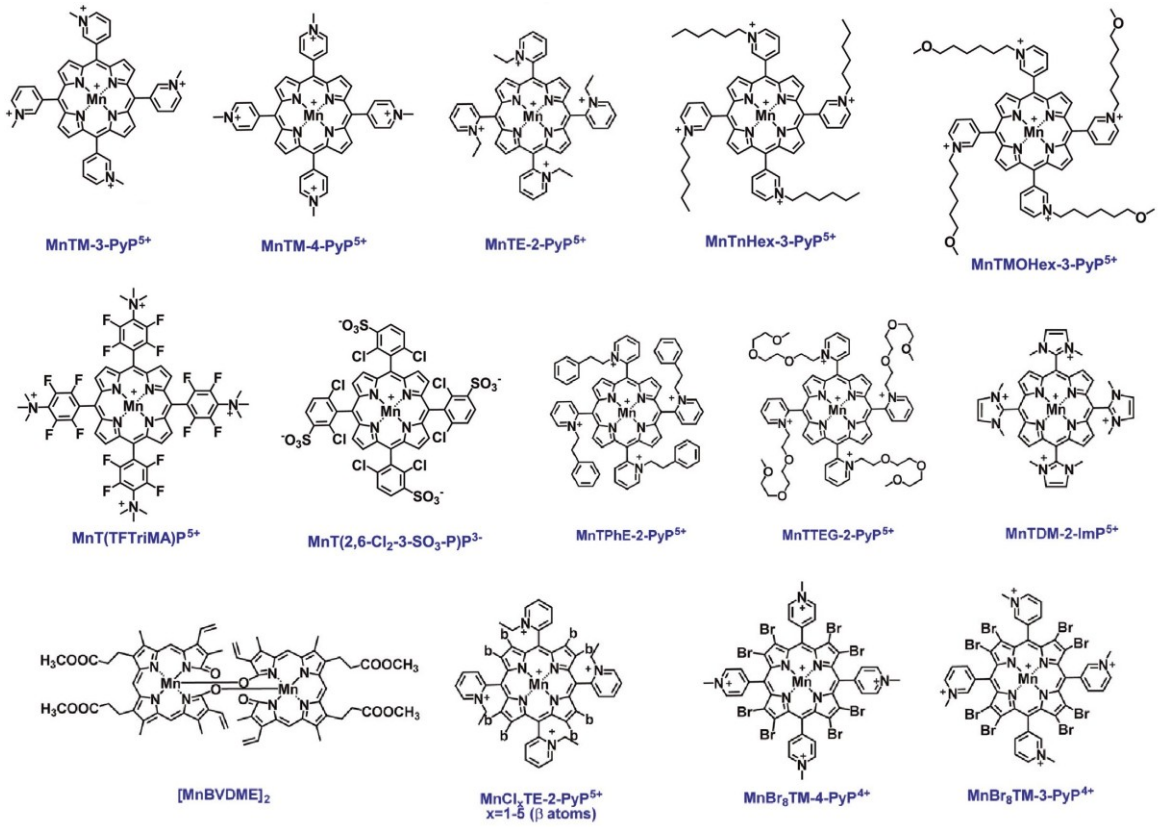

Figure 12. Schematic representation of the manganese porphyrin/corrole derivatives complexes.

The presence of positive charges, and their proximal distribution with respect to the metal center, favours the electrostatic scavenging of superoxide radical anion. However, this also poses a toxicity problem, as in the case of meso-tetra(N-methyl-4-pyridyl)porphine (MnTM-4-PyP^{5+}) due to their ability to adopt a near-planar structure and consequently to associate and intercalate into DNA.[89,90] Indeed, despite the bulkiness imposed by the water molecules axially bound to the Mn center limits the intercalation in the Mn(III) state, that is more electron deficient, in the electron-rich reduced Mn(II) state, formed during the catalytic cycle, water is weakly bound and its dissociation permits the DNA intercalation.[89,90]

This problem was solved by introducing *o*-alkypyridyl substituents or alkylated imidazolyl rings whose rotation is greatly limited due to the steric hindrance imposed by β-pyrrolic

hydrogen, and prevent the interaction with nucleic acids.[19] Tuning the length of the N-alkyl chain is also possible to modulate the lipophilicity of the porphyrin and a further toxicity reduction can be obtained by the insertion of an oxygen atom in the N-alkyl chain.[19,91]

For their high versatility and activity cationic porphyrin are the more studied and promising SOD mimic synzymes, with some compounds already in clinical trials.[47]

N,N'-bis(salicylidene)ethylenediamine, Mn-Salen complexes of Mn with (Figure 13) include derivatives EUK-8 and EUK-134, that are commercially available SOD synzymes Salen-type SODs have a fairly negative reduction potential for the $Mn^{III/II}$ redox couple, being -130mV (vs NHE), which is border-line considering the thermodynamics of $O_2^{\bullet-}$ dismutation.[92] Moreover, with only one positive charge on the Mn site, electrostatic scavenging of $O_2^{\bullet-}$ to the Mn site is depleted and while the ligand stability is lower compared to porphyrins.[93] A prooxidant activity, damaging free DNA, has been also reported for salen-type SODs.[94]

The overall SOD-like activity of salen complexes it is not so high with values of $\log k_{cat} \sim 6$ although recently an example of salen complex, (1R,3R,4S)-3,4-diazidocyclopentancarboxyamide, bearing amine apical group was reported to exhibit higher activity ($\log k_{cat} \sim 7.8$)(Figure 13 and 17). One interesting feature is that usually salen-type SODs display a combined catalase-like activity (see paragraph 1.4.2). [95]

Regarding solubility, generally salen-type SODs display a low water solubility, which is one major hurdle for in-vivo applications. [96–98]

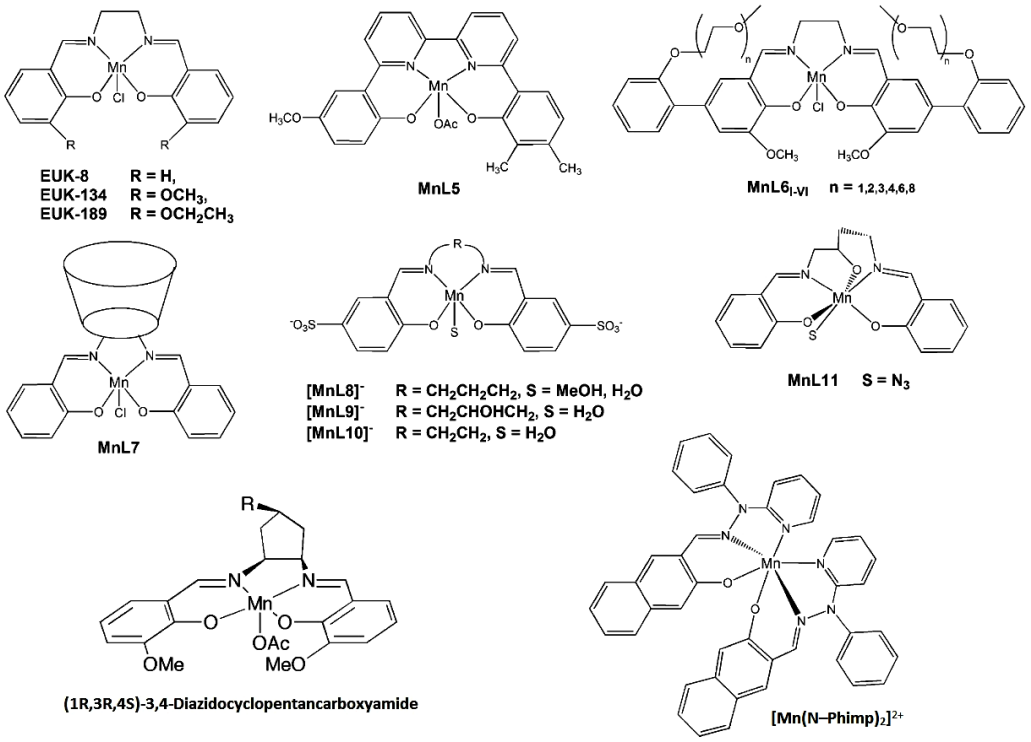

Figure 13. Schematic representation of the manganese salen/Schiff's base derivatives complexes.

The macrocycle 1,4,7,10,13-pentazacyclopentadecane has been used as a template ligand for Mn-based SOD mimetics. The Mn(II) complex M40403 is the prototype complexes of the family (Figure 14).[18,99] These type of Mn(II) complexes are proposed to function via a catalytic cycle where the rate-determining step is the oxidation of Mn(II) to Mn(III), permitted by the ligand conformational flexibility. This latter reorganizes from the planar into a folded conformation that can stabilize the necessary pseudo-octahedral geometry in the corresponding Mn(III) complex.[100,101] Interestingly, The $Mn^{III/II}$ redox potentials determined for these complexes (E ½ = 0.525, 0.464 and 0.452 V vs. NHE for M40403, M40401 and M40404, respectively) do not correlate with their SOD activity.

Regarding the reported in vivo efficacy, Mn cyclic polyamines may act as Mn transporters. Once Mn is lost from the complex, the ligand, which is an aza-crown ether with high affinity toward metals (mono and divalent), may bind other biologic cations, therefore exerting toxicity.[102]

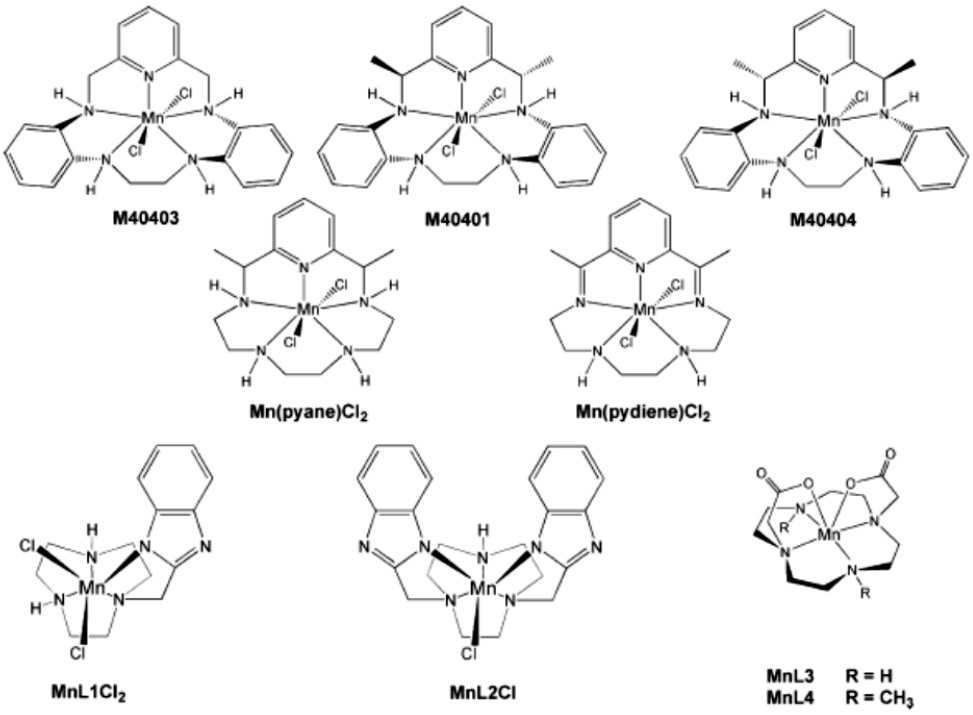

Figure 14. Schematic representation of the manganese macrocyclic complexes.

Acyclic multidentate ligands, designed to yield a bio-inspired N_3O_2 donor set, have been used to develop manganese sites surrounded by tertiary and secondary amines containing different pendant arms, namely imidazole, pyridine, carboxylate and phenolate.[103] In general this family of ligands generated mononuclear Mn(II) complexes able to scavenge superoxide anion cycling between the $Mn^{III/II}$ redox states. Studies demonstrated that the oxidation of Mn(II) to Mn(III) is the rate-limiting step, so the SOD activity ($logk_{cat}$~6-7) could be improved by stabilizing the Mn(III) oxidation state.[104] However, also these complexes had a low solubility in water.

Not only metal complexes are known to be efficient in superoxide scavenging but also nanozymes, in particular cerium oxide (CeO_2) nanoparticles have been reported to exhibit an outstanding SOD-like activity. The SOD activity of the nanoparticles is dependent on the size of the nanoparticles and the Ce^{4+}/Ce^{3+} ratio in these materials (Figure 15).[105] Polycrystalline nanoparticle preparation with 3-5 nm crystals was as effective as Cu,ZnSOD in scavenging superoxide (k_{cat} for this preparation was $3.6x10^9$ $M^{-1}s^{-1}$), preparations composed of agglomerated and relatively larger particles (5–8 nm) were less efficient.[105,106]

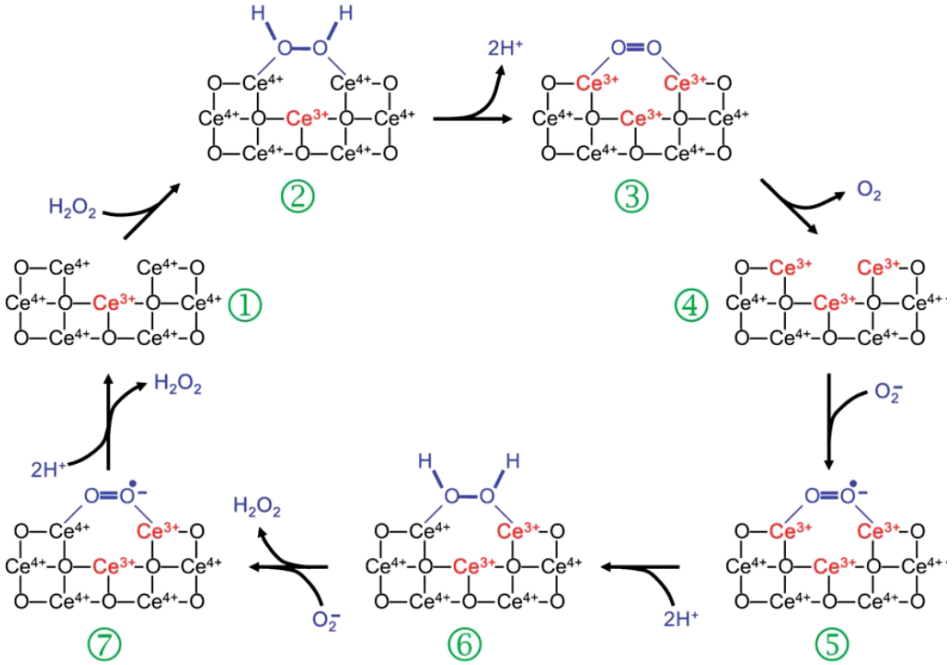

Figure 15. Proposed mechanisms of nanoceria based SOD mimic.[107]

A decrease in size of the particles is accompanied by a decrease in the Ce^{4+}/Ce^{3+} ratio, which is correlated with higher oxygen and electron vacancy in the solid. The increase in Ce^{3+} concentration at the surface has been directly related to the ability to scavenge superoxide.[105,106] Some studies on the in vitro and in vivo effects of cerium oxide nanoparticles have been reported showing a prevention of retinal degeneration induced by intracellular peroxide in rats and in vitro neuroprotection of rat spinal cord cells.[68,108]

Table 1. Literature benchmarks for natural and artificial SODs

Compound	$Mn^{III/II}$ E½/mV [a] vs NHE	IC_{50} [b] (M)	SOD activity [b] log $k_{cat}(O_2^{\bullet-})$	Reference
Mn-SOD (*human*)	~+400	$\sim 1.3\times10^{-9}$	~9.30	[109,110]
MnTM-4-PyP^{5+}	+60	6.70×10^{-7}	6.58	[111]
MnTE-2-PyP^{5+}	+228	4.50×10^{-8}	7.76	[112]
MnTDE-2-ImP^{5+}	+320	3.90×10^{-8}	7.83	[113]
$MnBr_8$TM-3-PyP^{4+}	+468	3.7×10^{-9}	≥8.85	[114]
[Mn(N–Phimp)$_2$]$^{2+}$	+143	7.6×10^{-7}	7.19	[115]
M40403	+525	2.2×10^{-7}	7.08	[18]
[MnH_2dapsox]$^{2+}$	+370	2.2×10^{-7}	7.08	[116]
Mn^{2+}	+850	2.0×10^{-6}	6.11	[88]
C_{60} water soluble	/	1.3×10^{-6}	6.30	[117]
CeO_2 nanoparticles	/	/	9.55	[105]

[a] $E_{1/2}$ is measured in 0.05 M phosphate buffer, pH 7.8, 0.1 M NaCl. [b] SOD activity and IC_{50} are measured by the cyt c assay.

1.4.2 Mimicry of Catalase (CAT)

Catalase enzymes are present in most aerobic forms of life and are responsible for the dismutation of hydrogen peroxide to molecular oxygen and water. Although most catalases contain the iron-protoporphyrin IX group, some bacteria utilize a non-heme manganese containing catalase (MnCAT).[15] The design of artificial CATs is an intriguing challenge considering that, at variance with SOD mimetics, actually no examples of efficient CAT synzymes are reported to work under physiological condition. Dismutation of H_2O_2 by Mn-CAT, occur cycling between the $Mn_2^{II/II}$ and $Mn_2^{III/III}$ co-factor oxidation states and shows a saturation kinetics on substrate, described by the Michaelis – Menten model.[27,28]

$$E + S \underset{k_{-1}}{\overset{k_1}{\rightleftharpoons}} ES \qquad ES \xrightarrow{k_2} E + P$$

$$V_0 = \frac{V_{max}[S]}{K_M + [S]} \qquad k_{cat}=V_{max}/[E_0] \qquad K_M= \frac{k_{-1} + k_2}{k_1}$$

Scheme 6. Michaelis-Menten equilibria, equation for the initial rates and kinetic constants k_{cat} and K_M.

The two parameters, k_{cat} and K_M, allow to compare artificial catalases with the natural one, indeed a Michaelis-Menten behavior is typical of an enzymatic systems. In this system, the intermediate, ES, specie is considered to respond to a steady state approximation conditions, which allows a straightforward determination of the maximum rate value (V_{max}) , the Michaelis constant (K_M) , and k_{cat} which depends from enzyme concentration. Furthermore the k_{cat}/K_M ratio is a useful parameter to evaluate the catalyst efficiency, the higher is the ratio, the higher is the catalytic efficiency. The natural enzymes display very high k_{cat} =0.3-2×10^5 s^{-1} while K_M is low (15-350 mM).[29,118]

The proposed catalytic cycle for artificial catalases is quite similar to that of the natural one, indeed the di-manganese core is expected to cycle between the $Mn^{II}Mn^{II}$ to $Mn^{III}Mn^{III}$ oxidation states whereby enabling the simultaneous reduction of hydrogen peroxide to water and its oxidation to oxygen. In the proposed cycle, (Scheme 7), there is a specific role of the bridging carboxylate ligand that opens up a Mn-coordination site for substrate binding. Indeed hydrogen peroxide coordination is envisaged to both Mn_2(II,II) and Mn_2 (III,III) redox states, whereby this latter is responsible for oxygen evolution. (Scheme 7).[30]

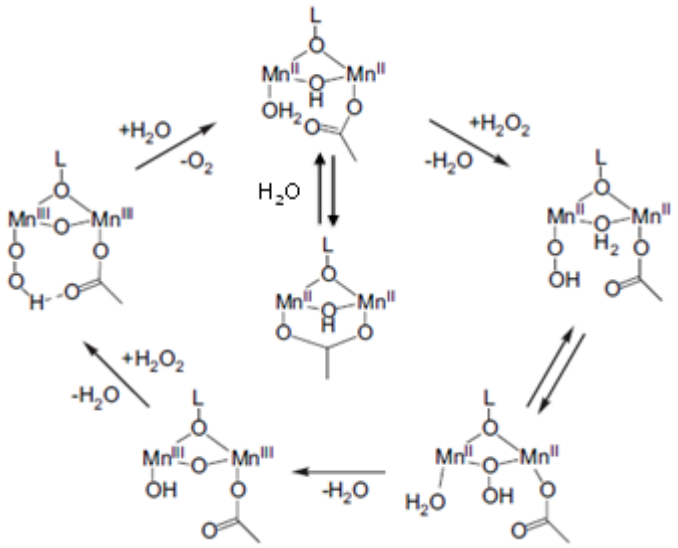

Scheme 7. Proposed catalytic cycle for artificial catalase systems with carboxylate apical ligands.

There are many literature example of CAT mimetics, containing alkoxo, phenoxo, oxo and carboxylate bridging units. Ligands can be divided in binucleating, in which one ligand coordinates two metal centers, and non-binucleating in which two or more ligands coordinate the two manganese atoms (Figure 16).[15] Since the ligand affects the Mn environment and the Mn-Mn distance, its coordination mode has a strong impact on the redox tuning of the catalytic core. High valent Mn_2^{IV} have been also traced with salen-type ligands. All these complexes should have a labile position where coordinate hydrogen peroxide, often this is occupied by a bridging carboxylate. It has been demonstrated that the presence of a carboxylate ligand could change drastically the reactivity of some complexes. Indeed if the ligand system favours the Mn_2^{II} form, catalase activity predominates, while if the Mn_2^{III} state is stabilized, catalase activity is depressed in favour of a peroxidase-like mechanism, occurring via oxygen transfer to suitable organic substrates.[119,120] To design an efficient CAT mimic synzyme the fine-tuning of Mn redox states appears as a critical feature, the electrochemical potentials (vs. NHE) for the two-electron O_2/H_2O_2 and H_2O_2/H_2O couples are +0.28 and +1.35 V, respectively.[15] The first example of a structural and functional Mn-catalase mimic has been reported by Dismukes: a dinuclear Mn_2^{II} complex based on a septadentate ligand, *N*,*N*,*N'*,*N'*-tetrakis(2-methylenebenzamidazolyl)-1,3-diaminopropan-2-ol (benzimpn), which binds two Mn ions through an alkoxide oxygen from the 2-propanol backbone, a second bridging site occupied by either a chloride or a hydroxide anion. The complex catalyzes disproportionation of hydrogen peroxide up to 200 TON (in methanol) before deactivation.[121]

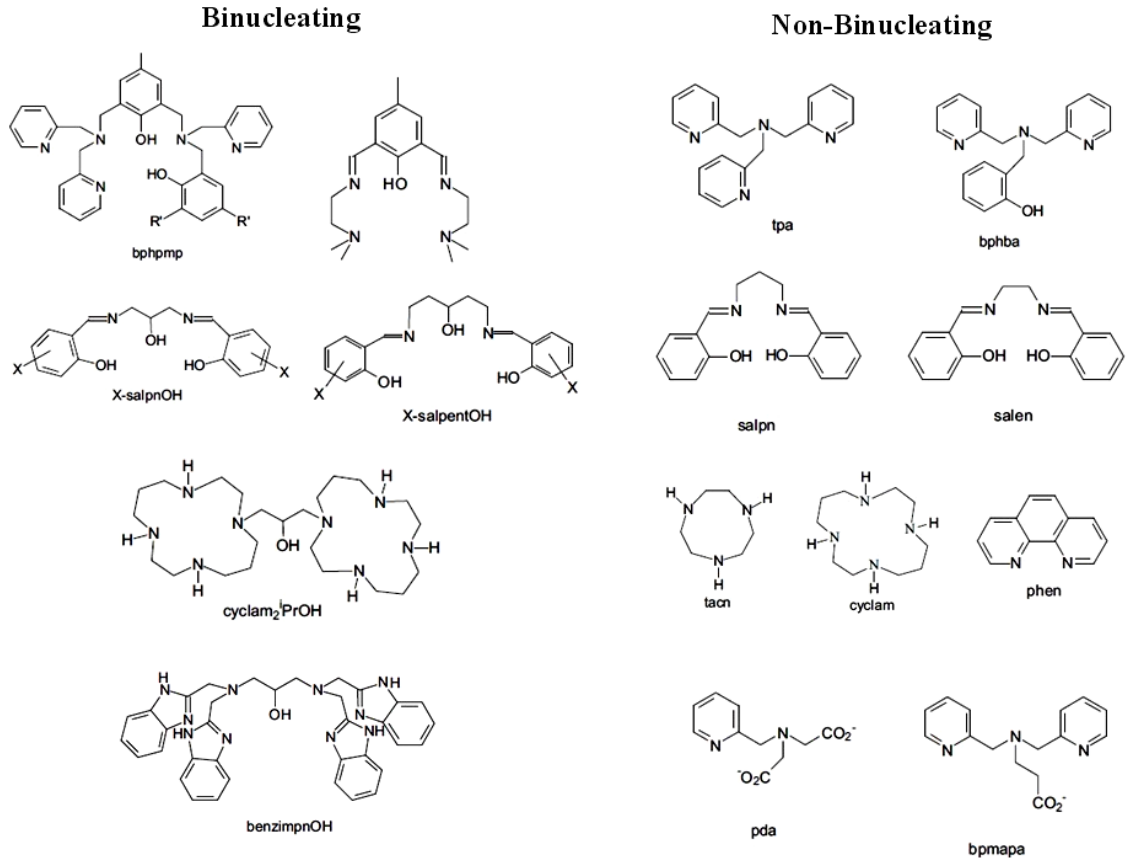

Figure 16. Some binucleating and non-binucleating ligands used in artificial dinuclear catalase synzymes.

The donor set around each Mn ion has an effect in modulating the Mn oxidation state, in fact an increase of the O/N ratio in the first-coordination sphere stabilizes the Mn-core in its higher valence state.[122,123] Dinucleating ligands which provide one phenoxo oxygen for the endogenous bridging of two metal ions, and two arms with polydentate chelating donor sets have proved to maintain the integrity of the dinuclear center through variable oxidation states.[122,123] Also the nature of the N-donor modulates the stability of the Mn oxidation state maintaining the same dinuclear structure, the imine/phenolato or imine/pyridine fragments stabilize the high oxidation states of the metal.[124] The chelate ring size is another factor to limit the stability of the dinuclear Mn complexes, chelating ligands that preclude short bonds or impose rigid distortion to the octahedral geometry destabilize the Mn^{III} state so the redox potential increase with the ring size.[15] The Mn redox potential could be also tuned by the inductive effects of the substituents, where electro-donating group generate a decreasing of the $Mn^{III/II}$ redox couple and electron-withdrawing group instead have the opposite effect.[125]

The presence of multiple carboxylate/oxo bridges is believed to have a critical role in H_2O_2 dismutation. Among complexes with the same terminal ligands, the number of bridging

acetato/oxo groups directly correlates with Mn oxidation states and CAT activity.[126] It was suggested that the lower oxidation state of Mn ions and the lower charge favour the dissociation of acetato bridge permitting the binding the substrate with the result of a CAT activity higher than for the di-Mn species in higher oxidation states presenting an oxo bridge.[127] In addition the carboxylato arms were used to mimic Glu35 and Glu148 of CAT from L. plantarum that act as proton acceptor groups during H_2O_2 disproportionation.[119]

Mono-nuclear Mn complexes have also shown CAT-like activity, which seems to be again related to the presence of at least one labile coordination position on the Mn coordination sphere.[128] Mn-salen complexes display CAT-like activity although they are not stable under catalytic condition and rapidly lose their activity.[129] These catalytic antioxidants have been proposed to react through a mechanism involving mononuclear Mn^{V}=O species or through formation of dimeric species in solution.[130–132]

The vast majority of CAT synzymes reported so-far are able to exhibit their activity only in organic solvent with a complete loss of activity in aqueous phase. The only example of catalysts that maintain their CAT-like activity in water are Mn salen and few mononuclear Mn complexes although they require basic conditions (pH>9) or additives like amines to work efficiently.[133–135] Therefore, the study of CAT-like activity of di-nuclear manganese complexes in biological media is still a frontier research area.

A recent breakthrough deals with totally inorganic synzymes based on molecular polyoxometalates. In particular, the tetraruthenate poyloxotungstate $Ru_4(SiW_{10})_2$ (Figure 68), has been found to evolve oxygen upon reaction with hydrogen peroxide in water at pH 7, with an outstanding TON >3000 (see chapter 5).[136]

CAT-like nanozymes include Mn and Fe oxides, and ceria nanoparticles that can combine SOD and CAT activity although the two activity are based on contrasting surface properties.[137–140]

Table 2. Literature benchmarks for natural and CAT mimetics

Enzymes and mimetics	CAT activity				
	k_{cat} (s^{-1})	K_M (mM)	k_{cat}/K_M ($M^{-1}s^{-1}$)	Solvent, T (°C)	References
Mn_2-CAT (*T.thermophilus*)	2.6×10^5	84	3.1×10^6	H_2O	[141]
[Mn(bpia)(μ-OAc)]$_2$	1070	32	3.4×10^4	DMF, 25	[142]
[$Mn_2(L^5)_2(Cl)_2$]*	140[e]	18[e]	7800[e]	H_2O:MeOH 98:2, 25	[125]
Mn_2(3-Me-5-SO_3-salpentO)	10.5[c]	6.6[c]	1600[c]	H_2O (pH 10.6), 25	[134]
[$Mn_3(L^1)_2$-(*μ*-OAc)$_4$]	1421[e]	1120[e]	1268[e]	H_2O:MeOH 98:2, 25	[143]
[Mn(μ-O)(salpn)]$_2$	250	250	1000	Cl_2CH_2/CH_3CN, 25	[144]
Mn_2(μ-O)(OAc)(benzimpn)]$^+$	2.7	6	450	MeOH:H_2O, 25	[30]

* data can't be reproduced, under experimental condition seem almost inactive.

1.4.3 Synzymes with dual SOD/CAT activity in water

Few synthetic catalysts have been reported to exhibit both SOD and CAT-like activity, a crucial feature to address an efficient ROS scavenging. However, only an handful of these are stable and maintain their activity in aqueous media (see previous discussion).

Actually salen-type mono-nuclear complexes have been reported to provide a dual SOD/CAT activity, in water. However, their SOD-like activity is quite low ($\log k_{cat}<6$) while the CAT-like performance is sluggish and limited by their short life-span.[15] The recent introduction of auxiliary acid−base axial ligands (Figure 17), is instrumental to enhance both SOD activity (IC_{50} = 0.044 μM) and the H_2O_2 dismutation rate and but the stability during turnover remains very low (TON=4-17).[95]

Some mononuclear Mn complexes are also been reported as dual SOD/CAT catalyst in aqueous media. These compounds, based on a seven-coordinate Mn(II) complex (Figure 17), present a higher SOD activity if compared with common salen (IC_{50}= 0.75 μM, $\log k_{cat}$ = 6.90) but their catalase activity is low and high pH >9 or additives like NaOH or imidazole are needed to reach high activity and quantitative H_2O_2 conversion (TON = 275).[135]

On the other hand, no example of di-nuclear Mn complexes, exhibiting CAT-like activity, are reported to show a combined SOD-like activity. The bi-nuclear structure enables a low-oxidation pathway for H_2O_2 dismutation with a two-electron mechanism, and therefore it controls side-reactions including self-degradation. The need of a SOD/CAT combined system is of particular importance as anti-oxidant strategy, its implementation requires a tailored synthetic design that can fulfil all the mechanistic requirements highlighted in the

previous sections. A novel approach to this objective has been investigated in this Thesis work, as described in the next section.

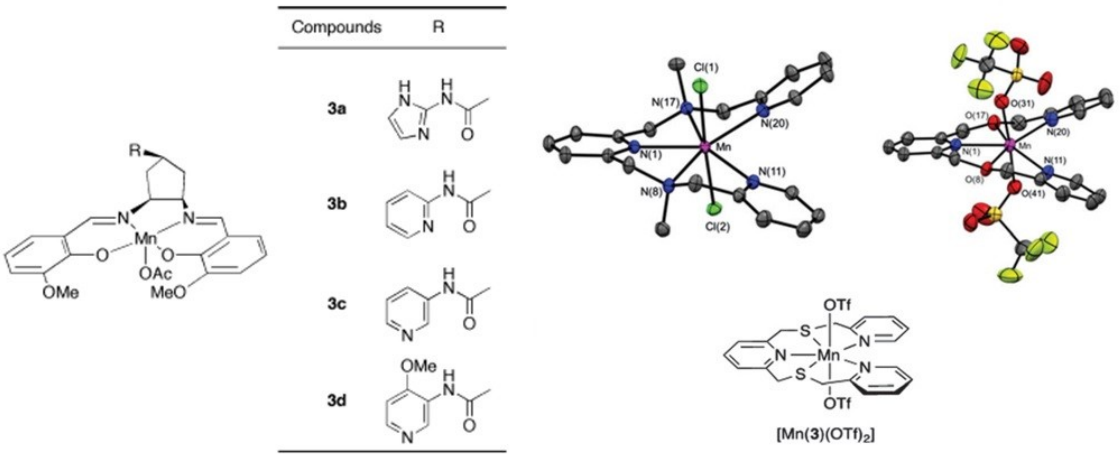

Figure 17. Dual SOD/CAT synzymes active in water.

Nanozymes based on metal oxide are recently reported as dual SOD/CAT mimic, a multi-nanozyme based on V_2O_5 nanowire served as a glutathione peroxidase (GPx) mimetic while MnO_2 nanoparticles were used to mimic SOD and CAT. Dopamine was used as a linker for the nanomaterial assembling.[145] This system was shown to be biocompatible and to exhibit an intracellular protecting effect, against oxidative stress. Also ceria nanoparticles exhibit both SOD/CAT activity although the two activity are based to an opposite design of the nanoparticle surface and so to an increase of the catalase activity correspond a decrease of SOD performance and vice versa.[105,137]

1.5 Aim of Thesis

The aim of this thesis is the synthesis and the study of functional organic complexes able to catalyze multi-electronic reaction, useful in various fields. This organic complexes are based on multidentate ligands with N and O as donors. One key idea is to pursue a novel "catalytic therapy" as alternative to conventional systemic antioxidants used as "sacrificial" scavengers against ROS induced-damage following bio-inspired guidelines. Small complexes could present several advantages as catalytic anti-oxidants compared to the native/engineered enzymes.

The main challenge was to study the effect of the nature of the ligand: coordination, donor set (N, O), nature of substituents, bridges and ligand adaptability to various oxidation state of the metal center. The first goal was to combine SOD/CAT mechanisms within the same

"synzyme", realizing a bi-functional di-zyme, containing both SOD and CAT co-factors. This latter goal has one important implication: the isolated SOD unit will cause a steady accumulation of H_2O_2, that eventually increases the risk of hydroxyl radical generation and cellular injury.

In our bio-inspired design, we have used a di-manganese complex that mimics the bacterial CAT, as a starting platform for the modular assembly of artificial SODs. These are cationic Mn(III)-porphyrins, that belong to the most active classes of SOD mimic compounds.

The resulting "di-zyme" features both SOD/CAT manifolds in their optimized stereo-electronic asset, while displaying a remarkable water solubility, and enabling a tandem catalytic action that prevents H_2O_2 accumulation. The kinetic parameters for both reactions were evaluated in vitro and the anti-oxidant effect was tested *in vivo* on green algae (Chlamydomonas reinhardtii) to evaluate the H_2O_2 scavenging.

A dinuclear Cu(II) catalyst was also synthesized and studied for its SOD/CAT activity. The goal of this study was to demonstrate that with a proper ligand set, is possible tune the reactivity of an harmful metal like copper, turns it to a benign anti-oxidant system. The novel X-ray structure, together with electrochemical and reactivity studies confirms that the Cu_2(II,II) core is an outstanding example of artificial SOD, that also displays oxygen evolution via a possible CAT-like pathway.

With the same strategy, novel di-nuclear Fe(III) and Co(II) complexes have also been isolated. Preliminary results indicate that a multi-redox manifold is available for both species and were tested in water splitting processes being able to perform both the process of water oxidation and proton reduction.

The application of oxygen evolving catalysts within functional materials has been explored in the field of porous membranes. This novel stimuli-responsive strategy against the irreversible fouling of porous materials and surfaces is based on the molecular design of catalytic pore walls that foster a chemo-mechanical, self-cleaning behaviour. To this aim, the catalase-like behaviour of the tetra-ruthenium substituted polyoxometalate, has been exploited for in-pore oxygen evolution so to induce an active fluid mixing and the displacement of foulant particles. The present study includes the fabrication of hybrid polymeric films with porous architecture embedding the tetra-ruthenium catalyst as artificial catalase to guarantee the material self-defence against pore occlusion and oxidative damage with aqueous H_2O_2 as mild chemical effector.

2. Di-zyme with dual SOD/CAT activity

2.1 Dual Strategy

The water-to-oxygen redox couple, H_2O/O_2, powers our aerobic life through the fundamental processes of natural photosynthesis and cellular respiration. Despite its vital role, any failure of this four-electron mechanism turns out to release O_2-derived toxic radicals (ROS), inducing a severe oxidative insult of any synthetic and biological materials exposed to the aerobic risk.[1,16] ROS give rise to fast, barrier-less, short-range and non-selective oxidation steps, being responsible for "oxidative stress", a key factor for cellular death, organ failure and aging diseases.[1,16] The biological defense against ROS-induced cellular damage stems from the combined action of "anti-oxidant" metallo-enzymes, as superoxide dismutase (SOD), and catalase (CAT).[14,15] A detoxification cascade occurs via SOD-induced dismutation of $O_2^{\bullet-}$ into O_2 and H_2O_2 which is then converted by CAT into H_2O and O_2 again. The SOD/CAT cascade prevents H_2O_2 accumulation and its radical-chain decomposition, thus ruling out possible reaction branching and exponential radical growth.[1,16] Moreover, oxygen is released in both SOD and CAT mediated reactions, thus mitigating any O_2-depletion causing mitochondrial dysfunction.[14,15]

Indeed, the oxygen-rich environment of photosynthetic organisms is one crucial risk-factor for photo-oxidative stress, readily induced under intense illumination, extreme temperatures and water deficit. Under these conditions, the photo-induced electron-flow generally exceeds the transport-chain capacity, so oxygen undergoes one-electron reduction forming the superoxide anion ($O_2^{\bullet-}$, the Mehler reaction), and H_2O_2 is eventually generated by its spontaneous or SOD-induced decay, or by a failure of the four electron water oxidation mechanism, collapsing to a bi-electronic peroxide-forming process.[9] Within photosynthetic organisms, the chloroplast membrane is one primary target of ROS-induced damage, so that photo-oxidative stress is one key factor limiting plant productivity, i.e. bio-mass yield and food. Noteworthy, similar parasite mechanisms of ROS-production are also lethal for the stability and performance of bio-inspired methods and materials for artificial photosynthesis.[146] As an anti-ROS strategy, the co-delivery/co-localization of overexpressed SOD/CAT natural enzymes has been studied to increase tolerance. However, the dual enzyme interplay is often plagued by their time-dependent cycles, cell-specific localization and possible system conflicts.[109,110,147] Building on these concepts, we have envisaged a novel, anti-ROS "domino defense" by joining SOD/CAT mechanisms in one synthetic architecture (Scheme 8).[95,135]

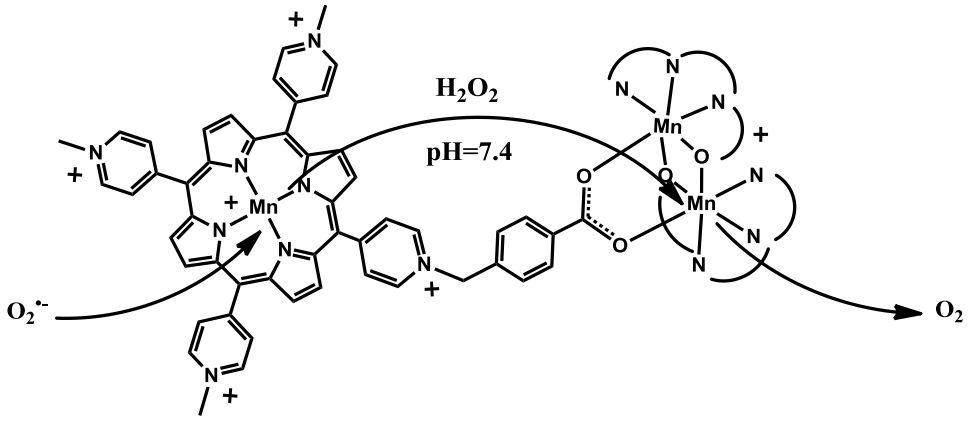

Scheme 8. Detoxification cascade envisaged for the di-zyme in water.

While SOD and CAT mimetics are generally optimized as distinct and separated units, our approach points to a dual synthetic enzyme (di-zyme) with enhanced antioxidant effect, based on the following bio-inspired guidelines: (i) SOD/CAT natural manifolds exist both as manganese forms; (ii) Mn(SOD)s have a mono-nuclear Mn(III) active site with a nitrogen-rich coordination sphere;[109,110,147] (iii) Mn(CAT)s have a di-nuclear Mn(II)-core shaped by bridging carboxylate and oxo-ligands.[118,148]

In particular, porphyrin, salen-type and other macrocyclic aza-complexes represent the state-of-the-art MnSOD mimetics (see Chapter 1).[95,135] However, single-site Mn species rarely exhibit a dual SOD/CAT regime, that usually occurs with impaired performance, and/or requiring extra additives/organic solvents for optimal catalytic turnover.[95,135] In particular Mn-salen are known to exhibit SOD/CAT activity in water, despite a quite good SOD activity (IC_{50} = 0.04-1.5 μM) they usually present a low solubility in water, are unstable in physiological condition and in presence of oxidants like H_2O_2 are able to perform only TON = 4-17.[95,135]

To face this problem, a single site Mn(III)-heme functional domain is herein implemented with a di-nuclear $Mn_2(II)L_2$ non-heme catalytic unit. Both manganese co-factors are specifically selected for a combined SOD and CAT activity and stability under physiological-like conditions (phosphate buffered saline, PBS, or Krebs-Henseleit, KH, perfusion buffer, Scheme 8).

2.2 Catalase mimic unit: Mn_2L_2Ac

The di-zyme assembly is conceived by choosing the bio-inspired $Mn_2(II)L_2Bz^+$ core, (HL = 2-{[[di(2-pyridyl)methyl] (methyl)amino]methyl}phenol), as the starting building block.[149] The di-manganese (II) complex, **$Mn_2L_2Bz^+$**, has been isolated by the Feringa's group, displaying a tetradentate pyridyl/phenolate environment, implemented by a bridging benzoate linker.[149] This dinuclear complex displays a tetra-dentate N_3O donor set provided by the bis-pyridyl, mono-amino and μ-oxo phenolate groups of the HL ligand, while the Mn apical positions are linked by an external benzoate (Bz) bridge (Figure 18).[149] The resulting $Mn_2(II,II)$-core mimics the geometrical motif and coordination environment of the natural CAT enzymes (Figure 18); however, due to a solubility issue, its CAT-like activity has been successfully demonstrated only in organic solvents (i.e. CH_2Cl_2, MeOH, CH_3CN). [55,149]

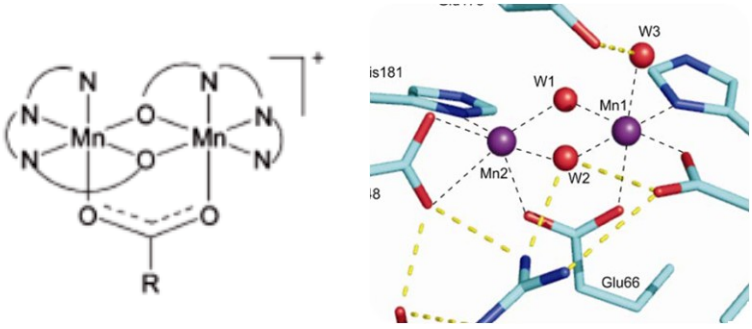

Figure 18. Comparison between catalytic cores of Mn_2L_2Bz and Mn-catalase from L. plantarum.

Our approach is based on a modification of the benzoate linker with the twofold aim of (i) extending the catalytic scope to aqueous phase; (ii) co-assembling a SOD-mimetic unit to yield the final di-zyme functional system.

As a proof-of-principle, the acetate analogue, **$Mn_2L_2Ac^+$** (Figure 19), has been readily isolated by a modified synthetic protocol, by mixing under nitrogen atmosphere a methanolic ligand and Mn(II) perchlorate solution followed by the addition of triethylamine (see Experimental Section).[149] Solution (ESI-MS, FT-IR, UV-vis and CV) and solid state characterization (FT-IR and X-ray) confirm a Mn(II)-dimer.

X-ray analysis of **$Mn_2L_2Ac^+$** shows an highly distorted octahedral geometry for both metal centres with an overall *pseudo*-C_2 symmetry, where each Mn(II) atom is coordinated in a facial configuration by the three nitrogen atoms of the tetradentate ligand, while the phenolate and acetate ligands act as a bridge between the two metal centres (Figure 19). In particular, the carboxylate anion exhibits a syn–syn μ η^1 η^1 bridging configuration,

whereby the Mn-Mn distance and the Mn−O−Mn angles of the two μ bridging phenolate residues are respectively 3.123(2)Å, 93.9(1) and 95.5(1)° (Figure 19).

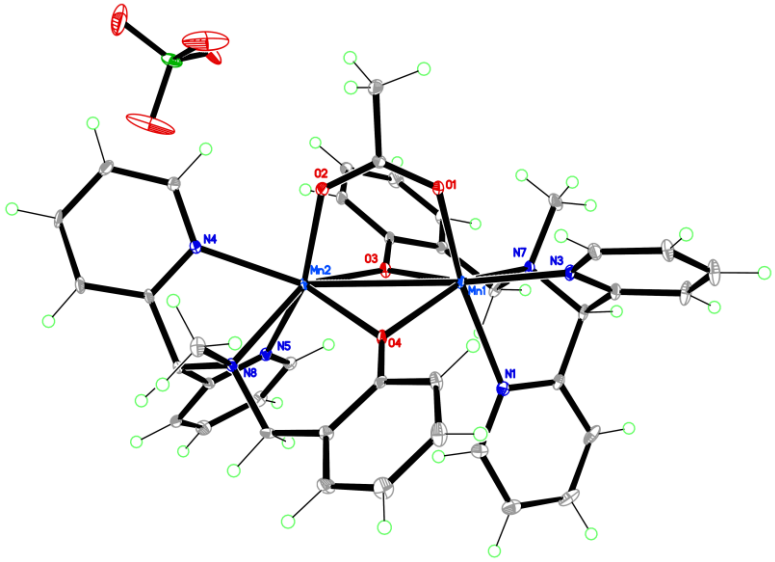

Figure 19. Crystallographic structure of $[Mn_2L_2Ac]ClO_4$.

In addition the complex presents strong IR bands at 1600 and 1576 cm^{-1} assigned to pyridine and phenolate absorptions in the Mn_2L_2 unit and two peaks at 1564 and 1450 cm^{-1} identify the anti-symmetric and symmetric stretching vibrations of the bridging acetate (Figure 20). The solution structure is confirmed by ESI-MS and FT-IR evidence (Figure 21-22).

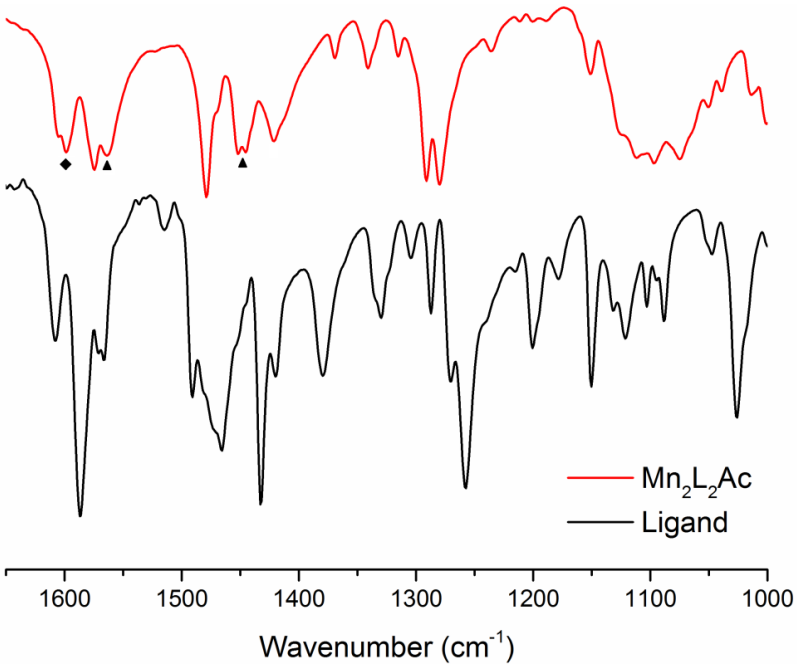

Figure 20. Stacked FT-IR spectra (KBr pellet, 1700-1000 cm^{-1} spectral region) of $[Mn_2L_2Ac](ClO_4)$ (red spectrum) and of HL (black spectrum). The bridging acetate stretchings are indicated with the full triangle symbol, while the stretchings of the aromatic residues pertaining to the organic ligand are indicated with the full diamond symbol.

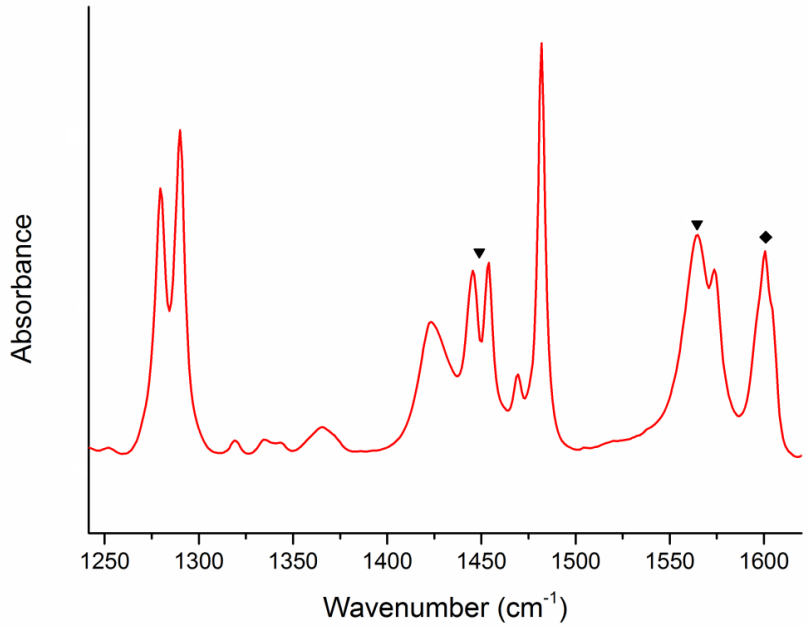

Figure 21. FT-IR spectrum of $Mn_2L_2Ac^+$ (1 mM CD_3CN solution, lightpath 1 mm, 1250-1650 cm^{-1} spectral region). Symmetric and asymmetric stretchings of the bridging acetate residue are indicated with the full triangle symbol, while the stretchings of the aromatic residues pertaining to the organic ligand are indicated with the full diamond symbol.

In particular the FT-IR, performed in acetonitrile deuterated to avoid overlap with complex signals, confirm a high stability of the complex in organic solution showing that the carboxylate bridge is maintained excluding a bridge opening or dissociation. For the complex **Mn_2L_2Ac** the same characterization could not be performed in water due to the its low solubility.

However, ESI-MS analysis performed by direct injection of a catalyst solution in aqueous media give us a clear information about the stability of the assembly in water at neutral pH observing only the presence of the molecular specie (Figure 22). In fact, despite the bridging carboxylate in water may be subjected to exchange by oxo-species, the low oxidation state of the complex (II,II), the neutral pH and the detection of only the molecular peak by ESI-MS, suggest a good stability of the complex also in water like reported for other Mn-complexes.[134,150] Stability is preserved also in saline buffer solution at pH 7.8 although, with an increasing of the pH, the strength of the carboxylate bridge is slightly decrease and also signals ascribable to water coordination to the metal centres, were detected (see Appendix).

Regarding the redox properties of the di-manganese system the cyclic voltammograms (CV) performed in acetonitrile show two irreversible anodic wave E^1_a = 1022 mV (Figure 23) and E^2_a = 1402 mV ascribed respectively to the monoelectronic $Mn_2^{II,II} \rightarrow Mn_2^{II,III}$ and

$Mn_2^{II,III} \rightarrow Mn_2^{III,III}$ oxidations. The second oxidation is reported to be overlapped with a ligand centred oxidation process (see Appendix).[125]

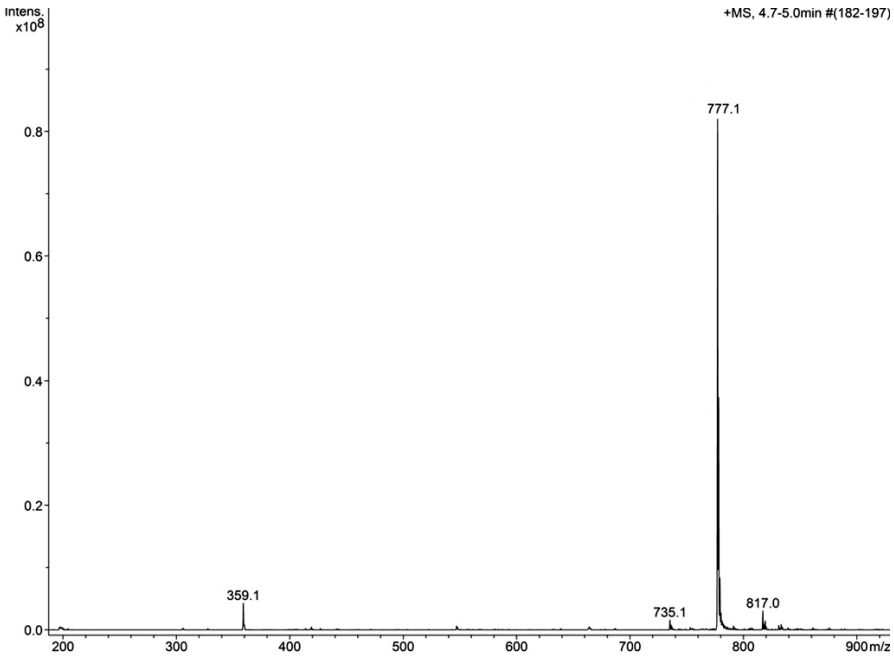

Figure 22. ESI-MS spectrum of Mn_2L_2Ac in water, where 777.1 m/z correspond to the molecular ion $Mn_2L_2Ac^+$.

Addition of water, to an acetonitrile solution of the complex, results in a steady shift of the $Mn_2^{III,II}$/ $Mn_2^{II,II}$ to lower redox potentials with an increasing of the reversibility of the process as reported in literature for other Mn complexes.[151]

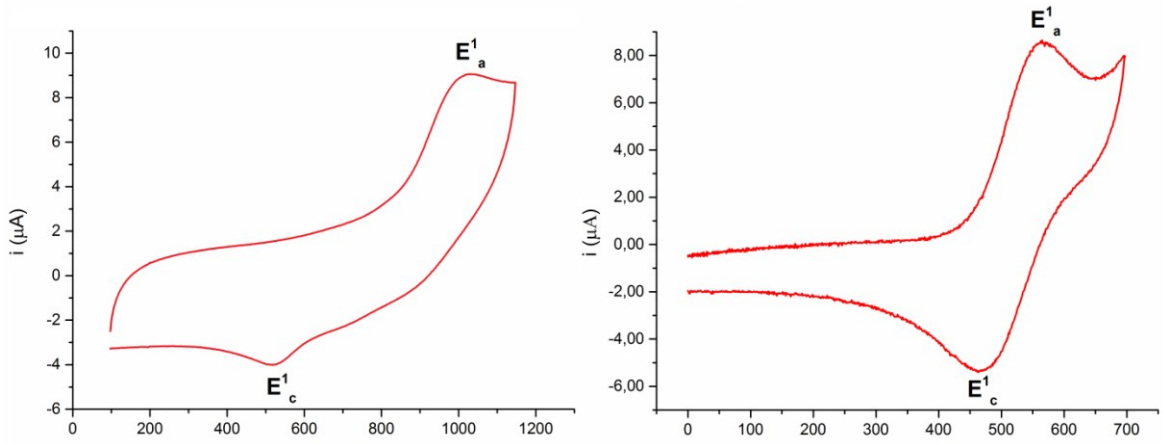

Figure 23. CV of $Mn_2L_2Ac^+$ 0.5 mM in CH_3CN ($TBAClO_4$ 0.1 M) on left, E^1_a = 1022 mV and E^1_c = 516 mV, and CV of $Mn_2L_2Ac^+$ 0.5 mM in 50 mM phosphate buffer (pH = 7.8, NaCl 0.1 M) on right, $E_{1/2}$ = 515 mV, ΔE = 102 mV. The waves are ascribed to monoelectronic $Mn_2^{III,II} \rightarrow Mn_2^{II,II}$ oxidation.

A reversible CV is an additional factor that indicates that no structural changes occur during the redox process, further confirming the stability of the carboxylate bridge.[120]

The CAT-activity exhibited by **$Mn_2L_2Ac^+$** (50 μM) towards H_2O_2 solutions (10 mM) was tested in different aqueous buffers including: borate buffer (BBS) 50 mM (pH=7.8) or Krebs-Henseleit buffer (KH) buffer (pH=7.4). The reactor was maintained at 25 °C by a thermostat, and the progress of O_2 evolution was determined by continuous detection of pressure variation, through a pressure transducer. Initial rates were calculated by linear regression of data within 10 % H_2O_2 conversion. Kinetic runs were performed in triplicate. Control experiments performed without the Mn-based catalyst, confirmed that no oxygen evolution is detected from the buffer solution in presence of H_2O_2. Inspection of data shows that **$Mn_2L_2Ac^+$**, exhibits its CAT-like activity also in water (borate buffer 50 mM pH= 7.8) with initial rate (R_0) of 27 μM O_2/s reaching complete H_2O_2 detoxification (TON=200) in 30 minutes. This unique performance has been observed also in biological-like Krebs-Henseleit buffer (KH)(pH=7.4), containing a mixture of salts (sulphates, phosphates, carbonates and chlorides) and glucose, commonly used in perfused and superfused preparation, obtaining an analogous initial rate (R_0) of 26 μM O_2/s.[152] In Figure 24 are shown the kinetics profiles. The small decrease of the initials rate in KH buffer are attributed mainly to the lower pH.[29,141]

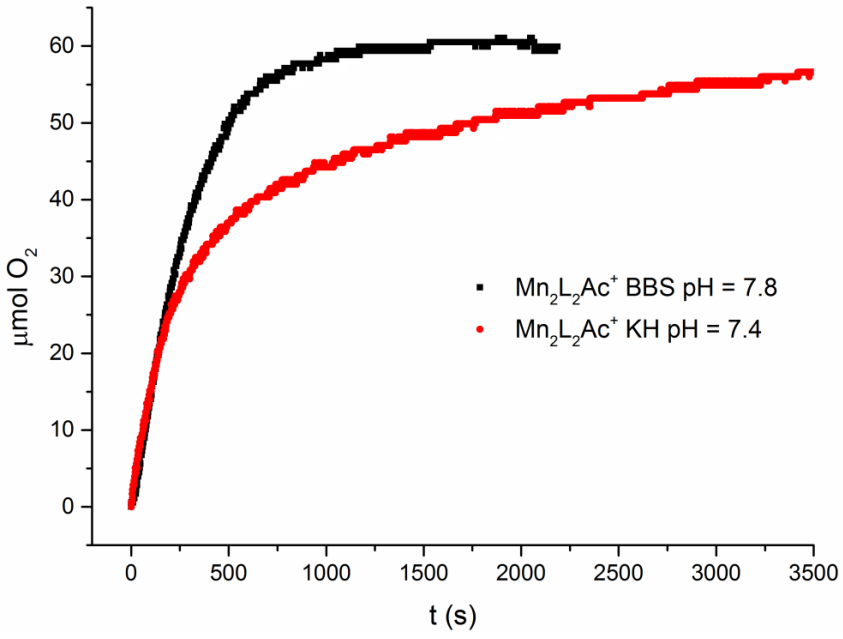

Figure 24. O_2 evolution kinetics by **$Mn_2L_2Ac^+$** (50 μmol) upon incubation with H_2O_2 (10 mM) in BBS (50 mM pH=7.8) and KH buffer (pH = 7.4).

Under the condition explored (H_2O_2 10 mM), the kinetics, show a regular behaviour, ruling out any major catalyst degradation pathways. Biphasic kinetics instead were observed at higher H_2O_2 concentration, due to a likely modification of the catalyst structure and redox

state as confirmed by CV experiments and by the formation of a brown precipitate at the end of reaction attributable to manganese oxides formation. Observing the kinetics performed in the two aqueous buffer no inhibitory effects were observed, comparing R_0, moving from BBS to KH buffer. However, the stability of catalyst seems to be affected by the salts present in solution, in particular by the PO_4^{3-} concentration. In fact using different PBS concentrations, under the same experimental condition (H_2O_2 10 mM, catalyst 50 μM), an increasing of the phosphate concentration leads to a decrease of the substrate conversion from the 100 % in 20 mM PBS to 50 % in 200 mM PBS (Figure 25).

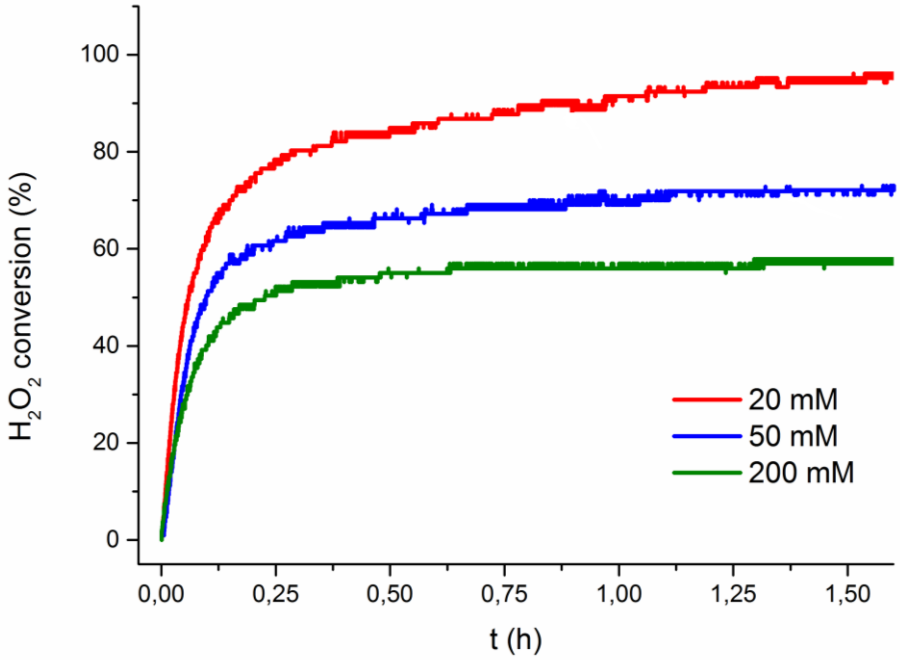

Figure 25. Effect of PBS concentration on the **$Mn_2L_2Ac^+$** (50 μM, [H_2O_2] = 10 mM, pH = 7.8) stability.

An interesting feature is that phosphate concentrations as low as 20 mM do not affect the stability of the catalyst, this means that physiological concentration of PO_4^{3-} can be considered innocent, as in the case of the KH buffer ([PO_4^{3-}] = 1,2 mM).

A saturation behaviour, amenable to a Michaelis-Menten treatment, has been verified for **$Mn_2L_2Ac^+$**, and the *turnover* number k_{cat}, the Michaelis constant K_M and k_{cat}/K_M were determined. To evaluate the Michaelis-Menten parameters, a solution of catalyst was added to a degassed solution of BBS 50 mM (pH=7.8) at different H_2O_2 concentrations (0.1-10 mM). The reactor was maintained at 25 °C by a thermostat, and the progress of reaction was determined by monitoring the dissolved oxygen concentration into a closed vessel with a Clark electrode. The k_{cat}/K_M value of 1245 place this catalyst between the best synzymes for CAT activity in water (Figure 26), with a unique behaviour maintained also under saline, KH buffer, conditions.[14,15]

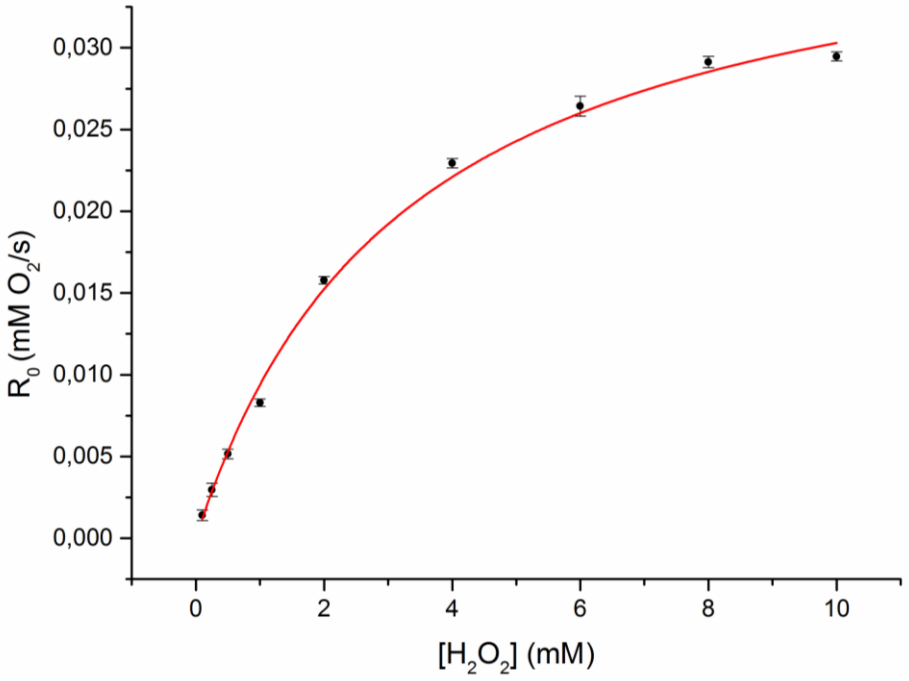

Figure 26. Effect of the H_2O_2 concentration on the initial rate of H_2O_2 disproportionation at 25 °C in a BBS buffer pH=7.8, [Mn_2L_2Ac]= 10 μM.

Comparing the values of k_{cat} and K_M with those of natural catalases, the *turnover* value k_{cat} is much lower respect to the natural enzyme, but the lower value obtained for K_M, index of a high affinity of the synzyme for the substrate, permits an efficient H_2O_2 scavenging.

Due to its promising redox properties, $E_{1/2}$ = +515 mV (vs NHE), **$Mn_2L_2Ac^+$** was also tested to evaluate its potential SOD-like activity, using the Xanthine oxidase/cytochrome *c* (cyt *c*) protocol, to evaluate the $O_2^{\bullet-}$ scavenging rate.[87] Reduction of cytochrome *c* was followed at 550 nm in 0.05 M phosphate buffer, pH 7.8 in presence of 15 mg/ml of catalase.[85] Since IC_{50} values are dependent upon the screening/detection conditions, apparent kinetic rates were calculated by the equation proposed by McCord and Fridovich with $k_{cyt\ c}$= 2.6 x 10^5 $M^{-1}s^{-1}$. The following equation was used for the calculated values of $k_{cat}(O_2^{\bullet-})$ reported in Table 3.[135]

$$k_{cat}(O_2^{\bullet-}) = k_{cyt\ c} \cdot [\text{cyt c}] / IC_{50}$$

The complex shows a SOD-like activity with $\log k_{cat}(O_2^{\bullet-})$ = 6.40 (IC_{50} = 1.04 μM) a value that sets **Mn_2L_2Ac** in the average of performance with the other non-heme manganese complexes reported in literature.[46] However, SOD-like activity is commonly reported only for mononuclear manganese complexes so the unreported SOD activity of the synzyme is an additional element of interest to take in account in the di-zyme design.

Concluding the synzyme $\mathbf{Mn_2L_2Ac^+}$ presents a dual CAT/SOD activity but it's only slightly soluble in water (~ 100 μM), a first landmark to increase complexity for multi-functionality in aqueous phase, and its SOD-like activity need to be improved to obtain a more efficient detoxification.

The tuning of the reactivity of the complex $\mathbf{Mn_2L_2Ac^+}$ was explored by small modification of the ligand. A structural analogue of the complex $\mathbf{Mn_2L_2Ac^+}$ was obtained by using directly as ligand the precursor of L, 2-({[Di(2-pyridyl)methyl]amino}methyl)phenol (L^1), that presents a secondary amine on the central nitrogen. This ligand should led to the formation of a di-Mn complex with a more accessible catalytic core due to a lower steric hindrance. In addition the presence of secondary amines close to the metal centres should facilitate the approach of the substrate and also the proton transfer processes, increasing in this way the rate of reaction.

X-ray analysis of $\mathbf{Mn_2L^1{}_2Ac^+}$, shows a structure analogue to $\mathbf{Mn_2L_2Ac^+}$ with a highly distorted octahedral geometry for both metal centres with an overall *pseudo*-C_2 symmetry, where each Mn(II) atom is coordinated in a facial configuration by the three nitrogen atoms of the tetradentate ligand, while the phenolate and acetate ligands act as a bridge between the two metal centres (Figure 27). In particular, the carboxylate anion exhibits a syn–syn μ η^1 η^1 bridging configuration, whereby the Mn-Mn distance and the Mn−O−Mn angles of the two μ bridging phenolate residues are respectively 3.11 Å, 93.6 and 92.8° (Figure 27).

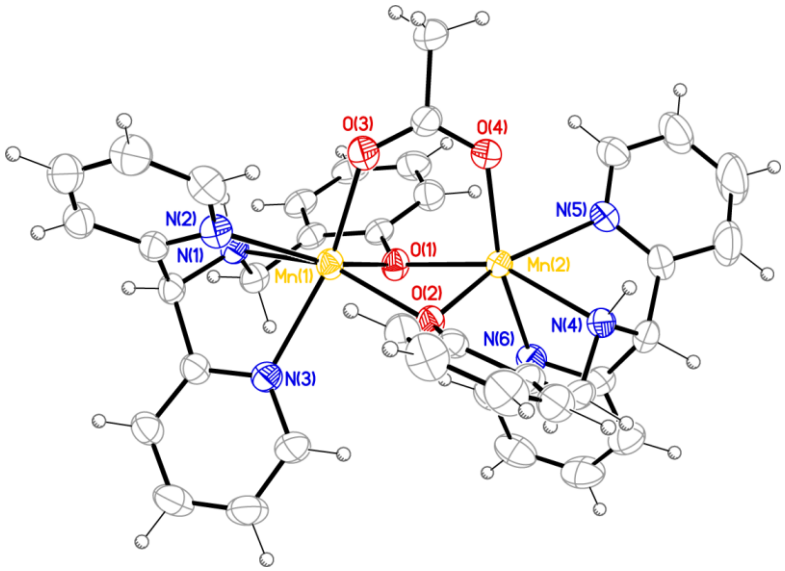

Figure 27. Crystallographic structure of $[Mn_2L^1{}_2Ac]ClO_4$.

The crystals obtained show a low air stability and turn from pale yellow to dark brown in a couple of days. This is probably associated to an oxidation of the manganese centres to $Mn^{II} \rightarrow Mn^{III}$ redox state.

The complex presents a strong IR band at 1600 cm^{-1} assigned to pyridine and phenolate absorptions in the $Mn_2L^1_2$ unit and two peaks at 1563 and 1470 cm^{-1} identified as the anti-symmetric and symmetric stretching vibrations of the bridging acetate (see Appendix).

The ESI-MS analysis of $\mathbf{Mn_2L^1_2Ac^+}$ were performed by direct injection of the sample both in acetonitrile than in water to obtain information about the assembly also in solution. The analysis performed in acetonitrile show only the presence of the molecular ion $[\mathbf{Mn_2L^1_2Ac}]^+$ with 749.1 m/z. The situation changes when analysis is performed in water (Figure 28).

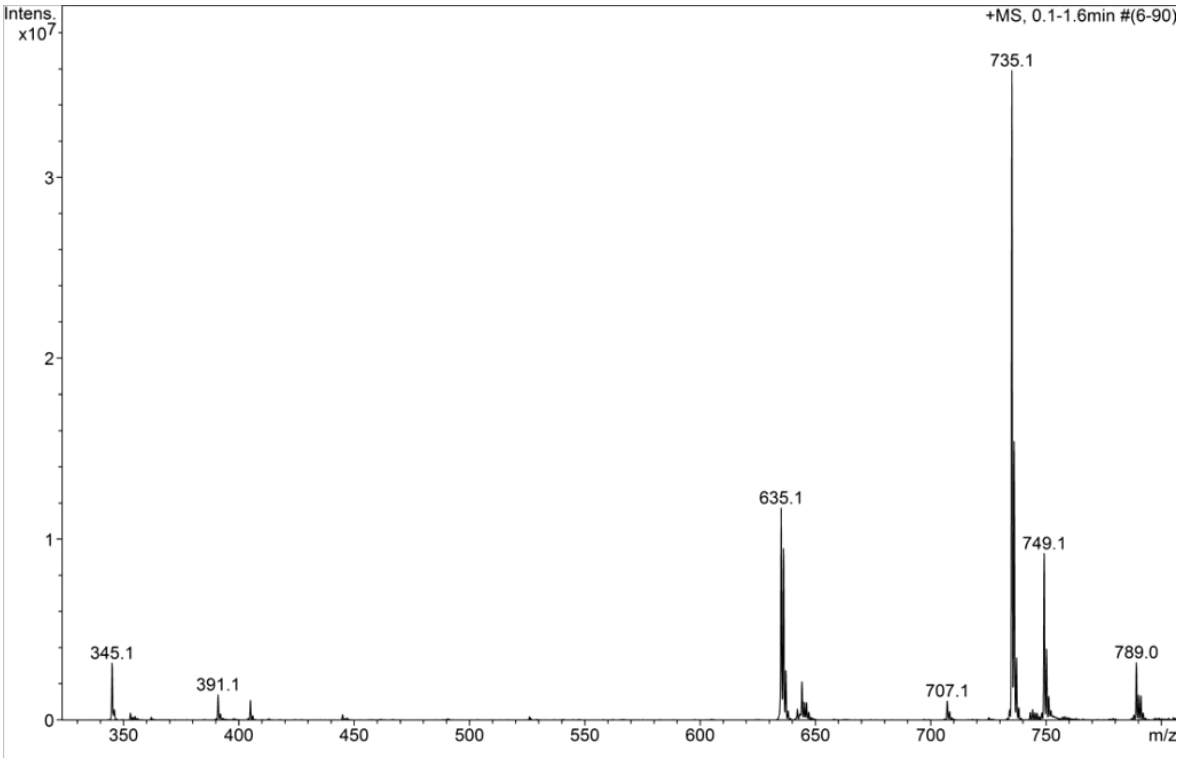

Figure 28. ESI-MS spectrum of $Mn_2L^1_2Ac$ in water, where 749.1 m/z correspond to the molecular ion $Mn_2L_2Ac^+$ and 735.1 m/z to $[Mn_2L_2+HCOO]^+$.

The complex seems to rapidly exchange the acetate with the traces of formic acid present in the ESI-MS. This could be considered as a consequence of the more accessible manganese sites leading the formation of a complex in which the carboxylate bridge is more labile.

Regarding the redox properties of the di-manganese complex, the cyclic voltammograms performed in acetonitrile show two irreversible anodic waves E^1_a = 916 mV (Figure 29) and E^2_a = 1336 mV ascribed respectively to the monoelectronic $Mn_2^{II,II} \rightarrow Mn_2^{II,III}$ and $Mn_2^{II,III} \rightarrow Mn_2^{III,III}$ oxidations. The second oxidation is reported to be overlapped with a ligand centred oxidation process (see Appendix).[125]

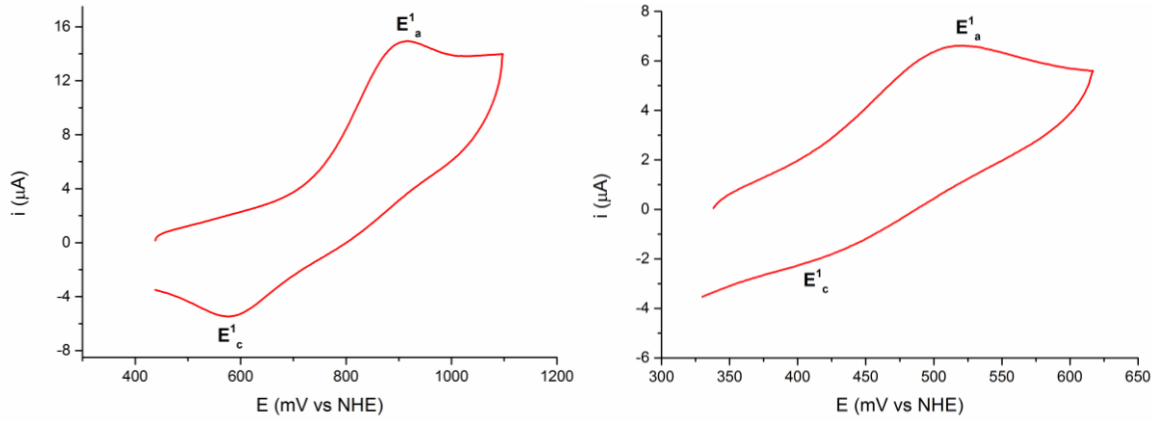

Figure 29. CV of $Mn_2L^1{}_2Ac^+$ 0.5 mM in CH_3CN ($TBAClO_4$ 0.1 M) on left, $E^1{}_a$ = 916 mV and $E^1{}_c$ = 577 mV, and CV of $Mn_2L^1{}_2Ac$ 0.5 mM $^+$ in 50 mM borate buffer (pH = 7.8, NaCl 0.1 M) on right, $E^1{}_a$ = 520 mV and $E^1{}_c$ = 408 mV,. The waves are ascribed to monoelectronic $Mn_2^{II,II} \rightarrow Mn_2^{II,III}$ oxidation.

Addition of small amounts of water, to an acetonitrile solution of the complex, results in a shift of the $Mn_2^{II,III}$/ $Mn_2^{II,II}$ couple to lower redox potential. However, contrary to **Mn_2L_2Ac**, no increase in the process reversibility was observed in agreement with the lower stability of the complex in water. The irreversible wave observed indicate a change in the coordination sphere of the complex ascribable to the lost of the bridging carboxylate as suggested by ESI-MS analysis.[120]

The CAT-activity exhibited by **$Mn_2L^1{}_2Ac^+$** (50 μM) towards H_2O_2 solutions (10 mM) was tested in borate buffer (BBS) 50 mM (pH=7.8). Inspection of data shows that **$Mn_2L^1{}_2Ac^+$**, exhibit its CAT-like activity in water (borate buffer 50 mM pH= 7.8) with initial rate (R_0) of 15 μM O_2/s reaching 30 % of H_2O_2 detoxification (TON = 65) in 30 minutes. Compared to **Mn_2L_2Ac,** this complex presents lower performance in terms of initial rate and H_2O_2 conversion, due to the lower stability under the catalytic conditions (Figure 30).

Thus the presence of the bulky methyl groups in alpha to active Mn sites seem fundamental to confer stability to the system and permit high turnover.

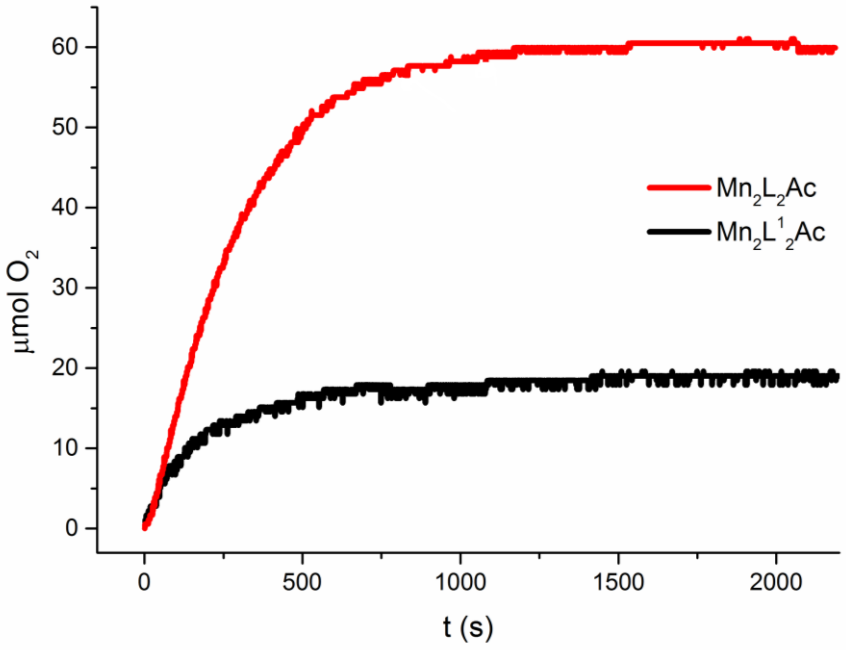

Figure 30. O_2 evolution kinetics by $\mathbf{Mn_2L_2Ac^+}$ and $\mathbf{Mn_2L^1{}_2Ac^+}$ (50 µmol) upon incubation with H_2O_2 (10 mM) in BBS (50 mM pH=7.8).

Concerning the SOD-like activity, the complex $\mathbf{Mn_2L^1{}_2Ac}$ shows a $\log k_{cat}(O_2^{\bullet-}) = 6.84$ (IC_{50} = 0.38 µM) a value that sets this catalyst between the best performing non-heme manganese complexes reported in literature. This complex presents a higher SOD-like activity if compared with $\mathbf{Mn_2L_2Ac}$. Considering the similar redox properties of the $Mn^{III/II}$ redox couple this activity increase is imputable to a more accessible manganese sites. This is due to a weaker coordination of the carboxylate bridge, but not only, the presence of an amine in alpha to the metal centre in fact can facilitate the approach of the oxygenated species to the active sites and to accelerate the catalysis by the hydrogen bonding interactions that assist the processes of proton transfer.[153]

Comparing the data obtained for the dual SOD/CAT activity of both the di-Mn complexes $\mathbf{Mn_2L_2Ac}$ has exhibited**,** despite the lower SOD activity, the better performance in terms of CAT-like activity and stability. For this reason this complex will be employed for the further studies.

To improve $\mathbf{Mn_2L_2Ac}$ properties and merge SOD and CAT domains, the Mn_2L_2 core has been further coupled with an asymmetric porphyrin scaffold bearing a poly-cationic periphery and one pendant carboxylate linker.

2.3 Superoxide dismutase mimic unit: cationic porphyrins

Inspection of literature data indicates that the SOD activity of synthetic porphyrins is mainly dictated by the Mn^{III}/Mn^{II} redox potential and by the overall positive charge.[19,154] Thus, cationic porphyrins, featuring a Mn^{III}/Mn^{II} redox potential in-between the $E_{1/2}$ for $O_2^{\bullet-}$ reduction to peroxide (+890 mV vs NHE) and its oxidation to O_2 (-180 mV vs NHE), are known to overarch neutral or anionic SOD-mimetics, with a rate increase of ca. two orders of magnitude.[19,154] Accordingly, two novel asymmetric porphyrins: Mn(III)-meso-tri(N-methyl-4-pyridyl)mono(4-carboxyphenyl) porphine (**P1**) and Mn(III)-meso-tri(N-methyl-4- pyridyl)mono(N-4-carboxy-benzyl-4-pyridyl) porphine (**P2**) have been synthesized to retain the SOD-mimicry properties, while being armed with a terminal carboxylate bridge to bind the CAT-like functional core (Figure 27).

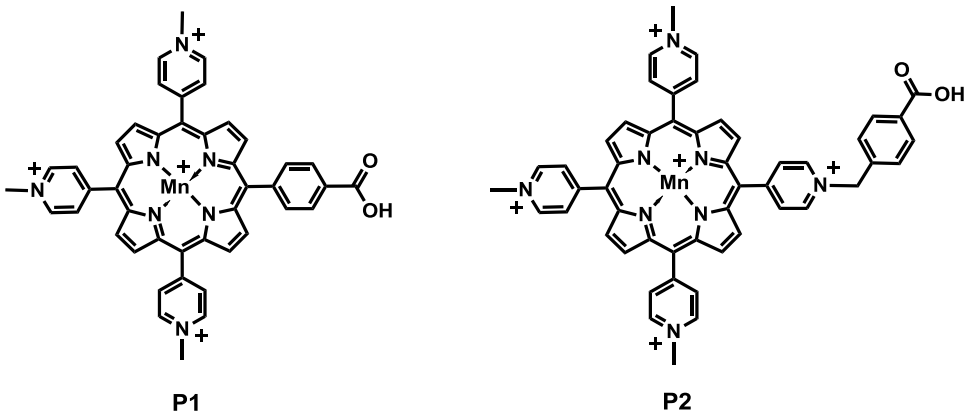

Figure 31. Cationic porphyrins with terminal carboxylate arm **P1** and **P2**.

Porphyrin **P1** is obtained in water by metallation of the commercially available free-base with $MnCl_2 \cdot 6H_2O$.[155,156] Porphyrin **P2** is obtained with a four-step protocol by alkylation of 5,10,15,20-tetra(4-pyridyl)-21*H*,23*H*-porphine with methyl 4-(bromomethyl)benzoate, permethylation with methyl iodine, methyl ester hydrolysis and anionic exchange. The metallation was accomplished with $MnCl_2 \cdot 6H_2O$ (Scheme 9, see Experimental section for synthetic and characterization details).

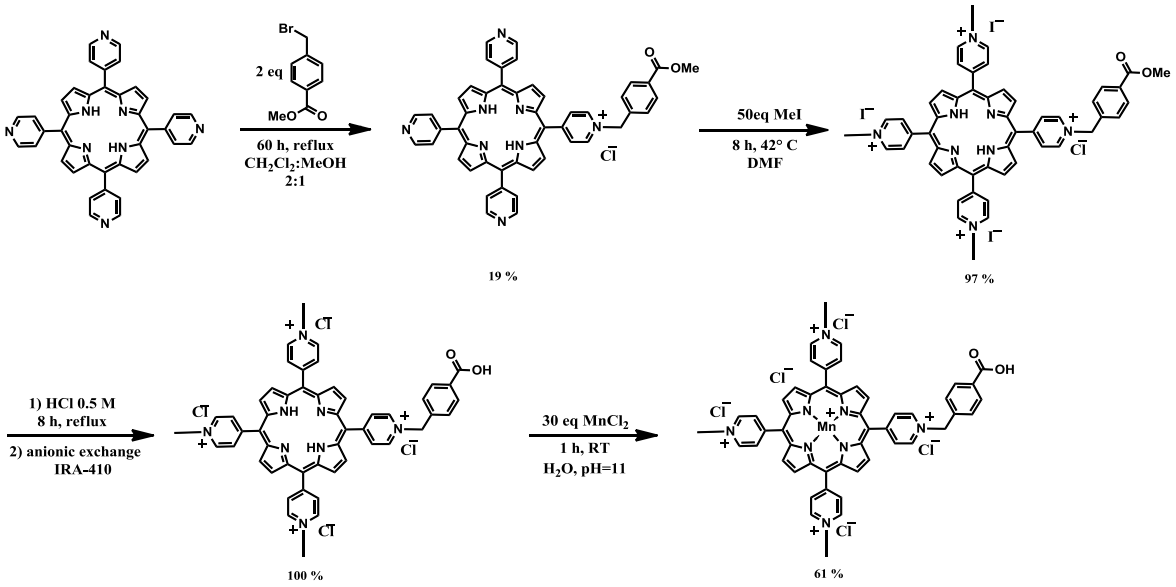

Scheme 9. Synthesis of Mn(III)-meso-tri(N-methyl-4-pyridyl)mono(N-4-carboxybenzyl-4-pyridyl)porphine (P2). Intermediates and product have been isolated, purified with chromatography and characterized by ^{1}H-NMR, ^{13}C-NMR, ESI-MS, UV-Vis spectroscopy. The isolated % yields for each step are reported in the scheme under the corresponding product structure.

Both **P1** and **P2** show the expected UV-Vis spectral signatures of Mn(III) cationic porphyrins, with the red shift of the Soret band from 420 to 460 nm and the coalescence of the Q bands, while ESI-MS confirms the overall positive charge of the heme residue (see Experimental Section and Appendix).[111]

P1 and **P2** show high solubility in water and display a reduction potential for the $Mn^{III/II}$ couple respectively at $E_{1/2}$ = - 32 mV and +10 mV (vs. NHE, PBS pH = 7.8). The more favorable reduction potential of **P2** is ascribed to a stronger electron-withdrawing effect of the porphyrin periphery with four tetra-alkylpyridiniumyl residues.[111]

The SOD-like activity was evaluated as previously reported and its value, $\log k_{cat}(O_2^{\bullet-})$ = 6.07 (IC_{50} = 2.28 μM) for **P1**, as expected is lower if compared with the analogous MnTM-4-PyP^{5+} system due the change of a pyridyl unit with the 4-carboxyphenyl moiety that, having a lower elector withdrawing effect, decrease the $Mn^{III/II}$ potential.[87] **P2** instead hold four alkylpyridiniumyl residues generating a higher electron-withdrawing effect on the manganese centre coupled with a higher positive charge, conferring to the porphyrin a higher SOD-like activity $\log k_{cat}(O_2^{\bullet-})$ = 6.87 (IC_{50} = 0.35 μM).

Regarding the possible catalase activity of the porphyrins, them do not show relevant oxygen production under the catalytic conditions screened and the low H_2O_2 conversion is ascribable to other oxidative processes in particular the bleaching of heme ligand (Figure 28). Should be underline that, like already reported in literature, a common porphyrin is

unable to scavenge hydrogen peroxide in absence of proper reducing agent and occur in a rapid degradation, in fact this is one of the weak point of heme-based catalytic antioxidants.[87,157]

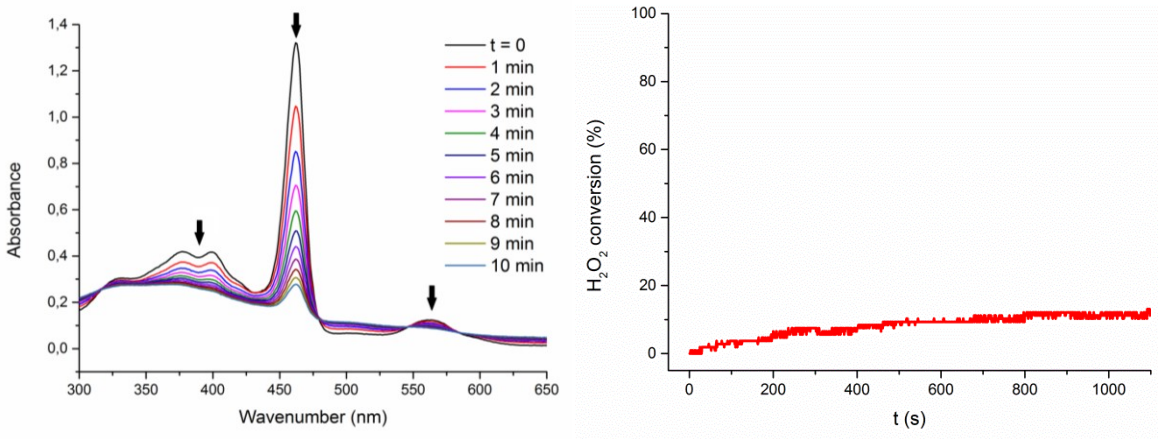

Figure 32. Representative absorbance bleaching registered over time for the Mn(III)-meso-tetra(N-methyl-4-pyridyl)porphine (10 µM) upon incubation with 50 eq of H_2O_2 in phosphate buffer solution (50 mM, pH=7.8)(left) and H_2O_2 conversion kinetics by P2 (50 µmol) upon incubation with H_2O_2 (10 mM) in BBS buffer (pH=7.8) (right).

2.4 Di-zymes

As anti-ROS strategy, the co-delivery/co-localization of overexpressed SOD/CAT natural enzymes has been studied to increase tolerance.[158,159] However, the dual enzyme interplay is often plagued by their time-dependent cycles, cell-specific localization and possible system conflicts.[158,159] Building on these concepts, we have envisaged a novel, anti-ROS "domino defense" by joining SOD/CAT mechanisms in one synthetic architecture (Figure 33).[95,135]

Mn-SOD mimetics have already entered in clinical trials and include porphyrins, salen-type and other macrocyclic aza-complexes (i.e. AEOL10150 and EUK-134, M40403).[46] However, single-site Mn species rarely exhibit a dual SOD/CAT regime, that usually occurs with impaired performance, and requires specific additives and/or organic solvents for optimal catalytic turnover.[135]

To face this problem, a single site Mn(III)-heme functional domain (**P1** and **P2**) is herein implemented with a di-nuclear $Mn_2(II)L_2$ non-heme catalytic unit.

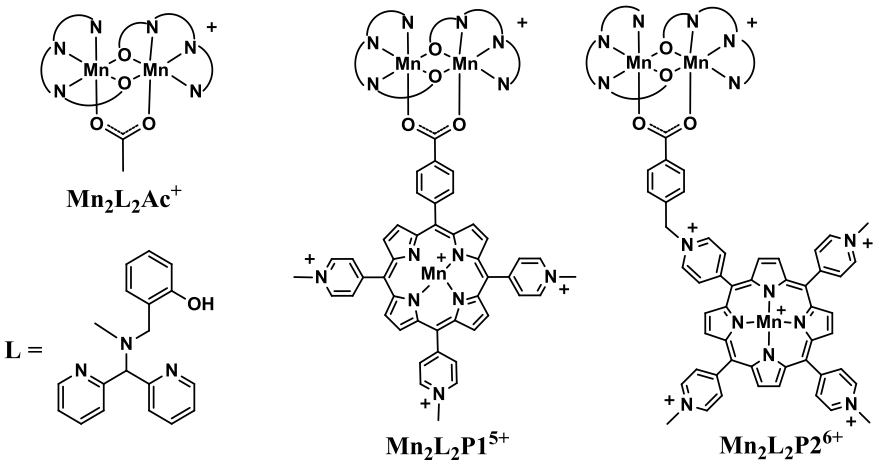

Figure 33. Dual synzyme $Mn_2L_2Ac^+$ and di-zymes $Mn_2L_2P1^{5+}$ and $Mn_2L_2P2^{6+}$.

Assembly of **P1** and **P2** with the Mn_2L_2 core is readily obtained following the synthetic protocol optimized for **$Mn_2L_2Ac^+$**, and leading to **$Mn_2L_2P1^{5+}$** and **$Mn_2L_2P2^{6+}$** respectively (see Experimental section).

Characterization of the di-zymes assembly is provided by FT-IR spectra showing the expected signatures for both heme and non-heme domains and signals arising from the carboxylate bridge. In particular, the Mn_2L_2 core bands are registered at 1600 cm^{-1} together with additional carboxylate absorptions observed at 1500-1400 cm^{-1}, that partially overlap with the porphyrin bands (Figure 34).[160]

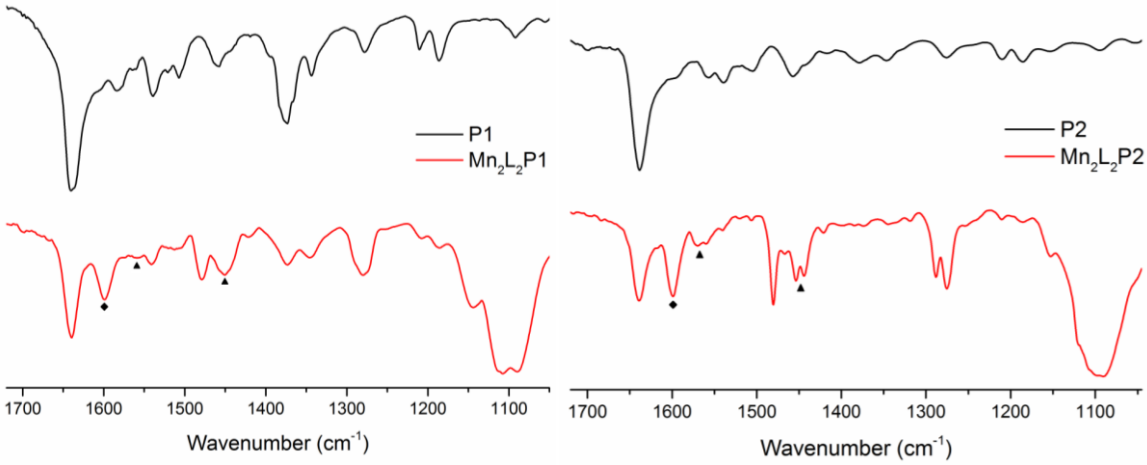

Figure 34. Stacked FT-IR spectra (KBr pellet, 1700-1000 cm^{-1} spectral region) of $[Mn_2L_2P1](ClO_4)_5$ (red spectrum) and P1 (black spectrum) (left) and $[Mn_2L_2P2](Cl)_2(ClO_4)_4$ (right). The bridging carboxylate stretchings of the porphyrin residues are indicated with the full triangle symbol, while the stretchings of the aromatic residues pertaining to the organic ligand are indicated with the full diamond symbol.

The FT-IR spectrum registered in D_2O:CD_3OD (40:60), gives a direct proof of the stability of the bridging carboxylate ligand in aqueous solution, as the relative bands can be identified around 1565 and 1450 cm^{-1} (Figure 35).

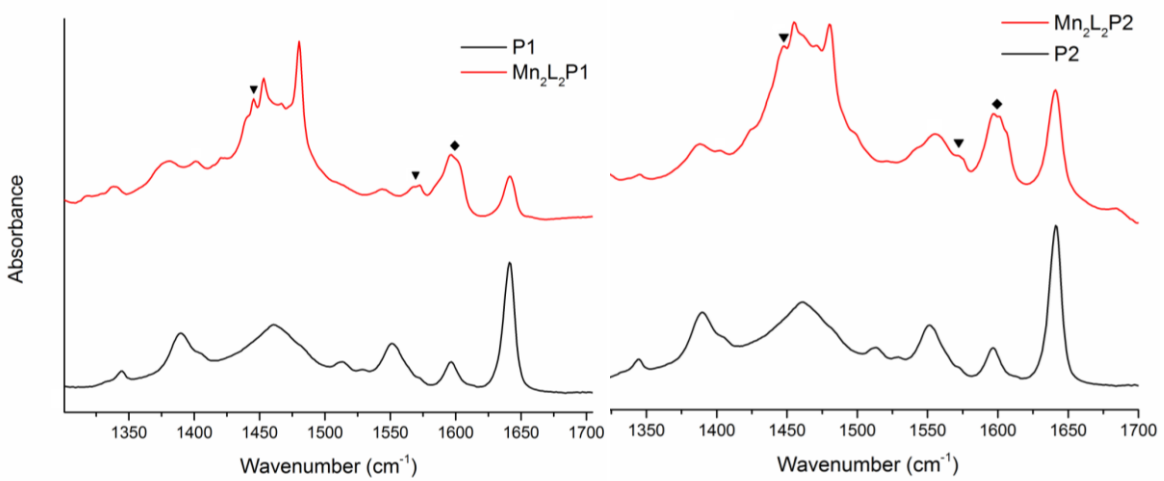

Figure 35. Stacked FT-IR spectra ($CD_3OD:D_2O$ = 60:40 solution, lightpath 0.05 mm) of $Mn_2L_2P1^{5+}$ (5 mM, red spectrum) and P1 (10 mM, black spectrum) on left and $Mn_2L_2P2^{6+}$ (8 mM, red spectrum) and P2 (10 mM, black spectrum) on right. The bridging carboxylate stretchings are indicated with the full triangle symbol, while the stretchings of the aromatic residues pertaining to the organic ligand are indicated with the full diamond symbol.

By virtue of the polycationic charge of the heme-periphery, the water solubility of both **$Mn_2L_2P1^{5+}$** and **$Mn_2L_2P2^{6+}$** is improved by ca. one order of magnitude (> 1 mM).

The redox properties of both heme and non-heme manganese sites have been determined by cyclic voltammetry (CV) experiments performed in buffer solution (0.5 mM in phosphate buffer, 50 mM, pH = 7.8). The redox potentials of the isolated components are maintained within the integrated system, with no substantial changes (Table 3), this confirms that the redox properties of Mn_2L_2 are not affected by the nature of the bridging carboxylate. Composite CV curves are thus registered for the assembled **$Mn_2L_2P1^{5+}$** and **$Mn_2L_2P2^{6+}$** systems, where multiple quasi-reversible redox features are observed respectively at $E_{1/2}$= +515, -32 mV and $E_{1/2}$= 515, +10 mV vs NHE (Table 3, Figure 36 and Figure 37).

The di-zymes, differently to Mn_2L_2 and heme units, could not be detected by ESI-MS analysis.

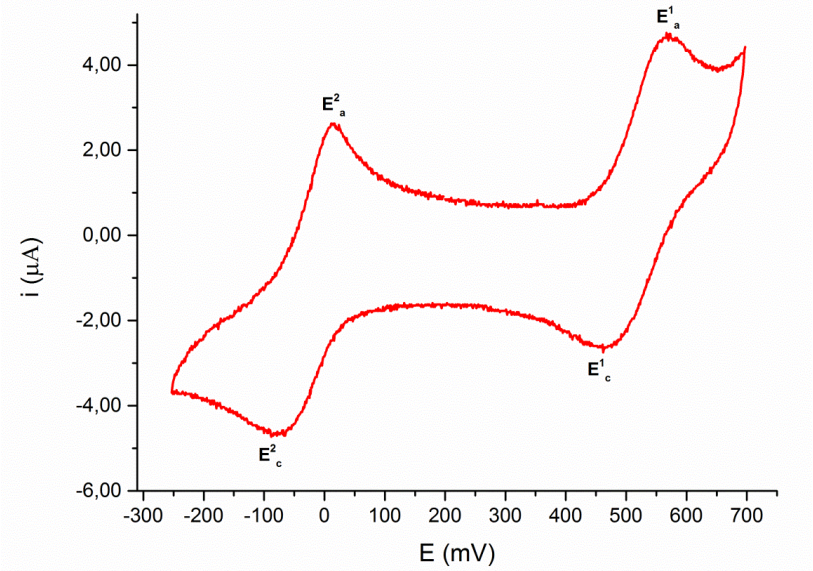

Figure 36. CV of $Mn_2L_2P1^{5+}$ 0.5 mM in 50 mM phosphate buffer (pH = 7.8, NaCl 0.1 M), $E_{1/2}$ = -32 mV, ΔE = 92 mV is ascribed to the Mn^{III}/Mn^{II} redox couple of the heme residue, $E_{1/2}$ = 515 mV, ΔE = 110 mV, is ascribed to the $Mn_2^{II,III}$/ $Mn_2^{II,II}$ redox couple of the Mn_2L_2 core.

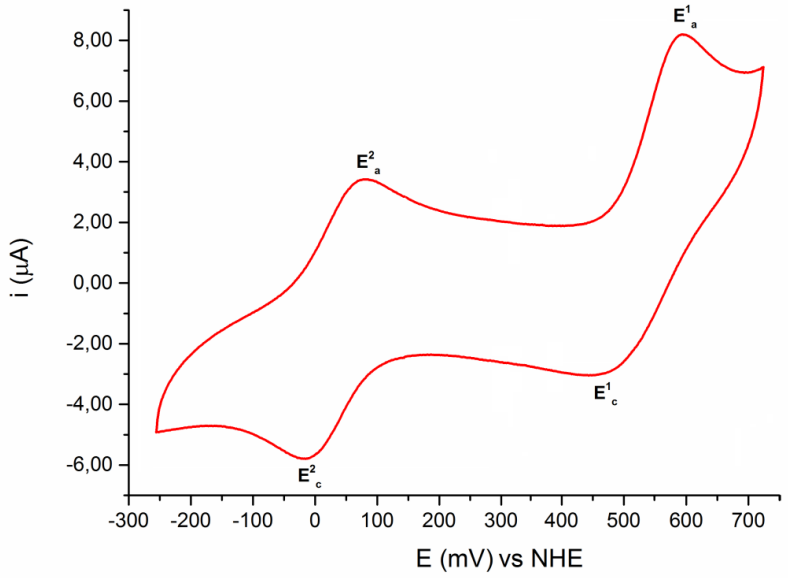

Figure 37. CV of $Mn_2L_2P2^{6+}$ 0.5 mM in 50 mM phosphate buffer (pH = 7.8, NaCl 0.1 M); $E_{1/2}$ = 10 mV, ΔE = 98 mV, is ascribed to the Mn^{III}/Mn^{II} redox couple of the heme residue, $E_{1/2}$ = 515 mV, ΔE = 142 mV is ascribed to the $Mn_2^{II,III}$/ $Mn_2^{II,II}$ redox couple of the Mn_2L_2 core.

The SOD-like activity measured for the di-zymes arises from the combined SOD performance of the two units obtaining a value of $\log k_{cat}(O_2^{\bullet-})$ = 6.64 (IC_{50} = 0.60 μM) for **$Mn_2L_2P1^{5+}$** and a $\log k_{cat}(O_2^{\bullet-})$ = 7.05 (IC_{50} = 0.23 μM) for **$Mn_2L_2P2^{6+}$** (Table 3). The higher value of SOD activity obtained for **$Mn_2L_2P2^{6+}$**, dictated by the better performance of the porphyrin **P2**, is analogous to that obtained for other synzymes like M40403 and Mn(III)-TE-2-PyP^{5+} that are actually under clinical trials on humans.[154]

Vice-versa, the Mn_2-core dictates the CAT-like activity, as similar H_2O_2 dismutation rates are observed for either the isolated and integrated systems (Table 3, Figure 38). The CAT-activity of **$Mn_2L_2P1^{5+}$** and **$Mn_2L_2P2^{6+}$** (50 μM) was tested upon incubation with H_2O_2 (10 mM) in aqueous buffers at 25.0 °C and compared with that of **$Mn_2L_2Ac^{+}$**, (see Table 3, Figure 38). The conjugate Mn_2-core of both the di-zyme maintains its activity in borate buffer (50 mM, pH=7.8) with initial rate, R_0, up to 36 μM O_2/s (Figure 38a), > 99% H_2O_2 conversion, turnover number, TON, up to 200, and turnover frequency, TOF up to 0.73 s^{-1}. A similar behaviour has been also confirmed in the Krebs-Henseleit buffer (KH buffer, pH=7.4), (Figure 38b).[152] O_2 evolution kinetics show R_0 in the order **$Mn_2L_2P2^{6+}$**~**$Mn_2L_2P1^{5+}$**>**$Mn_2L_2Ac^{+}$** (Figure 38) obtaining as a result of conjugation also an increase of the catalase activity.

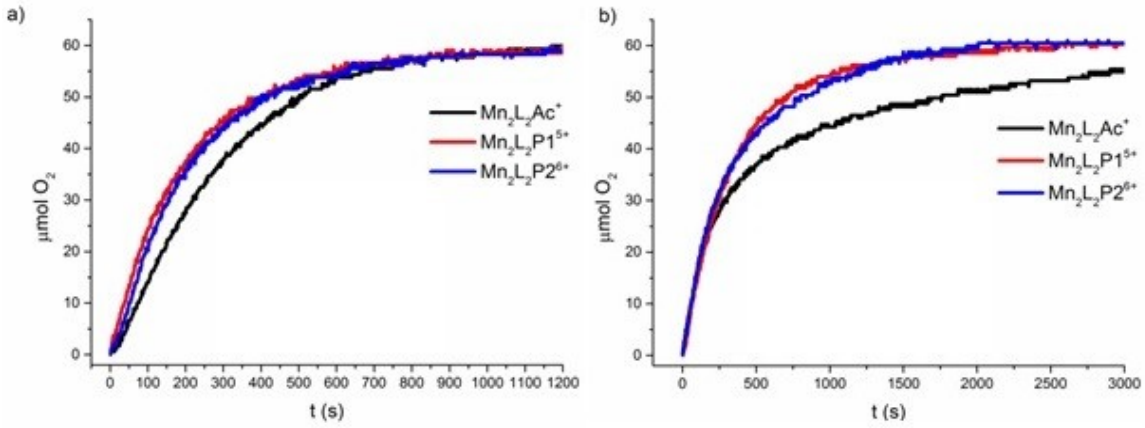

Figure 38. Time dependence of O_2 evolution after addition of $Mn_2L_2Ac^{+}$, $Mn_2L_2P1^{5+}$, $Mn_2L_2P2^{6+}$ ([cat] = 50 μmol) to a 10 mM H_2O_2 aqueous solution in (a) BBS 50 mM pH=7.8 and (b) KH buffer pH=7.4.

Considering both SOD/CAT activities of the di-zymes, **$Mn_2L_2P2^{6+}$** is the one that presents the best performance and for this reason more detailed study have been performed only on this compound.

A saturation behaviour, amenable to a Michaelis-Menten treatment, has been verified also for the best performing **$Mn_2L_2P2^{6+}$** conjugate (Figure 39). Accordingly, the CAT-like performance can be evaluated on the basis of the catalytic turnover constant, $k_{cat}(H_2O_2)$, of the Michaelis constant, K_M, and of the resulting $k_{cat}(H_2O_2)/K_M$ ratio (Table 3). Noteworthy the $k_{cat}(H_2O_2)/K_M$ value of 1890 places the **$Mn_2L_2P2^{6+}$** di-zyme among the top-performing artificial catalases in water (see literature benchmarks in Table 3), with a unique behaviour maintained also under saline, KH buffer, conditions.[15]

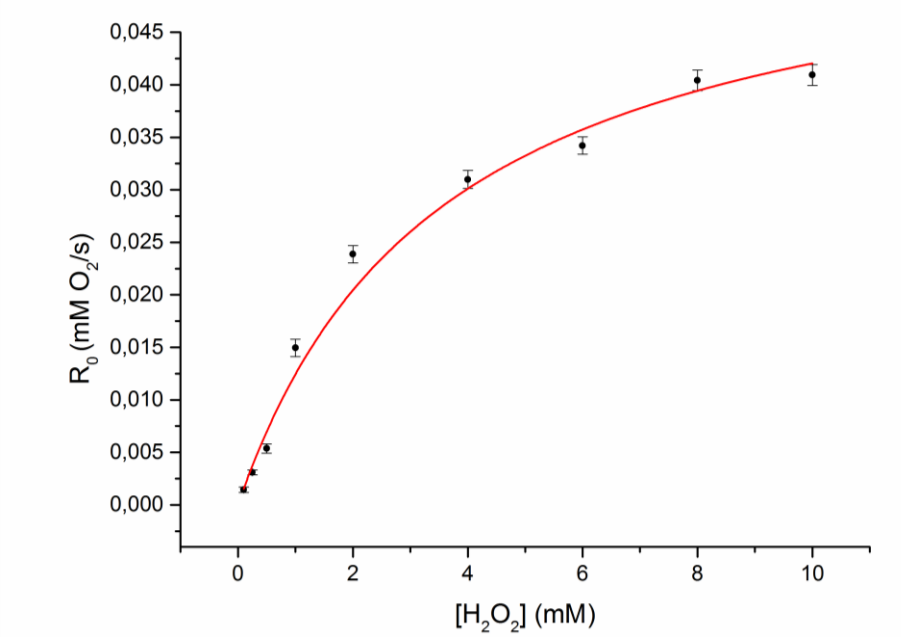

Figure 39. Effect of the H_2O_2 concentration on the initial rate of H_2O_2 disproportionation at 25 °C in a BBS buffer pH=7.8, [Mn_2L_2P2]= 10 µM.

The value of the ratio k_{cat}/K_M, shows an increasing of the enzymatic performance respect to **$Mn_2L_2Ac^+$**, this is due to a lower value of K_M that indicate an higher affinity for the substrate and also to a higher turnover number k_{cat}.

Table 3. Catalytic anti-oxidants featuring SOD and CAT activity in water under physiological conditions.

Catalytic Anti-oxidant	$E_{½}$/mV[a] vs NHE		SOD activity [b]		CAT activity [c]			
	$Mn_2^{III,II/II,II}$	$Mn^{III/II}$	IC_{50} (M)	log $k_{cat}(O_2^{\bullet-})$	k_{cat} (s^{-1})	K_M (mM)	k_{cat}/K_M ($M^{-1}s^{-1}$)	Ref.
Mn-SOD (*human*)	/	~+400	~1.3×10^{-9}	~9.30	/	/	/	[110,147]
Mn_2-CAT (*T.thermophilus*)	/	/	/	/	2.6×10^{5}	84	3.1×10^{6}	[29,141]
$Mn_2L_2Ac^+$	+515	/	1.04×10^{-6}	6.40	4.0	3.2	1245	this work
$Mn_2L^1{}_2Ac^+$	+520	/	3.80×10^{-7}	6.84	nd	nd	nd	this work
P1	/	-32	2.28×10^{-6}	6.07	/	/	/	this work
$Mn_2L_2P1^{5+}$	+515	-32	5.99×10^{-7}	6.64	nd	nd	nd	this work
P2	/	+10	3.53×10^{-7}	6.87	/	/	/	this work
$Mn_2L_2P2^{6+}$	+515	+10	2.34×10^{-7}	7.05	4.8	2.3	1890	this work
Mn_2(3-Me-5-SO_3-salpentO)	+95	/	/	/	10.5	6.6	1600	[134]
$[Mn_3(L^1)_2(\mu\text{-OAc})_4]$	/	/	/	/	1421	1120	1268	[143]
MnTE-2-PyP^{5+}	+228	/	4.50×10^{-8}	7.76	/	/	/	[112]
M40403	+525	/	2.2×10^{-7}	7.08	/	/	/	[18]

[a] $E_{1/2}$ is measured in 0.05 M phosphate buffer, pH 7.8, 0.1 M NaCl. [b] SOD activity is measured by the cyt c assay, [c] The oxygen concentration was determined using a Clark electrode. Conditions: [cat]= 10 µM, [H_2O_2]= 0.1-10 mM in BBS 50 mM pH=7.8 at 25 °C.

Regarding the weak point of heme-based functional systems generally associated to the porphyrin fragility when exposed to the oxidative risk we have explored the self-protection ability of the **$Mn_2L_2P2^{6+}$** di-zyme compared to the **MnTM-4-PyP^{5+}** unit upon exposure to H_2O_2 (50-500 μM, see Experimental section), mimicking harsh oxidative stress conditions. Heme-bleaching is conveniently monitored by UV-Vis spectroscopy over time (Figure 40).

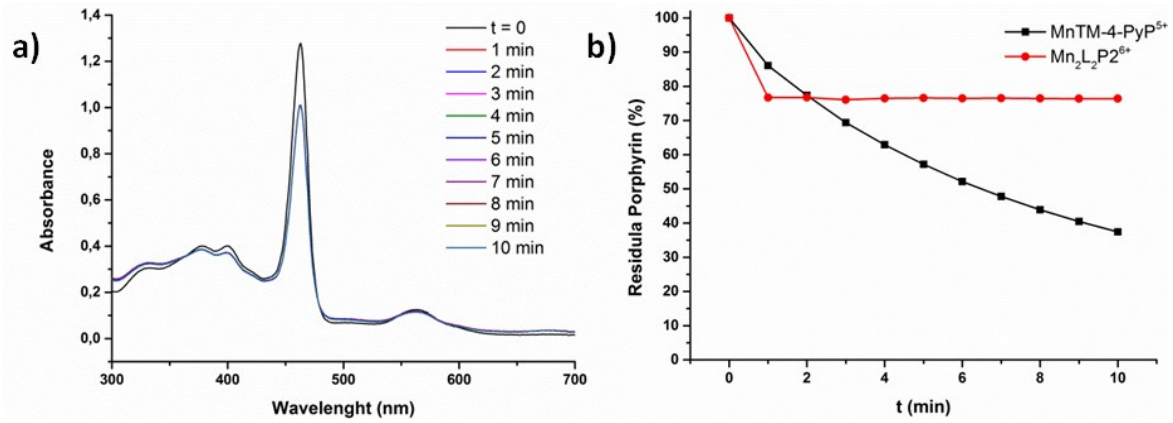

Figure 40. a) UV-Vis spectral decay recorded for **$Mn_2L_2P2^{6+}$** and b) bleaching kinetics, recorded at λ= 463 nm, for both **MnTM-4-PyP^{5+}** and **$Mn_2L_2P2^{6+}$** (10 μM) upon exposure to H_2O_2 (200 μM) in phosphate buffer (50 mM, pH=7.8); the residual porphyrin amount was estimated at λ= 463 nm by the ratio (A_t/A_0).

While a steady bleaching of the reference porphyrin is observed in ca. 10 minutes (Figure 40 and Appendix), its coupling with the Mn_2-core stops the oxidative degradation process after few seconds, with a porphyrin recovery in the range 85-75% based on the residual Soret absorbance (Figure 41).[157]

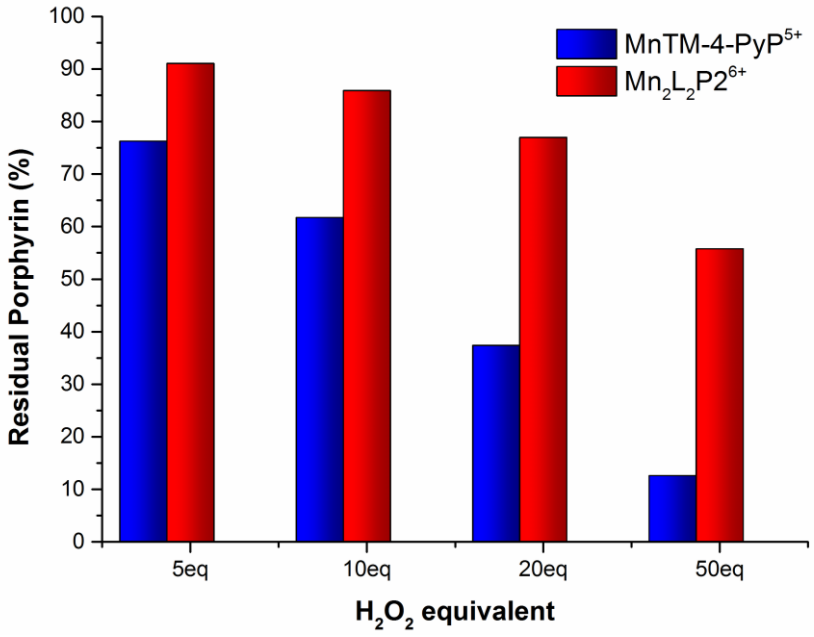

Figure 41. Residual porphyrin absorbance as registered after 10 minutes from the addition of different amount of H_2O_2 in phosphate buffer (50 mM, pH = 7.8) for **MnTM-4-PyP^{5+}** (blue) and **$Mn_2L_2P2^{6+}$** assembly (red).

The initial intensity decay observed for the Soret band of the porphyrin in the di-zyme is higher if compared with that of the commercial porphyrin. The evidence of a faster degradation seems in contrast with the data obtained for the residual amount of the porphyrin. Inspection of the bleaching kinetics in fact shows that a fast heme degradation occurs for the di-zyme soon after addition of H_2O_2, likely induced by a simultaneous Mn-dependent self-oxidation (Figure 42 and Appendix). The porphyrin concentration was estimated from the Lambert-Beer law and a pseudo-first-order linear plots of experimental rate constants vs $[H_2O_2]$ were obtained, where v_b is the bleaching rate and k_b is the bleaching constant.[87]

$$v_b = k_b[P2][H_2O_2]$$

To better understand the real behavior of the synzyme in solution in presence of hydrogen peroxide we define a new parameter to take in account all the possible phenomena.

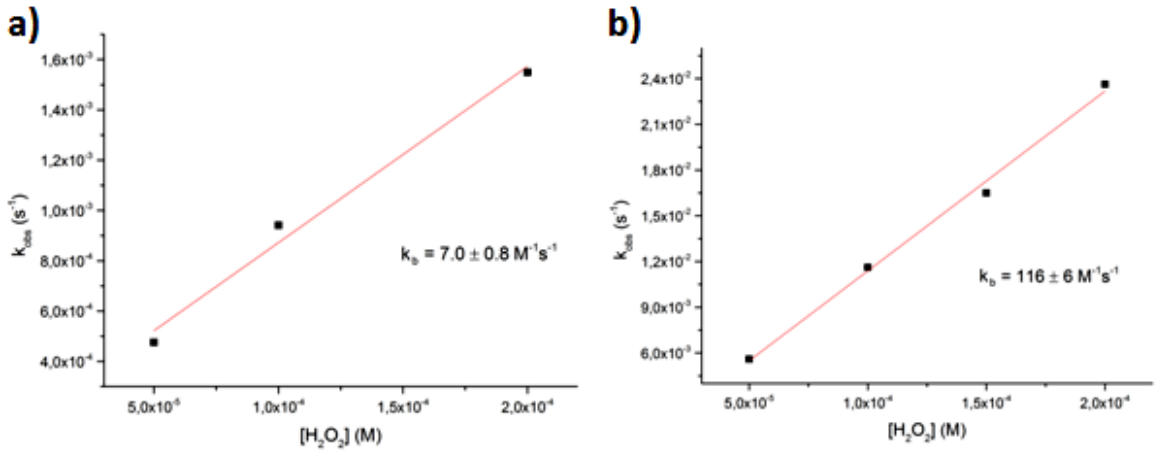

Figure 42. (a) Linear dependence of pseudo-first-order rate constants k_{obs} on $[H_2O_2]$, varied in the range 10^{-5}-10^{-4} M, determined for **Mn(III)-TM-4-PyP^{5+}** (10 μM) at 25°C in phosphate buffer (50 mM, pH 7.8) and (b) for **$Mn_2L_2P2^{6+}$** (8 μM) at 25 °C in phosphate buffer (50 mM, pH 7.8). The second-order rate constants were determined from linear plots of the observed k_{obs} vs $[H_2O_2]$, $k_{obs} = k_b[H_2O_2]$.

We propose a straightforward evaluation of the protection effect, exhibited by the Mn_2L_2 unit, against the irreversible porphyrin bleaching. The grade of protection can be defined on the basis of a new parameter "***p***" , resulting from the relative rates of two competitive and Mn-dependent reactions, namely: (i) the catalase-like dismutation of H_2O_2 (v_{cat}) and (ii) the parallel catalytic oxidation of the porphyrin ligand (v_b). Accordingly we can express the catalase-like dismutation rate by using the Michaelis-Menten parameters determined for the **$Mn_2L_2P2^{6+}$** di-zyme (k_{cat} and K_M) and the bleaching rate constant k_b determined for the **P2** domain with spectrophotometric kinetics.

The resulting expression is the following:

$$p = \frac{v_{cat}}{v_b} = \frac{\dfrac{k_{cat} \cdot [\mathbf{Mn_2L_2P2}] \cdot [H_2O_2]}{K_M + [H_2O_2]}}{k_b \cdot [P2] \cdot [H_2O_2]}$$

where $[\mathbf{Mn_2L_2P2}]$= [**P2**] considering the di-zyme structure, so the equation becomes:

$$p = \frac{v_{cat}}{v_b} = \frac{k_{cat}}{k_b(K_M + [H_2O_2])}$$

The protection parameter "***p***" show only a small dependence by H_2O_2, but under physiological condition it can be easily assumed as constant, in fact $[H_2O_2] << K_M$ and so the equation becomes:

$$p = \frac{v_{cat}}{v_b} \approx \frac{k_{cat}}{k_b K_M}$$

As shown the protection factor "***p***" become constant depending only by the kinetics constant of the synzymes employed in the di-zyme design.

The value of $\boldsymbol{p} = 16$ obtained for $\mathbf{Mn_2L_2P2^{6+}}$ (Figure 43) indicate that the Mn_2L_2 unit is able to scavenge hydrogen peroxide more efficiently respect to oxidize the heme centre, guarantee in this way an effective protection of the porphyrin against bleaching in accordance with the data previously obtained.

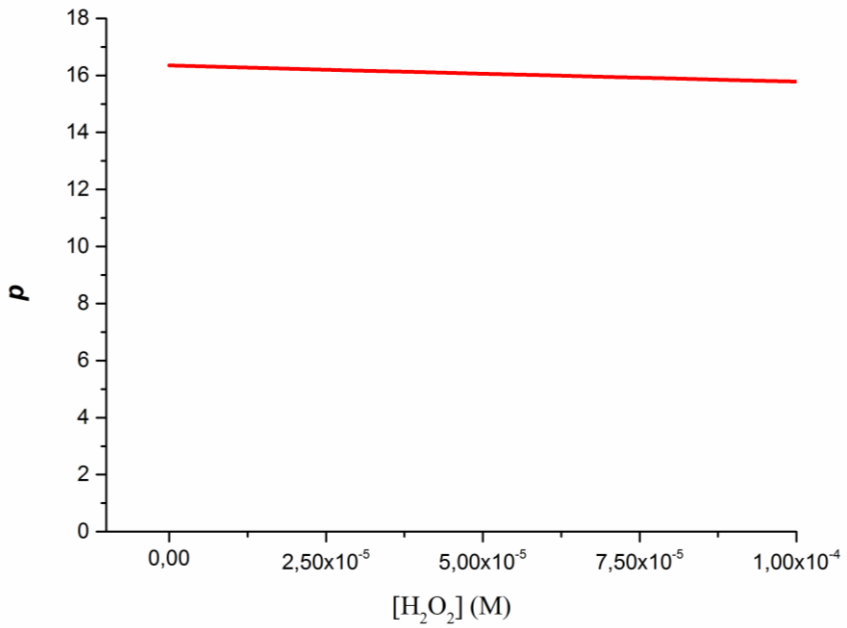

Figure 43. Dependence of the protection factor "***p***" on the concentration of H_2O_2, in a physiological range. The high catalase-like activity of the $Mn_2L_2P_2^{6+}$ di-zyme (k_{cat}/K_M) affords a value of $\boldsymbol{p} = 16$.

This feature is not only interesting for the catalyst design, by tuning the individual components, but the conjugation with the Mn_2L_2 unit seems also an interesting strategy to increase the resistance of molecules and materials under oxidative stress conditions.

After the catalytic screening an evaluation on the possible toxic effects of the di-zyme is necessary. The positive charges at the porphyrin periphery are expected in fact to facilitate mitochondrial-targeting and cross-membrane translocation by the artificial di-zyme.[111] The potential interaction of the synthetic di-zyme with nucleic acids has been addressed by spectrophotometric titrations with calf-thymus DNA (CT-DNA).[90,161–164] Upon exposure to CT-DNA, **$Mn_2L_2P_2^{6+}$** and the reference **MnTM-4-PyP^{5+}** porphyrin show a similar behavior, with ca. 15-20 % hyperchromic effect and a negligible shift of the Soret absorption (λ_{max} = 463 nm) (Figure 44).

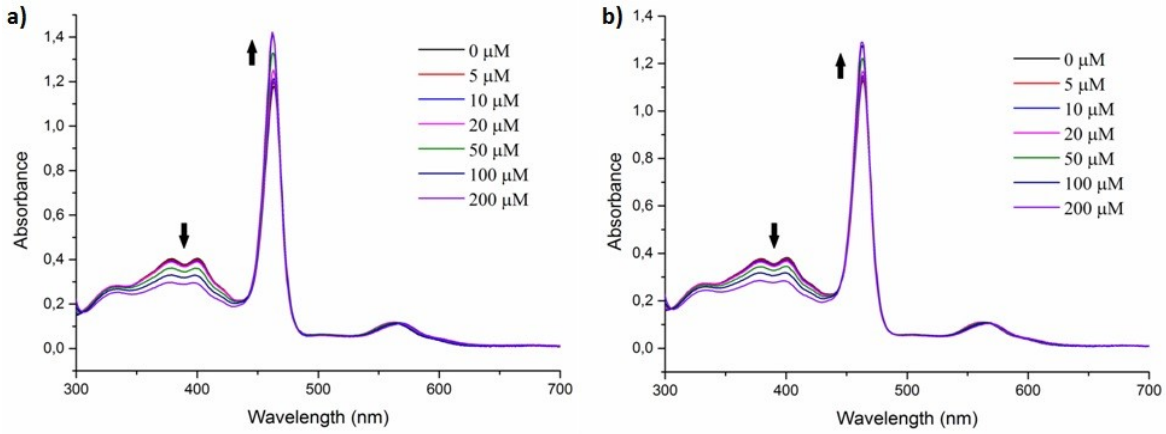

Figure 44. a) Spectrophotometric titration of Mn(III)-TM-4-PyP^{5+} (6 µM) and (b) of $Mn_2L_2P2^{6+}$ (6 µM) with nucleic acids (CT-DNA): phosphate buffer 10 mM pH 6.8, 1 mM EDTA , μ = 0.2 M, 25 °C.

Table 4. Effect of nucleic acids on the wavelength maximum of the porphyrin Soret Band for free-base and metallo-complexes for 0.02 < r_o < 1.20a.

Compounds		**calf thymus DNA**	
	λ_{max} (nm)	λ_{max} (nm)	% *H* [b]
H_2TM-4-PyP^{4+}	423	432	49
Mn(III)-TM-4-PyP^{5+}	463	463	-21
$Mn_2L_2P2^{6+}$	463	463	-15

[a] r_o ration between porphyrin and DNA concentration. [b] hypochromicity (% *H)* was determined from (ε_p - ε_b)/ ε_p X 100, where p represents free porphyrin, b represents bound porphyrin, and ε_p and ε_b were determined at the respective Soret maxima. Phosphate buffer 10 mM pH 6.8, 1 mM EDTA , µ = 0.2 M, 25 °C.

This result can be ascribed to electrostatic surface interactions, while ruling out DNA intercalation and major toxicity effects.[90,161–164] Comparison with the intercalating free base porphyrin H_2TM-4-PyP^{4+} indeed shows a different behaviour with a relevant hyphocromic effect and a red shift of the Soret band (see Appendix). As a matter of fact,

there are already some examples of cationic porphyrin scaffolds approved for pre-clinical and clinical tests.[19,154]

2.5 In vivo tests on green algae

The synzymes activity was tested in vivo, by evaluating H_2O_2 accumulation in photosynthetic algae (Chlamydomonas reinhardtii) exposed to high-light illumination conditions (1 h with white light, 800 µmol photons m^{-2} sec^{-1}). To this aim, cells were grown in tris-acetate phosphate medium (TAP) in the presence of the synthetic Mn-cofactors, (**Mn_2L_2Ac**, **Mn_2L_2P2**, **P2**). The concentration of catalyst that do not show toxicity and therefore inhibition on algal growth are respectively 0.5 µM for **Mn_2L_2Ac** and 0.1 µM for **Mn_2L_2P2** and **P2**. The toxicity of the di-zyme seems to be associated to the porphyrin moiety although an exact relation is unknown.

ROS production in vivo, under high-photon flux irradiation for 1 hour, was then evaluated using the 3,3-diaminobenzidine (DAB) colorimetric assay (Figure 45).

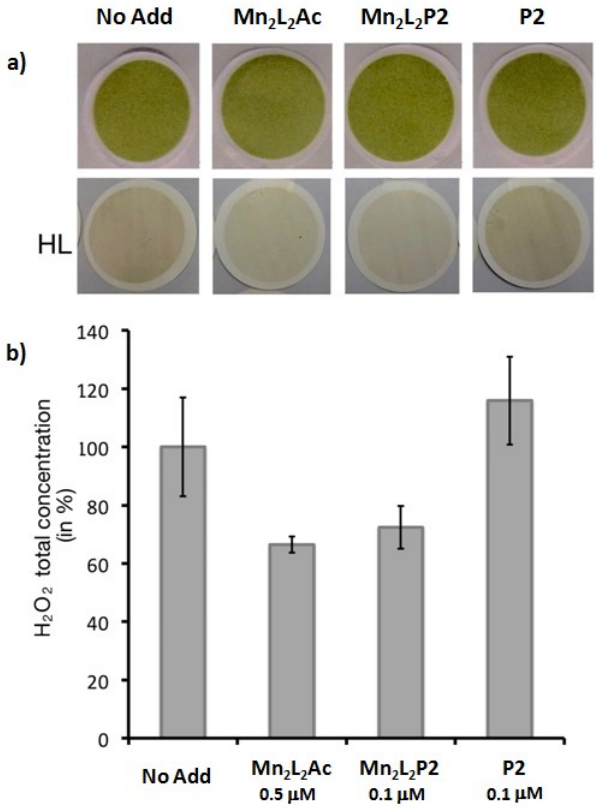

Figure 45. In vivo ROS detoxification of photosynthetic green algae (*Chlamydomonas reinhardtii*) during illumination (white light, 50-800 µmol photons m^{-2} sec^{-1}). a) cw15 strain cells grown and incubated in the absence/presence of **Mn_2L_2Ac** (0.5 µM), **Mn_2L_2P2** (0.1 µM) and **P2** (0.1 µM) in TAP medium (48 h) then harvested on filters (upper-row) and stained with 3,3-diaminobenzidine (DAB, 5 mM) under 1 h irradiation with high-light conditions (bottom row). b) corresponding H_2O_2 accumulation (DBA colorimetric test) normalized with respect to the control experiment (No Add, 100%).

Our results indicate that the synzymes present a relevant activity in vivo if compared to the control experiment (No-Add). The **Mn_2L_2P2** di-zyme provides a remarkable abatement of H_2O_2 accumulation, about 60% of residual H_2O_2 at a nominal concentration as low as 0.1 μM, a clear improvement of activity if compared to the effect registered for **Mn_2L_2Ac**, which require a higher dosage (0.5 μM) to obtain the same detoxification.

These results are in agreement with the trend of performance obtained in the catalytic screening with an increasing of activity moving from **Mn_2L_2Ac** to **Mn_2L_2P2**, while the isolated porphyrin **P2** is silent (Figure 45).

In conclusion, the co-localization of the Mn-based SOD/CAT mimetics provides a novel anti-oxidant di-functional system with an outstanding solubility in physiological conditions, peak performance ($\log k_{cat}(O_2^{\bullet-}) \geq 7$; $k_{cat}(H_2O_2)/K_M = 1890$), and self-protection (> 75% survival in H_2O_2 200 μM). These key features are instrumental in vivo, to enhance photo-protection of photosynthetic cells under oxidative stress, a highly important target for improving the photosynthetic efficiency under adverse/extreme growth conditions.

This modular approach permits also a fine tuning of the units to modulate the reactivity and the possibility to explore the reactivity with different metal centres like Cu and Fe as will be discussed in the next chapters.

3. Dinuclear copper complexes

3.1 Copper-Zinc superoxide dismutase

Copper-Zinc superoxide dismutase (Cu-ZnSOD) is an essential enzyme in natural antioxidant systems since it is able to catalyze the dismutation of superoxide to hydrogen peroxide and oxygen. A copper-zinc heterobimetallic complex is located at the active site of Cu-ZnSOD, in which Cu^{2+} is penta-coordinated by four His residues and one water molecule with a distorted tetragonal pyramid coordination, while Zn^{2+} is bound by three His, two bridged between Cu^{2+} and Zn^{2+} atoms and an Asp in a tetrahedral coordination (Figure 46). Copper is the redox-active metal, with an oxidation states changing between +2/+1 during the redox catalysis, while zinc appears to play a role in overall enzyme stability and in facilitating a broader pH independence. [165,166]

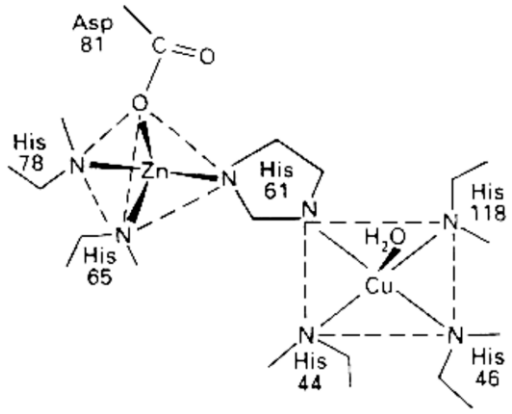

Figure 46. Structure of *human* Cu-ZnSOD active center.

The overall mechanism by which Cu-ZnSOD catalyzes the disproportionation of superoxide radicals has been called a ‘‘pingpong’’ mechanism since the copper center is cyclically reduced and oxidized by superoxide: superoxide first reduces the Cu^{2+} center to produce dioxygen (i), and then another molecule of superoxide oxidizes the Cu^{+} center to produce hydrogen peroxide (ii).[166]

$$O_2^{\bullet-} + Cu^{II} - Zn^{II}SOD \rightarrow O_2 + Cu^{I} - Zn^{II}SOD \quad \text{(i)}$$

$$O_2^{\bullet-} + 2H^{+} + Cu^{I} - Zn^{II}SOD \rightarrow H_2O_2 + Cu^{II} - Zn^{II}SOD \quad \text{(ii)}$$

The oxidation step (i) consists of an inner sphere electron transfer between the coordinated superoxide and Cu^{2+} center. Upon reduction, the bridging imidazole coordination and the water molecule are lost and Cu^{+} ion becomes three coordinated; the imidazolate is protonated by the solvent and dioxygen is released. The reduction step (ii) is an inner sphere electron transfer between the superoxide anion and Cu^{+}. The histidyl imidazole coordinated to zinc acts in the second step of the enzymatic redox cycle to protonate the

formed copper peroxides (Scheme 10). Both reactions occur with the same, nearly diffusion controlled, rate constant ($k = 2 \cdot 10^9$ $M^{-1}s^{-1}$), which, in both cases are pH independent over the pH range 5-9.5.[166–168]

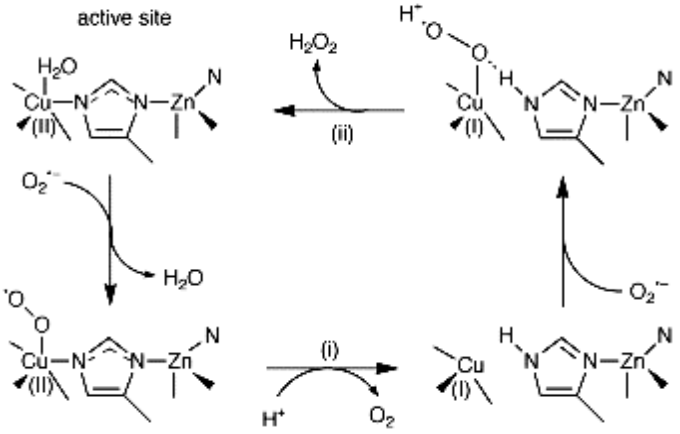

Scheme 10. Proposed mechanism of Cu-ZnSOD.

It is important to underline that Cu-ZnSOD is also involved in a peroxidative cycle, in which hydrogen peroxide reacts with both oxidized and reduced form of the enzyme, forming hydroxyl radicals.

$$H_2O_2 + Cu^{II} - Zn^{II}SOD \rightarrow H^+ + HO_2^{\bullet} + Cu^{I} - Zn^{II}SOD$$

$$HO_2^- + Cu^{I} - Zn^{II}SOD \rightarrow OH^{\bullet} + Cu^{II} - Zn^{II}SOD - OH^-$$

This cycle involve a Fenton-type reaction, so that when superoxide and peroxidase cycles are combined, the reaction may also lead to the catalytic formation of radicals. In turn, the last ones can attack the copper-binding His residue leading to a deactivation of Cu-ZnSOD.[166] The direct utilization of Cu-ZnSOD as a pharmaceutical agent has many problems such as i) solution instability, ii) immunogenicity, iii) cost of production and iv) short half-lives in circulating blood (6 min). Therefore, considerable efforts have been directed to the research of stable, non-toxic, low molecular weight copper complexes with SOD-like activity, that can be used as functional analogues for Cu-ZnSOD.

3.2 Copper based catalytic anti-oxidants

Copper ions, as centers of active site of various metalloproteins, play a vital role in a number of widely differing biological processes like electron transfers, oxidations and dioxygen transport.[169,170] Small molecular weight copper complexes are studied as structural and functional models of the active centers of copper containing enzymes.[170–172] Homo and hetero dinuclear metal complexes containing one or two copper ions are already known for their SOD-like activity.[173–177] These complexes mimic the core motif of the natural Cu-ZnSOD, an essential enzyme in antioxidant systems, able to catalyze the dismutation of superoxide to hydrogen peroxide and oxygen. In addition, binary and ternary copper (II) complexes have been studied as models for copper containing enzymes such as Cu,Zn-superoxide dismutase and catechol oxidase.[178–183]

SOD enzymes protects the living cell against various pathological conditions involving cardiovascular diseases, cancer, inflammation, diabetes and aging.[8] The clinical use of this SOD has many shortcomings, including its short life-time, high cost and low membrane permeability. Small molecular weight complexes seems to be a good solution to the problem being a structural and functional models of metal containing enzymes. In particular non-steroidal anti-inflammatory copper (II) complexes have been widely studied since they are found to be more active and low toxic than today's steroidal drugs that presents renal, gastrointestinal and cardiovascular side effect.[179]

The class of Cu,Zn hetero dinuclear metal complexes, show moderate SOD activity, although it is rather low in comparison with the native Cu,Zn–SOD. The highest IC_{50} values obtained from the cytochrome *c* assay method using the xanthine oxidase reaction as a superoxide source are 0.24-0.32 μM for the Cu,Zn hetero dinuclear complexes (Figure 47).[177,184]

Also mononuclear copper complexes been reported as SOD mimic, although these complexes with macrocyclic or acyclic polyamine ligands show lower activity; their IC_{50} values were about 70–2000 μM, which are less SOD active if compared with the Cu,Zn artificial dinuclear ones.[153] However, a class of mononuclear copper (II) complexes based on bidentate 2-substituted benzimidazole ligands is reported to show the highest activity with IC_{50} = 0.09-0.34 μM, although they are not very stable (Figure 47).[173]

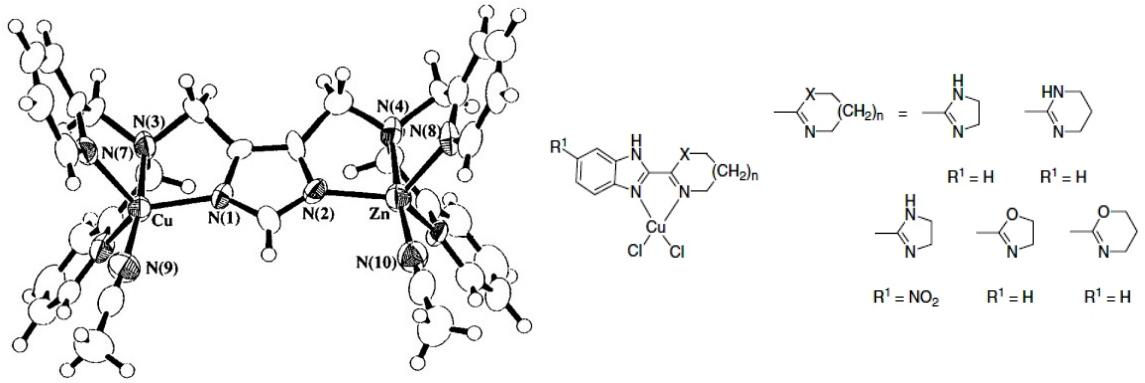

Figure 47. Structure of the best performing SOD synzymes: Cu,Zn hetero dinuclear complexes (left) and mononuclear benzimidazole complex (right).

Concerning the potential catalase activity of the copper complexes, few example of this reactivity are reported. This is related to the nature of the dismutation process, that requires a two electron mechanism and it is hardly accomplished by a single copper centre, cycling between the Cu^{II}-Cu^{I} redox states.

Few mononuclear copper complex have been reported to scavenge hydrogen peroxide by a two step reaction involving two mono-electronic processes.[185,186]

Only one example of a macrocyclic di-nuclear copper based catalyst, able to dismutate hydrogen peroxide with a catalase-like mechanism, is reported to cycle between the $Cu_2^{II,II}$-$Cu_2^{I,I}$ redox states.[187]

3.3 Dinuclear Copper Complexes with dual SOD/CAT activity

The design of systems which integrates a SOD/CAT functional mimicry in one artificial dual-synzyme is fundamental in order to achieve a complete ROS detoxification. The majority of the copper based SOD-like synzymes are based on a mononuclear metal center so are unable to perform multi-electronic processes like hydrogen peroxide dismutation. Dinuclear copper complexes instead may present some catalase mimic activity due to the cooperation between the metals centers. Actually really few examples of dinuclear copper synzymes with CAT-like activity are reported and no one of these is shown to exhibit dual SOD/CAT activity under physiological-like conditions without the addition of additives.[187–189]

The dinuclear copper (II) complex (**Cu_2L_2**), was synthesised by adding to the ligand (HL = 2-{[[di(2-pyridyl)methyl] (methyl)amino]methyl}phenol)) a methanol solution of copper perchlorate and triethylamine giving a green precipitate.[149] The complex, obtained as

green precipitate, was recrystallized by heating until boiling point and adding acetonitrile. Green crystals were isolated upon cooling. (Figure 48).

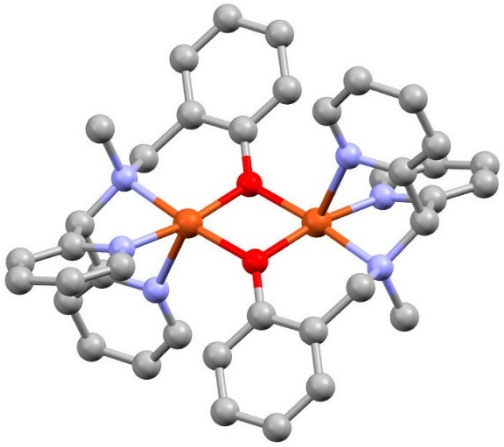

Figure 48. X-ray crystal structure of Cu_2L_2.

The complex consists of one di-cationic $[\mathbf{Cu_2L_2}]^{2+}$ unit, two perchlorate counter ions and four acetonitrile as solvation molecules (not shown). The crystal structure of $\mathbf{Cu_2L_2}$, displays an inversion center and shows a dinuclear copper(II) complex where a tetra-dentate N_3O donor set is provided by the bis-pyridyl, amino and μ-oxo phenolate groups of the ligand. $\mathbf{Cu_2L_2}$ shows a distorted octahedral geometry for both metal centers, where each copper atom is coordinated by the three nitrogen atoms of the tetradentate ligand, while the phenolate ligands act as a bridges between the two metal centers. The equatorial plane is approximately defined by two copper centers, two oxygen atoms from the phenol molecules, one pyridine nitrogen atom and one amine nitrogen atom from the ligand. Considering this equatorial plane, each copper atom presents an apical position occupied by the other pyridine nitrogen atom, while the other apical position is free due to the high Jahn–Teller distortion of the Cu^{2+} ions. The Cu-Cu distance and the Cu−O−Cu angles of the two μ bridging phenolate residues are respectively 3.01 Å, 100.2° (Figure 48).

The FT-IR spectrum of the complex shows the ligand coordination to the metal centers by the shift, at higher frequencies, of the pyridines and phenol absorptions located at 1613 and 1601 cm^{-1} (Figure 49).[190]

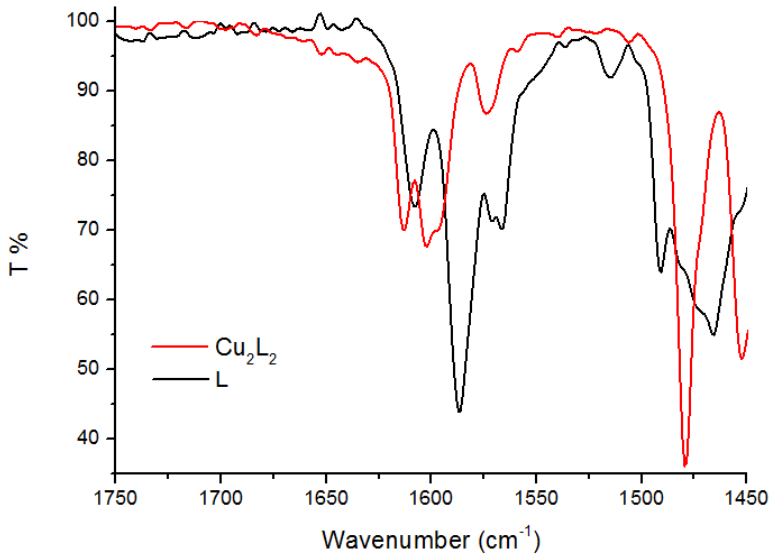

Figure 49. Superimposition FT-IR spectra (KBr pellet, 1700-1450 cm^{-1} spectral region) of $[\mathbf{Cu_2L_2}](ClO_4)_2$ (red spectrum) and ligand (black spectrum).

The solution structure of the dinuclear complex is confirmed by ESI-MS and UV-Vis. The ESI-MS peaks for the molecular ion are 779.0 $[\mathbf{Cu_2L_2}+HCO_2]^+$ and 833.0 m/z for $[\mathbf{Cu_2L_2}+ClO_4]^+$ (see Appendix, formic acid was present in the eluent). A fragmentation peak at 367.1 m/z attributed to $[CuL]^+$ specie is also observed for the break of the dinuclear system in the ion source.

The UV-Vis spectra were collected both in organic medium ($[\mathbf{Cu_2L_2}]$ = 60 µM, CH_3CN) and in aqueous medium ($[\mathbf{Cu_2L_2}]$ = 60 µM, PBS 50 mM, pH 7.8) (Figure 50). The complex shows an absorption band in the UV-region, with a maximum at 269 nm (π-π* transition of pyridines, ε = 20500 $M^{-1}cm^{-1}$) shifted to lower energy respect to UV band of the ligand (256 nm in CH_3CN, Appendix) and a broad, weaker absorption with a maximum at around 410 nm due to the ligand to metal charge transfer (LMCT, ε = 2880 $M^{-1}cm^{-1}$), operated by the phenol moiety.[187–189,191] These features are characteristic of the phenol derivatives when the complexation is accompanied by the deprotonation of the hydroxyl group.[192] A d-d transition at higher wavenumber (675 nm, ε = 375 $M^{-1}cm^{-1}$) was also observed (see Appendix). No significant spectral changes were observed between the two media, as already verified by ESI, thus highlighting the stability of the complex also in water. The small difference in the intensity of the LMCT are attributable to the solvent itself that can coordinate in the free position of the complex changing the intensity of the absorption and to the hydrogen bonding network in water.[193]

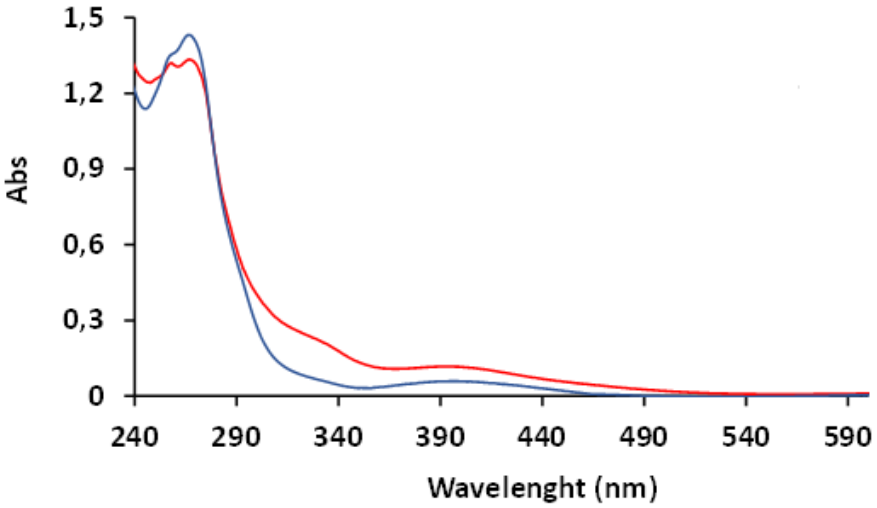

Figure 50. UV-Vis spectra of Cu_2L_2 (60 µM), in PBS 50 mM, pH 7.8 (blu line), in CH_3CN (red line).

The redox properties were determined by cyclic voltammetry (CV) experiments performed in buffer solution (**Cu_2L_2** 0.5 mM in phosphate buffer, 50 mM, pH = 7.8) in reduction (Figure 51) and in acetonitrile (**Cu_2L_2** 1 mM) in oxidation (Figure 52). In aqueous media the complex shows a quasi-reversible feature for the cathodic and anodic waves attributed to the Cu^{II}/Cu^{I} redox couple with $E_{1/2}$ = -161 mV (vs NHE). Moreover, only one pair of redox peaks were detected, meaning that the environment around the two copper ions is the same, so the expected process is $Cu_2^{II,II} \rightarrow Cu_2^{I,I}$, in agreement with the symmetry of the complex, as shown by the crystal structure analysis (Figure 48).

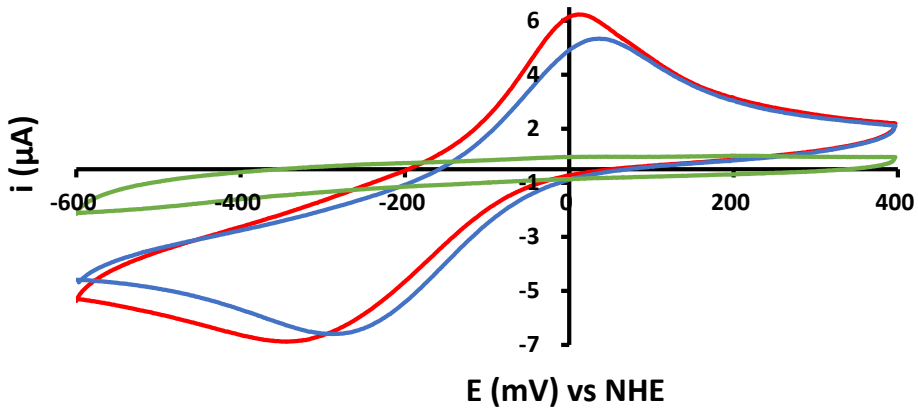

Figure 51. Cyclic voltammetry of Cu_2L_2 $E_{1/2}$ = -161 mV (red line), Cu_2L_2 in situ $E_{1/2}$ = -155 mV (blue line), and voltammogram of the unpolished electrode (green line) in 50 mM phosphate buffer (pH = 7.8, NaCl 0.1 M); for $Cu_2^{II,II}$/ $Cu_2^{I,I}$ couple $E_{1/2}$ = -161 mV,

In addition, at higher potential in acetonitrile was detected another quasi-reversible wave (Figure 52), absent for the free ligand (see Appendix), attributed to the Cu^{III}/Cu^{II} redox couple, with $E_{1/2}$ = 967 mV (vs NHE). Other oxidation waves above 1.2 V are ascribed to the oxidation of the phenolic moiety.[122]

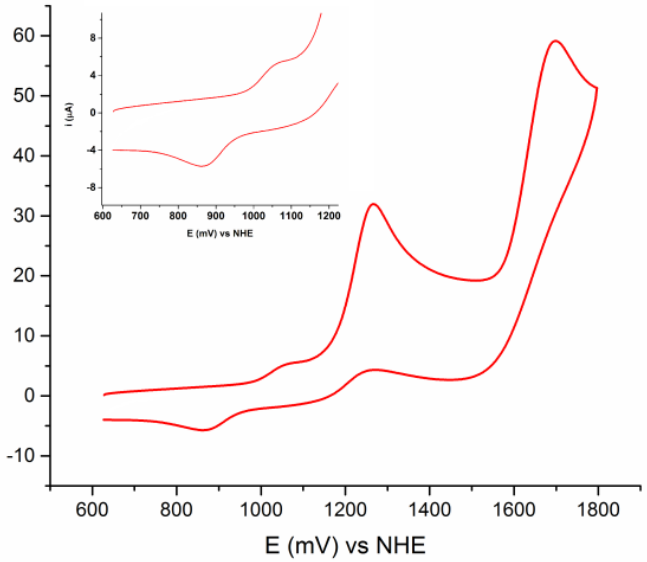

Figure 52. Cyclic voltammetry of Cu_2L_2 in acetonitrile ($TBAClO_4$ 0.1M), for $Cu_2^{III,III}$/ $Cu_2^{II,II}$ couple $E_{1/2}$ = 967 mV in the inset.

The ability of the ligand to bind copper in aqueous solution and forming in dinuclear complex **Cu_2L_2** was also evaluated. The assembly was accomplished by adding an aqueous solution of the ligand to $Cu(ClO_4)_2$ (120 μM). After the ligand addition, the solution, turns immediately green, meaning that the binding of the copper has occurred.

The solution was then analysed by UV-vis, ESI-MS and CV to verify the nature of complex formed in-situ. As first evidence the two UV-vis spectra, recorded under the same condition (H_2O), are perfectly superimposable (Figure 53). Cyclic voltammetry of the complex obtained in situ is also similar (Figure 51) with an $E_{1/2}$ = -155 mV (vs NHE) in PBS 50 mM (pH = 7.8, $NaClO_4$ 0.1M). ESI-MS analysis is also consistent with the expected structure. The solution analysis shows the same peaks of isolated Cu_2L_2 at 779.0 and 833.0 m/z and the corresponding fragment at 367.0 m/z.

The possibility to directly assemble in situ the catalyst, taking advantage of the chelating action of the ligand, could be interesting not only in terms of an easier synthetic procedure but also, in perspective of a possible application as metal chelator for the scavenging of the free copper ions in-vivo, to prevent Cu-induced ROS generation and related pathologies like Parkinson and Alzheimer disease.[194–196]

The redox potential of the metal centre is one parameter that can be useful to predict SOD activity. An optimal SOD activity in aqueous solution requires redox potentials close to 0.36 V (vs. NHE), which is the intermediate value between the one-electron reduction potential for oxygen (-0.16 V, pH = 7) and the one-electron reduction potential for

superoxide radical (0.89 V, pH = 7). Thus, both processes are equally favored for thermodynamics and both reduction and oxidation reactions in the dismutation process are predicted with the same rate constant (k_{cat}=2·10^9 M^{-1}s^{-1}).[46,154,166]

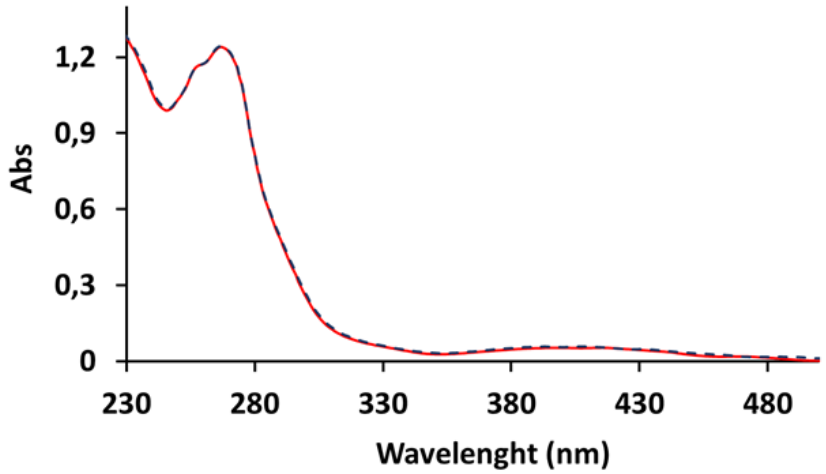

Figure 53. Superimposition of the UV-vis spectra in water of **Cu_2L_2** (60 μM) isolated as crystal (blu line) and obtained in situ (red line).

Within this scenario, the **Cu_2L_2** has an $E_{1/2}$ for Cu^{II}/Cu^{I} redox couple set at the lower limit. In addition, in order to exhibit a good SOD-like activity copper(II) complexes must fulfill other requirements: i) have a flexible arrangement of the ligands around Cu^{2+} center to allow an easy reduction and stabilization of Cu^{+}; ii) have an accessible site for binding of $O_2^{\bullet-}$; iii) have hydrogen bonding sites close to the metal center to contribute to the transport of superoxide anion to the active site as well as to stabilize the peroxo-species bound to the metal ion during the catalytic cycle.[153,185] The SOD-like activity has been assessed by using the Xanthine oxidase/cytochrome *c* (cyt *c*) protocol to evaluate the $O_2^{\bullet-}$ scavenging rate, comparing the activities as IC_{50}, (i.e. 50% inhibition of cyt *c* reduction, monitored at 550 nm in 0.05 M phosphate buffer, pH 7.8, using Xanthine/Xanthine oxidase system as the source of $O_2^{\bullet-}$) and on the basis of the resulting kinetic constant ($\log k_{cat}(O_2^{\bullet-})$).[85,87]

SOD performance observed for **Cu_2L_2** (Table 5) show a $\log k_{cat}(O_2^{\bullet-})$ = 6.80 with an IC_{50} = 0.40 μM that set this catalyst between the best performing Cu-based complexes for its SOD-like activity.[165] Despite the low redox potential of $Cu^{II/I}$ redox couple the catalyst shows a good SOD-like activity, this is attributable to different factors. The $E_{1/2}$ = -161 mV in fact is expected to boost the reduction step of the superoxide anion (0.89 V vs NHE). In addition the complex presents two copper ions with a vacancy in the coordination sphere (Figure 48) accessible to a ligand like superoxide and two bridging oxygen able to accelerate catalysis by hydrogen bonding interaction, assisting the processes of proton

transfer.[85,87] In addition the SOD-like activity of the in situ generated catalyst was tested with cyt c assay, confirming the retained activity with an IC_{50} = 0.48 μM and $\log k_{cat}(O_2^{\bullet -})$ = 6.72, obtaining in this way from the copper scavenging a complex with anti-oxidants activity.

Table 5. Best performing Copper-based SOD-like catalysts.

Catalytic Anti-oxidant	$E_{½}$/mV vs NHE[a]	SOD activity IC_{50} (μM)	Ref.
Cu,ZnSOD	~400	~0.001[b]	[168,197]
$[Cu_2L_2]^{2+}$	-161	0.40[c]	this work
$[Cu_2L^1{}_2]^{2+}$	-55	0.14[c]	this work
$[Cu_2L^2{}_2]^{2+}$	+60	0.07[c]	this work
Cu_2(tz-tol)$_4$	/	0.13[d]	[175]
$[Cu_2$(bpzbiap)$Cl_3]$	+180	0.26[d]	[176]
CuZn(bdpi)$(CH_3CN)_2$	+167	0.24[c]	[177]
Cu(TAAB)$^{2+}$	+230	0.14[e]	[174]
Cu(dib)Cl_2	/	0.09[c,f]	[173]
$Cu(SO)_4$	+155	30[e]-72[c]	[165,174]

[a] $E_{1/2}$ is measured in 0.05 M phosphate buffer, pH 7.8, 0.1 M NaCl. [b] SOD activity is measured by pulse radiolysis. [c] SOD activity is measured by cyt c assay. [d] SOD activity is measured by NBT assay [e] SOD activity is measured by INT assay. [f] complex presents low stability.

Dinuclear copper based catalysts Cu_2(II) reported for their catalase-like activity are rare if compared with other metals like manganese.[15,187–189] The reaction of hydrogen peroxide dismutation is a bi-electronic process in which the peroxide is converted in H_2O and O_2. At pH 7, the electrochemical potentials (vs. NHE) for the two-electron O_2/H_2O_2 and H_2O_2/H_2O couples are +0.28 V and +1.35 V (vs. NHE), respectively. Thus in order to perform this reaction a catalyst needs a metal centre with a redox potential intermediate between these values. **Cu_2L_2** could be able to catalyze the reaction by cycling between the $Cu_2^{III,III} \rightarrow Cu_2^{II,II}$ redox states that present an optimal potential ($E_{1/2}$ = 967 mV) and involve a bi-electronic process.

The CAT activity of **Cu_2L_2** was tested upon incubation with H_2O_2 (30 mM) in aqueous borate buffer (BBS, pH= 7.8) and Krebs- Henseleit buffer (KH buffer, pH=7.4, commonly used in perfused and superfused solution protocols) at 25°C following the O_2 production with a pressure transducer (Figure 54).[152] The dinuclear complex **Cu_2L_2** presents CAT-like activity in borate buffer (50 mM, pH=7.8) with rate, up to 52 μM O_2/min (Figure 54), H_2O_2 conversion up to 35%, turnover number, TON, up to 52, and turnover frequency, TOF up to 0.26 min^{-1}. The complex maintains its activity also in KH buffer containing a mixture of salts (sulphates, phosphates, carbonates and chlorides) and glucose, and despite the longer lag phase and lower rate it presents a higher stability with rate, up to 31 μM

O_2/min (Figure 54), H_2O_2 conversion up to 75%, turnover number, TON, up to 110, and turnover frequency, TOF up to 0.16 min^{-1}.

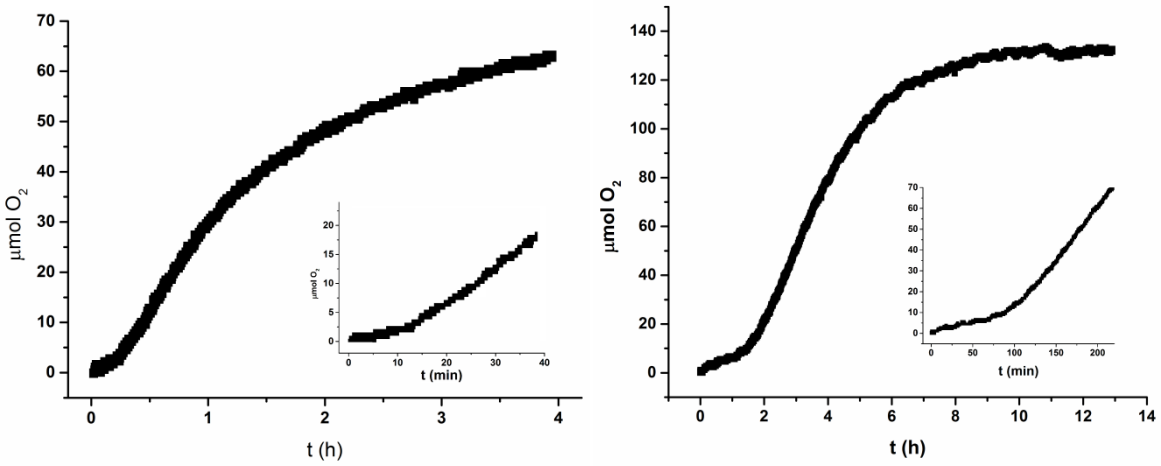

Figure 54. O_2 evolution kinetics by $\mathbf{Cu_2L_2}$ (200 µmol) upon incubation with H_2O_2 (30 mM) at 25°C in BBS (50 mM pH=7.8) (left) and in KH buffer (pH=7.4) (right).

Regarding the initial lag phase this is attributable to different factors, first of all the approach of H_2O_2 to the metal centre is subject to steric hindrance from the substituent at nitrogen and also to the presence of competitive binder for the copper sites.[198] The lag phase in fact, is about 10 min in BBS, a non coordinating ion, whereas is about 100 min in KH buffer that contain a complex mixture of salts, in particular phosphate (2 mM). The phosphate anion is known to interact and inhibit the activity of copper complex, and in fact performing the reaction in phosphate buffer solution (20 mM, pH = 7.8) the activity of the complex is strongly inhibited with the lag phase increased up to 4 h.

To better understand the reaction and obtain information about the mechanism, the reaction was followed, both in acetonitrile and in BBS, by UV-vis spectroscopy and ESI-MS.[199]

The reaction of the complex (200 µM) with hydrogen peroxide (30 mM) was followed by monitoring the spectral changes in the region of LMCT around 400 nm, characteristic of the copper-phenolate interactions. As shown (Figure 55a), in acetonitrile a decrease in the intensity of the LMCT at 410 nm and d-d bands at 675 nm was observed, with the formation of three isosbestic points. It is important to underline that $\mathbf{Cu_2L_2}$ does not show any catalase activity in acetonitrile under the conditions explored (see Appendix). This suggests a process of catalyst degradation also confirmed by ESI-MS, showing the depletion over time of the signals associated to the dinuclear complex (see Appendix).

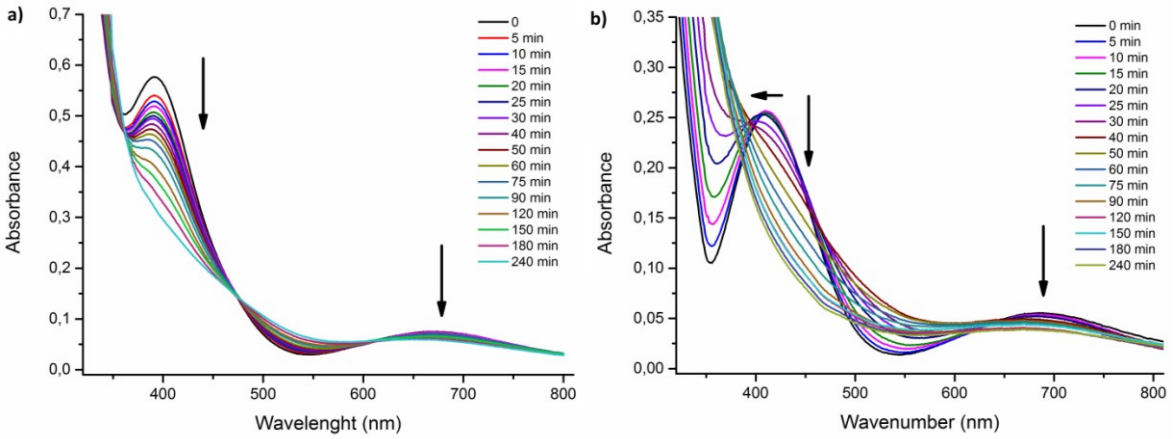

Figure 55. UV-vis spectra over time of the reaction ([$\mathbf{Cu_2L_2}$] = 200 μM, [H_2O_2] = 30 mM) in a) acetonitrile and b) BBS 50 mM pH = 7.8.

When the reaction is performed in water (BBS 50 mM, pH 7.8) instead the UV-vis spectra over time show not only the decrease of the LMCT and d-d bands but also a shift to lower wavelength of the band maximum with no isosbestic point. This suggest that during hydrogen peroxide dismutation, new catalytic intermediates are formed over time.

This hypothesis was confirmed by following the reaction by ESI-MS (see Appendix) where, after the initial lag phase, the formation of a new peak at 657.0 m/z was observed and attributed to the specie $\mathbf{Cu_2L^*_2}$ ((2), Scheme 11). This peak is formed since the beginning of the reaction, then it reaches a maximum around 30 minutes (see Figure 54) and it fades during the reaction until its disappearance after about 150-180 min. In correspondence with the depletion of $\mathbf{Cu_2L^*_2}$ was also observed the simultaneous formation of the 384.0 m/z peak attributed to $Cu^{(III)}L(OH)$ (**CuL*,** (3)) that reach it maximum at the end of reaction (see Figure 58). These peaks are attributed to catalyst degradation occurred during the catalytic cycle (see Scheme 11 and 12). These species are originated probably by the oxidation and cleavage of one of the phenolic moiety of the ligand, catalyzed by the copper sites, as it has been reported in literature for analogous compounds.[200–202]

Evidence of the ligand oxidation is provided by ESI-MS, showing a peak at 849.0 m/z (M^{2+}+ClO_4+14) corresponding to the oxidation of the phenol α-methylene group to ketone. A further oxidation then should lead to bond cleavage yielding $\mathbf{Cu_2L^*_2}$ (Scheme 11).[200,201] The cleavage of the phenolate unit should also release another vacancy in the copper coordination sphere, favouring hydrogen peroxide coordination between the two metal centres. The coordination of oxygenated species to the catalyst are suggested by the

relative abundance of the ESI peaks between 680 and 750 m/z (see Appendix) observed during the reaction.

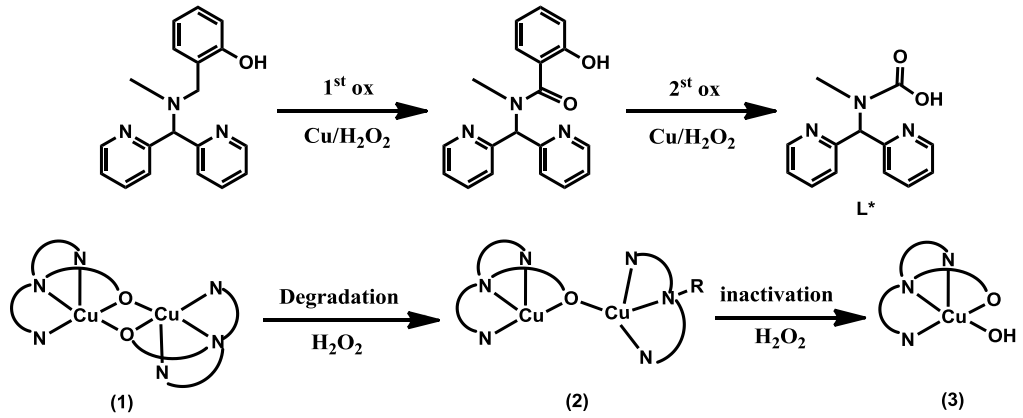

Scheme 11. Proposed oxidation of the ligand in presence of H_2O_2 (above) and the proposed product of activation (2) and deactivation (3) of the catalyst during H_2O_2 dismutation (below).

The mononuclear specie **CuL*** is likely inactive, considering that it can cycle only between Cu^{III}/Cu^{II} redox states while hydrogen peroxide dismutation needs a bi-electronic process. The formation of this inactive specie prevents copper release in solution and also the formation of copper oxides that can induce radical-type mechanisms. As a matter of fact no precipitate formation is observed and the reaction stops in presence of only the mononuclear specie. In presence of free copper, under the same experimental conditions indeed, a brown precipitate is immediately formed and hydrogen peroxide dismutation occurred at constant rate without any depletion (see Appendix).

To confirm that the oxygen production occurs via a CAT-like mechanism, excluding possible Fenton-like mechanisms, and better describe the catalytic process the reaction was also conducted in presence of a typical ·OH radical scavenger, NaBr, added at different concentration, and following the oxygen evolution kinetics.[203,204] The reaction was conducted in BBS (50 mM, pH 7.8) with a fixed catalyst concentration (200 μM) and increasing the amount of added NaBr. The addition of NaBr induces an increase of the reaction rates and of TONs (Figure 56).

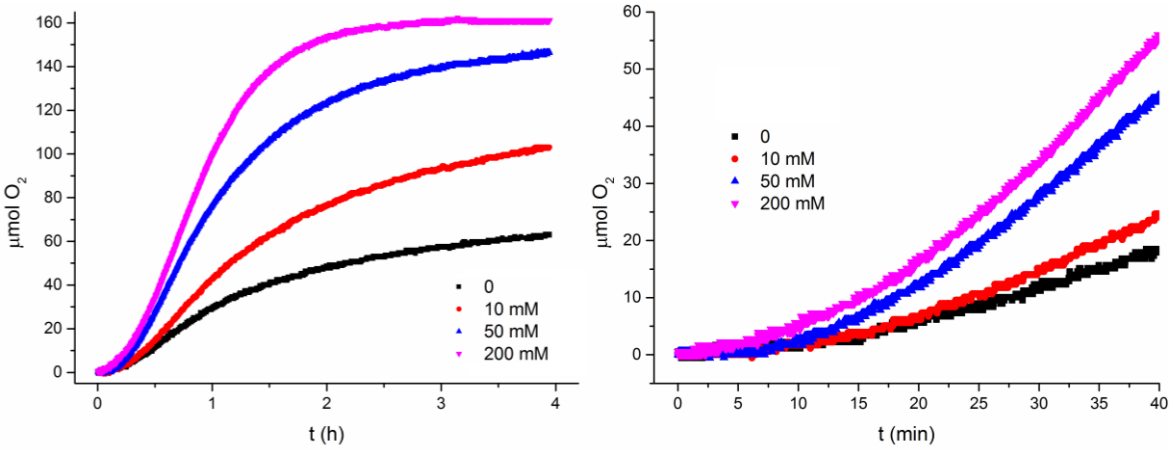

Figure 56. O_2 evolution kinetics by Cu_2L_2 (200 µmol) upon incubation with H_2O_2 (30 mM) at 25°C in BBS (50 mM pH=7.8) with different concentration of NaBr, on right a magnification of the initial lag phase.

This effect speaks in favour of a non radicalic pathway for O_2 production (Figure 57). Interestingly, the initial lag phase is maintained upon addition of NaBr meaning that no oxygen evolution occurs by a parallel process induced by the NaBr/H_2O_2 system. The remarkable rate and TON increase upon addition of NaBr, showing a saturation behaviour (Figure 57) is likely explained by an increase of the stability of the competent catalyst and indicates that the catalyst deactivation is likely due to off-cycle Fenton reactions.

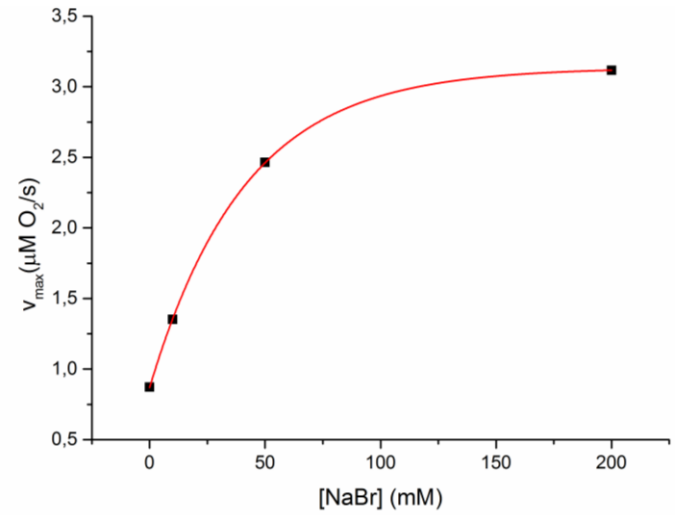

[NaBr] (mM)	R_{max} (µM O_2/s)	TON
0	0,87	52
10	1,35	87
50	2,46	122
200	3,11	134

Figure 57. Dependence of the reaction rate of O_2 production with **Cu_2L_2** in presence of NaBr at different concentration in BBS (50 mM, pH 7.8).

The high concentration of NaBr employed (50-200 mM) permits, despite the overall O_2 yield of about 90 %, a complete conversion of H_2O_2. Thus, the second route of hydrogen peroxide degradation, ascribed to a radicalic Fenton mechanism, can be quantified with a selectivity of 10 %, in agreement with the data reported in literature for complexes with the same side activity.[205]

As previously the course of reaction in presence of NaBr (50 mM) was followed by ESI-MS analysis (Figure 58). The stability of molecular complex **Cu_2L_2** is greatly increased with a lower degradation to **$Cu_2L^*_2$** (657 m/z and 787 m/z $[Cu_2L^*_2(Br)(H_2O)_2]^+$) and **CuL*** (421 m/z $[Cu(III)L^*(Br)(H_2O)_2]^+$) that start only after 45 min (see Appendix).

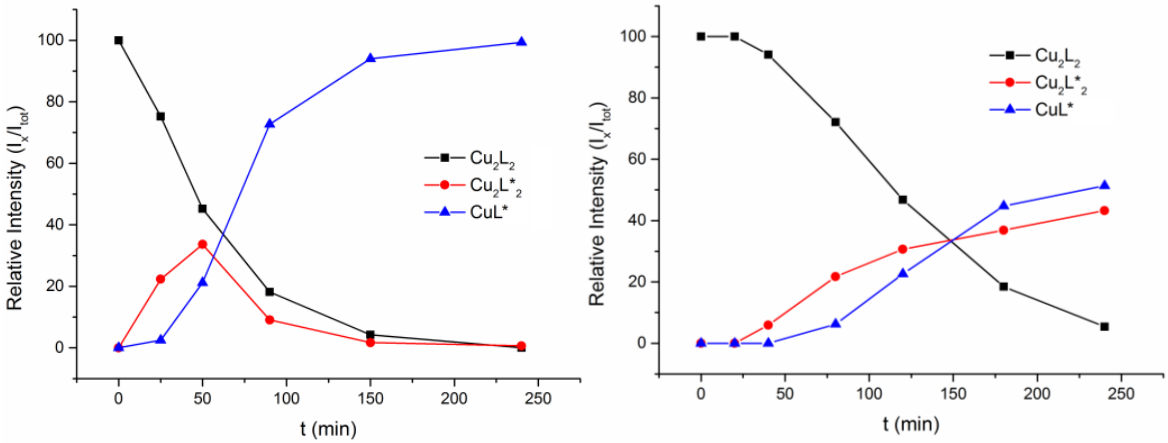

Figure 58. Catalyst evolution during the catalytic cycle ([**Cu_2L_2**]= 200 μM, [H_2O_2]= 30 mM in BBS 50 mM) monitored by ESI-MS without (left) and in presence of [NaBr] = 50 mM. Relative amount of the species were measured by the ratio between the intensity of the peaks attribute to a specie (I_x) over total species amount (I_{tot}).

This behaviour permits also to confirm that the molecular catalyst **Cu_2L_2** is the active specie in the catalytic cycle considering that the reaction start in presence of this specie alone. However also first product of degradation **$Cu_2L^*_2$**, obtained by two step oxidation of the α-methylene (Scheme 11) is still active an active specie, as confirmed by oxygen evolution profile (Figure 54). Indeed, the kinetics profile in the range from 10-75 min, a time frame in which the inactive specie formation **CuL** in negligible, does not show any rate depletion suggesting that **Cu_2L_2** and **$Cu_2L^*_2$** should present analogues activity.

$$v_{cat} = k_{cat}[Cu_2L_2][H_2O_2]$$

$$v'_{cat} = k'_{cat}[Cu_2L_2][H_2O_2] + k''_{cat}[Cu_2L^*_2][H_2O_2]$$

$$v_{cat} \cong v'_{cat} \rightarrow k'_{cat} \cong k''_{cat}$$

$$v_{cat} = k_{cat}[Cu_2L_2 + Cu_2L^*_2][H_2O_2]$$

The depletion in the catalyst activity are indeed attributed to the formation of the mononuclear inactive species **CuL**.

On the basis of the results obtained we can propose the catalytic cycle of dismutation of hydrogen peroxide by **Cu_2L_2** (Scheme 12) in which both **Cu_2L_2** and **$Cu_2L^*_2$** are involved

in the hydrogen peroxide dismutation cycling between the $Cu_2^{II,II} \rightarrow Cu_2^{III,III}$ redox states. Specie **Cu_2L_2** (1) can be converted in **$Cu_2L^*_2$** (2) by the oxidative action of hydroxyl radical and then degraded to the inactive specie **CuL** (3) by an additional hydroxyl radical damage.

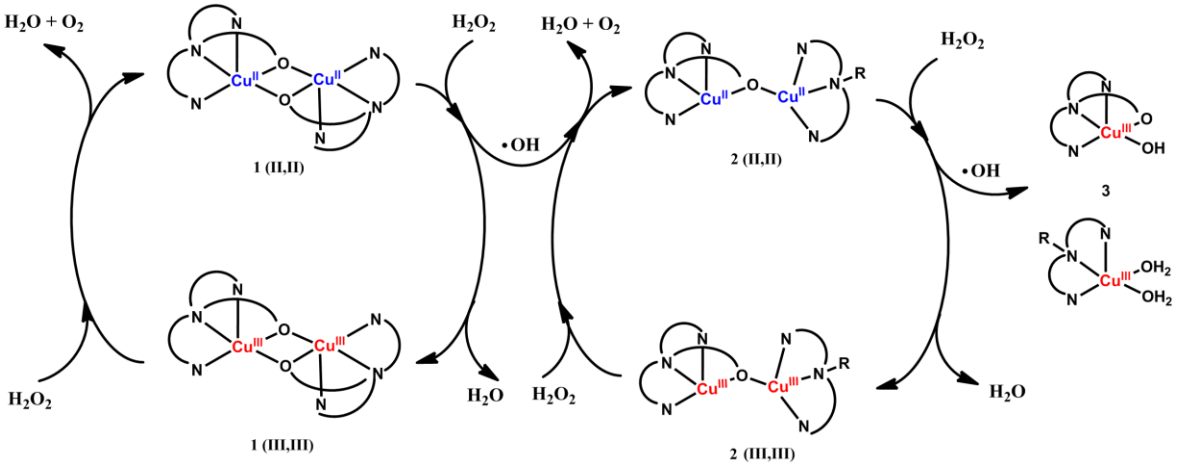

Scheme 12. Proposed catalytic cycle for decomposition of hydrogen peroxide by **Cu_2L_2**.

The second order rate constant k_{H2O2} was also evaluated working in great excess of hydrogen peroxide. In this condition we can assume a pseudo-first order for the reaction and the reaction rate can be simplified giving the apparent rate constant k_{obs} from which is possible to extrapolate $k_{H2O2} = 0.26\ M^{-1}s^{-1}$(Figure 59).

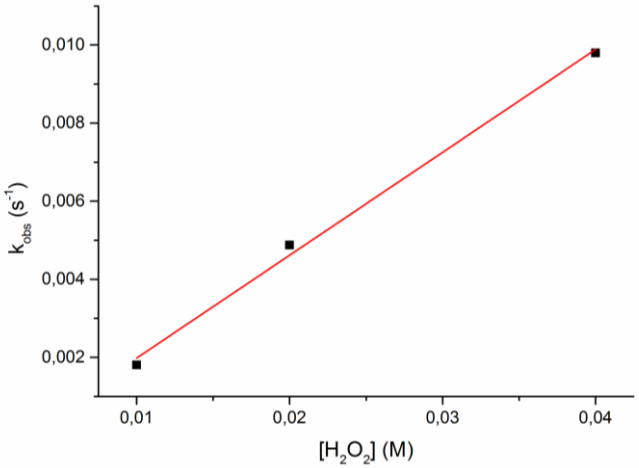

Figure 59. Linear dependence of pseudo-first-order rate constants k_{obs} on $[H_2O_2]$, determined for hydrogen peroxide dismutation by **Cu_2L_2** (200 µM) at 25°C in borate buffer (50 mM, pH 7.8). The second-order rate constants were determined from linear plots of the observed k_{obs} vs $[H_2O_2]$, $k_{obs} = k[H_2O_2]$.

By increasing the hydrogen peroxide concentration a deviation from the linearity was observed. As for **Mn_2L_2Ac** also the rate of oxygen production with **Cu_2L_2** shows a saturation behaviour amenable with Michaelis-Menten equation (see Appendix).

The rate of hydrogen peroxide dismutation shown by copper complexes in generally low, and the great excess of substrate required for this test is free to perform a wide range of side reactions. In particular, the catalytic pathways described in the literature for mononuclear complexes are two steps processes, in which the radicalic species involved can be also responsible for catalyst decomposition.[185,186]

$$H_2O_2 + Cu^{II} \rightarrow H^+ + HO_2^{\bullet} + Cu^{I}$$

$$HO_2^{\bullet} + Cu^{I} + H^+ + H_2O_2 \rightarrow H_2O + O_2 + Cu^{II}$$

For this reason, the rate constants reported for mononuclear complexes, and obtained employing high hydrogen peroxide concentration (0.1-1 M), may be affected by the formation copper oxide, able to scavenge hydrogen peroxide with a Fenton-like mechanism.[185,186]

In our case, **Cu_2L_2**, that presents a stronger ligand shell if compared with other complexes reported in literature based on bi and tridentate ligands, is stable and able to perform hydrogen peroxide dismutation at substrate concentration up to 60 mM.[173] At higher concentration the degradation of the catalyst occurs, and the oxides formation, associated to precipitate formation and changes in the kinetic profile (see Supporting Information), become relevant, making impossible the attribution of the activity observed to the pristine catalyst but instead to the copper oxides formed. The kinetics evolve with the increasing of hydrogen peroxide concentration from an S-shape profile related to a process that involve an activation/deactivation of the catalyst at low hydrogen peroxide concentration, to a straight profile with no rate change and depletion associated to the copper oxides based processes (see Supporting Information). To exclude these contributes the k_{H2O2} was measured with a hydrogen peroxide concentration lower than 60 mM.

Indeed the proved activity of the molecular **Cu_2L_2** at lower hydrogen peroxide concentration, thanks to the synergic effect of the dinuclear core able to perform bi-electronic processes, confirm the CAT-like activity of this complex, reported for the first time for a di-copper based catalyst in water.

The prooxidant (peroxidase-like) activity of the catalyst, that may be triggered by addition of H_2O_2, has also been explored to evaluate the contribute of the off cycle radical production.

Peroxidase are enzymes able to catalyze the oxidation of a broad range of organic and inorganic substrates by hydrogen peroxide or organic peroxides.[206] Obviously this is an undesired competitive reactivity for antioxidants that could cause negative side effects and also catalyst deactivation. However, peroxidase-like activity often is exhibited by complexes for which catalase activity was reported.[186] For these reasons we evaluate the pro-oxidant activity of **Cu_2L_2** in presence of hydrogen peroxide (10-30 mM, [**Cu_2L_2**] = 50 μM) by following the oxidative degradation of morin, chosen as a model chomophore, in BBS (50 mM, pH = 7.8) at 390 nm (Scheme 13).[186]

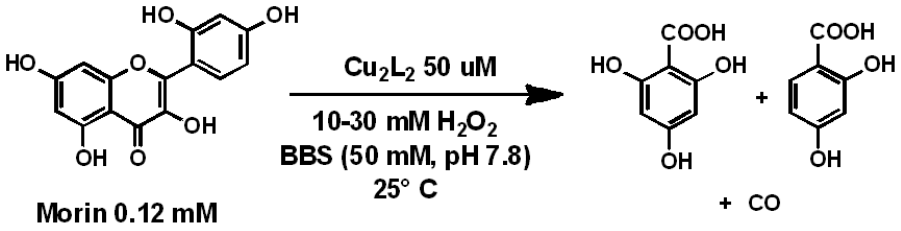

Scheme 13. Degradation of morin catalysed by peroxidase-like catalyst.

Morin oxidation is a commonly used benchmark test for bleaching catalysts as this substance belongs to the flavonoid plant dyes.[207,208] The oxidative degradation of morin in presence of H_2O_2 at pH = 7.8 is negligible under the conditions explored.

As shown in Figure 60 only a really slow depletion of the morin absorbance at 390 nm can be observed, despite the high concentration of catalyst employed (50 μM). The formation of an isosbestic point at ~350 nm is consistent with the formation of two analogous degradation products (Scheme 13).

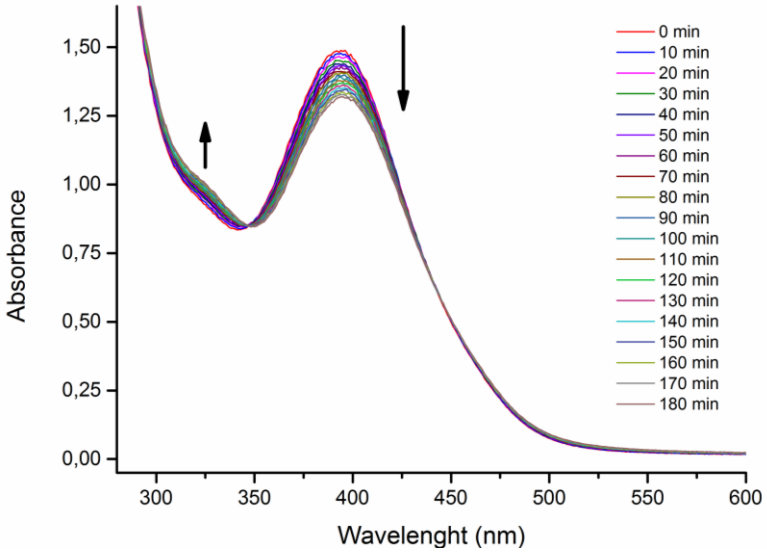

Figure 60. UV–vis spectra over time of a 0.12 mM solution of morin in BBS 50 mM pH 7.8 in the presence of 10 mM H_2O_2 and Cu_2L_2 50 μM.

The rate of reaction changes linearly with H_2O_2 concentration thus working in great excess of hydrogen peroxide we can assume a pseudo-first order conditions and the kinetic rate can be simplified giving the apparent rate constant k_{obs}.[209]

$$-d[morin]/dt = k_{obs}\,[morin][H_2O_2]$$

$$-d[morin]/dt = k_{obs}[morin]$$

A second-order rate constant was determined from linear plots of the observed pseudo-first-order rate constants vs $[H_2O_2]$, $k_{obs} = k[H_2O_2]$ (Table 6).

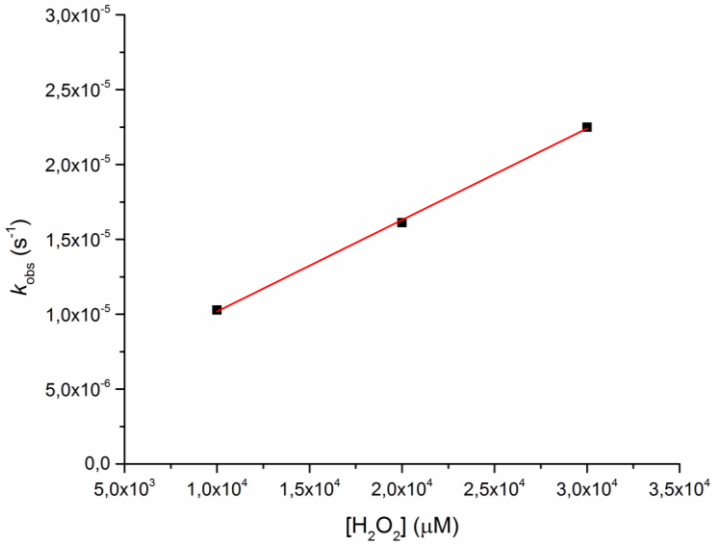

Figure 61. Linear dependence of pseudo-first-order rate constants k_{obs} on $[H_2O_2]$, varied in the range 10-30 mM, determined for oxidation of morin by **Cu_2L_2** (50 μM) at 25°C in borate buffer (50 mM, pH 7.8). The second-order rate constant was determined from linear plots of the observed k_{obs} vs $[H_2O_2]$, $k_{obs} = k[H_2O_2]$.

Table 6. Pseudo-first-order rate constant k_{obs} and second order rate constant k for oxidative degradation of morin with Cu_2L_2.

	$[H_2O_2]$ (mM)		
	10	20	30
k_{obs} (s^{-1})	$1{,}0\times10^{-5}$	$1{,}6\times10^{-5}$	$2{,}2\times10^{-5}$
k ($M^{-1}s^{-1}$)		$6{,}1\times10^{-4}$	

Considering the low value of k obtained for the oxidation of morin it is possible assume that **Cu_2L_2** does not show peroxidase-like activity versus external substrates. This means that this catalyst should exhibit a dual SOD/CAT activity without showing any pro-oxidant side mechanism.

These data are in agreement with the mechanism of the self-degradation observed for the catalyst, whereby, the organic ligand provides an intra-molecular sacrificial scavenger for

the highly oxidizing species formed at the copper centres, depleting any external oxidative damage.[202]

In conclusion, this new dinuclear copper (II) complex is able to efficiently scavenge ROS on the basis of the catalytic screening and in vitro assay. This complex is the first reported example of a dinuclear copper species showing a dual SOD/CAT activity in water under physiological-like conditions, with high SOD-like activity (IC_{50} = 0.40 μM) and a parallel CAT-like activity, which is unprecedented for a Cu-based catalyst. The dual activity of **Cu_2L_2** and the possibility to self-assemble the catalyst in solution are also of interest, in the perspective, of developing new catalytic drugs against oxidative stress and related diseases while addressing metal dyshomeostasis turning the toxic copper ions into benign anti-oxidants.

The tuning of the reactivity of the complex **Cu_2L_2** was also evaluate by small modification of the ligand. A structural analogue of the complex **Cu_2L_2** was obtained by using directly as ligand the precursor of L, 2-({[Di(2-pyridyl)methyl]amino}methyl)phenol (L^1), that presents a secondary amine on the central nitrogen (see Experimental Section). This ligand should led to the formation of a di-Cu complex with a more accessible catalytic core due to a lower steric hindrance and the presence of a secondary amine close to the metal centre should also facilitate the approach of the substrate and also the proton transfer processes, increasing in this way the rate of reaction.

X-ray analysis confirms the formation of the di-copper complex analogous to **Cu_2L_2** (Figure 62).

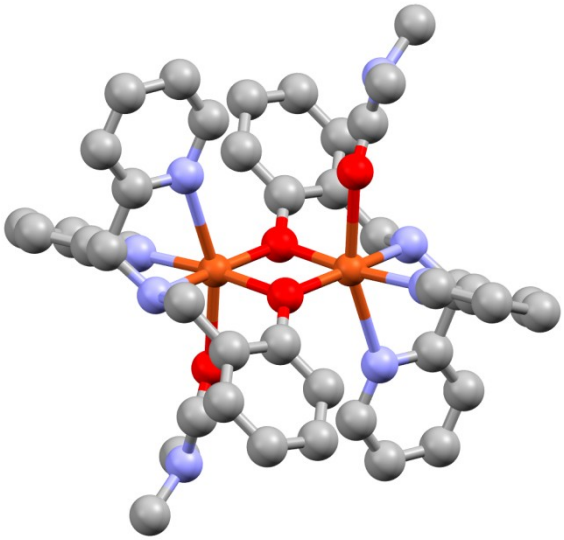

Figure 62. X-ray crystal structure of $Cu_2L^1_2$.

The structure of $\mathbf{Cu_2L^1_2}$, displays an inversion center and shows a dinuclear copper(II) complex where a tetra-dentate N_3O donor set is provided by the bis-pyridyl, amino and μ-oxo phenolate groups of the ligand. $\mathbf{Cu_2L^1_2}$ shows a distorted octahedral geometry for both metal centers, where each copper atom is coordinated by the three nitrogen atoms of the tetradentate ligand, while the phenolate moieties act as a bridges between the two metal centers. The equatorial plane is approximately defined by two copper centers, two oxygen atoms from the phenol molecules, one pyridine nitrogen atom and one amine nitrogen atom from the ligand. Considering this equatorial plane, each copper atom presents an apical position occupied by the other pyridine nitrogen atom, while the other apical position is occupied by a dimethylformamide molecule. This is an evidence of a lower Janh-Teller distortion and a higher accessibility of the copper sites if compared with $\mathbf{Cu_2L_2}$. The Cu-Cu distance and the Cu−O−Cu angle of the two μ bridging phenolate residues are respectively 3.02 Å, 100.2° (Figure 62).

The FT-IR spectrum of the complex shows the ligand coordination to the metal centers by the shift, at higher frequencies, of the pyridines and phenol absorptions located at 1610, 1597 and 1573cm^{-1} (see Appendix).[190]

The solution structure of the dinuclear complex is confirmed by ESI-MS and UV-Vis. The ESI-MS peaks for the molecular ion are 751.0 $[\mathbf{Cu_2L^1_2}+HCO_2]^+$ and 805.0 m/z for $[\mathbf{Cu_2L^1_2}+ClO_4]^+$ (see Appendix, formic acid was present in the eluent). A fragmentation peak at 353.1 m/z attributed to $[CuL^1]^+$ specie is also observed from the break of the dinuclear system in the ion source.

The UV-Vis spectrum was collected in aqueous medium ($[\mathbf{Cu_2L^1_2}]$ = 70 μM, PBS 50 mM, pH 7.8) (Figure 63). The complex shows an absorption band in the UV-region, with a maximum at 265 nm (π-π* transition of pyridines, ε = 23000 $M^{-1}cm^{-1}$) slightly shifted to lower energy respect to UV band of the ligand (261 nm in water, Appendix) and a broad, weaker absorption with a maximum at around 397 nm due to the ligand to metal charge transfer (LMCT, ε = 3600 $M^{-1}cm^{-1}$), operated by the phenol moiety.[187–189,191] A d-d transition at higher wavenumber (668 nm, ε = 620 $M^{-1}cm^{-1}$) was also observed (Figure 63).

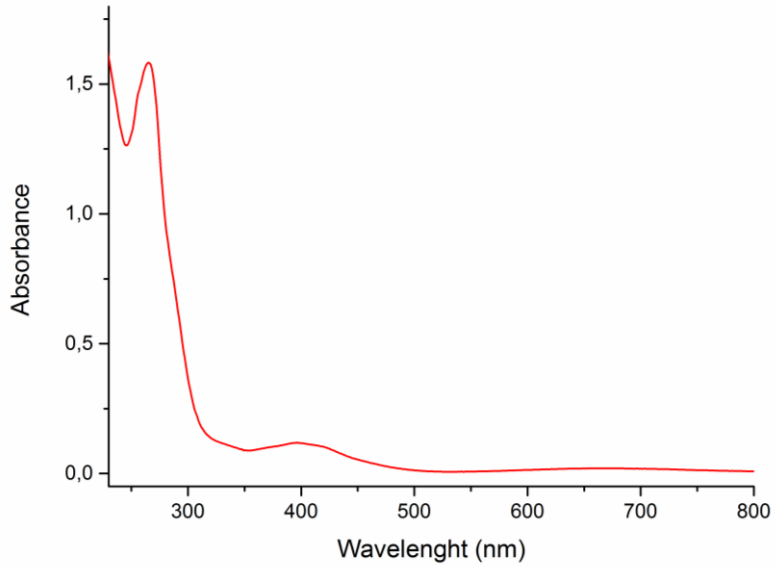

Figure 63. UV-vis spectrum in water of $\mathbf{Cu_2L^1_2}$ (70 μM).

The redox properties were determined by cyclic voltammetry (CV) experiments performed in buffer solution ($\mathbf{Cu_2L^1_2}$ 0.5 mM in phosphate buffer, 50 mM, pH = 7.8) and in acetonitrile ($\mathbf{Cu_2L^1_2}$ 0.5 mM) (Figure 64 and 65). In organic media, in reductive scan, the complex shows two irreversible cathodic waves at E^1_c = -96 mV and E^2_c = -465 mV (vs NHE) attributed respectively to the $Cu_2^{II,II} \rightarrow Cu_2^{II,I}$ and $Cu_2^{II,I} \rightarrow Cu_2^{I,I}$ redox couples. In water (PBS 50 mM, pH = 7.8, NaCl 0.1M), only one pair of reversible redox peaks were detected $E_{1/2}$ = -55 mV, meaning that in water the two processes occur simultaneously at more favourable potential due to the stabilization operated by the hydrogen bonding network of the water that facilitate the processes of electron transfer.

The complex $\mathbf{Cu_2L^1_2}$ presents a redox couple $Cu_2^{II,II} \rightarrow Cu_2^{I,I}$ with a higher potential if compared with $\mathbf{Cu_2L_2}$ and this feature should favour the catalytic process of superoxide dismutation.[46,154,166]

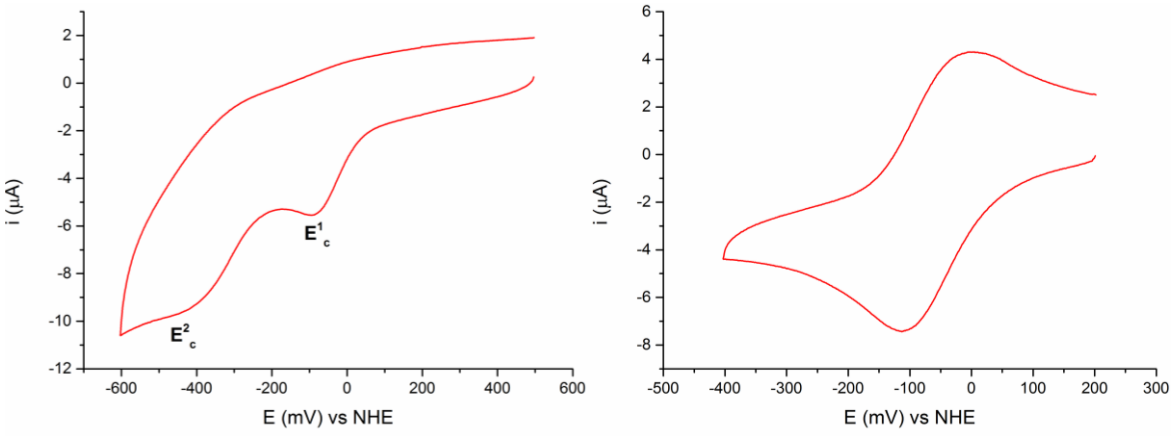

Figure 64. CV of $Cu_2L^1_2$ 0.5 mM in CH_3CN ($TEABF_4$ 0.1 M) (left), E^1_c = -96 mV and E^2_c = -465 mV and CV of $Cu_2L^1_2$ 0.5 mM in 50 mM phosphate buffer (pH = 7.8, NaCl 0.1 M), $E_{1/2}$ = -55 mV (right).

In addition at higher potential, in acetonitrile, other two quasi-reversible waves were detected, that are absent in the free ligand CV (see Appendix), thus are attributed to the $Cu_2^{III,II} \rightarrow Cu_2^{II,II}$ and $Cu_2^{III,III} \rightarrow Cu_2^{III,II}$ redox couples with $E_{1/2}$ = 1218 mV and E^3_a = 1620 mV (vs NHE) (Figure 65).

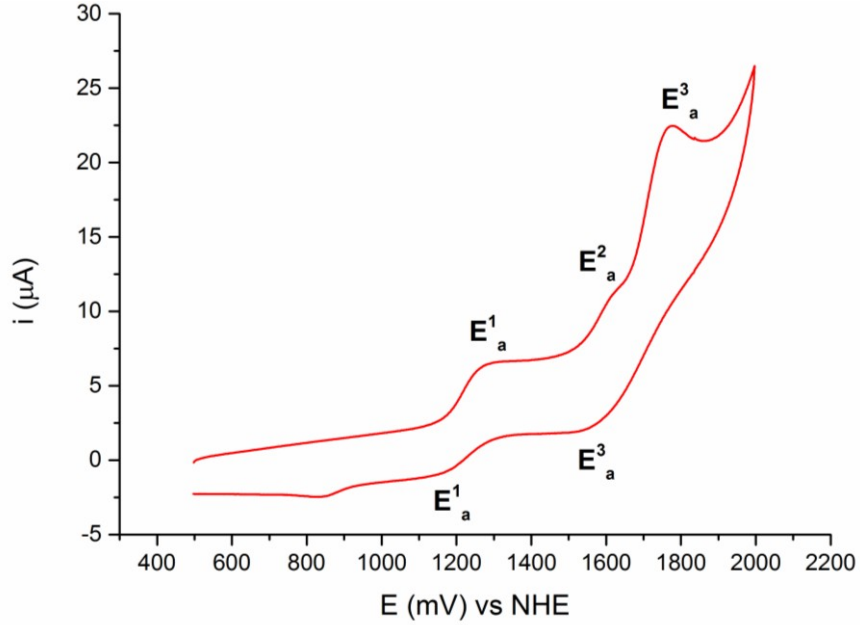

Figure 65. Cyclic voltammetry of $Cu_2L^1_2$ in acetonitrile ($TEABF_4$ 0.1M), for $Cu_2^{III,II} \rightarrow Cu_2^{II,II}$ and $Cu_2^{III,III} \rightarrow Cu_2^{III,II}$ redox couples with $E_{1/2}$ = 1218 mV and E^3_a = 1620 mV (vs NHE).

The redox potential for $Cu_2^{III,III}$- $Cu_2^{II,II}$ is higher respect to **Cu_2L_2** and seems to be too high to accomplished the process of hydrogen peroxide dismutation (+0.28 V and +1.35 V). However, in water the redox potentials are shifted to lower values and the bi-electronic transition to $Cu_2^{III,III} \rightarrow Cu_2^{II,II}$ occur simultaneously at 1180 mV (see Appendix) a potential adequate to perform the dismutation process.

The SOD performance observed for $\mathbf{Cu_2L^1_2}$ (Table 5) show a $\log k_{cat}(O_2^{\bullet -})$ = 7.27 with an IC_{50} = 0.14 μM that sets this catalyst as one of the best performing Cu-based complexes for its SOD-like activity.[165] The higher activity in comparison with $\mathbf{Cu_2L_2}$ is attributable to different factors: i) the higher redox potential of the $Cu^{II/I}$ redox couple; ii) the more accessible copper sites; iii) a higher hydrogen bonding network, due to the presence of the secondary amines, that can better assist the processes of proton transfer.[85,87] In addition the higher solubility in water of the ligand $\mathbf{L^1}$ (1 mM) could be useful for an easier synthesis in situ like previously reported for $\mathbf{Cu_2L_2}$.

The CAT activity of $\mathbf{Cu_2L^1_2}$ was tested, like previously, upon incubation with H_2O_2 (30 mM) in aqueous borate buffer (BBS, pH= 7.8) and KH buffer (pH=7.4), at 25°C following the O_2 production with a pressure transducer (Figure 66).[152] The dinuclear complex $\mathbf{Cu_2L^1_2}$ presents CAT-like activity in borate buffer (50 mM, pH=7.8) with rate, up to 4.4 μM O_2/s (Figure 66), H_2O_2 conversion up to 40%, turnover number, TON, up to 60, and turnover frequency, TOF up to 1.3 min^{-1}. An interesting feature is that for $\mathbf{Cu_2L^1_2}$ no lag phase was observed confirming that it was related to the access of the substrate to the active site, more accessible in $\mathbf{Cu_2L^1_2}$ due to the absence of the bulky methyl groups. In addition the higher hydrogen bonding network could drive the hydrogen peroxide to the active site and facilitate the processes of proton transfer, increasing the reaction rate. The complex maintains its activity also in KH buffer and despite a short initial lag phase (~20 min) and a lower rate it presents a higher stability with rate, up to 1.1 μM O_2/s (Figure 66), H_2O_2 conversion up to 75%, turnover number, TON, up to 110, and turnover frequency, TOF up to 0.32 min^{-1}.

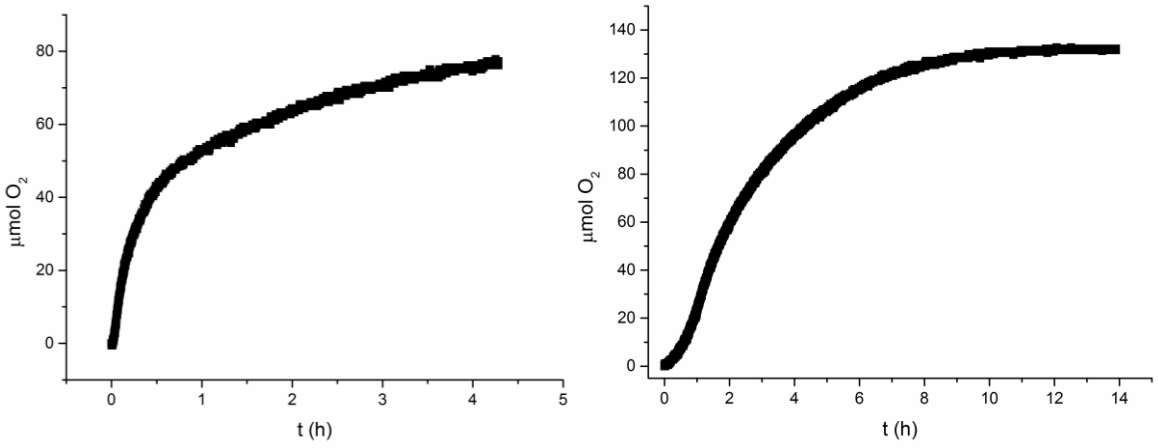

Figure 66. O_2 evolution kinetics by $\mathbf{Cu_2L^1_2}$ (200 μmol) upon incubation with H_2O_2 (30 mM) at 25°C in BBS (50 mM pH=7.8) (left) and in KH buffer (pH=7.4) (right).

The second order rate constant k_{H2O2} was also evaluated working in great excess of hydrogen peroxide obtaining a k_{H2O2} = 0.58 $M^{-1}s^{-1}$(see Appendix) in agreement with the increasing of activity observed.

Summarising the removal of the α-methylene permits to obtain a copper catalyst with more accessible active sites, a higher redox potential and a higher hydrogen bonding network permitting to obtain a catalyst with both better SOD (three times higher) and CAT (five times higher) activities.

In light of the results obtained a further modification of the ligand $\mathbf{L^1}$ was planned by the insertion of an electron-withdrawing group in the para-position of the phenolic ring. The substituent chosen for this scope is the nitro group, obtaining the ligand 2-({[Di(2-pyridyl)methyl]amino}methyl)-4-nitrophenol ($\mathbf{L^2}$) (see Appendix). X-ray analysis confirms the formation of the di-copper complex analogous to $\mathbf{Cu_2L^1_2}$ (Figure 67).

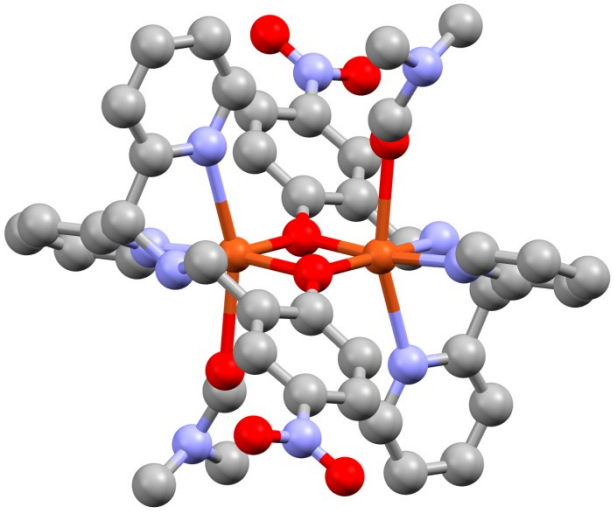

Figure 67. X-ray crystal structure of $Cu_2L^2_2$.

The structure of $\mathbf{Cu_2L^2_2}$, displays like $\mathbf{Cu_2L^1_2}$, a distorted octahedral geometry for both metal centers, where each copper atom is coordinated by the three nitrogen atoms of the tetradentate ligand, while the phenolate ligands act as a bridges between the two metal centers and two dimethylformamide molecules complete the coordination sphere. The Cu-Cu distance and the Cu–O–Cu angle of the two μ bridging phenolate residues are respectively 3.03 Å, 99.8° (Figure 67).

The FT-IR spectrum of the complex shows the ligand coordination to the metal centers by the shift, at higher frequencies, of the pyridines and phenol absorptions located at 1600 and 1575cm^{-1} (see Appendix).[190]

The solution structure of the dinuclear complex is confirmed by ESI-MS and UV-Vis. The ESI-MS peaks in water for the molecular ion are 841.2 $[\mathbf{Cu_2L^2_2}+HCO_2]^+$ and 895.1 m/z for $[\mathbf{Cu_2L^2_2}+ClO_4]^+$ (see Appendix, formic acid was present in the eluent). A fragmentation peak at 398.1 m/z attributed to $[CuL^2]^+$ specie is also observed from the break of the dinuclear system in the ion source.

The UV-Vis spectrum was collected in aqueous medium ($[\mathbf{Cu_2L^2_2}]$ = 50 µM, PBS 50 mM, pH 7.8) (Figure 68). The complex shows an absorption band in the UV-region, with a maximum at 256 nm (π-π* transition of pyridines, ε = 21000 $M^{-1}cm^{-1}$) and a broad, intense absorption with a maximum at 376 nm due to a sum of the ligand to metal charge transfer operated by the phenol moieties and the absorption of the nitrophenol itself (ε = 23000 $M^{-1}cm^{-1}$).[187–189,191] The peak maximum is also shifted to higher energy if compared with the free ligand $\mathbf{L^2}$ (λ_{max} = 411 nm, ε = 14200 $M^{-1}cm^{-1}$). A d-d transition at higher wavenumber (652 nm, ε = 240 $M^{-1}cm^{-1}$) was also observed (Figure 68).

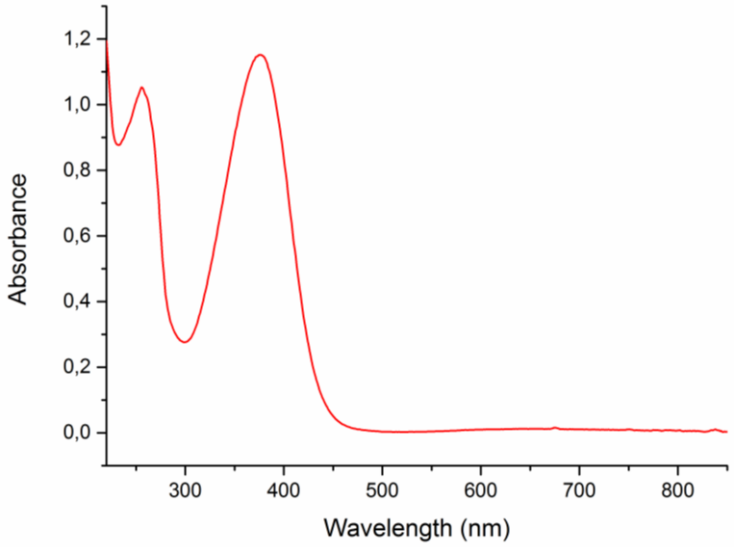

Figure 68. UV-vis spectrum in water of $\mathbf{Cu_2L^2_2}$ (50 µM).

The redox properties were determined by cyclic voltammetry (CV) experiments performed in buffer solution ($\mathbf{Cu_2L^2_2}$ 0.5 mM in phosphate buffer, 50 mM, pH = 7.8) and in acetonitrile ($\mathbf{Cu_2L^2_2}$ 0.5 mM) (Figure 69 and 70). In organic media, in reductive scan, the complex shows two irreversible cathodic waves at E^1_c = 62 mV and E^2_c = -273 mV (vs NHE) attributed respectively to the $Cu_2^{II,II} \rightarrow Cu_2^{II,I}$ and $Cu_2^{II,I} \rightarrow Cu_2^{I,I}$ redox couples. In water (PBS 50 mM, pH = 7.8, $TEABF_4$ 0.1M), only one pair of quasi-reversible redox peaks were detected $E_{1/2}$ = 60 mV, meaning that in water, like previously, the two processes occur simultaneously at more favourable potential.

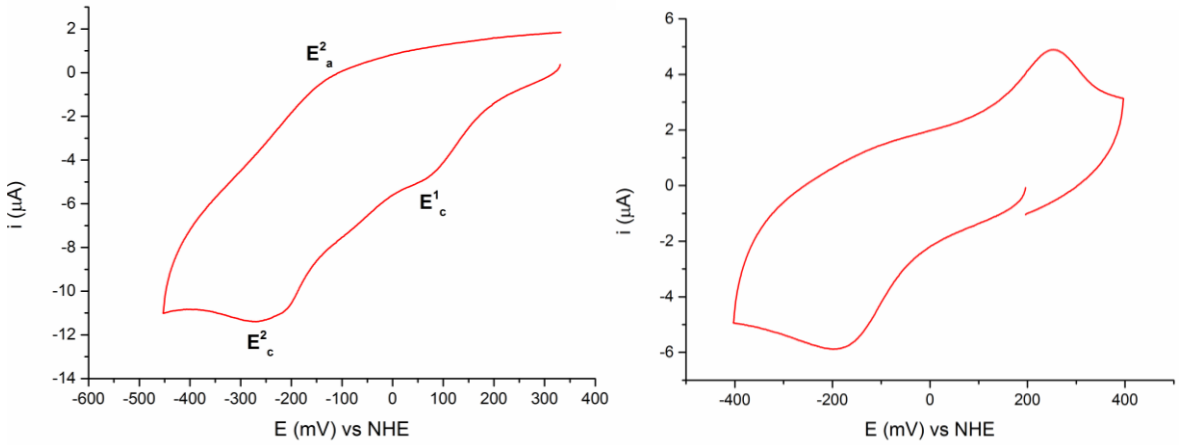

Figure 69. CV of $Cu_2L^2_2$ 0.5 mM in CH_3CN ($TEABF_4$ 0.1 M) (left), E^1_c = 62 mV and E^2_c = -273 mV and CV of $Cu_2L^2_2$ 0.5 mM in 50 mM phosphate buffer (pH = 7.8, $TEABF_4$ 0.1 M) (right), $E_{1/2}$ = 60 mV.

The complex **$Cu_2L^2_2$** presents a further increase of the $Cu_2^{II,II} \rightarrow Cu_2^{I,I}$ redox potential if compared with **$Cu_2L^1_2$** and this feature should favour the catalytic process of superoxide dismutation.[46,154,166]

In acetonitrile, at higher potential, other two irreversible waves were detected, that are absent in the free ligand CV (see Appendix), thus are attributed to the $Cu_2^{III,II} \rightarrow Cu_2^{II,II}$ and $Cu_2^{III,III} \rightarrow Cu_2^{III,II}$ redox couples with E^1_a = 1.56 V and E^2_a = 2.19 V (vs NHE) (Figure 70).

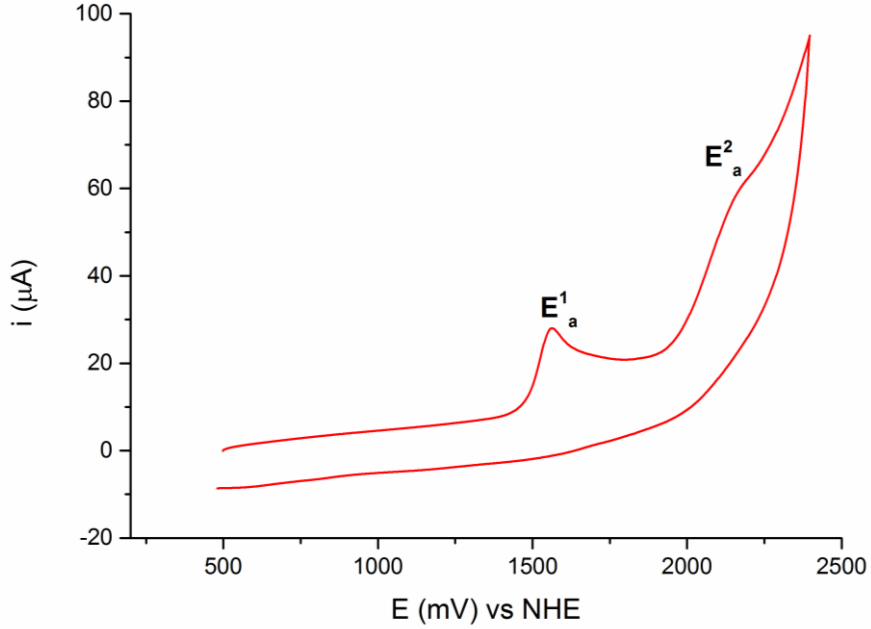

Figure 70. Cyclic voltammetry of Cu_2L_2 in acetonitrile ($TEABF_4$ 0.1M), for $Cu_2^{III,II} \rightarrow Cu_2^{II,II}$ and $Cu_2^{III,III} \rightarrow Cu_2^{III,II}$ redox couples with E^1_a = 1.56 V and E^2_a = 2.19 V (vs NHE).

The redox potentials of $Cu_2^{III,III}$- $Cu_2^{II,II}$ are too high to accomplished the process of hydrogen peroxide dismutation (+0.28 V and +1.35 V). However, also for **$Cu_2L^2_2$**, in presence of water the redox potentials are shifted to lower values and the transition

$Cu_2^{III,III} \rightarrow Cu_2^{II,II}$ occurs around 1.3 V (see Appendix) a potential close to the upper edge of the dismutation process.

The SOD performance observed for $\mathbf{Cu_2L^2_2}$ (Table 5) show a $\log k_{cat}(O_2^{\bullet -}) = 7.55$ with an $IC_{50} = 0.072$ μM that sets this catalyst as the best performing Cu-based complexes for its SOD-like activity.[165] The higher activity in comparison with $\mathbf{Cu_2L^1_2}$ is attributable to the higher redox potential of the $Cu^{II/I}$ redox couple.[85,87]

The CAT activity of $\mathbf{Cu_2L^2_2}$ was tested, like previously, upon incubation with H_2O_2 (30 mM) in aqueous borate buffer (BBS, pH= 7.8) and KH buffer (pH=7.4), at 25°C (Figure 71).[152] The dinuclear complex $\mathbf{Cu_2L^2_2}$ presents CAT-like activity in borate buffer (50 mM, pH=7.8) with rate, up to 4.3 μM O_2/s (Figure 71), H_2O_2 conversion up to 40%, turnover number, TON, up to 60, and turnover frequency, TOF up to 1.3 min^{-1}. No lag phase was observed also for $\mathbf{Cu_2L^2_2}$ confirming that it was related to the access of the substrate to the active sites. The catalytic performance are analogue to $\mathbf{Cu_2L^1_2}$ meaning that an higher redox potential of the copper centers do not favor the process of dismutation. In fact the optimal redox potential for the process should be intermediate between the potentials of oxidation and reduction of H_2O_2 (+0.28 V and +1.35 V vs NHE). These data also confirm that the increase of performance observed for $\mathbf{Cu_2L^1_2}$ is mainly attributable to a more accessible catalytic sites and to the higher hydrogen bonding network that facilitate the processes of proton transfer and not to the redox potential change.

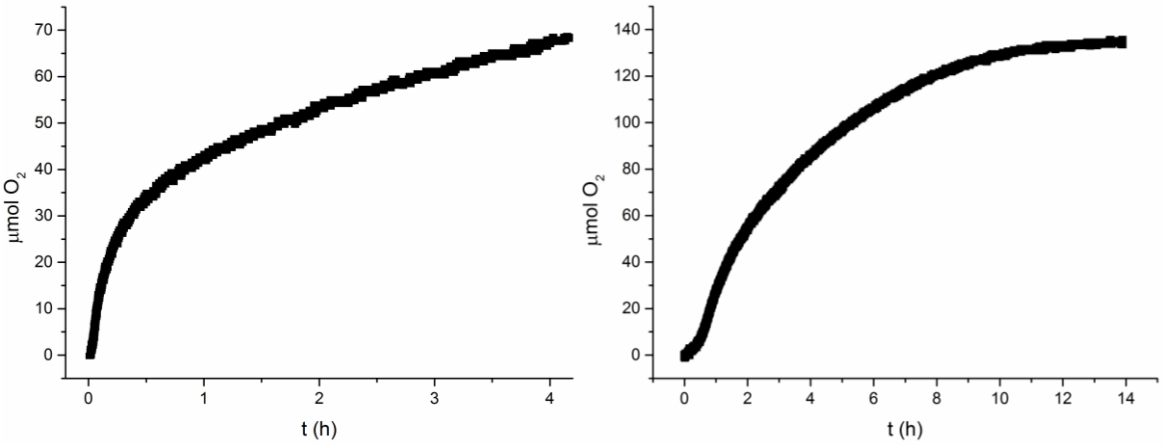

Figure 71. O_2 evolution kinetics by $\mathbf{Cu_2L^2_2}$ (200 μmol) upon incubation with H_2O_2 (30 mM) at 25°C in BBS (50 mM pH=7.8) (left) and in KH buffer (pH=7.4) (right).

The complex maintains its activity also in KH buffer and despite a short initial lag phase and lower rate it presents, like $\mathbf{Cu_2L^1_2}$, a higher stability with rate, up to 1.0 μM O_2/s (Figure 71), H_2O_2 conversion up to 75%, turnover number, TON, up to 110, and turnover frequency, TOF up to 0.31 min^{-1}. The second order rate constant k_{H2O2} was also evaluated

working in great excess of hydrogen peroxide obtaining a k_{H2O2} = 0.57 $M^{-1}s^{-1}$(see Appendix) analogue to **$Cu_2L^1_2$**.

Concluding in this chapter it was demonstrated that with a proper set of ligands it is possible to tune the reactivity of a metal center moving from the harmful activity of the free copper to a benign catalytic antioxidant. These complexes are the first reported examples of dinuclear copper species showing a dual SOD/CAT activity in water under physiological-like conditions, with an outstanding SOD-like activity (IC_{50} up to 0.072 µM) and a parallel CAT-like activity (Figure 72), which is unprecedented for a Cu_2-based catalyst. These activities are also coupled with no external prooxidant activity thanks to the intra-molecular sacrificial scavenger. This approach permit also a fine tuning of the activity of the species, by introducing bulky group and substituents in to the phenol ring in fact is it possible to modulate the lag phase and the SOD/CAT performances (Table 7). In particular the outstanding performance obtained for **$Cu_2L^2_2$** make this synzyme an alternative to manganese porphyrins as antioxidant for therapeutic purpose considering the analogous SOD performance and the higher stability to oxidative bleaching, coupled also with relevant CAT-like activity.[19,154,210]

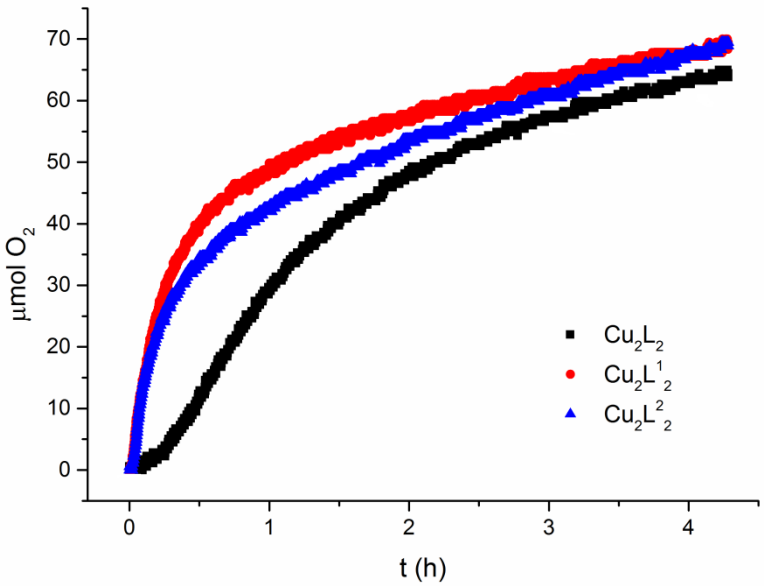

Figure 72. Comparison of O_2 evolution kinetics by $[Cu_2L_2]^{2+}$, $[Cu_2L^1_2]^{2+}$ and $[Cu_2L^2_2]^{2+}$ (200 µmol) upon incubation with H_2O_2 (10 mM) in BBS (50 mM pH=7.8).

Table 7. Catalytic performances for di-copper dual SOD/CAT synzymes.

Catalysts	$E_{½}$/mV[a] vs NHE		SOD activity[b]		CAT activity[c]			
	$Cu_2^{II,II/I,I}$	$Cu_2^{III,III/II,II}$	IC_{50} (μM)	$\log k_{cat}(O_2^{\bullet -})$	R_0 (μM O_2/s)	TOF (min^{-1})	k_{H2O2} ($M^{-1}s^{-1}$)	TON
$[Cu_2L_2]^{2+}$	-161	+967	0.40	6.80	0.87[c]; 0.51[d]	0.26[c]; 0.16[d]	0.26	52[c]; 110[d]
$[Cu_2L^1_2]^{2+}$	-55	+1180	0.14	7.27	4.4[c]; 1.1[d]	1.3[c]; 0.32[d]	0.58	60[c]; 110[d]
$[Cu_2L^2_2]^{2+}$	+60	+1310	0.07	7.55	4.3[c]; 1.0[d]	1.3[c]; 0.31[d]	0.57	60[c]; 110[d]

[a] $E_{1/2}$ is measured in 0.05 M phosphate buffer, pH 7.8, 0.1 M NaCl; [b] SOD activity is measured by cyt c assay; [c] Measured in BBS 50 mM pH=7.8 at 25 °C. [d] Measured in KH buffer 50 mM pH=7.4 at 25 °C.

4. Iron and Cobalt complexes

4.1 Iron complexes

The polydentate ligand (HL = 2-{[[di(2-pyridyl)methyl] (methyl)amino]methyl}phenol) has shown a specific binding affinity towards first row transition metals, yielding dinuclear manganese and copper complexes. [211] We have further explored the case of iron species.

Two different iron complexes, could be obtained by the reaction of the HL ligand, with different iron precursors (Scheme 14).[212]

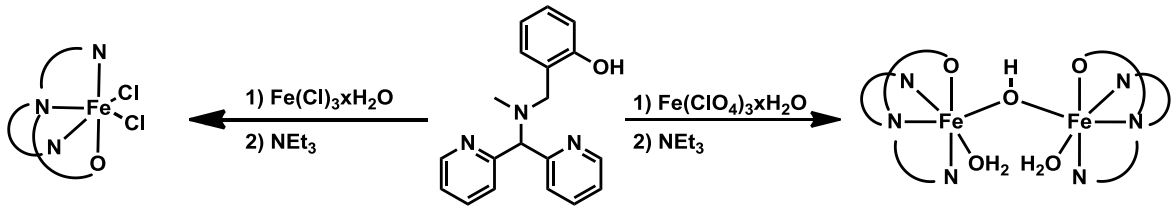

Scheme 14. Synthesis of iron based complexes, structures based on crystallographic data.

A mononuclear iron complex has been isolated by using Fe(III) chloride followed by the addition of triethylamine (see Experimental Section).[149] Solid state characterization (FT-IR and X-ray) confirms Fe(III)-monomer (Scheme 14).

X-ray analysis of **$FeL(Cl)_2$** shows a highly distorted octahedral geometry for the metal centre, where the Fe(III) atom is coordinated in a facial configuration by the three nitrogen atoms of the tetradentate ligand, while the phenolate and chloride ligands complete the coordination sphere (Figure 73).

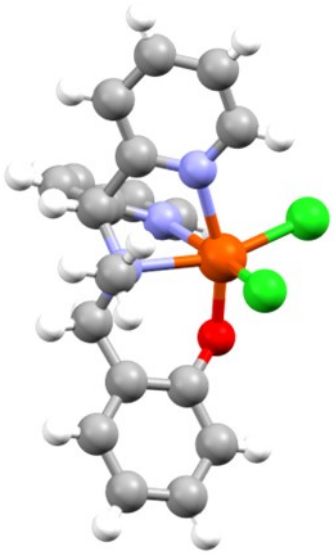

Figure 73. X-ray crystal structure of $FeL(Cl)_2$.

The complex presents strong IR bands at 1604 and 1600 cm^{-1} assigned to pyridine and phenolate absorptions in the FeL unit (Figure 74).

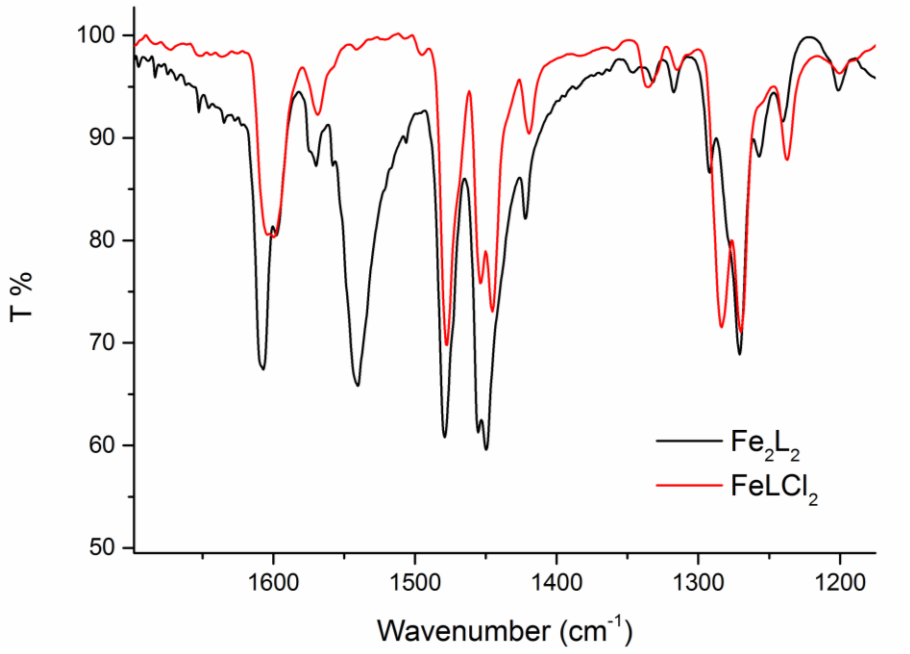

Figure 74. Comparison of the FT-IR spectra of **FeL** and **Fe_2L_2**.

The dinuclear iron complex could be obtained with the same protocol but using Fe(III) perchlorate instead chloride (see Experimental Section). Formation of a **Fe_2L_2** dimer is confirmed by FT-IR and X-ray analysis.

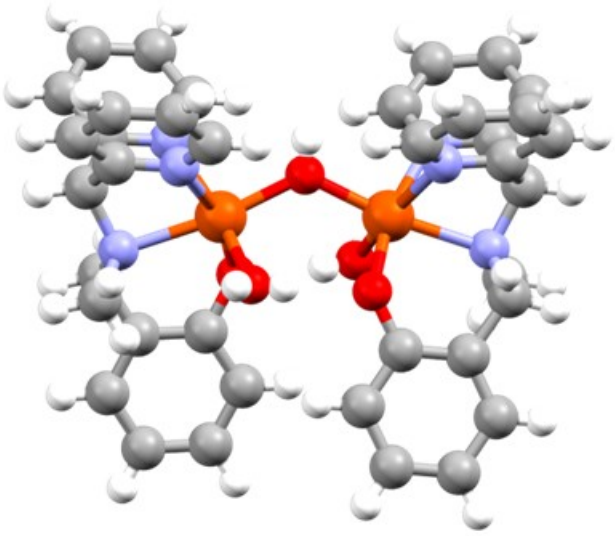

Figure 75. X-ray crystal structure of $Fe_2L_2(\mu\text{-}OH)(H_2O)_2$.

X-ray analysis of **Fe_2L_2** shows the formation of a dimer constituted by the joining of two FeL^{2+} units operated by a μ-(OH) bridge. The coordination sphere is completed by the binding of a water molecule for each iron centre. The Fe-O distance and the Fe−O−Fe

angles of the μ-(OH) bridge are respectively 1.95 Å and 127.2° whereas the Fe-Fe distance is 3.50 Å (Figure 75). The overall structure is stabilized by a wide hydrogen bonding network constituted by the interaction between crystallization and coordination water molecules among them, with the phenols and the μ-(OH) bridge (second coordination sphere of water molecules were al detected). The structure of this complex is different if compared with the **Mn_2L_2Ac** and **Cu_2L_2** analogues, this is due to the propensity of the Fe(III) to form μ-(OH) and μ-(O) bridges, like reported for several iron based complexes, despite form μ-phenolate bridges.[212–215]

The dinuclear complex **Fe_2L_2** presents strong IR band at 1607 and 1598 cm^{-1} assigned to pyridine and phenolate absorptions in the FeL unit although the peaks are shifted if compared with **FeL,** meaning that a different structure was obtained. In particular a strong band associated to the Fe-O-Fe asymmetric stretching was detected in the fingerprint region at 765 cm^{-1} (see Appendix).[216]

The structural differences between the monomeric and dimeric form of the iron complexes are maintained only in the solid state and in organic solution. When dissolved in acetonitrile in fact **FeL** and **Fe_2L_2** show different spectra in particular in the 300-800 nm region (Figure 76 and Appendix).

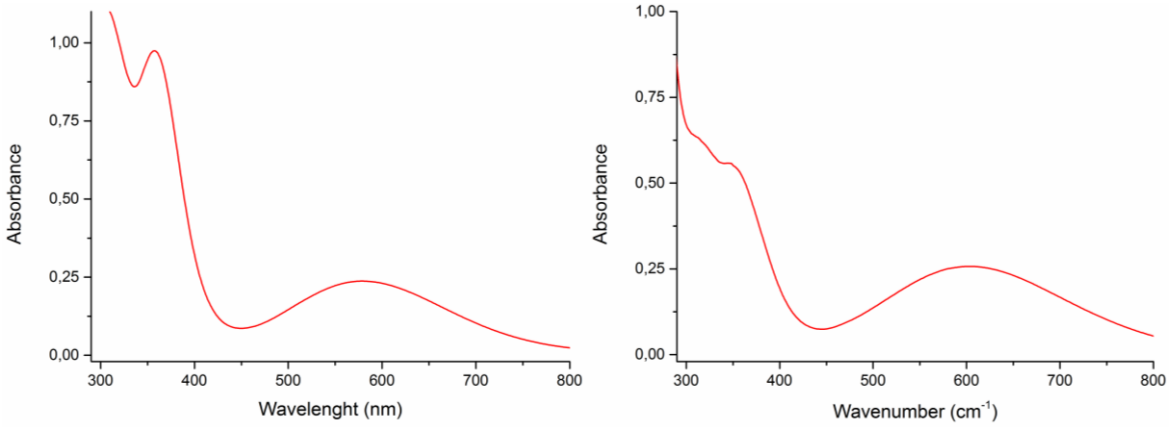

Figure 76. UV-vis spectra of **FeL** (140 μM) (left) and **Fe_2L_2** (75 μM) (right) in acetonitrile.

FeL presents two absorptions with a maximum at around 358 nm due to the ligand to metal charge transfer (LMCT, ε = 6970 $M^{-1}cm^{-1}$) pπ → dσ* transitions from the phenolate to the metal and another band at higher wavelength 580 nm (ε = 1700 $M^{-1}cm^{-1}$) attributable to pπ→ dπ* transitions again from the phenolate to the Fe(III) metal center.[217–219]

Fe_2L_2 instead presents two absorptions with one maximum at around 345 nm due to the ligand to metal charge transfer (LMCT, ε = 7410 $M^{-1}cm^{-1}$) pπ → dσ* transitions from the

phenolate to the metal and the other band observed at higher wavelength 604 nm (ε = 3430 $M^{-1}cm^{-1}$) attributable to pπ → dπ* transitions from the phenolate to the Fe(III) metal center in the dimeric unit.[217–219]

When water (10 % v/v) was added to the organic solution of **FeL** some spectral changes were observed. The intensity of the lower (λ_{max} = 358 nm) LMCT band decrease and the other (λ_{max} = 580 nm) is red shifted. This phenomena is simply due to the interconversion of the monomer **FeL** into the dimer **Fe_2L_2** that occur in presence of water (Figure 77).

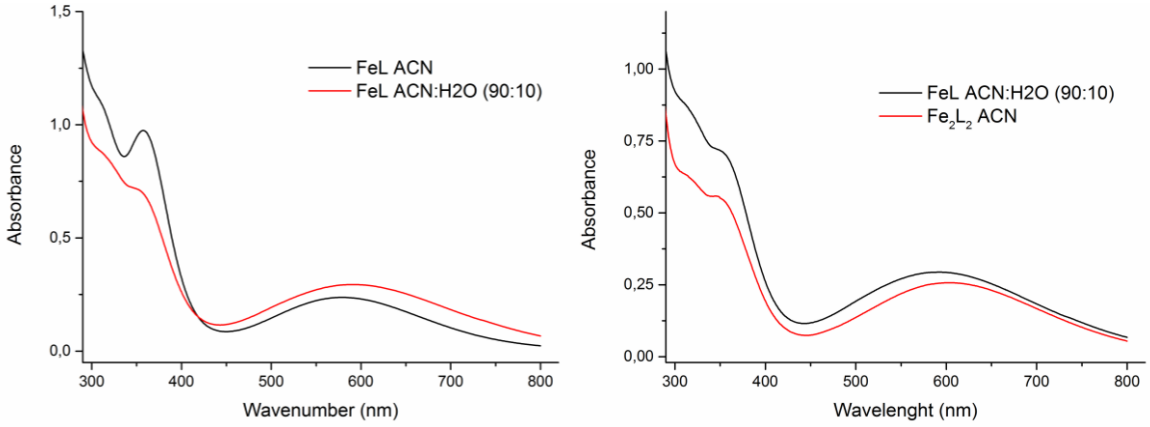

Figure 77. Comparison of the UV-vis spectra of **FeL** (140 μM) in acetonitrile before and after addition of 10% of H_2O (left) and comparison with **Fe_2L_2** (75 μM) (right) in acetonitrile.

The relative intensity of the bands in pure acetonitrile and in presence of water are different due to in large part to hydrogen-bonding interactions between the solvent and the oxo-oxygen atoms. In the present case the decrease of the absorbance in the visible region is caused by the addition of small amounts of water.[220]

Regarding the dimer **Fe_2L_2** in ACN:H_2O (90:10) a colour change from blue to pink was observed after few minutes. This change is attributable to a pH variation of the solution and consequently to another equilibrium involving the **Fe_2L_2**, in particular due to the protonation of the bridging oxygen (see X-ray structure Figure 75). This hypothesis was confirmed by the addition of a small acid aliquot to the ACN:H_2O solution. In this condition the LMCT of **Fe_2L_2** are shifted respectively to 328 nm (ε = 10900 $M^{-1}cm^{-1}$) and 499 nm (ε = 3780 $M^{-1}cm^{-1}$) (see Appendix).

When the crystals of FeL and Fe_2L_2 are dissolved in water instead the formation of the same specie was observed independently of the starting compound.[212] To evaluate this behaviour the two species were studied in solution by UV-vis and ESI-MS analysis both in acetonitrile and in water at different pH.

The ESI-MS analysis of the solution reveals that the dimer, with peaks at 368, 398 and 795 m/z, that are respectively attributed to $[\mathbf{Fe_2L_2}]^{2+}$, $[\mathbf{Fe_2L_2}+H^+ + H_2O + ACN]^{2+}$ and $[\mathbf{Fe_2L_2}+H_2O+ACN]^{+}$, is the only specie detected in organic solution independently by the starting iron complex. In contrast with the UV-vis analysis in organic solution, this result could be explained considering that in the ESI-MS there are always present traces of water and acids that are sufficient to interconvert the greater part of the monomer **FeL** in to the dimer $\mathbf{Fe_2L_2}$.

Moving from organic to aqueous solution the situation becomes more complicated. In water the monomer-dimer equilibrium is dictated by the pH with two main colour changes observed moving from acidic (blue) to basic solution (pale yellow) associated with a blue shift of the maximum of LMCT bands (Figure 78).

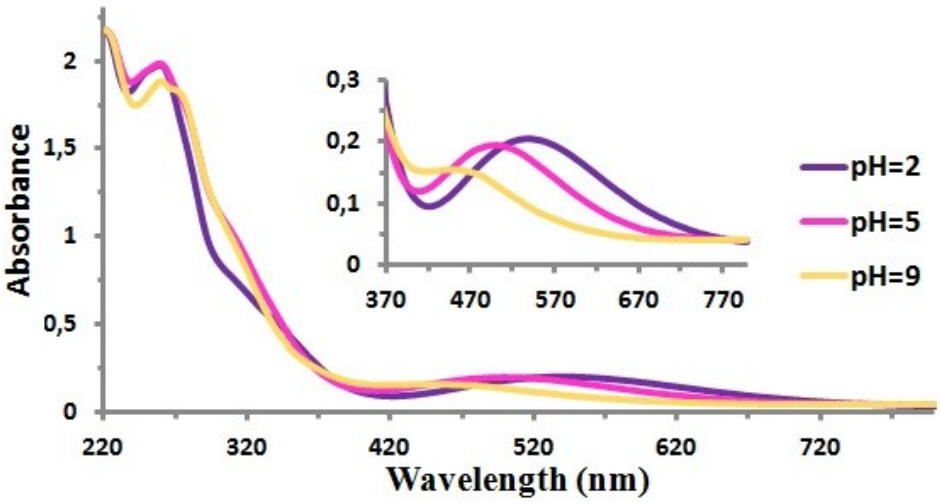

Figure 78. UV-vis spectra for $\mathbf{Fe_2L_2}$ (60 μM) in water at different pH.

These spectral changes are attributable to structural changes of the complex in solution. This hypothesis was confirmed by ESI-MS analysis of the complex at different pH.[212] The ESI-MS analysis in acid conditions (pH = 3) shows that the more stable specie is the monomer, responsible to the blue colour, with the correspondence peaks at 377, 395 and 462 m/z associated respectively to $[\mathbf{FeL}]^{2+}$ plus hydroxide, chloride and perchlorate (see Appendix). At higher pH the colour turns to pink around pH= 7. This variation is associated to a change in the assembly of the iron complex that moves from the monomeric form in the acidic conditions to the dimeric form, prevalent in the organic solution, as confirmed by the ESI-MS peaks at 781 and 835 m/z (see Appendix). A further increase of the pH, around 9, is associated to another change of the solution colour that turned pale yellow followed by the formation of a brown precipitate. This change is associated to the

demetallation of the iron complex in alkaline conditions with the simultaneous formation of iron hydroxide. As expected, the ESI-MS recorded at pH = 9 shows no peaks associated to the monomeric and dimeric species and the presence of four new peaks at 1331, 1001, 677, 350 m/z differing for 327 m/z each one, are associated to the chelation of the Na^+ by the ligand, forming polinuclear clusters. The peaks observed are ascribed respectively to the molecular ions $[Na_5L_4]^+$, $[Na_4L_3]^+$, $[Na_3L_2]^+$ and $[Na_2L]^+$. Smaller peaks related to K^+ chelation were also observed (see Appendix).

It is important to underline that all the species detected at various pH are in equilibrium and interconvert by tuning the pH, whereby the dimeric **Fe_2L_2** turns out to be formed again from iron hydroxide and the ligand-sodium clusters that are present in solution upon addition of NaOH at pH>9 (Scheme 15).

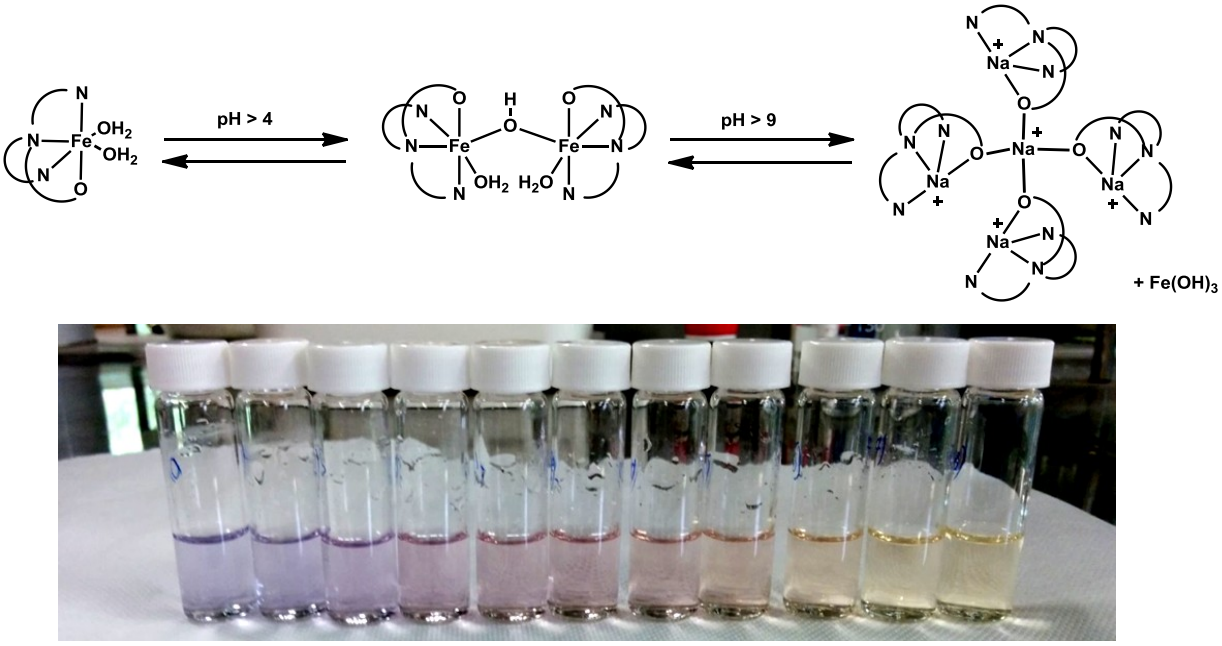

Scheme 15. Reversible interconversion and speciation of the iron complex in aqueous media at different pH.

The redox properties of **FeL** and **Fe_2L_2** were determined by cyclic voltammetry (CV) experiments performed in buffer solution (0.5 mM in ACN, $TBAClO_4$ 0,1 M).

In the oxidative scan, **FeL** shows an irreversible anodic wave E^2_a = 1.49 V (vs NHE) due to a ligand based process. [221] In addition another low intensity wave E^2_a = 1.17 V (vs NHE) is attributable to the $Fe^{III} \rightarrow Fe^{IV}$ oxidation process (Figure 79). In the reductive scan, under analogous experimental conditions the mononuclear complex shows a

quasireversible peak $E_{1/2}$ = -16 associated to the monoelectronic $Fe^{III} \rightarrow Fe^{II}$ reduction.

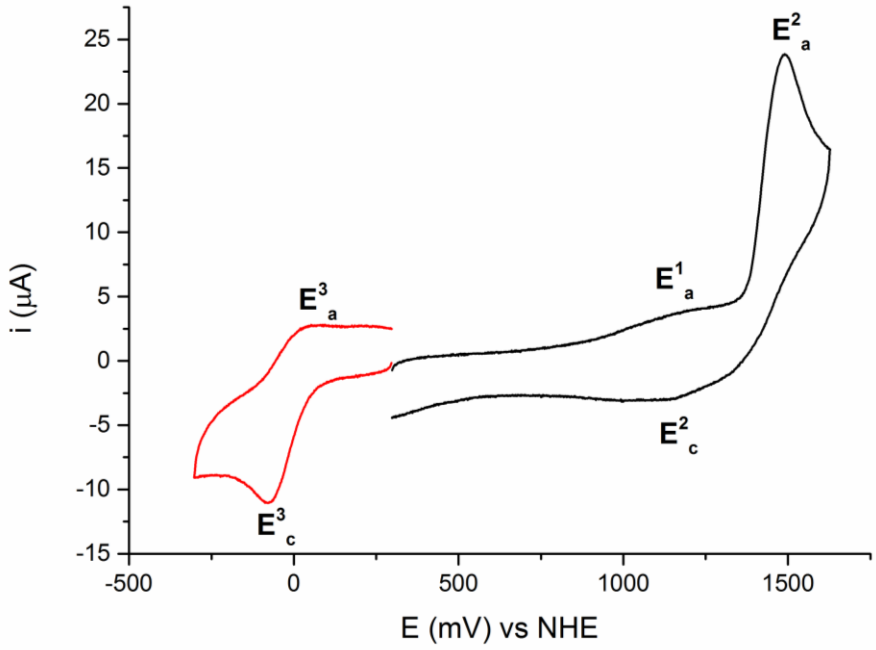

Figure 79. CV of 0.5 mM FeL in CH_3CN ($TBAClO_4$ 0.1 M). The anodic peak E^1_a = 1170 is ascribed to monoelectronic $Fe^{III} \rightarrow Fe^{IV}$ oxidation. The cathodic peak $E_{1/2}$ = -16 is ascribed to monoelectronic $Fe^{III} \rightarrow Fe^{II}$ reduction.

The cyclic voltammetry of **Fe_2L_2** shows several peaks attributable to the iron-centered redox couples both in the oxidation and in reduction scans(Figure 80). In the oxidative scan, **Fe_2L_2** shows two irreversible peaks at E_a^1 = 1310 and E_a^2 = 1470 mV (vs NHE) attributable respectively to the $Fe_2^{III,III}$-$Fe_2^{IV,III}$ and $Fe_2^{IV/III}$-$Fe_2^{IV,IV}$ redox couples and another irreversible peak at E_a^3 = 1695 mV due to a ligand based process.[221] In reductive scan, under the same experimental conditions the dinuclear complex shows two quasi-reversible peaks with $E_{1/2}$ = 257 mV and $E_{1/2}$ = 12 mV associated respectively to the monoelectronic reduction of the $Fe_2^{III,III}$-$Fe_2^{III,II}$ and $Fe_2^{III/II}$-$Fe_2^{II,II}$ redox couple and one irreversible peak E_c^5 = -345 mV that can be ascribed to the complex reduction to the $Fe_2^{II/II}$-$Fe_2^{II,I}$ redox state.[217] Another peak at lower potential, E_c^4 = -614 mV, corresponds to a ligand based process.

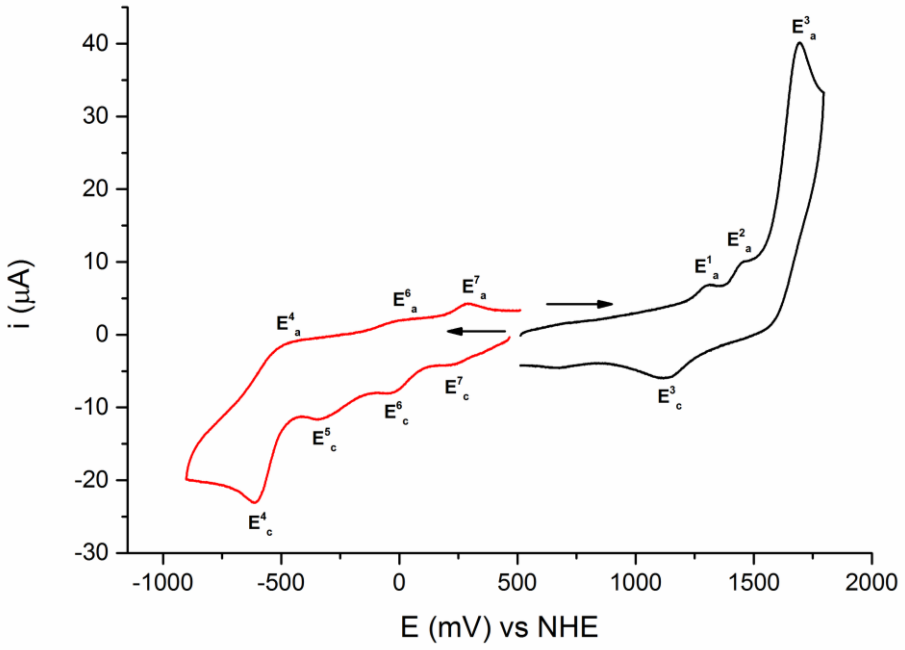

Figure 80. CV of 0.5 mM Fe_2L_2 in CH_3CN (TBAClO_4 0.1 M). The anodic peak $E^1_a = 1310$ is ascribed to monoelectronic $Fe_2^{III,III} \rightarrow Fe_2^{IV,III}$ oxidation and the second $E^2_a = 1470$ mV to $Fe_2^{IV,III} \rightarrow Fe_2^{IV,IV}$ oxidation. The cathodic peak $E_{1/2} = 257$ is ascribed to monoelectronic $Fe_2^{III,III} \rightarrow Fe_2^{III,II}$ reduction, the second $E_{1/2} = -28$ mV to $Fe_2^{III/II}$-$Fe_2^{II,II}$ reduction and peak $E_c^5 = -360$ mV ascribed to the complex reduction to the $Fe_2^{II/II}$-$Fe_2^{II,I}$ redox state.

Table 8. Redox processes of **Fe_2L_2** (0.5 mM) in ACN (TBAClO_4 0.1 M).

	$Fe_2^{IV/IV}$-$Fe_2^{IV,III}$	$Fe_2^{IV/III}$-$Fe_2^{III,III}$	$Fe_2^{III/III}$-$Fe_2^{III,II}$	$Fe_2^{III/II}$-$Fe_2^{II,II}$	$Fe_2^{II/II}$-$Fe_2^{II,I}$	Ligand
E_a (mV)	+1470	+1310	+206	-36	-360	+1695
E_c (mV)	-	-	+308	+62	-	1120;-614
$E_{1/2}$ (mV)	-	-	+257	+12	-	-

FeL and **Fe_2L_2** were screened as anti-oxidant catalysts, considering that under physiological conditions the dimeric form would be prevalent. The screening of SOD-like activity, despite the suitable $Fe_2^{III/II}$ redox potential, does not show any relevant activity with a value of $\log k_{cat} < 5$ and so it is not detectable with cyt c assay and too low to be considered of interest for possible applications. In addition iron species could be directly involved into harmful Fenton-like radical reaction.[2]

Fe_2L_2 does not shows also relevant CAT-like activity under the screened conditions, indeed the redox couple, $Fe_2^{IV/IV}$-$Fe_2^{III/III}$, in water (see Appendix), displays a too high for H_2O_2 dismutation(the intermediate potential should fall between the O_2/H_2O_2 and

H_2O_2/H_2O couples which are respectively 0.28 and 1.35 V). For these reasons this system is not of interest for SOD or CAT-like properties.

On the other hand the high redox potential and the presence of vacancies in the coordination sphere of the iron centers, accessible to water and to other substrates, make this complex an interesting catalyst for water oxidation and/or for the oxidation of organic substrates like alcohols .[215,221]

To evaluate the activity of the iron complexes in the water oxidation (WO) reaction some cyclic voltammetry were conducted in organic media (acetonitrile) in presence of small amounts of added water (Figure 81).

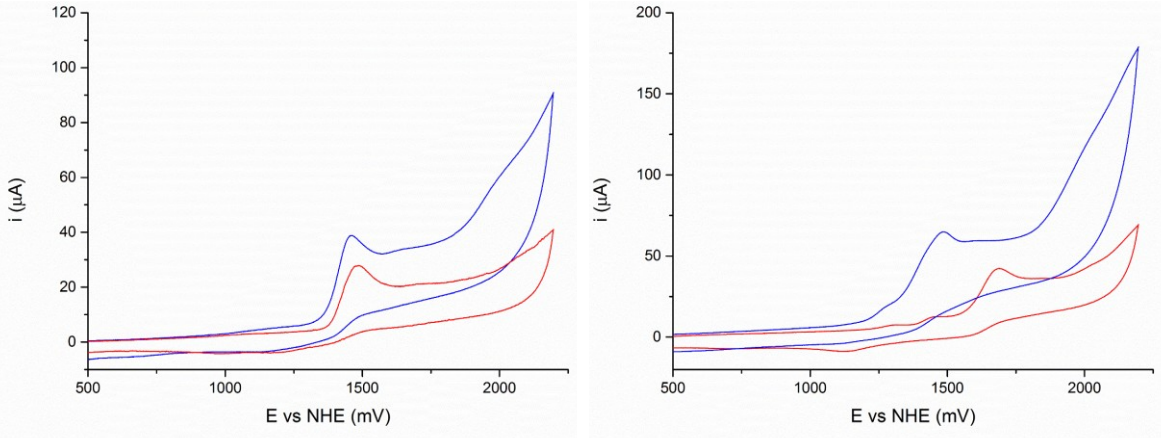

Figure 81. CV of FeL 0.5 mM on left and Fe_2L_2 0.5 mM on right in CH_3CN ($TBAClO_4$ 0.1 M) (red) and in CH_3CN in presence of 2 M of H_2O (blue).

As shown in Figure 81,addition of H_2O 2 M (~10% v/v) to the acetonitrile solutions of **FeL** to **Fe_2L_2** results in similar CV traces (blue line), which is consistent with the expected prevalence of the dimeric form in the CH_3CN-H_2O solution. The ligand anodic wave is shifted to lower potential E = 1.46 V, in addition another more intense wave was observed at potential E > 1.75 V (vs NHE) that could be attributed to water oxidation suggesting a catalytic activity for the of dimeric complex **Fe_2L_2**.

On the basis of these preliminary results the CV for both iron complexes were performed in mixed solvent ACN:H_2O (50:50) at controlled pH, in this way it is possible to discriminate the activity of the monomeric and the dimeric catalyst.

In particular as additive to the CH_3CN solution, acidic water (H_2SO_4 0.1M , pH = 1) was used to stabilize the monomer **FeL** while a PBS buffer, (0.1M , pH = 7) was used to favour the dimeric form **Fe_2L_2**. Under these conditions, the CV of the monomeric **FeL** in acidic conditions shows an anodic wave E_a= 1.62 V (vs NHE) attributable to the ligand

oxidation (Figure 82), while no other processes were detected at higher potential, this indicate that the monomer **FeL** is inactive in the process of WO.

Regarding the solution of the dimer under neutral conditions the first peak attributed to the ligand is set at E_a= 1.28 V (vs NHE) at potential significantly lower if compared with the corresponding peak under acidic conditions. Furthermore an additional anodic process starts at higher potential E = 1.4 V with a peak at 2.06 V (vs NHE) (Figure 82).

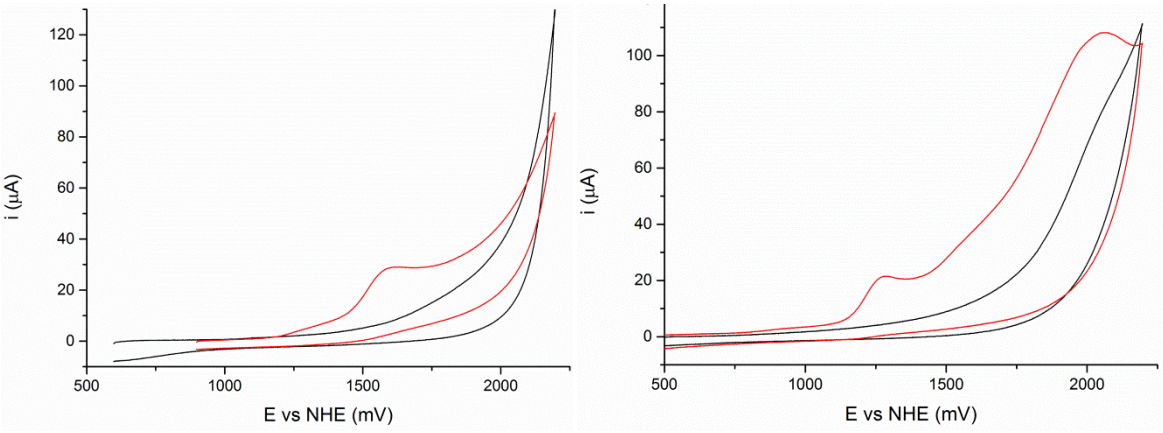

Figure 82. CV of FeL 0.5 mM in ACN:H_2SO_4 0.1 M (50:50) on left and Fe_2L_2 0.5 mM in ACN:PBS 0.1 M pH 7 (50:50). The blank is represented by the black line.

The wave intensity is ascribable to catalytic water oxidation for which it is possible to estimate an overpotential of 0.58 V from the difference between the onset potential (1.4 V) and the potential for the couple O_2/H_2O (0.82 V vs NHE at pH 7).

This overpotential is higher if compared with the di-iron complex $[(ppq)(OH_2)Fe(\mu\text{-}O)Fe(Cl)ppq)]^{3+}$ (Table 9) for which is reported an overpotential of about 280 mV although the screening conditions are different.[222]

Table 9. Benchmark iron based electro-catalysts for water oxidation.

Catalyst	Conditions	Overpotential (mV)	TOF (s-1)	TON	Ref.
Fe_2L_2	ACN:PBS (1:1) (pH 7)	580	/	/	this work
$[Fe^{II}(N_4Me_2)(ACN)_2]^{2+}$	CF_3SO_3H (pH 1)	370	/	/	[223]
$[Fe^{III}(dpaq)(H_2O)]^{2+}$	PC[a]/8% H_2O	/	/	29	[221]
$[(ppq)_2(OH_2)Fe(\mu\text{-}O)(Cl)]^{3+}$	PBS (pH 1)	276	/	/	[222]
$[Fe^{II}_4Fe^{III}(\mu_3\text{-}O)(\mu\text{-}L)_6]^{3+}$	CH_3CN/H_2O (10:1)	/	1900	10^6-10^7	[224]

[a] PC: propylene carbonate.

However, considering the extremely low number of iron based electro-catalysts for water oxidation reported in literature (Table 9) the reported activity is interesting. In particular the activity of the dimer **Fe_2L_2** suggests a synergistic effect of the two metal centres in the catalytic process.

In addition the wave observed in reduction under 0 mV for the $Fe^{II/I}$ redox couple is also promising for catalytic proton reduction processes like reported for other iron complexes.[217] Di-nuclear iron complexes can be considered as the synthetic analogues of iron hydrogenase cores.[225]

To evaluate the activity of the di-iron complexes in the proton reduction cyclic voltammetry were conducted in organic media (acetonitrile) in the presence of small amounts of water (Figure 83).

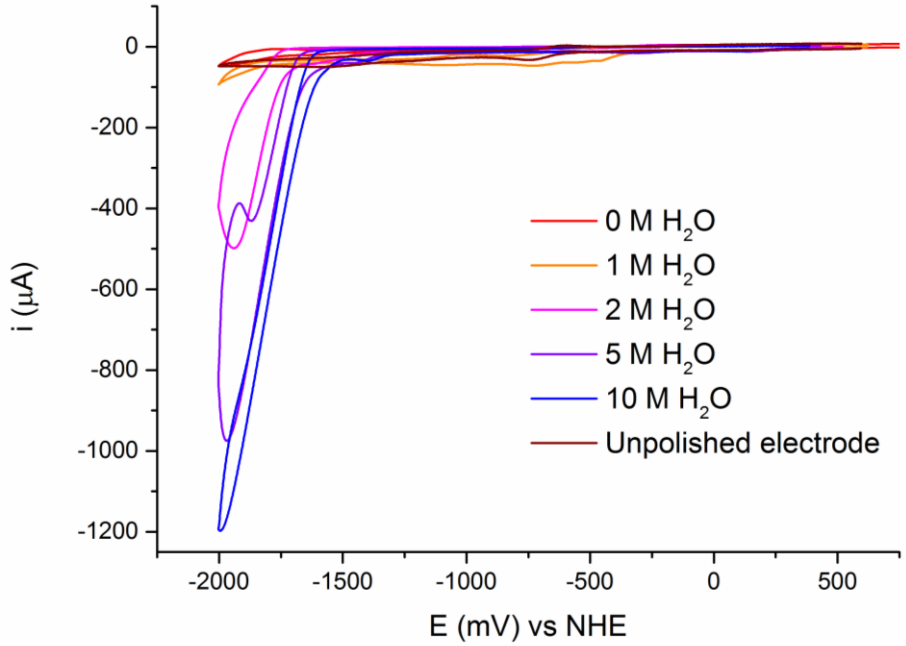

Figure 83. CV of Fe_2L_2 0.5 mM in CH_3CN ($TEABF_4$ 0.1 M) in presence of increasing amounts of H_2O.

The catalyst shows an increasing of a high anodic current upon addition of water, up to 1.2 mV, associated with a shift of the onset potential to higher potential. The process is accompanied with a vigorous bubble evolution on the electrode surface. The unpolished test reveals that no deposition of active species occur during the catalytic process.

On the basis of these preliminary results the CV were performed in mixed solvent H_2O:ACN (85:15) at controlled pH = 7 (PBS 5 mM, $TEABF_4$ 0.1 M) (Figure 84) to verify if the activity is maintained in water.

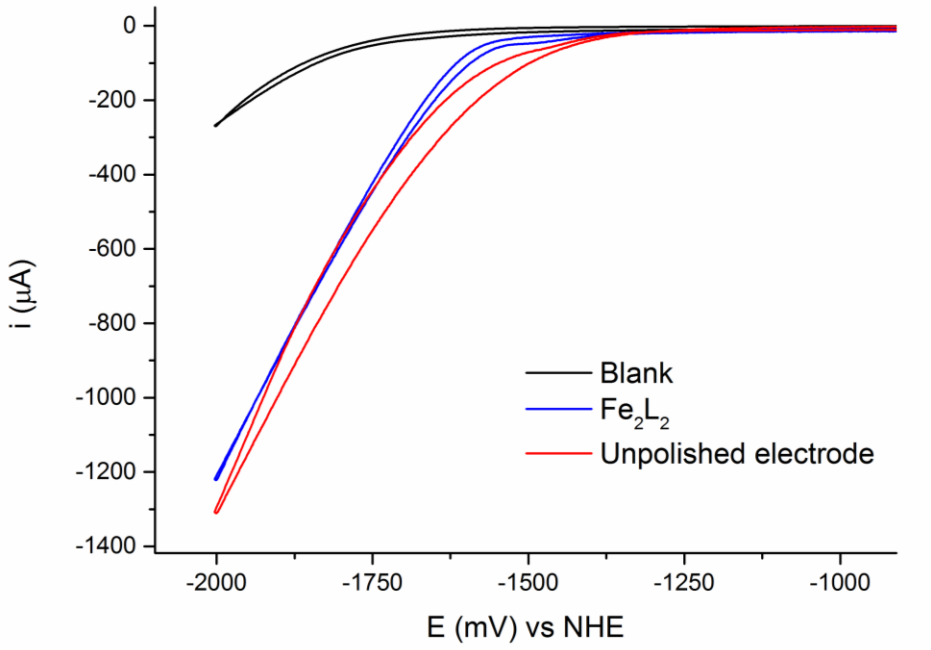

Figure 84. CV of Fe_2L_2 0.5 mM in ACN:PBS (5 mM pH 7) (15:85).

The complex **Fe_2L_2**, maintains its activity also in aqueous media with an onset potential at -1.52 V and an overpotential of 1.1 V (-0.41 V vs NHE at pH 7). However the unpolished test reveals the deposition of an active specie on the electrode surface ascribable to catalyst deposition.

The preliminary results obtained in the reaction of proton reduction are very promising considering that were obtained using directly water at pH 7, a very weak proton source that usually requires harder conditions if compared with the organic acids commonly used in literature (Table 10).[226–229]

Table 10. Electrochemical data for water-compatible iron catalysts for hydrogen evolution.

Catalyst	Fe^{n+}/Fe^{n-1} (V vs NHE)	Applied potential (V vs NHE)	Conditions	Reference
$[Fe_2L_2]^{2+}$	-	1.52[a]	PBS(pH 7):ACN (85:15)	this work
Fe_2[1-(PTA·H^+)$_2$]	-1.38	-1.70	HAc, 1:3 H_2O–ACN	[228]
Fe_2[2-PTA]	-1.70[b]	-1.63[b]	HAc, 1:3 H_2O–ACN	[227]
Fe_2[3-(PMe_3)$_2$]	-	-1.26	ACN spiked with H_2O	[226]
$Fe_2(bdt)(CO)_6$	-	-0.66	HAc, pH 3 water	[229]

[a] Onset potential; [b] Potentials were referenced to $Ag/AgNO_3$.

However further studied are needed to evaluate the activity of the complex under different conditions, in particular at more acid pH to favor the process of proton reduction and also with the use of organic acid to better understand the mechanism of reaction.

4.2 Cobalt complexes

A dinuclear cobalt(II) complex has been isolated by mixing methanolic ligand and Co(II) perchlorate solution followed by the addition of acetic acid and triethylamine (see Experimental Section).[149] Solution (ESI-MS, UV-vis and CV) and solid state characterizations (FT-IR and X-ray) confirm a Co(II)-dimer.

X-ray analysis of **Co_2L_2Ac** shows, like for **Mn_2L_2Ac**, a highly distorted octahedral geometry for both metal centres, where each Co(II) atom is coordinated in a facial configuration by the three nitrogen atoms of the tetradentate ligand, while the phenolate and acetate ligands act as a bridge between the two metal centres (Figure 85). In particular, the carboxylate anion exhibits a syn–syn μ η^1 η^1 bridging configuration, whereby the Co-Co distance and the Co−O−Co angles of the two μ bridging phenolate residues are respectively 3.07 Å, 96.7° and 95.2 ° (Figure 85).

The synthesis could be also accomplished in the same conditions but without adding acetic acid. The complex obtained is again a dinuclear Co(II) complex, with a structure similar to **Cu_2L_2** (Figure 85). The crystal structure of **Co_2L_2**, displays an inversion center and shows a dinuclear cobalt(II) complex where a tetra-dentate N_3O donor set is provided by the bis-pyridine, amino and μ-oxo phenolate groups of the ligand. **Co_2L_2** shows a distorted octahedral geometry for both metal centers, where each cobalt atom is coordinated by the three nitrogen atoms of the tetradentate ligand in a facial configuration, while the phenolate ligands act as a bridges between the two metal centers and two coordination methanol complete the coordination sphere. The equatorial plane is approximately defined by two cobalt centers, two oxygen atoms from the phenol molecules, one pyridine nitrogen atom and one amine nitrogen atom from the ligands. Considering this equatorial plane, each cobalt atom presents an apical position occupied by the other pyridine nitrogen atom, while the other apical positions by a methanol molecule. The Co-Co distance and the Co−O−Co angles of the two μ bridging phenolate residues are respectively 3.15 Å, 100.4° (Figure 85).

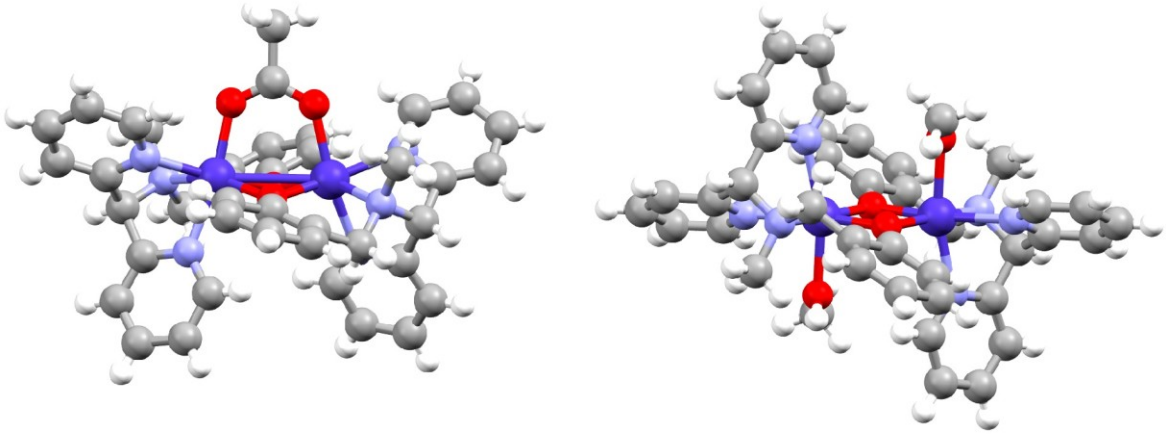

Figure 85. X-ray crystal structure for Co_2L_2Ac (left) and Co_2L_2 (right).

The dinuclear complexes present the same strong IR bands at 1602 cm^{-1} assigned to pyridine and phenolate absorptions in the Co_2L_2 unit and **Co_2L_2Ac** presents also two strong absorptions at 1572 and 1447 cm^{-1} associated to the stretching of the bridging carboxylate (Figure 86 and Appendix).

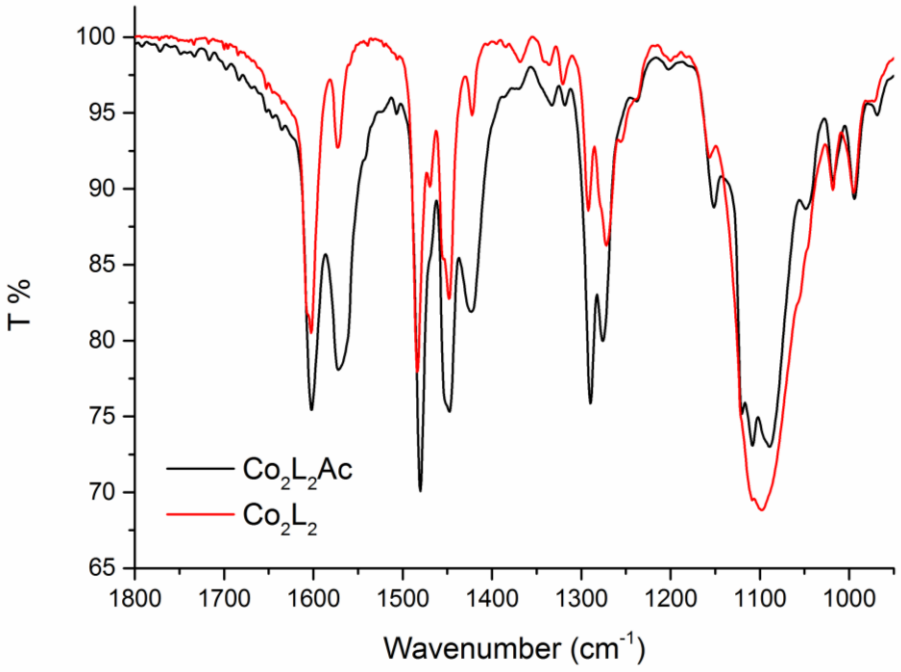

Figure 86. Comparison of the FT-IR spectra of **Co_2L_2** and **Co_2L_2Ac**.

The structures in solution of the dinuclear complexes are confirmed by ESI-MS and UV-vis. The signals obtained with ESI-MS for the molecular ions are 771.0 $[\mathbf{Co_2L_2}+HCO_2]^+$, 785.0 $[\mathbf{Co_2L_2Ac}]^+$ and 825.0 m/z for $[\mathbf{Co_2L_2}+ClO_4]^+$ (see Appendix, formic acid was present in the eluent). A fragmentation peak at 363.2 m/z attributed to $[CoL]^+$ specie is also observed for the break of the dinuclear system in the ion source.

The UV-Vis spectra were collected in organic medium (50 μM, CH_3CN) (Figure 87). The complexes show similar absorptions in the UV-region, with a maximum at 246 nm (ε = 24300 $M^{-1}cm^{-1}$) for **Co_2L_2Ac** and at 242 nm (ε = 20250 $M^{-1}cm^{-1}$) for **Co_2L_2** assigned to π-π* transitions of pyridines shifted to lower wavelength respect to the free ligand. Other weaker absorptions in the UV region where detected under 300 nm and for **Co_2L_2** also a weak broad band above 400 nm ascribable to a LMCT (Figure 87).

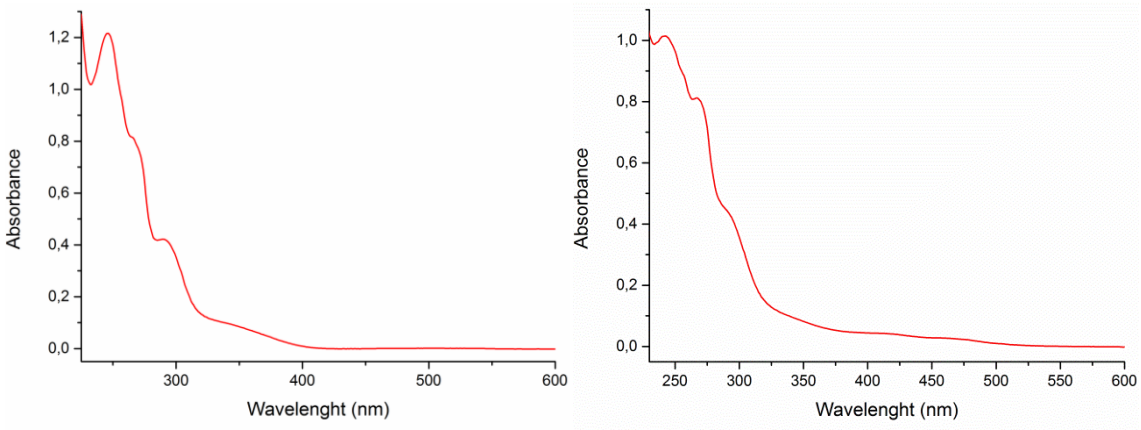

Figure 87. UV-vis spectra of Co_2L_2Ac (left) and Co_2L_2 (right) (50 μM) in acetonitrile.

The redox properties of **Co_2L_2** and **Co_2L_2Ac** were determined by cyclic voltammetry (CV) experiments performed in buffer solution (0.5 mM in ACN, $TEABF_4$ 0,1 M).

In the oxidative scan, **Co_2L_2** shows several peaks attributable to cobalt redox couples (Figure 88), a quasi-reversible peak at $E_{1/2}$ = 672 mV (vs NHE) is attributable to the $Co_2^{III,II}$-$Co_2^{II,II}$ oxidation and another irreversible peak E_a^2 = 1480 mV (vs NHE) is attributable to the $Co_2^{III,III}$-$Co_2^{III,II}$ redox couple. At higher potential the other irreversible peak detected at E_a^3 = 1630 mV is due to a ligand based process.[221] In the same conditions **Co_2L_2Ac** shows an irreversible wave E^1_a = 1080 mV (vs NHE) attributable to the $Co_2^{III,II}$-$Co_2^{II,II}$ oxidation process and another irreversible wave E^2_a = 1548 mV, attributable to the $Co_2^{III,III}$-$Co_2^{III,II}$ redox couple, overlapped with the ligand oxidation E^3_a = 1690 mV (Figure 88).

Comparing the two CVs, it is clear that the presence of the bridging carboxylate generates a consistent shift to higher potential (~ 200 mV) of the $Co_2^{III,II}$-$Co_2^{II,II}$ redox couple, in addition the lower reversibility of the peaks of **Co_2L_2Ac** is consistent with a modification in the coordination sphere of the cobalt core, probably due to a change in the carboxylate bridge coordination.

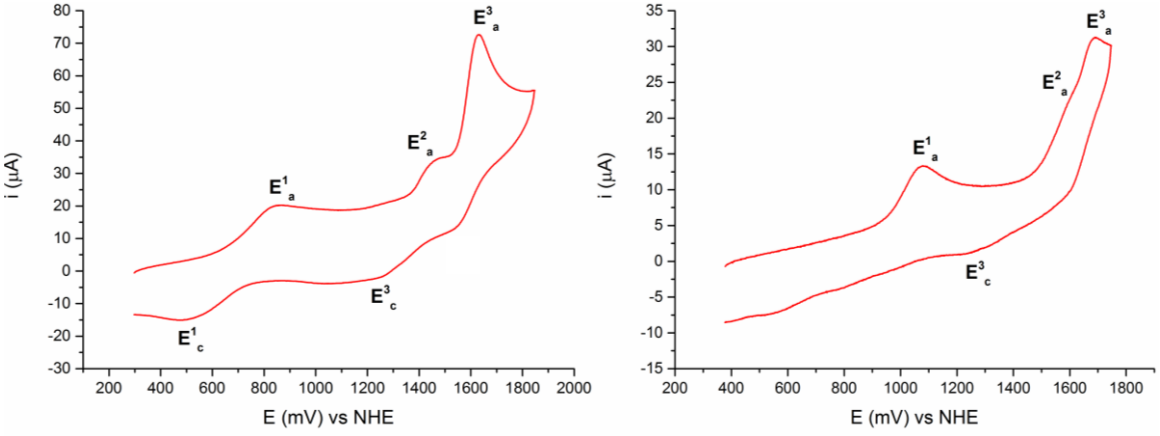

Figure 88. CV of 0.5 mM Co_2L_2 (left) and Co_2L_2Ac (right) in CH_3CN ($TEABF_4$ 0.1 M). For Co_2L_2 the anodic peak $E_{1/2} = 672$ is ascribed to monoelectronic $Co_2^{III,II} \rightarrow Co_2^{II,II}$ oxidation and the second E^2_a = 1480 mV to $Co_2^{III,III} \rightarrow Co_2^{III,II}$ oxidation. For Co_2L_2Ac the anodic peak $E^1_a = 1080$ is ascribed to monoelectronic $Co_2^{III,II} \rightarrow Co_2^{II,II}$ oxidation and the second E^2_a = 1548 mV to $Co_2^{III,III} \rightarrow Co_2^{III,II}$ oxidation. The anodic peak E^3_a is a ligand based process.

Table 11. Redox processes of **Co_2L_2** (0.5 mM) in ACN ($TEABF_4$ 0.1 M).

	$Co_2^{III,III}$-$Co_2^{III,II}$	**$Co_2^{III,II}$-$Co_2^{II,II}$**	**$Co_2^{II,II}$-$Co_2^{II,I}$**	**$Co_2^{II,I}$-$Co_2^{I,I}$**	**Ligand**
E_a (mV)	+1480	+864	-	-	+1630, -1391
E_c (mV)	-	+480	-1228	-1372	+1257, -1850, -1588
$E_{1/2}$ (mV)	-	+672	-	-	-

Table 12. Redox processes of **Co_2L_2Ac** (0.5 mM) in ACN ($TEABF_4$ 0.1 M).

	$Co_2^{III,III}$-$Co_2^{III,II}$	**$Co_2^{III,II}$-$Co_2^{II,II}$**	**$Co_2^{II,II}$-$Co_2^{II,I}$**	**$Co_2^{II,I}$-$Co_2^{I,I}$**	**Ligand**
E_a (mV)	+1548	+1080	-	-	+1690, -89
E_c (mV)	-	-	-620	-1557	+1230, -1099, -731
$E_{1/2}$ (mV)	-	-	-	-	-

In the reductive scan, under analogous experimental conditions, **Co_2L_2** shows two irreversible peaks attributable to cobalt redox couples (Figure 89), E_c^1 = -1228 mV (vs NHE) is attributable to the $Co_2^{II,II}$-$Co_2^{II,I}$ redox couples and E_c^2 = -1372 mV (vs NHE) is attributable to the $Co_2^{II,I}$-$Co_2^{I,I}$ redox couples. At lower potential the other irreversible peaks detected at E_c^3 = -1588 mV and E_c^4 = -1850 mV are due to a ligand based processes. In the same conditions **Co_2L_2Ac** shows some weak irreversible waves attributable to cobalt

redox couples (Figure 89), E_c^1 = -620 mV (vs NHE) is attributable to the $Co_2^{II,II}$-$Co_2^{II,I}$ redox couples and E_c^2 = -1372 mV (vs NHE) is attributable to the $Co_2^{II,I}$-$Co_2^{I,I}$ redox couples. At intermediate potential the other irreversible peaks detected at E_c^3 = -731 mV and E_c^4 = -1099 mV are due to a ligand based processes.

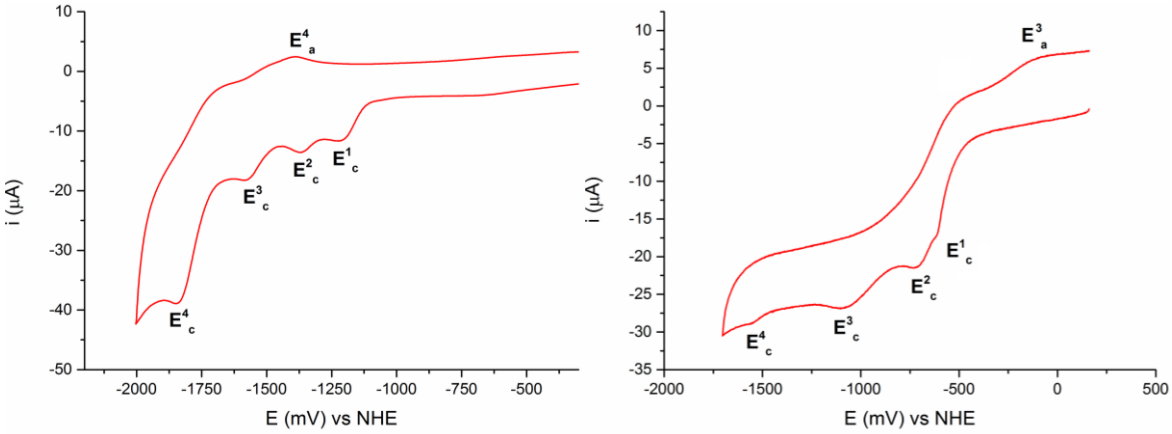

Figure 89. CV of 0.5 mM Co_2L_2 (left) and Co_2L_2Ac (right) in CH_3CN ($TEABF_4$ 0.1 M). For Co_2L_2 the cathodic peak E^1_c = -1228 mV is ascribed to monoelectronic $Co_2^{II,II} \rightarrow Co_2^{II,I}$ reduction and the second E^2_c = -1372 mV to $Co_2^{II,I} \rightarrow Co_2^{I,I}$ reduction. For Co_2L_2Ac the cathodic peak E^1_c = -620 is ascribed to monoelectronic $Co_2^{II,II} \rightarrow Co_2^{II,I}$ reduction and the second E^2_c = -1557 mV to $Co_2^{II,I} \rightarrow Co_2^{I,I}$ reduction.

These Co-complexes like the iron ones do not show SOD or CAT-like activity under the screened conditions and are not of interest for their anti-oxidant properties. On the other hand the high redox potential of the species and the presence of vacancies in the coordination sphere of the complexes, accessible to water, make these complexes an interesting catalysts for the process of water oxidation.[230,231] To evaluate the activity of the two cobalt complexes in the water oxidation (WO) reaction some cyclic voltammetry were conducted in organic media (acetonitrile) in presence of small amounts of water (Figure 90).

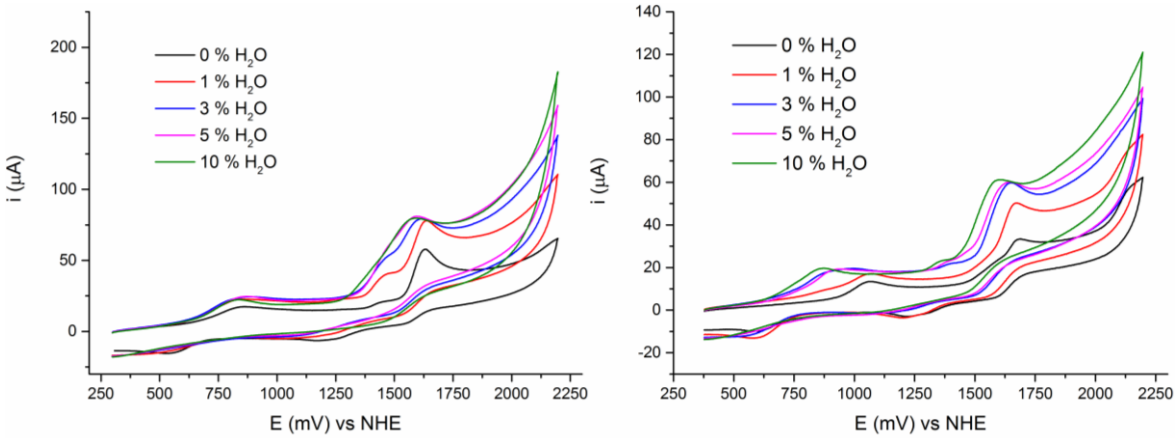

Figure 90. CV of Co_2L_2 0.5 mM (left) and Co_2L_2Ac 0.5 mM (right) in CH_3CN ($TEABF_4$ 0.1 M) with increasing amounts of H_2O.

As shown in Figure 90 with the addition of increasing amounts of H_2O to the acetonitrile solutions of the two complexes a shift to lower redox potential for the $Co_2^{III,III}$-$Co_2^{III,II}$ and $Co_2^{III,II}$-$Co_2^{II,II}$ was observed. This effect is more evident on the CV of **Co_2L_2Ac** where the $Co_2^{III,III}$-$Co_2^{III,II}$ redox wave is shifted (Table 12) at 1360 mV and the $Co_2^{III,II}$-$Co_2^{II,II}$ at 870 mV (vs NHE). This shift is also accompanied with an increase in the reversibility of the redox process like previously reported for **Mn_2L_2Ac**. Concerning the anodic wave attributed to the ligand his peak is shifted to lower potential E_c = 1600 mV. In addition another more intense wave was observed at potential E > 1.70 V (vs NHE) that could be attributed to water oxidation process suggesting a catalytic activity for the dimeric cobalt complexes.

On the basis of these preliminary results, the CV for both cobalt complexes were performed in aqueous media (PBS 0.2 M, pH = 7). Concerning the CV of the dimer **Co_2L_2** the first peak attributed to the $Co^{III/II}$ redox couple is set at 745 mV and the ligand wave is shifted at E= 1370 mV (vs NHE) a potential significantly lower if compared with the same peaks in organic media. Furthermore an additional anodic wave starts at higher potential E = 1.5 V (Figure 91). This wave ascribable to a catalytic oxidation process, cannot be associated to the catalyst, in fact as highlighted by the unpolished test it is associated with cobalt oxide CoO_x deposition on the electrode, active in the WO process, meaning that the catalyst is not stable under the screening conditions and release cobalt that is oxidized and deposited on the electrode surface like previously reported for other systems in literature.[232]

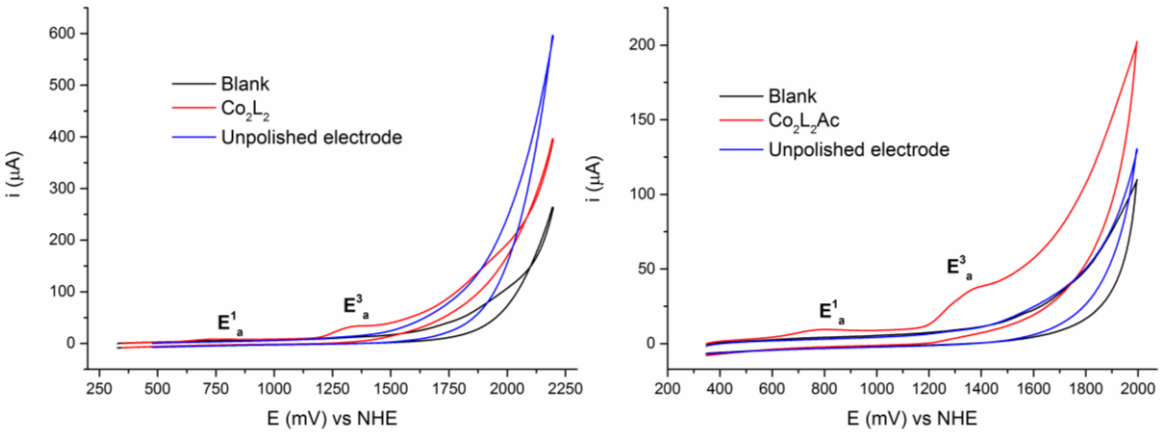

Figure 91. CV of Co_2L_2 0.3 mM (left) and Co_2L_2Ac 0.3 mM (right) in PBS 0.2 M (pH = 7). The blank is represented by the black trace and the unpolished test by the blue trace.

Regarding the CV of **Co_2L_2Ac** the first peak attributed to the $Co^{III/II}$ redox couple is set at 795 mV and the ligand wave is shifted at E= 1400 mV at potential significantly lower if compared with the same peak in organic media. In addition an anodic process starts at higher potential E = 1.4 V (vs NHE) (Figure 91). The wave intensity is ascribable to catalytic water oxidation for which it is possible to estimate an overpotential of 460 mV from the difference between the onset potential (1.28 V) and the potential for the couple O_2/H_2O (0.82 V vs NHE at pH 7). The test unpolished confirm also the activity and the stability, probably conferred by the carboxylate bridge, of the molecular catalyst with no cobalt oxides deposition on the electrode.

The complex **Co_2L_2Ac** shows interesting feature in WO reaction and in perspective a deeper study of its properties seems fundamental. A coupled analysis made by spectroelectrochemistry and electrolysis could permit to better describe the processes involved and to quantify the oxygen production.

Concerning the waves observed in reduction for the $Co_2^{II,II/I,I}$ redox couple seem promising for catalytic proton reduction processes like reported for other cobalt complexes.[49] Cobalt complexes do not have natural hydrogenases analogues, however the majority of the reported small-molecule metal catalysts in aqueous media employ cobalt centers.[233] The ultimate objective for these systems is to use water as a feedstock, although often are not soluble or stable in aqueous environments.[234]

For these reasons the activity of the cobalt complexes in proton reduction was screened in organic media (acetonitrile) in presence of small amounts of water (Figure 92 and 93).

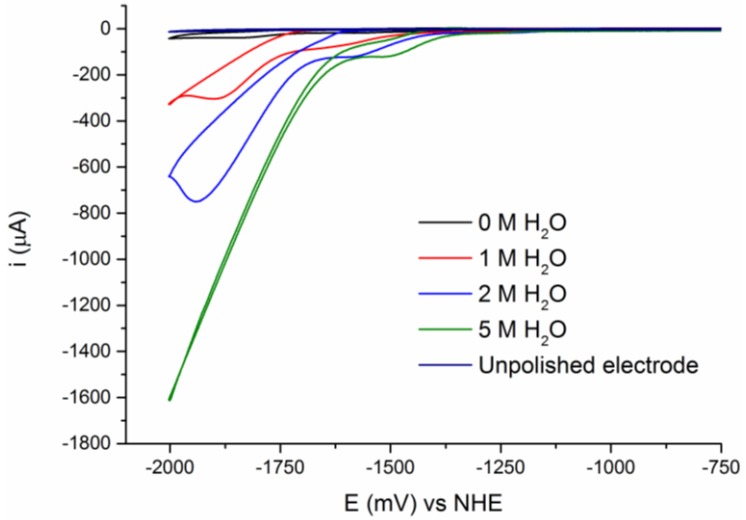

Figure 92. CV of Co_2L_2 0.5 mM in CH_3CN ($TEABF_4$ 0.1 M) in presence of increasing amounts of H_2O.

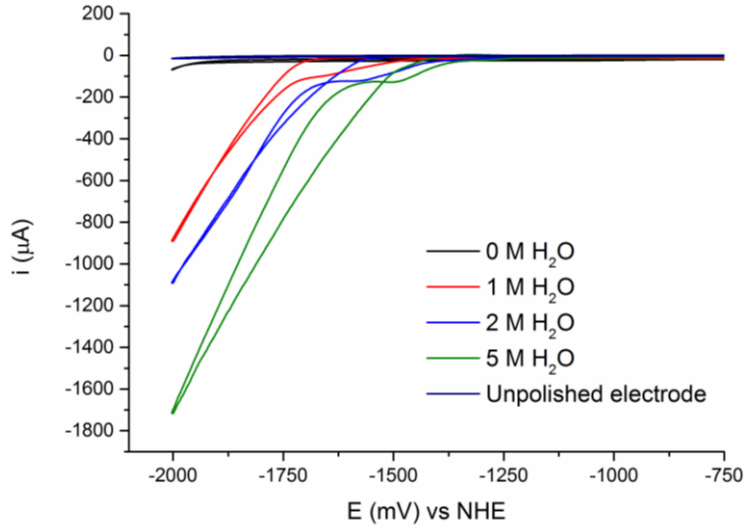

Figure 93. CV of Co_2L_2Ac 0.5 mM in CH_3CN ($TEABF_4$ 0.1 M) in presence of increasing amounts of H_2O.

The catalysts show an increasing high anodic current upon addition of water, up to 1.7 mV, associated with a shift of the onset potential to a more favourable potential. The process is accompanied by a vigorous bubble evolution on the electrode surface. The unpolished test reveals that no deposition of active species occur during the catalytic process.

On the basis of these preliminary results the CV were performed in water (H_2O:ACN, 9:1) at controlled pH = 7 (PBS 5 mM, $TEABF_4$ 0.1 M) (Figure 94) to verify if the activity is maintained in water.

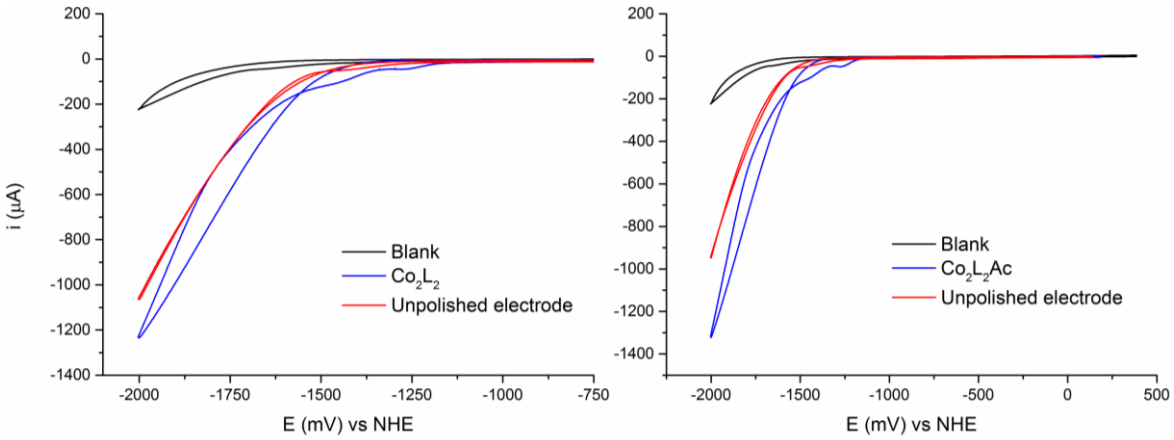

Figure 94. CV of Co_2L_2 0.5 mM (left) and Co_2L_2Ac 0.5 mM in ACN:PBS (5 mM pH 7) (1:9).

In water the redox couples are shifted to a more favourable potential and the bi-electronic transition to $Co_2^{III,III} \rightarrow Co_2^{II,II}$ seems occur simultaneously at -1.27 V. The complexes, maintain their activity also in aqueous media with an onset potential at -1.38 V for both the species with an overpotential of 0.97 V (-0.41 V vs NHE at pH 7). However the unpolished test reveals the deposition of an active specie on the electrode surface ascribable to catalyst

deposition. The CV of the complexes are really similar in water suggesting a possible lost of bridging carboxylate and the presence of only **Co_2L_2** as active specie in aqueous solution.

The preliminary results obtained in the reaction of proton reduction are promising considering that were obtained using directly water as proton source at pH 7, however further studied are needed to evaluate the activity of the complexes under different conditions, in particular at more acid pH to favor the process of proton reduction and also with the use of organic acids to better understand the mechanism of reaction.[49,234]

Table 13. Electrochemical data for water-compatible cobalt catalysts for hydrogen evolution.

Catalyst	Co^{II}/Co^{I} (V vs NHE)	Applied potential (V vs NHE)	Conditions	Reference
$[Co_2L_2]^{2+}$	-1.27	-1.38[a]	PBS(pH 7)	this work
$[Co(cyclam)]^{2+}$	-	-1.36	H_2O	[235]
$[Co(diammac)]^{3+}$	-	-0.79	PBS (pH 7)	[236]
$[Co(dpg)_3(BF)_2]^{+}$	-	-0.75	PBS (pH 7)	[237]
$[(PY5Me_2)Co]^{2+}$	-1.00	-1.30	PBS (pH 7)	[238]
$[Co(DPA\text{-}Bpy)]^{2+}$	-0.90	-1.40	PBS (pH 7)	[239]

[a] Onset potential.

5. Anti-fouling Membranes

5.1 Membrane Filtration Processes

The membrane filtration processes can be defined as separations that employ a semipermeable membrane for split the supply into two portions: the filtrate, which consists in the material passing through the membrane (permeate), and the material that is retained (retentate). The membranes can be classified according to pores size and their molecular weight cut off (MWC).

Table 14. Classification of membranes for filtration.

Membrane	Pores dimension (nm)	Mechanism of separation	Flux	P (bar)
Reverse Osmosis	< 1	Diffusion/Exclusion	low	50-80
Nanofiltration (NF)	1-8	Diffusion/Exclusion	medium	5-15
Ultrafiltration (UF)	3-100	Sieve	high	0.5-5
Microfiltration (MF)	> 50	Sieve	high	0.3-3

The characteristics features that a membrane should exhibit are: high permeate flow, high capacity to retain the contaminants, high durability, good chemical resistance and low cost. Currently, the organic membranes are the most widely used since the inorganic, despite the high chemical and thermal resistance, appear to be fragile and more expensive. The polymeric membranes are generally constituted by a thin active layer, possibly placed on a microporous polymeric support so that obtain the desired mechanical strength.

The polymers generally used include: cellulose acetate, polyamides, polypropylene, polyethylene, polysulfone and polyvinylidene fluoride (PVDF). Depending on the material, porosity and configuration of the module is possible to remove a wide range of contaminants from the feed treated.

Depending of the removed contaminants, the membranes can be applied in three main areas:

- Solid-liquid separation
- Organic contaminants removal
- Inorganic contaminants removal

In particular, the membranes for solid-liquid separation are widely used for a wide range of processes and are able to remove the residual turbidity from the previous steps in water

treatment processes and eliminate pathogens resistant to disinfecting agents such as *Giardia spp.* and *Cryptosporidium spp*. [240]

Regarding the removal of organic species, the degree of removal varies greatly depending on the size of the pores of the membrane. In general, MF and UF membranes remove only a part of the organic substances (about 15%), even if the efficiency can be increased with a coagulation pretreatment. Using membranes for NF and RO, however, it is unable to obtain efficient removal of numerous compounds, including natural organic substances, pesticides and disinfection by-products (DBPs). The removal is efficient to the point that it is preferable to adsorption on activated carbon.[241]

For these systems the porous texture is crucial to shape both interfacial and surface areas, however it provides also one major weakness of the system that suffers from severe damage and deactivation by fouling-induced phenomena.[242–246]

5.2 Membrane Fouling

By the term fouling, it is intended the deposition of particulates on surfaces or baffles that will affect the correct operation. Deposition of particles onto the porous matrix is responsible for a progressive modification of the outer surface properties and occlusion of the internal channels. Depending on the foulant environment, pore occlusion can occur by micro-organisms (biofouling), proteins and other organic macromolecules (organic fouling), or salt residues (inorganic fouling).[242–246] Remediation is generally accomplished by physical or chemical means employing pressure back-flushing and/or harsh pH cleaning conditions with high operation cost and limited efficiency. These conventional protocols are generally employed to counteract a reversible type of fouling due to particles/residues loosely attached to the porous matrix (Figure 95).

However, a severe challenge comes from what is considered strongly irreversible fouling.[242–247] This type of fouling is attributed to pore constriction/blocking caused by solid particles whose morphology and dimensions are comparable with the material pores, that eventually precipitate or deposit inside the porous network. This is one major obstacle to a long-term efficiency and function of the porous interface.[242–246]

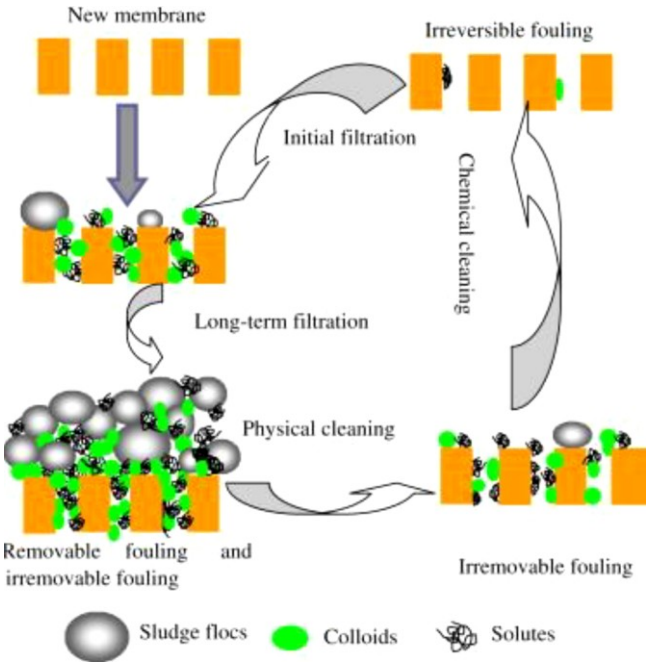

Figure 95. Fouling and cleaning cycle of the membranes.

To prevent this phenomena, antifouling strategies are currently being explored by a tailored modification of the surface morphology via the grafting of polymer brushes, polypeptides, enzymes, antimicrobial agents, or photocatalytic agents as TiO_2 particles, that can induce a self-cleaning action.[242–247] These "smart" coatings can exhibit a stimuli-responsive dynamics/function to actively prevent fouling via a mechanical sweeping or decontamination of the local areas. Indeed, while the "on-surface" approach is meant to counteract the initial stages of the fouling mechanism, it fails to deal with a deeper pore constriction by particles whose size approaches the pore dimensions eventually blocking the pore access toward the inner structure.[242–247]

When the level of fouling causes a too marked decrease of the filtered flow is necessary a cleaning operation and also, if the latter is not able to return the membrane to optimal conditions, is required a replacement of the same. The costs associated with the regeneration and replacement of the membrane are the main limiting factor to the development of this type of technologies.

The goal to pursue is to get membrane more resistant to this phenomenon and easily cleanable so as to enhance the life times.

5.3 Polyoxometalates (POMs)

The polyoxometalates (POMs) are a class of compounds based on discrete anionic oxides of variable sizes (from Ångstrom to 10 nm), which have significant potential for use in various fields such as catalysis, materials science and medicine.[248]

Early studies of these compounds date back to the XIX century, when it was discovered that some of the metals belonging to the first periods of the transition series (such as Nb, V, Ta, Mo, W) in their highest oxidation state (d^0 configuration or d^1) are able to form in aqueous solution at controlled pH, temperature and concentration discrete polyoxoanions of variable size.[60,249–251]

Two are the fundamental parameters to have got these structures:

1. Cationic radii able to host an octahedral coordination;
2. Empty *d* orbitals able to form terminal double bond metal oxygen.

Commonly they are formed by octahedral MO_6 (sometimes pentahedral MO_5 or tetrahedral MO_4) where one or at least two oxygen (Lipscomb's principle) form a double bond with the metal. Terminal oxygens are essential for the formation of discrete structures and avoid the formation of widespread structures like in metal oxides.[252]

Polyoxometalates could be divided in isopolyanions (A) or heteropolyanions (B) depending on chemical composition:

A. $[M_mO_y]^{p-}$
B. $[X_xM_mO_y]^{q-}$

Where M is the transition metal in high oxidation state and X is another *d*-group metal or a non-metal atom (P, Si, As, Sb, Bi).

One of the most studied and famous class of these compounds is the α-Keggin, with a general formula $[X^{n+}M_{12}O_{40}]^{(8-n)-}$ with M= Mo^{VI} or W^{VI} and X= Si^{IV}, Ge^{IV}, P^{V}, As^{V} and Sb^{V}. The heteroatom is in the center of the structure with a tetrahedral coordination XO_4 surrounded by 12 octahedral metal centers MO_6 of molybdenum or tungsten that are usually divided in triplets M_3O_{13} in which each octahedral unit shares the edges. These triplets are linked by the corner of octahedral units, the particular disposition gives a T_d symmetry to the POMs structure (Figure 96).

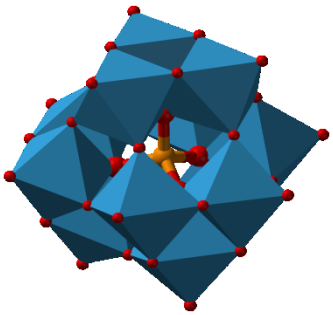

Figure 96. Polyhedric structure of α-Keggin polyanion $[PW_{12}O_{40}]^{3-}$. Octahedra WO_6 in blue and internal tetrahedral heteroatom P(orange).

The structure described is the most stable and is labeled as α form, many isomers less stable, are characterized by the rotation of 60° of one (β isomer), two (γ isomer), three (δ isomer) or four (ε isomer) triplets M_3O_{13} around their symmetry axes.[253] These compounds are called saturated because of their low anionic charge, high stability and high symmetry. It is possible to synthesize lacunary structures in which one or more tetrahedral units MO^{4+} are removed from the saturated structure, generating monovacant ($XM_{11}O_{39}$), divacant ($XM_{10}O_{36}$) and trivacant (XM_9O_{34}) structures (Figure 97).[253]

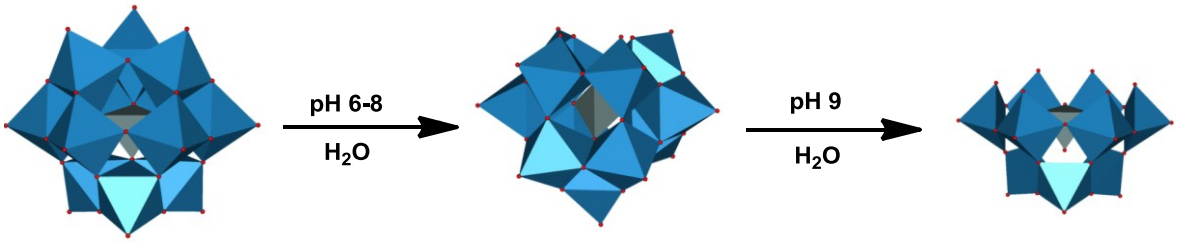

Figure 97. Formation of α-SiW_{11} and α-SiW_9 starting from α-SiW_{12}.

Exploiting the nucleophilic oxygens of the lacuna it is possible to insert different functionalities, for example other metal centers such as $Fe^{II/III}$, $Mn^{II/III}$, $Co^{II/III}$, $Ru^{II/III/IV}$.[254–256] These compound are synthesized starting from the lacunary POMs and metal precursors (M-L) and are called *Transition Metals-Substituted Polyoxometalates* (TMSPs) (Figure 98).[257]

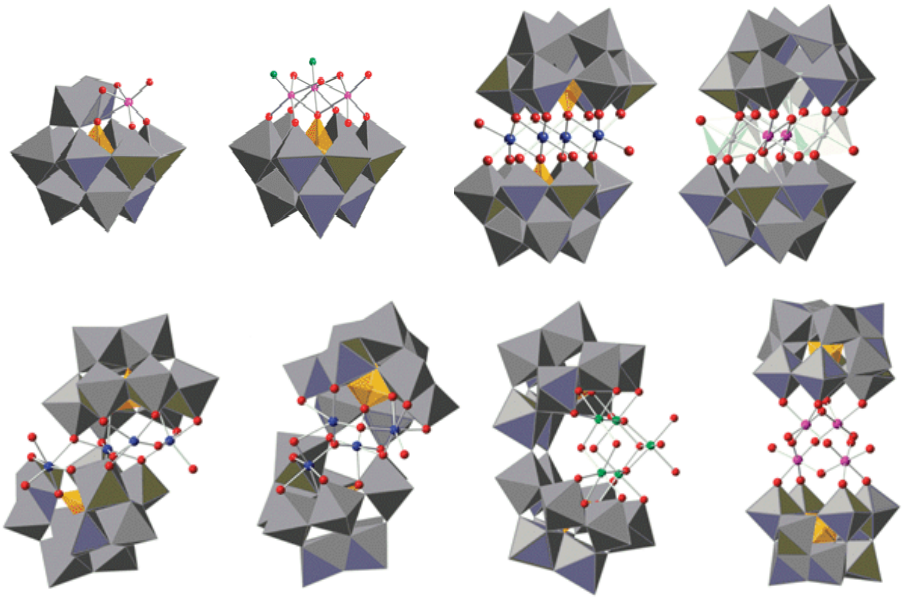

Figure 98. Example of transition metal substituted polyoxometalates.

The simplest case of TMSP is when a single metal M is coordinated in the lacunary site of a monovacant POM (Figure 98). The lacunary polyoxometalates can also act as an inorganic polydentate ligand coordinating more metal atoms usually stabilized by sandwich-like or dimeric/trimeric structures.[258] The resulting TMSPs display coordination analogies with porphyrins and enzymes, and in some cases, a biomimetic activity has also been recorded. This feature, coupled with a high robustness to oxidative conditions is of great interest for catalytic applications.[259,260]

Due to their redox properties, POMs can oxidize several organic substrates, including biological targets.[261] These features, coupled with the possibility to interact with positively charged domains of proteins and enzymes, makes POMs interesting inorganic nanodrugs candidates with antitumoral, antiviral, antibacterial activity. There are also evidences of POM containing Lewis acid sites acting as proteases, so they are able to cut and disassemble complex proteins.[262–266]

In particular a tetraruthenium substituted polyoxometalate, firstly synthesized in our research group, shows an interesting oxygenic activity: indeed it is able to oxidize water and also to dismutate hydrogen peroxide.[64,267,268] Its molecular formula is $Na_{10}[Ru_4O_4(OH)_2(H_2O)_4(\gamma\text{-}SiW_{10}O_{36})_2]$ (**$Ru_4(SiW_{10})_2$**) and it is characterized by an adamantane-like tetraruthenium core that can perform multi-electronic reactions, stabilized by two dilacunary decatungstosilicate anions $[SiW_{10}O_{36}]^{8-}$ (Figure 99).

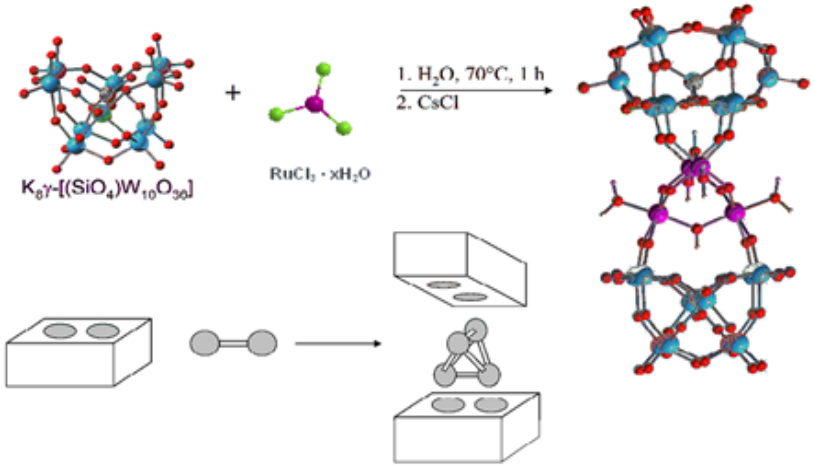

Figure 99. Synthesis and structure of $[\{Ru_4O_4(OH)_2(H_2O)_4\}(\gamma\text{-}SiW_{10}O_{36})_2]^{10-}$ (**$Ru_4(SiW_{10})_2$**).

The oxidation state of the ruthenium atoms in the core is Ru^{IV}, while during the catalytic cycle all ruthenium atoms are supposed in the oxidation state (+V).[267] It has a high negative charge (-10) and is resistant to oxidative and hydrolytic conditions. For the aim of this thesis, the H_2O_2 dismutation ability is an added value that characterize this POM.

$Ru_4(SiW_{10})_2$ can act as artificial catalase, in particular in phosphate buffer (50 mM) it can reach a TON of 2200 with a bimolecular rate constant $k = 36.8 M^{-1}s^{-1}$.[136]

The properties of this POM have been already exploited for the construction of composite materials, in which the **$Ru_4(SiW_{10})_2$** was associated with carbon nanotubes or to positively charged polymers.[136,269]

One goal of this thesis is to assess if this oxygenic activity can be maintained and even exploited for a POM inserted into the membrane. The possibility to develop oxygen directly inside the pores of the membranes in the presence of H_2O_2 could in fact be an innovative method to obtain the self-cleaning of the membranes and reducing the fouling.

5.4 Catalytic Pores Armed with Oxygenic Polyoxometalates

Porous interfaces, that regulate key phenomena at solid–liquid contacts, are a pillar technology with the unique potential of coupling high surface area, separation/recognition processes with site confinement phenomena.[270,271] This is a key strategy to control selectivity and performance in one integrated function. As such, the porous interface is pivotal for functional material design with a widespread use in catalysis, sensoring, biotechnology and biomedical applications.[242–247]

In this chapter is shown a novel chemo-mechanical strategy to arm the surface pores with an oxygen evolving catalysts that is known to liberate nascent oxygen gas when exposed to aqueous H_2O_2 as chemical trigger.[136,267,268,272,273] Analogous catalytic machines are found at the heart of oxygenic enzymes as the natural catalases (CAT) or the photosynthetic II complex (PSII).[136,267,268,272,273] The core concept of this approach is the "in-pore" generation of oxygen bubbles, resulting in a definite propulsion force and turbulence phenomena, thus inducing an active fluid mixing in the pore proximity and the mechanical displacement of solid foulant particles. This strategy builds on our recent study which identifies nanodimensional, molecular metal oxides as the inorganic functional analogues of CAT enzymes.[136,267,268,272,273] In particular, the catalase-like behaviour of the tetra-ruthenium substituted polyoxometalate with formula $[Ru_4(H_2O)_4(\mu\text{-}O)_4(\mu\text{-}OH)_2(\gamma\text{-}SiW_{10}O_{36})_2]^{10-}$ (**$Ru_4(SiW_{10})_2$**), has been assessed in the presence of H_2O_2, both in solution, on heterogeneous supports, or within a confined environment, resulting in quantitative and continuous oxygen evolution.[136,267,268,272,273] Moreover, **$Ru_4(SiW_{10})_2$** is stable in a broad pH range, from very acidic to neutral solutions, and in the presence of concentrated saline buffers, which guarantees its functional response in aqueous phase under diverse environmental conditions.[136,267,268,272,273] We have shown that catalytic production of "nascent oxygen" by **$Ru_4(SiW_{10})_2$** works as a chemomechanical effector to induce the autonomous movement of nano/micromotors, useful in applications involving trafficking and fluid displacement in synthetic circuits.[272,273] The present study includes: (i) the fabrication of polymeric films with porous architecture, (ii) the pore embedding of **$Ru_4(SiW_{10})_2$** as oxygen evolving catalyst, (iii) remediation of pore occlusion with mild antifouling protocols employing aqueous H_2O_2 as chemical effector. Under the conditions adopted, the through pore catalytic oxygen evolution yields >85% removal of model foulant particles, carrying a fluorescent tag, as probed by direct imaging of the polymeric surface with confocal fluorescence microscopy (CFM).

Polyoxometalate affinity toward the polymeric environment can be tuned by hydrophobic cations, namely, long-chain alkyl ammonium salts, to produce the so called surfactant encapsulated polyoxometalates (SEPs) which are readily obtained after cation metathesis.[274–276] Tailored SEPs are thus optimized to be dissolved in the casting solution of various polymeric blends, giving rise to nanocomposites that retain the catalytic function of the polyoxometalate additive.[274–276] With this aim, **$Ru_4(SiW_{10})_2$** has been obtained according to literature protocols, and isolated as dimethyldioctadecylammonium (DODA) salt after extraction from a biphasic $H_2O/CHCl_3$ system (see Experimental Section). The resulting $(DODA)_{10}/Ru_4(SiW_{10})_2$, (DODA–SEP), turns out to be soluble in $CHCl_3$, as required for the dissolution of amorphous PEEK-WC (polyether ether ketone with "cardo" groups), being the polymer of choice for the preparation of composites with excellent mechanical and chemical resistance.[277]

The casting solution of the polymer blend is prepared at room temperature upon dissolution of PEEK-WC (10% wt) in $CHCl_3$, together with the DODA-SEP (0.5% wt), and in the presence of 1,4-butanediol (4 wt%) and *i*-propanol (6 wt%) as porogenic solvents. The solution is then casted on a glass plate inside a glovebox kept under controlled humidity (U = 75%), to allow solvent evaporation (Scheme 16).[278]

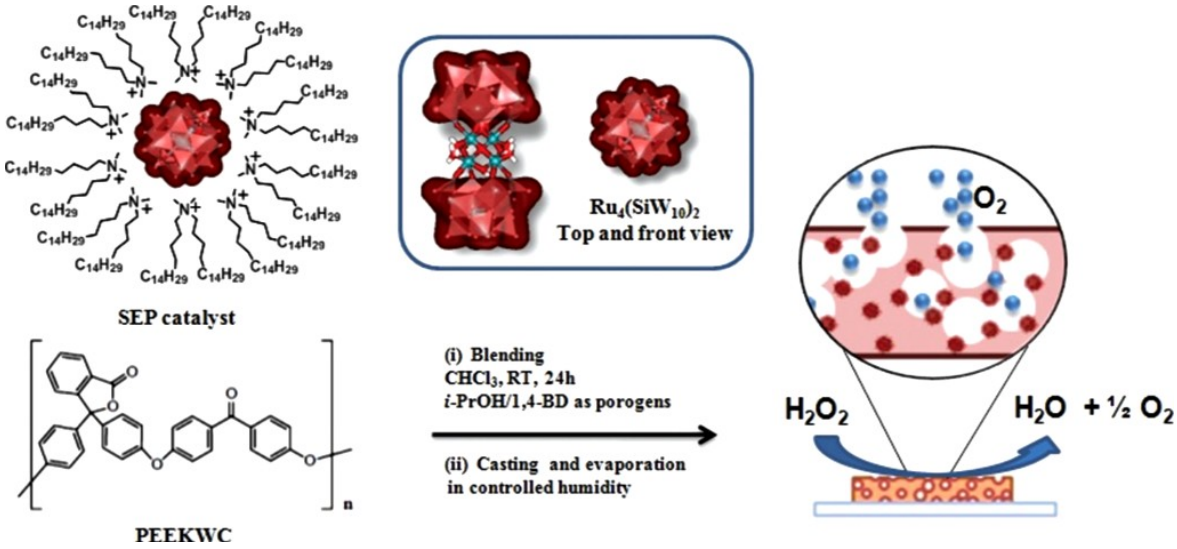

Scheme 16. Molecular components and membrane fabrication scheme: blending of a $CHCl_3$ solution containing the surfactant encapsulated catalyst (SEP catalyst) $DODA_{10}/Ru_4(SiW_{10})_2$, the PEEK-WC polymer, and porogens (*i* -propanol and 1,4-butanediol) was followed by casting and the solvent evaporation under controlled humidity (U = 75%). A porous texture is obtained with embedded oxygenic catalysts. The catalyst structure, $Ru_4(SiW_{10})_2$, is highlighted in the box.

Under the conditions adopted (see the Experimental Section), the combined effect of porogens with templating water droplets turns out to yield a 3D pore array structure within the polymeric film inner and surface layers as indicated by environmental scanning electron microscopy (ESEM) images collected over selected surface and section areas.[279–282] In particular, the resulting membrane exhibits an air-exposed front-side with average pore diameter in the range 0.5–5.0 μm, an overall thickness of about 70 μm, and the back-side with pore diameter up to 5.0 μm (Figure 100).

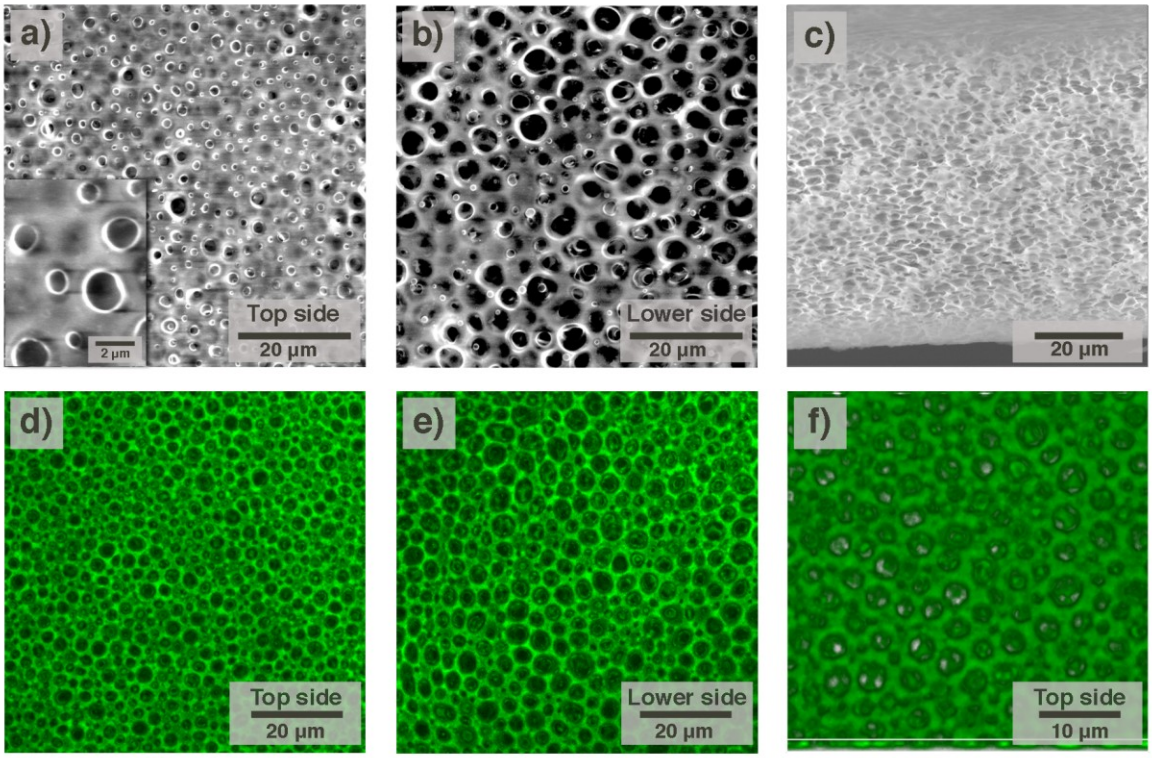

Figure 100. Environmental scanning electron microscopy (ESEM) images of PEEK-WC 2 membrane top surface a), back surface b), cross section c) showing a bulk porous structure. Confocal fluorescence microscopy (CFM, laser at 488 nm) of PEEK-WC 2 membrane top surface image d), back surface e), and 3D reconstructed image of the bulk material f).

The associated energy dispersive X-ray analysis (ESEM/EDX) has been used to map the tungsten content, the W element accounts for 60% of the catalyst weight, and gives a direct evidence of the equal dispersion of the catalyst on surface areas and inner layers of the bulk material (see Appendix). The overall catalyst loading (in the range 1.4%–2.0% wt%, see Table 15) has been determined by thermogravimetric analysis (TGA) (see Appendix). Noteworthy, the templating effect of water droplets during film formation is expected to foster localization of the DODA–SEP domains on the pore walls and their periphery. The reason is that the hydrophilic SEPs can stabilize the on surface condensation of water droplets, which then evolve to catalytic pores upon solvent evaporation.[283]

Table 15. Catalytic performance of oxygenic membranes embedding $Ru_4(SiW_{10})_2$

Membrane [a]	$Ru_4(SiW_{10})_2$ loading, [% wt] [b]	Pore size, [μm] [c]	Contact Angle vs H_2O [d]	O_2 evolution rate, [μmol/h] [e]	O_2 Yield, [%] (TON) [f]	TOF, [h^{-1}] [g]
PEEK-WC **1**	1.7 ± 0.3	dense	82.0° ± 2.0	2.65 ± 0.09	11 (1915)	80
PEEK-WC **2**	1.7 ± 0.1	0.5÷5.0	79.0° ± 1.6	5.88 ± 0.12	24 (4450)	185

a) in all reactions, a flat membrane disk (d=22 mm, about 20 mg) has been incubated with aqueous H_2O_2 (12 ml, 0.1 M) at 25°C; PEEK-WC **1** and PEEK-WC **2** have been isolated upon film casting respectively in dry atmosphere and under humidity controlled environment (see experimental part); b) determined by TGA analysis; c) range of pore size distribution on the top membrane surface, determined by ESEM analysis; d) determined for the top membrane surface; e) initial rate of oxygen evolution monitored by differential pressure variation up to 10% H_2O_2 conversion; f) based on H_2O_2 conversion after 24h, turnover number (TON) is calculated on the embedded catalyst amount resulting from the experimental %wt loading; g) turnover frequency (TOF) is defined as the TON per hour, based on the evolution of oxygen after 24 h reaction.

Imaging of catalytic clusters on the pore mouth and inner walls is obtained by ESEM microscopy with back-scattered electron detection mode, showing the polyoxometalate domains within bright areas. A magnification of the catalytic pores (ESEM BSD mode) shows small catalyst clusters localized in the pore walls and periphery (inset in Figure 101).

The porous morphology of the resulting polymeric film is further assessed by CFM, which exploits the luminescent properties of the PEEK-WC polymer with $\lambda_{max\ (ex)}$ = 400 nm and $\lambda_{max\ (em)}$ = 460 nm (see Appendix). CFM allows for a rapid, non invasive, 3D inspection of the porous structure, mapping the first 5 μm depth from the membrane surface (Figure 100 d–f, Supporting Information). The oxygen evolving activity of the polymer embedded catalyst has been evaluated in the presence of aqueous H_2O_2 (0.1 M) by monitoring the pressure variation over time, using a differential pressure transducer (see the Experimental Section).

The impact of the porous morphology on the catalytic activity stems from the oxygen evolution kinetics recorded for a dense, nonporous membrane (Figure 102 , **PEEK-WC 1**) as well as for the analogous porous film (Figure 100 , **PEEK-WC 2**), and compared to the catalyst free polymer as the control reaction (Figure 101, blank). The membrane **PEEK-WC 1** was prepared using the same procedure reported in the experimental section but the casting was performed under atmospheric conditions (*Evaporation induced phase separation, EIPS)*.

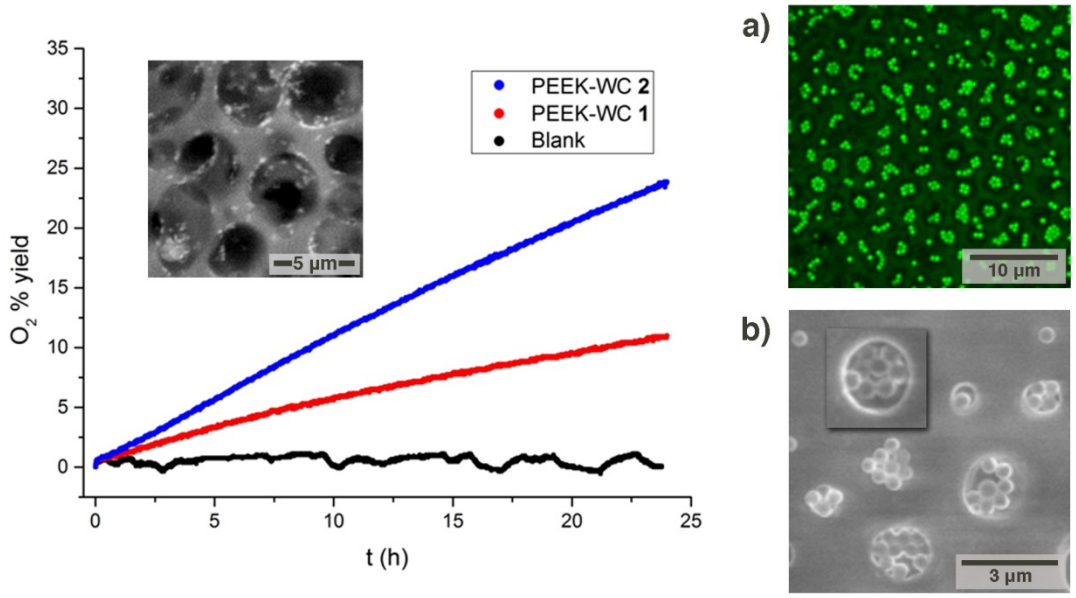

Figure 101. Oxygen evolution kinetics at 25 °C stemming from a dense, nonporous membrane surface (PEEK-WC 1, red line), and the porous analogue (PEEK-WC 2, blue line) during incubation with aqueous H_2O_2 (0.1 M). In both membranes the $Ru_4(SiW_{10})_2$ loading is calculated to be 1.7% wt. In the absence of the catalytic additive PEEW-WC membranes do not display oxygen evolution activity. Images on the right show the fouled state and pore constriction by fluorescent polystyrene beads (0.5 µm) upon visualization with CFM a) and ESEM analysis b).

The membrane obtained is asymmetric, as shown in Figure 102, and presents a dense air-exposed skin, due to the rapid evaporation of the solvent, that does not allow the formation of a porous layer. The porous structure of the rear and the bulk, generated by the porogens templating action, is still present. Comparing the top side of the membrane **PEEK-WC 1** with the membrane **PEEK-WC 2**, the effect of the humidity on the porosity is conspicuous.

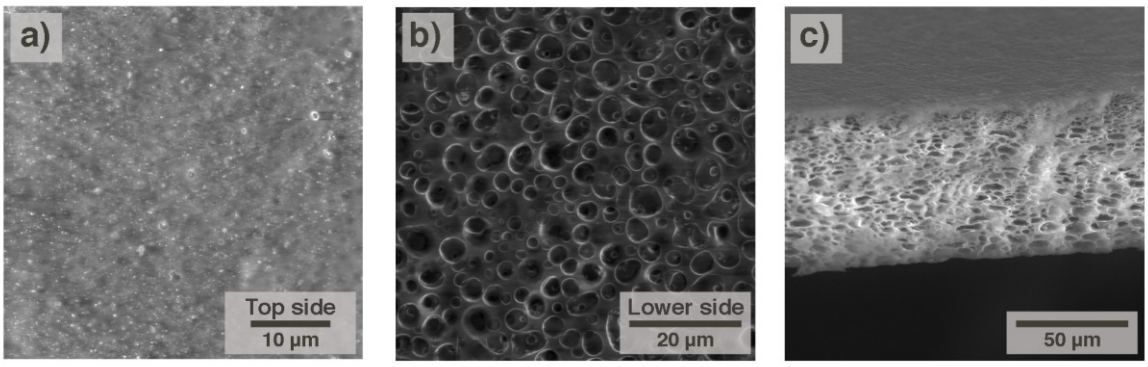

Figure 102. Environmental Scanning Electron Microscopy (ESEM) images of PEEK-WC **1** membrane top surface (a), back surface (b), cross section (c) showing a bulk porous structure obtained by evaporation induced phase separation.

The relative catalytic performance can be evaluated in terms of the O_2 evolution rate, % yield, total turnover number (TON), and turnover frequency (TOF). Inspection of data in

Table 15 shows that the wettability and interfacial behaviour of both membranes (contact angle ≈80°) are dictated by the moderate hydrophilic properties of the PEEK-WC polymer, and that the key factor to boost reactivity is associated to the porous texture of the membrane surface, which fosters a favourable H_2O_2 diffusion through the catalyst sites and a continuous oxygen evolution over 24 h (Table 15).

Oxygen evolution through the catalytic pores offers a dynamic trigger against irreversible fouling, a type of fouling for which actually there are no remediation. The self-cleaning potential of the oxygenic pores has been assessed in the presence of polystyrene latex beads, carrying an orange-fluorescent label (λ_{abs} = 475 nm, λ_{em} = 540 nm). These fluorescent beads have been chosen to serve as standard foulants of the **PEEK-WC 2** membrane, by virtue of: (i) a sub-pore diameter size (0.5 μm), (ii) selective excitation wavelength with respect to the polymer matrix (λ_{exc} = 400 nm), and (iii) robustness against H_2O_2-induced bleaching. Visualization of pore occlusion is readily achieved by CFM, with 488 nm CW Ar laser excitation, upon treating the membrane surface with increasing bead concentration in aqueous suspension followed by solvent removal. As expected, the fouled membrane shows an extensive localization of the fluorescent beads within the surface pores, which is also confirmed by ESEM analysis (Figure 103 a,b). With this protocol, fouling by solid particles models an irreversible pore constriction (Figure 103 a).

The confinement of particles within the pore walls hampers an efficient removal of foulants by simple washing cycles. Indeed, an extensive washing treatment of the membrane surface, under tangential water flow, does not produce any major modification of the fouled state (Figure 103 b). Remarkably, the efficient removal of the solid particles is instead obtained by applying aqueous H_2O_2 (2.0 M, 24 h incubation) which acts as the chemical stimulus for through-pore oxygen evolution.

The developed pressure and the propulsion force exerted by the liberated gas are such enough to enable beads ejection from the pores. This cleaning effect is readily visualized by CFM which witnesses a major reduction of the fluorescent spots on the membrane surface (Figure 103 c).

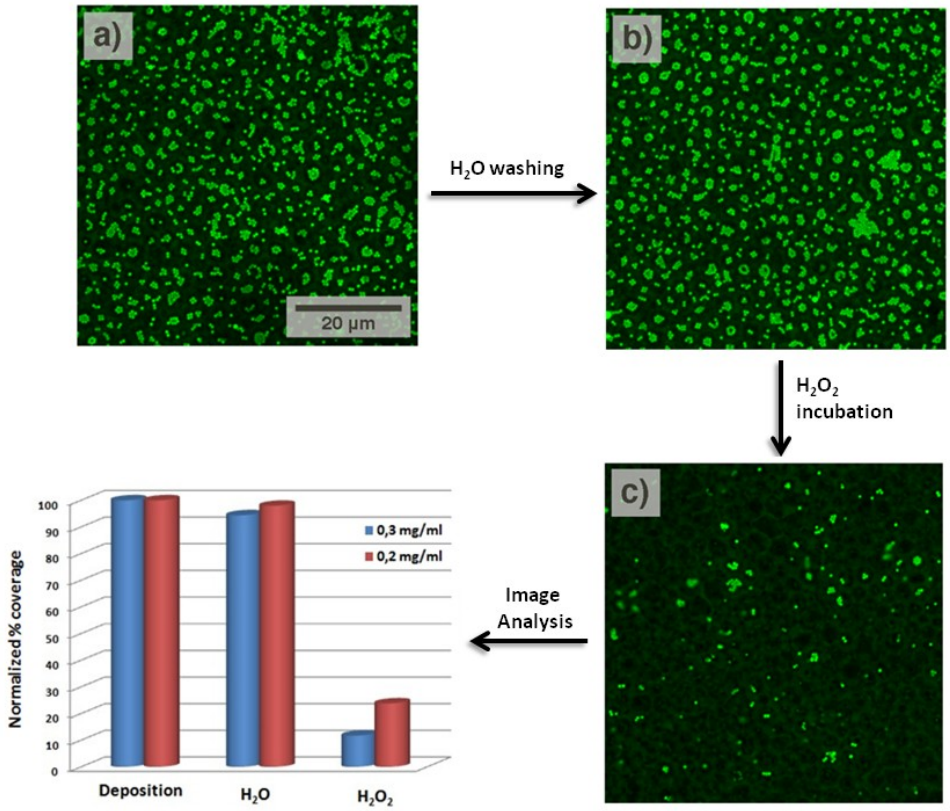

Figure 103. CFM (488 nm excitation): visualization of the fouled membrane surface obtained by deposition of fluorescent beads from a 0.3 mg mL^{-1} aqueous solution a), after washing with water b), and after 24 h incubation in H_2O_2 2.0 M c). The efficiency of the antifouling oxygenic treatment is highlighted by the histogram plot where the modification of the membrane surface obtained after deposition of latex beads at increasing concentration is quantified as normalized % coverage in its initial state and after H_2O and H_2O_2 antifouling treatment.

Computer-aided image analysis (ImageJ software) allows quantifying the antifouling effect up to 88% of bead removal. In particular oxygenic antifouling is effective for pore occlusion in the 20%–30% surface area (initial state) with a remediation outcome that reduces the fouled state below 5% of the overall surface (Table 16).

Table 16. Self-cleaning properties of the membrane.

	latex beads concentration [a] (mg/ml)	**Fouled (A%) [b]**	**Area after H_2O cleaning (A%) [b]**	**Area after H_2O_2 cleaning (A%) [b]**	**Fouling after H_2O cleaning (%) [c]**	**Fouling after H_2O_2 cleaning (%) [c]**
test (a)	0.2	18.8	18.4	4.5	98	24
test (b)	0.3	26.2	24.7	3.1	94	12

a) latex fluorescent beads (diameter 0.5 µm, λ_{ex}= 475 nm, λ_{em}= 540); b) A% is the area of the images covered by fluorescents beads; c) the % fouling was evaluation by the ratio from the A % before and after the cleaning.

The stability of the beads was tested to verify the robustness of the fluorophore embedded into the polystyrene matrix under the same experimental conditions. To this aim 0.2 mg/ml

latex beads dispersion was incubated for 24 h with a 2.0 M hydrogen peroxide solution and of **$Ru_4(SiW_{10})_2$** (60 nmol) (corresponding to the overall membrane loading). The fluorescence data of the beads were collected before and after the test, irradiating the sample at 480 nm. As shown in Figure 104 the fluorescence of the beads is unmodified.

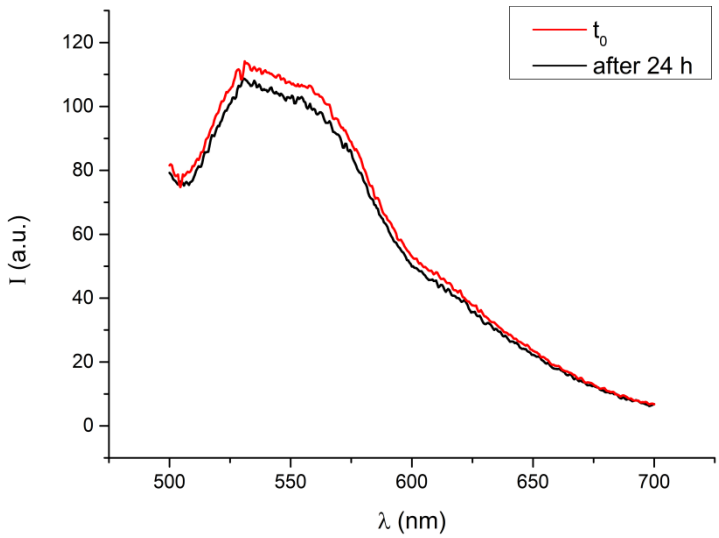

Figure 104. Fluorescence of the latex beads collected before (red line) and after (black line) 24 h incubation in a solution of H_2O_2 2.0 M containing $Ru_4(SiW_{10})_2$ (60 nmol).

In summary, functional pores with oxygenic activity offer an unprecedented strategy for the autonomous cleaning of porous materials and surfaces under mild conditions. Noteworthy, H_2O_2 dismutation to O_2 provides the chemical stimulus to trigger the catalytic antifouling response of the material. The "in-pore" self-cleaning activity guarantees a long-term efficiency of the material, removing foulant particles from the inner structure reaching out to the surface of the porous architecture. The engineering of the organic–inorganic texture of the pore walls exploits a straightforward self-assembly protocol, based on the strong inclusion of the nanodimensional SEP clusters within the polymeric matrix. The generality of the synthetic method has been demonstrated with different polymeric phases, as well as with hydrogels and carbon nanostructures including graphene composites.[269,284,285] Control experiments have shown a negligible leaching of the polyoxometalate cores in aqueous solution. [269,284,285]

The proposed innovation offers a definite advantage with respect to recent strategies based on the stepwise modification of the surface by covalent chemistry, and/or of the coating morphology, to elicit foulant–repellent properties. The complexity of such methods are exposed to a high risk of long-term failure, due to the possible degradation of the coating architecture under prolonged function.[242,243] On the contrary, totally inorganic

polyoxometalates as additives exhibit an exceptional robustness and stability both under homogeneous and heterogeneous catalysis conditions, coupling a recognized antimicrobial activity.[269,284,285] A further benefit of these catalytic pores is their antioxidant behaviour, mimicking the catalase enzymes, which offers a protection barrier against hydroxyl radicals and reactive oxygen species (ROS), to enhance the material stability under operating conditions.[135,136]

6. Conclusions

6. Conclusions

The core concept of the Thesis project deals within a main effort to mimic the functional metallo-biosites as artificial models of fundamental enzymes that activate small and vital molecules including: H_2O, O_2, H_2, H_2O_2.

Our approach is based on the use of polydentate ligands, including: (i) non-heme mono and di-nucleating N,O-donors; (ii) heme-macrocycles (porphyrins); (iii) totally inorganic polyoxotungstates (POMs). A synthetic strategy has been adopted to investigate the formation metallocomplexes of Mn, Cu, Fe, Co and Ru, providing a functional mimicry of natural enzymes including superoxide dismutase (SOD), catalase (CAT), hydrogenases and the oxygen evolving center of the photosynthetic protein (OEC-PSII). Their reactivity have been evaluated for the application as ROS scavengers in biological environments and in water splitting for sustainable energy systems.

With this aim, the Thesis project has tackled one key challenge of artificial enzymes that is to learn from nature and advance beyond its limits. In all catalytic systems presented herein, we have zoomed into structure-reactivity relationships to map the competent species and their mechanistic specificity according to generally accepted bio-inspired guidelines. However, we have moved one a step-forward, by overarching the typical enzyme specificity and looking to a multi-faceted performance to optimize the functional target. With this scope, we present herein novel bio-inspired catalytic cores that display a unique “dual” enzyme mimicry.

In particular we have addressed a combined SOD/CAT antioxidant catalysis by merging heme and non-heme Mn-cofactors (Mn_2L_2P1 and Mn_2L_2P2, Chapter 2) and by a unique Cu_2L_2 manifold (Chapter 3). Moreover a dual water oxidation/reduction electrocatalysis has been achieved at neutral pH by a Fe_2L_2 and Co_2L_2 analog that responds to the applied potential and enables both oxygen and hydrogen evolution on reversible scans (Chapter 4). Worth of notice is the application of the bio-inspired catalysis concept to the production of self-cleaning, anti-fouling, porous membranes integrating the highly stable catalase analog, known as $Ru_4(SiW_{10})_2$ (Chapter 5). The Thesis results are summarized below:

I. **Dinuclear manganese complex $Mn_2(II,II)L_2$ coupled with polycationic Mn(III)-porphyrins**.

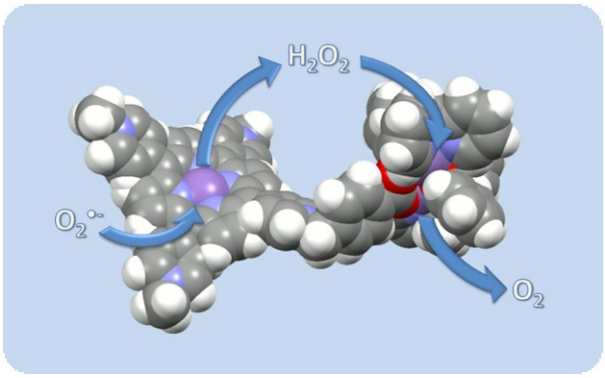

The co-localization of the Mn-based SOD/CAT mimetics provides a novel anti-oxidant di-functional system with an outstanding CAT and SOD activities coupled with a self-protection mechanism (Table 17). The in vivo tests to evaluate the effect on H_2O_2 accumulation in photosynthetic algae (Chlamydomonas reinhardtii) exposed to high-light illumination conditions provide a remarkable abatement of H_2O_2.

II. **Dinuclear copper complexes $Cu_2(II,II)L_2$**.

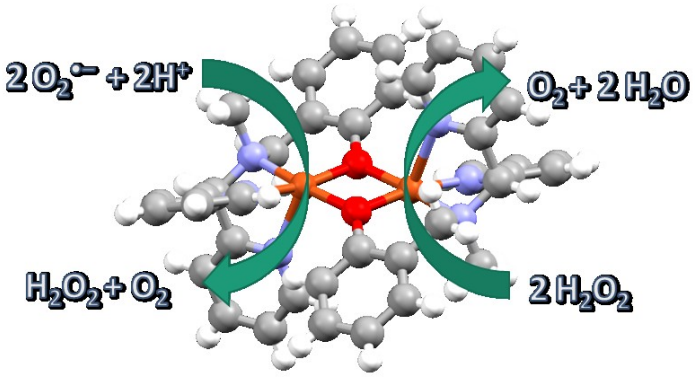

These complexes are the first reported examples of a dinuclear copper species showing a dual SOD/CAT activity in water under physiological-like conditions, with up to date, the highest SOD-like activity reported for a copper complex and a parallel CAT-like activity, which is unprecedented for a Cu_2-based catalysts (Table 17). These activities are also coupled with no external prooxidant effects thanks to the intra-molecular sacrificial scavenger. Thus it was demonstrated that a proper set of ligand it is able to tune the reactivity of an harmful metal centre like free copper to a benign catalytic antioxidant.

III. **Iron complexes (Fe(III)L and $Fe(III)_2L_2$) and dinuclear cobalt complexes $Co_2(II)L_2$.**

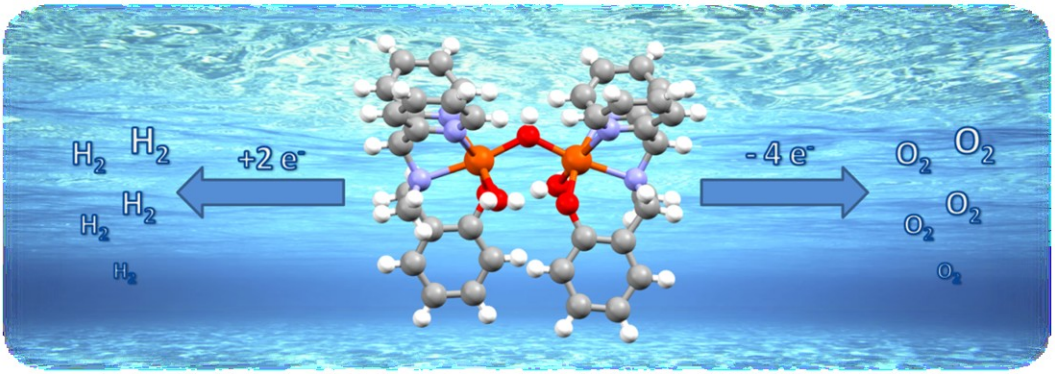

Preliminary tests show that the dinuclear Fe and Co complexes present a dual activity in water splitting processes being able to perform both the water oxidation than the proton reduction reactions in water at neutral pH, (Table 18) a key feature to obtain sustainable energy sources from water.

IV. **Polymeric membrane with embedded polyoxometalate $Ru_4(SiW_{10})_2$.**

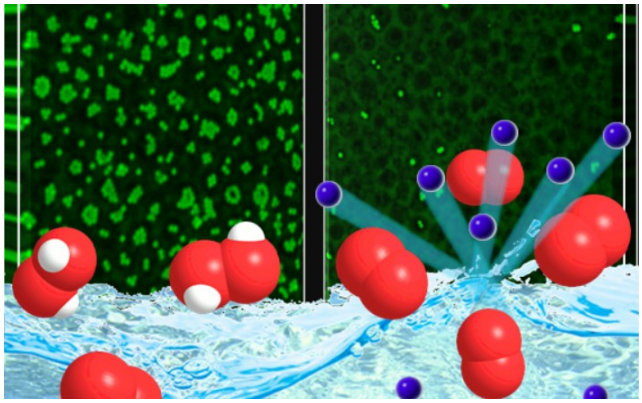

This system is based on the molecular design of catalytic pore walls that foster a chemo-mechanical, self-cleaning behaviour under neutral pH and mild conditions of pressure and temperature. This approach built on bioinspired remediation mechanisms involving H_2O_2 dismutation offer an unprecedented strategy for the autonomous cleaning of porous materials and surfaces from irreversible fouling. The tests on "in-pore" self-cleaning activity show an high efficiency in removing foulant particles from the inner structure of the material.

Table 17. Collection of relevant results, obtained for the complexes with dual SOD/CAT activities in water under physiological conditions (pH 7.8).

Compound	SOD		CAT	
	IC_{50} (μM)	$\log k_{cat}(O_2^{\bullet-})$	k ($M^{-1}s^{-1}$)	TON
Mn_2L_2Ac	1.04	6.40	1245	200
$Mn_2L^1{}_2Ac$	0.38	6.84	nd	65
Mn_2L_2P1	0.60	6.64	nd	200
Mn_2L_2P2	0.23	7.05	1890	200
Cu_2L_2	0.40	6.80	0.26	52
$Cu_2L^1{}_2$	0.14	7.27	0.58	60
$Cu_2L^2{}_2$	0.07	7.55	0.57	60

Table 18. Collection of relevant results, obtained for the complexes in water splitting (PBS pH 7).

Compound	Water Oxidation	Proton Reduction
	Overpotential (V)	Overpotential (V)
Fe_2L_2	0.58	1.1
Co_2L_2	nd	1.0
Co_2L_2Ac	0.46	1.0

7. Experimental Section

7.1 Materials

All commercially available reagents and solvents were used without further purifications. MilliQ-deionized water (Millipore) was used for the reactions, buffers preparation and for spectrometric measurements.

Solvents and deuterated (d) solvents:

- diethyl ether, methanol, 2-propanol, chloroform, dichloromethane, N,N-dimethylformamide, acetone, chloroform-d, acetonitrile-d_3, methanol-d_4, DMF-d_7, DMSO-d_6, D_2O, dichloromethane-d_2 (Sigma-Aldrich);
- ethanol (Fluka)
- DMSO, acetonitrile (VWR);
- 1,2-dichloroethane, pyridine (Carlo Erba).

Reagents:

- meso-tri(N-methyl-4-pyridyl)mono(4-carboxyphenyl)porphine trichloride, 5,10,15,20-tetra(N-methyl-4-pyridyl)-21*H*,23*H*-porphine and meso-tetra(4-pyridyl)porphine (Frontier Scientific).
- Manganese(II) chloride hydrate, potassium carbonate, potassium chloride, boric acid, (Farmitalia Carlo Erba).
- Manganese(II) perchlorate hydrate, Copper (II) perchlorate hydrate, ruthenium chloride, 4-(bromomethyl)benzoate, methyl iodide, morin, di-2-pyridyl ketone, hydroxylamine hydrochloride, pyridine, ammonium acetate, zinc powder, salicylaldehyde, 2-hydroxy-5-nitrobenzaldehyde, sodium borohydride, sodium triacetoxyborohydride, formaldehyde aqueous solution 37 % wt, xanthine, xanthine oxidase from bovine milk, cytochrome c from horse heart, catalase from bovine liver, DNA sodium salt from calf thymus, acetic acid, triethylamine, Amberlite® IRA-410 chloride form, potassium bromide, potassium nitrate, ammonium chloride, magnesium sulphate, sodium dihydrogen phosphate, sodium metasilicate, sodium tungstate dihydrate, tetrabutylammonium chloride, tetrabutylammonium perchlorate, dimethyldioctadecylammonium chloride, cesium chloride, 1,4-butanediol, latex beads fluorescent orange, Sephadex-G50™ (Sigma Aldrich).
- Silica gel (particle size 0.040-0.064 mm, 230-400 mesh) (Machery-Nagel).
- Ammonium hexafluorophosphate (Fluka).
- PEEK WC (224 kDa) from Institute of Applied Chemistry of Changchun (CN).

7.2 Instrumentation

^{1}H-NMR and *^{13}C-NMR* spectra were recorded with a Bruker 300 spectrometer operating at 300 MHz. Chemical shift were determined using solvent residual peaks as reference. For the protonic spectra, the following symbols have been used: s: singlet, d: doublet, t: triplet, q: quartet, m: multiplet.

^{1}H-NMR analysis of porphyrins were performed on a Bruker AVIII 500 MHz with probe 5 mm BBI z gradient.

FT-IR spectra were recorded with a Nicolet 5700-Thermo Electron Corporation instrument. For FT-IR spectra following symbols have been used: w: weak signal, m: medium signal, s: strong signal, b: broad signal.

UV-Vis spectra were recorded with a Varian Cary 50 and Varian Cary 100 spectrophotometer.

Fluorescence measurements were performed with a Perkin Elmer LS50B instrument with a cell length of 1cm.

ESI-MS spectra have been obtained with a Agilent LC/MSD Trap SL spectrometer.
Solvent used: MeOH, ACN, H_2O

Environmental scanning electron microscopy (ESEM) measurements were obtained using a FEI QUANTA 200 + modulo EDAX at CUGAS University of Padova.

Thermogravimetric analysis were performed using a TGA Q5000, working in air with heating ramp of 10°C/min until 700°C.

Porosity was measured using a perporometer PMI.

Contact angle where measured using a CAM100.

For catalytic experiments of hydrogen peroxide dismutation a home-made pressure transducer, with a septum for sample injection was used.

pH measurements were performed with a pH-meter HI 223 Hanna Instrument with a glass electrode. Calibration was carried out with Sigma-Aldrich buffers (pH 7-10).

7.3 Synthetic procedures

-Synthesis of: di-2-pyridy-ketoxime[286]

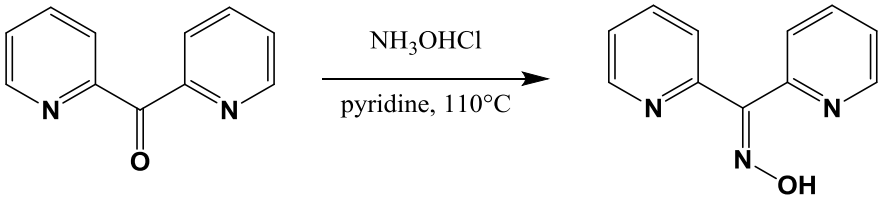

Di-2-pyridyl ketone (2.00 g, 10.7 mmol) and hydroxylamine hydrochloride (1.57 g, 22.2 mmol) were dissolved in 5 ml of pyridine and heated at 110° C for 4-5 hours. After cooling to 0° C, 10 ml of water were added and a white precipitate appeared (if it necessary, scratch with a glass rod help the precipitation). Product was filtered on a gootch and washed abundantly with water and dried under vacuum. Yield: 2.13 g (10.4 mmol, 97 %).

FT-IR (KBr, cm^{-1}): 3395 (s, br), 2996 (s, br), 2801 (s, br), 1621 (w), 1593 (s), 1566 (s), 1475 (s), 1432 (s), 1337 (m),1282 (m), 1153 (m), 1096 (m), 1050 (w), 1017 (s), 999 (s), 949 (s), 904 (w), 791 (s),758 (m), 690 (m), 659 (m), 622 (m), 580 (m), 495 (w).

^{1}H-NMR (300 MHz, MeOD) δ: 8.60 (d, *J* = 4.4 Hz, 1H), 8.44 (d, *J* = 4.3 Hz, 1H), 7.96 (t, *J* = 7.1 Hz, 1H), 7.87 (s, 2H), 7.63 (d, *J* = 7.8 Hz, 1H), 7.52 – 7.42 (m, 1H), 7.42 – 7.28 (m, 1H).

-Synthesis of: di-2-pyridyl-methylamine[287]

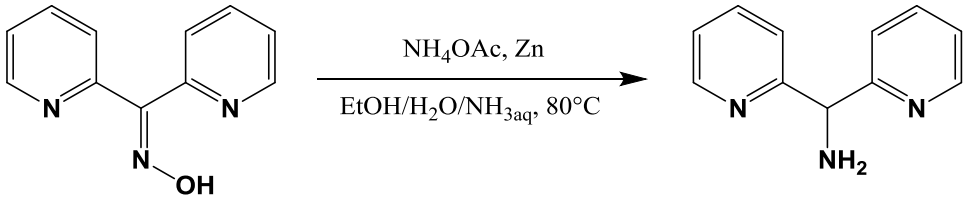

Di-2-pyridyl-ketoxime (2.0 g, 10.0mmol) was dissolved in a mixture of 17 ml of ethanol, 10 ml of water and 11 ml of 28% aqueous NH_3. NH_4OAc (1.92 g, 25.0mmol) was added and solution was heated to 80°C. Zinc powder (2.95g, 45.0mmol) was added in 30

minutes, then reaction was left refluxed for 4.5 hours. Solution was then filtered on paper, to remove residual solid, and concentrated under vacuum, until a white-yellow precipitate appeared. The resulting aqueous solution (~5ml) was basified with NaOH 10 M, solid disappeared and solution turned to yellow color. Basification continued until solution turned reddish-pink and a white precipitate appeared, then it was extracted with dichloromethane (5 ml x 3). Organic fraction was washed with brine (5 ml x 3) and water (5 ml x 3), dried with $MgSO_4$ and solvent was evaporated under reduced pressure. A yellowish oil was obtained. Yield: 0.69 g (3.75 mmol, 42 %)

^{1}H-NMR (300MHz, CD_3OD) δ: 8.50 (dd, *J* = 3.6, 1.3 Hz, 2H), 7.77 (td, *J* = 7.8, 1.7 Hz, 2H), 7.48 (d, *J* = 7.9 Hz, 2H), 7.35 – 7.16 (m, 2H), 5.27 (s, 1H).

-Synthesis of: 2-({[Di(2-pyridyl)methyl]imino}methyl)phenol[149]

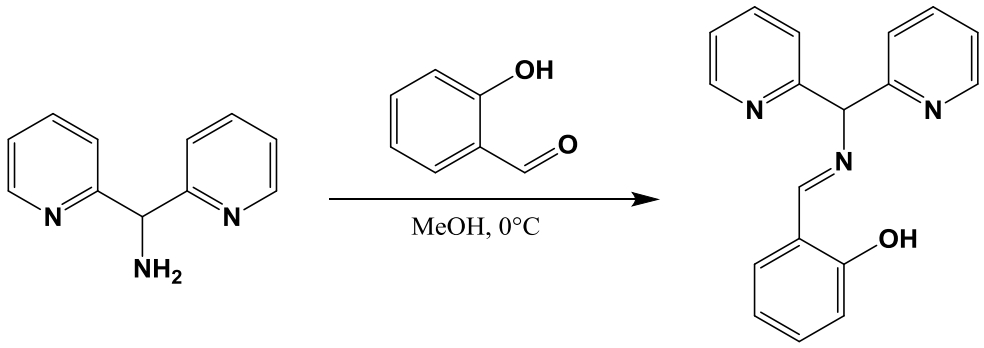

To a stirred solution of di-2-pyridyl-methylamine (0.65 g, 3.4 mmol) in 5 mL of methanol was added neat salicylaldehyde (0.42g, 3.4 mmol). The solution immediately turned yellow. After stirring for about 5 min a yellow crystalline material appeared. The reaction mixture was cooled to 0º C and stirred for other 30 minutes. The solid was isolated by vacuum filtration, washed with ice-cold methanol and dried under vacuum. A yellow powder was obtained. Yield: 0.85 g (3.0 mmol, 88%).

FT-IR (KBr, cm^{-1}): 3441 (w, br), 3046 (w), 3009 (w), 1626 (s), 1585 (s), 1498 (m), 1463 (s), 1431 (s), 1382 (w), 1312 (w), 1280 (s), 1216 (w), 1201 (w), 1152 (m), 1058 (m), 988 (m), 876 (w), 857 (w), 775 (s), 760 (s), 666 (w),610 (m), 541 (m), 464 (m), 436 (w).

^{1}H-NMR (300 MHz, CD_2Cl_2) δ: 13.34 (s, 1H), 8.63 (s, 1H), 8.54 (d, *J* = 4.2 Hz, 2H), 7.70 (t, *J* = 7.7 Hz, 2H), 7.44 (d, *J* = 7.8 Hz, 2H), 7.33 (t, *J* = 6.8 Hz, 2H), 7.20 (t, *J* = 6.8 Hz, 2H), 6.91 (dd, *J* = 16.4, 8.5 Hz, 2H), 5.89 (s, 1H).

-Synthesis of: 2-({[Di(2-pyridyl)methyl]amino}methyl)phenol (L^1)[149]

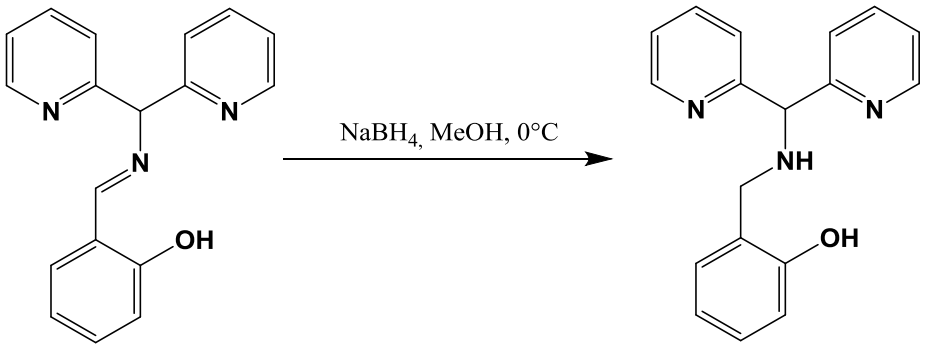

To a stirred solution of 2-({[di(2-pyridyl)methyl]imino}methyl)phenol (0.800 g, 2.8 mmol) in 15 ml methanol at 0º C $NaBH_4$ (107 mg, 2.8 mmol) was added in 3 portions during 15 min. The reaction mixture was stirred for 4 h. The mixture was then acidified with 2 M aq. HCl to pH 1 and stirred for 15 min. Subsequently the reaction was neutralized with 2 M aq. NH_3 and 30 ml water was added (pH ~8), methanol was removed under reduced pressure and the mixture extracted with ethyl acetate (5ml x 3). The combined organic layers were dried with Na_2SO_4 filtered and solvent was removed under vacuum to yield a reddish oil (it turned into a glass after few weeks). Yield: 0.77 g (2.6 mmol, 95%).

FT-IR (KBr, cm^{-1}): 3229 (w), 3049 (w), 3011 (w), 2901 (w), 2876 (w), 2855 (w), 2780 (w), 2732 (w), 2710 (w), 1612 (m), 1587 (s), 1567 (s), 1488 (s), 1468 (s), 1433 (s), 1411 (s), 1331 (m), 1289 (m), 1256 (s), 1211 (m), 1147 (m), 1096 (m), 1036 (m), 984 (m), 934 (m), 850 (w), 813 (w), 777 (m), 749 (s), 679 (w),647(w), 606 (w), 549 (w), 540 (w).

^{1}H-NMR (300 MHz, CD_2Cl_2) δ: 11.06 (s, 1H), 8.58 (d, J = 4.2 Hz, 2H), 7.65 (t, J = 7.6 Hz, 2H), 7.45 (d, J = 7.8 Hz, 2H), 7.24 – 7.04 (m, 4H), 6.93 (d, J = 7.4 Hz, 1H), 6.81 (d, J = 8.0 Hz, 1H), 6.70 (t, J = 7.3 Hz, 1H), 4.91 (s, 1H), 3.60 (s, 3H).

-Synthesis of: 2-{[Di(2-pyridyl)methyl](methyl)amino]methyl}phenol (L)[149]

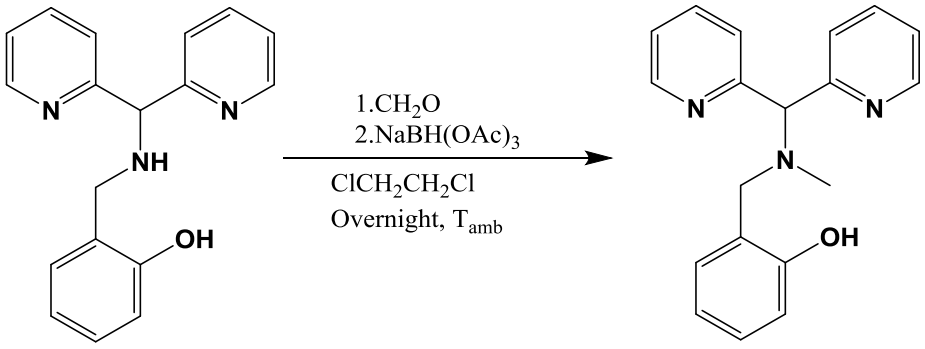

To a solution of 2-({[di(2-pyridyl)methyl]amino}methyl)phenol (0.75 g, 2.58 mmol) in 25 mL of $ClCH_2CH_2Cl$ was added aqueous 30% formaldehyde (300 µl, 5.1 mmol) and after

15 min of stirring $NaBH(OAc)_3$ (1.18 g, 5.1 mmol) was added in small portions during 20 minutes. Subsequently the reaction was vigorously stirred overnight. Dichloromethane (20 mL) was added and the organic layer was washed consecutively with 2 M aq. NH_3 (10 ml x 3), and twice with water (10 ml x 3). After drying with $MgSO_4$, filtration and evaporation of the solvents under reduced pressure, the product was obtained as a sticky oil which was purified by chromatography on silica using diethyl ether. A white solid was obtained. Yield: 0.64 g, (2.1 mmol, 81%).

FT-IR (KBr, cm^{-1}): 3048 (m), 3007 (m), 2970 (m), 2924 (m), 2849 (m), 2712 (m), 1607 (m), 1586 (s), 1490 (m), 1466 (s), 1432 (s), 1379 (w), 1330 (m), 1287 (m), 1257 (s), 1199 (m), 1149 (m), 1120 (m), 1102 (w), 1025 (m), 993 (m), 931 (m), 869 (w), 857 (w), 785 (m), 748 (s), 722 (m), 679 (w),617 (m), 540 (w), 448 (w).

^{1}H-NMR (300 MHz, CD_2Cl_2) δ: 8.62 (d, *J* = 4.1 Hz, 2H), 7.70 (t, *J* = 7.7 Hz, 2H), 7.50 (d, *J* = 7.9 Hz, 2H), 7.33 – 7.09 (m, 3H), 6.98 (d, *J* = 7.2 Hz, 1H), 6.87 (d, *J* = 7.9 Hz, 1H), 6.75 (t, *J* = 7.4 Hz, 1H), 4.98 (s, 1H), 3.66 (s, 2H), 2.20 (s, 3H).

-Synthesis of: 2-({[Di(2-pyridyl)methyl]imino}methyl)-4-nitrophenol

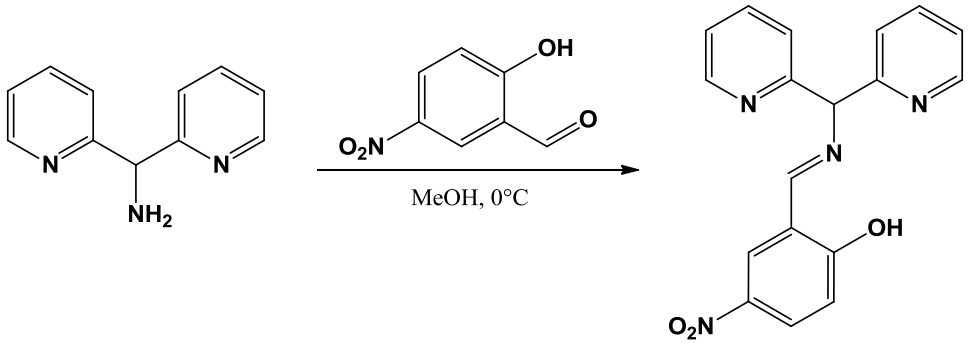

To a stirred solution of di-2-pyridyl-methylamine (350 mg, 1.8 mmol) in 5 mL of methanol was added neat 2-hydroxy-5-nitrobenzaldehyde (300 mg, 1.8 mmol). The solution immediately turned dark yellow. After stirring for about 5 min a dark yellow crystalline material appeared. The reaction mixture was cooled to 0º C and stirred for other 30 minutes. The solid was isolated by vacuum filtration, washed with ice-cold methanol and dried under vacuum. A dark yellow powder was obtained. Yield: 550 mg (1.65 mmol, 91%).

^{1}H-NMR (300 MHz, CD_2Cl_2) δ 8.65 (s, 1H), 8.59 (d, *J* = 4.1 Hz, 1H), 8.28 (d, *J* = 2.7 Hz, 1H), 8.19 (dd, *J* = 9.3, 2.8 Hz, 1H), 7.73 (t, *J* = 7.7 Hz, 2H), 7.41 (d, *J* = 7.9 Hz, 2H), 7.25 (t, *J* = 9.5, 2H), 6.99 (d, *J* = 9.2 Hz, 1H), 6.03 (s, 1H).

-Synthesis of: 2-({[Di(2-pyridyl)methyl]amino}methyl)-4-nitrophenol (L^2)

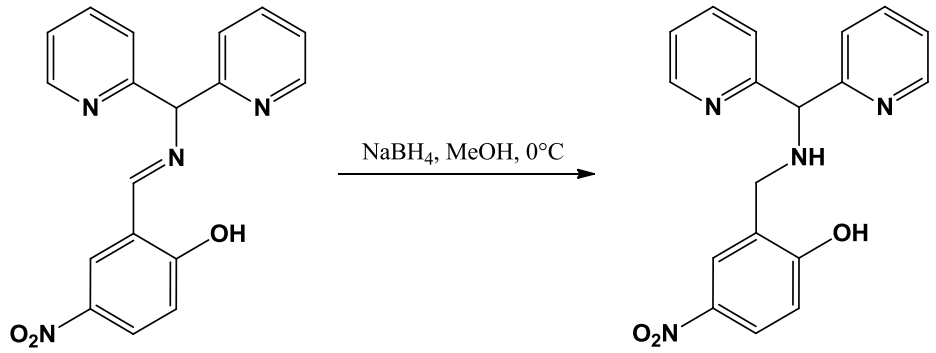

Same procedure for L^1 starting from 2-({[Di(2-pyridyl)methyl]imino}methyl)-4-nitrophenol (550 mg, 1.65 mmol) there was obtained a brown oil which turned into a glass after several days. Yield: 545 mg (1.6 mmol, 99%).

^{1}H-NMR (300 MHz, CD_2Cl_2) δ 8.58 (d, *J* = 4.3 Hz, 2H), 8.05 (dd, *J* = 8.9, 2.7 Hz, 1H), 7.87 (s, 1H), 7.67 (td, *J* = 7.7, 1.6 Hz, 2H), 7.33 – 7.18 (m, 4H), 6.85 (d, *J* = 9.0 Hz, 1H), 5.13 (s, 1H), 4.00 (s, 2H).

FT-IR (KBr): ν (cm^{-1}) 3422(w), 3296(w), 3056(w), 3010(w), 2920(w), 2853(w), 1615(m), 1589(s), 1572(m), 1511(m), 1479(s), 1434(s), 1337(s), 1287(s), 1171(m), 1150(m), 1090(s), 1050(m), 995(m), 931(m), 904(m), 831(w), 752(m), 670(w), 640(w), 613(w), 551(w), 449(w).

-Synthesis of: Mn_2L_2Ac

360 mg (1 mmol) of $Mn(ClO_4)_2{\cdot}6H_2O$ and ligand 2-{[[di(2-pyridyl)methyl](methyl)amino]methyl}phenol (305 mg, 1 mmol) were dissolved in 10 mL of methanol under N_2 atmosphere. Subsequently, acetic acid (24 µL, 0.5 mmol) was added. After all solids were dissolved, triethylamine was added (21 µL, 1.5 mmol) and the solution turned pale green. After stirring, a formation of a solid precipitate occurred. The solution was heated until boiling and gradually acetonitrile was added until complete dissolution of the solid. The solution was then let cool down. After a week pale green crystals were obtained, washed with methanol and ether and finally dried under vacuum. Yield: 246 mg, 56 %.

UV-Vis (CH_3CN): λ_{max}/nm (ε/M^{-1} cm^{-1}) 243.8 ($3.2{\cdot}10^4$), 256.7 ($2.0{\cdot}10^4$), 267.0 ($2.1{\cdot}10^4$) and 271.5 ($2.1{\cdot}10^4$).

FT-IR (KBr): ν (cm^{-1}) 3064(w), 3028(w), 3007(w), 2977(w), 2936(w), 2882(w), 2857(w), 2846(w), 2806(w), 1605(s), 1599(s), 1575(s), 1564(s), 1479(s), 1452(s), 1446(s), 1422(s), 1341(w), 1291(s), 1280(s), 1112(s), 1096(s), 1075(s), 1001(m), 884(m), 790(m), 761(s), 730(m), 624(s), 558(m), 531(m).

ESI(+)-MS m/z calcd. for $C_{40}H_{38}N_6O_4Mn_2^+$ (M) 777.2, found 777.1.

Elemental Analysis, calcd. for $C_{40}H_{38}N_6O_8Mn_2Cl$: C = 50.78, H = 4.48, N = 9.58; found C = 50.46, H = 4.62, N = 9.78.

-Synthesis of: $Mn_2L^1{}_2Ac$

70 mg (0.2 mmol) of $Mn(ClO_4)_2{\cdot}6H_2O$ and ligand 2-({[di(2-pyridyl)methyl]amino}methyl)phenol (60 mg, 0.2 mmol) were dissolved in 5 mL of ethanol under N_2 atmosphere. Subsequently, acetic acid (5 μL, 0.1 mmol) was added. After all solids were dissolved, triethylamine was added (4 μL, 0.3 mmol). After stirring, the formation of a solid precipitate occurred. The solution was heated until boiling and gradually DMF was added until complete dissolution of the solid. The solution was then let cool down at 0° C. After a couple of days white crystals were obtained, washed with ethanol and ether and finally dried under vacuum. Yield: 44 mg, 52 %.

UV-Vis (CH_3CN): λ_{max}/nm (ε/M^{-1} cm^{-1}) 243.9 ($2.7{\cdot}10^4$), 264.2 ($1.5{\cdot}10^4$), 269.1 ($1.5{\cdot}10^4$) and 287.9 ($6.7{\cdot}10^3$).

FT-IR (KBr): ν (cm^{-1}) 3281(m), 3062(w), 3024(w), 2926(w), 2860(w), 1600(s), 1572(s), 1563(s), 1481(s), 1470(m), 1445(s), 1422(m), 1340(w), 1289(s), 1277(s), 1121(s), 1108(s), 1090(s), 1013(m), 983(w), 905(m), 864(w), 779(m), 759(s), 732(w), 687(w), 626(m).

ESI(+)-MS m/z calcd. for $C_{38}H_{35}N_6O_4Mn_2^+$ (M) 749.2, found 749.1.

-Synthesis of: Mn(III)-meso-tri(N-methyl-4-pyridyl)mono(4-carboxyphenyl)porphine trichloride (P1)

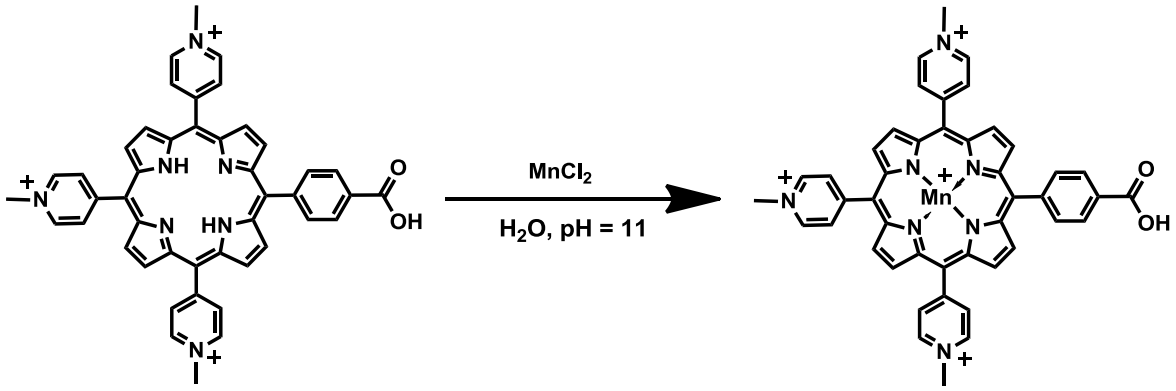

41.8 mg (50 µmol) of meso-tri(N-methyl-4-pyridyl)mono(4-carboxyphenyl)porphine were dissolved in 15 ml of water and the pH was adjusted to 11.5 with 0.5 M NaOH, $MnCl_2 \cdot 6 H_2O$ (256,4 mg, 700 µmol) was then added. Metallation was accomplished in 1 h monitoring the reaction by UV-Vis spectroscopy until disappearing of the Soret band (422 nm) of the free base porphyrin. Upon completion of metallation the solution was filtered, the product was precipitated by adding a 2-propanol:diethyl ether (1:1) solution and thoroughly washed with the 2-propanol:diethyl ether solution to remove the excess of metal. Yield: 28.5 mg, 55 %.

UV-Vis (H_2O): λ_{max}/nm ($\varepsilon/M^{-1}\,cm^{-1}$) 379.7 ($4.3 \cdot 10^4$), 402.1 ($4.6 \cdot 10^4$), 464.9 ($1.2 \cdot 10^5$) (Soret bands), 561.9 ($1.2 \cdot 10^4$) (Q bands).

FT-IR (KBr): ν (cm^{-1}) 3093(w), 3039(w), 1640(s), 1584(m), 1539(m), 1506(m), 1458(w), 1373(s), 1343(m), 1279(w), 1211(w), 1186(w), 1092(w), 1028(m), 1011(s), 866(w), 806(m), 777(w), 712(w), 564(w).

ESI(+)-MS m/z calcd. for $C_{45}H_{32}MnN_7O_2^{3+}$ ($M\text{-}H^+$) 252.9, found 253.1 and for $C_{45}H_{34}MnN_7O_3^{3+}$ ($M - H^+ + H_2O$) 258.9 found 258.7.

Elemental Analysis, calcd. for $C_{45}H_{33}MnN_7NaO_2 \bullet 6H_2O$: C = 52.39, H = 4.40, N = 9.50; found C = 52.23, H = 4.61, N = 9.28.

-Synthesis of: meso-tri(4-pyridyl)mono(N-4-methoxyformylbenzyl-4-pyridyl)porphine chloride

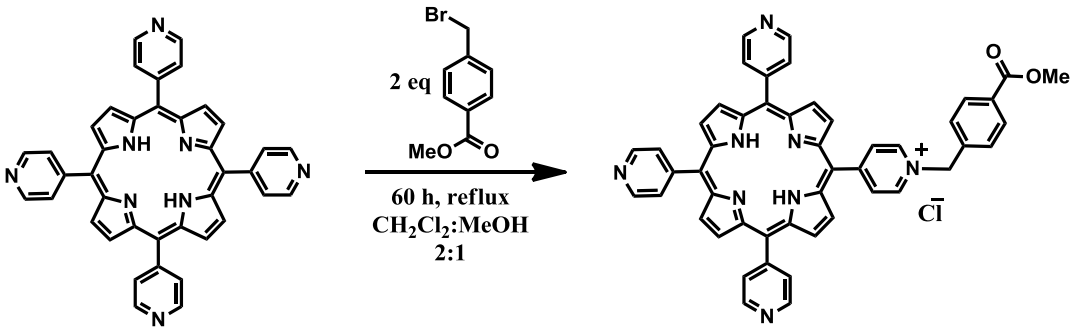

1.60 g (4.8 mmol) of methyl 4-(bromomethyl)benzoate were added to 5,10,15,20-tetra(4-pyridyl)-21*H*,23*H*-porphine (1.50 g, 2.4 mmol) in 180 ml of refluxing CH_2Cl_2:CH_3OH (2:1). After 60 h, the solvent was removed under vacuum. The crude material was then purified by flash column chromatography on silica gel using CH_2Cl_2:CH_3OH (70:30) NH_4Cl saturated as eluent. The purified material was collected after solvent removal under vacuum, washed with water to remove the NH_4Cl and silica, and dried under vacuum. Yield: 363 mg, 19 %. R_f = 0.50 (CH_2Cl_2:CH_3OH 70:30 on silica gel).

UV-Vis (CH_3OH): λ_{max}/nm (ε/M^{-1} cm^{-1}) 415.4 ($1.6\cdot10^5$) (Soret bads); 512.9 ($1.2\cdot10^4$), 550.2 ($5.3\cdot10^3$), 588.9 ($4.3\cdot10^3$), 645.9 ($1.8\cdot10^3$) (Q bands).

ESI(+)-MS m/z calcd. for $C_{49}H_{35}N_8O_2^+$ (M) 767.3, found 767.3.

^{1}H NMR (500 MHz, CD_3OD): δ (ppm) 9.51 (d, 2H, *J* = 10.6 Hz), 9.02 (m, 14H), 8.30 (m, 8H), 7.95 (d, 2H, *J* = 13.6 Hz), 6.30 (s, 2H), 3.98 (s, 3H). ^{13}C NMR (300 MHz, CD_3OD): δ (ppm) 175.7, 172.3, 166.9, 166.0, 153.9, 153.4, 148.5, 142.7, 141.8, 140.3, 140.0, 139.8, 139.5, 125.6, 125.5, 125.3, 62.2, 57.8.

-Synthesis of: meso-tri(N-methyl-4-pyridyl)mono(N-4-methoxyformylbenzyl-4-pyridyl)porphine tetraiodine

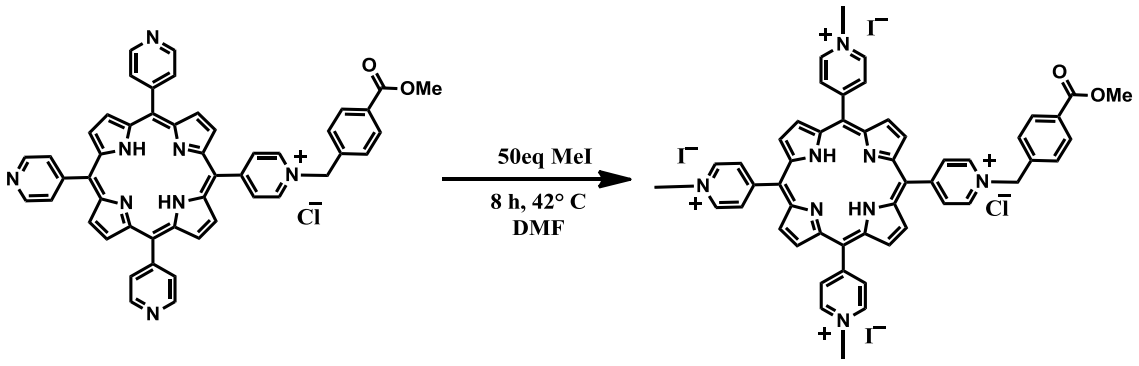

1.164 ml (18.7 mmol) of CH_3I were added to meso-tri(4-pyridyl)mono(N-4-methoxyformylbenzyl-4-pyridyl)porphine chloride (300 mg, 375 µmol) in 80 ml of DMF at 42° C. After 8 h the product was precipitated by adding CH_2Cl_2 and the precipitated was thoroughly washed with CH_2Cl_2. Yield: 447 mg, 97%. R_f = 0.30 (1:1:8= $KNO_{3(sat)}$:H_2O:acetonitrile on silica gel).

UV-Vis (H_2O): λ_{max}/nm ($\varepsilon/M^{-1}\,cm^{-1}$) 423.8 ($2.0\cdot10^5$) (Soret bands); 519.6 ($1.3\cdot10^4$), 555.8 ($5.4\cdot10^3$), 585.5 ($6.0\cdot10^3$), 639.6 ($1.3\cdot10^3$) (Q bands).

ESI(+)-MS m/z calcd. for $C_{52}H_{43}N_8O_2^{3+}$ ($M\text{-}H^+$) 270.5, found 270.6 and calcd. for $C_{52}H_{42}N_8O_2^{2+}$ ($M\text{-}2H^+$) 405.2, found 405.1.

^{1}H NMR (500 MHz, DMSO-d_6): δ 9.66 (d, 2H, *J* = 10.0 Hz), 9.48 (d, 6H, *J* = 10.0 Hz), 9.28 (d, 2H, *J* = 7.0 Hz), 9.19 (s, 6H), 9.06 (d, 2H, *J* = 10.5 Hz), 8.99 (d, 2H, *J* = 10.0 Hz), 8.21 (d, 2H, *J* = 14.0 Hz), 8.04 (d, 2H, *J* = 13.5 Hz), 6.32 (s, 2H), 4.73 (s, 9H), 3.93 (s, 3H),-3.10 (s,2H). ^{13}C NMR (300 MHz, DMSO-d_6): δ (ppm) 160.0, 159.3, 159.2, 145.6, 144.8, 137.0, 134.7, 134.0, 131.8, 130.4, 117.1, 117.1, 116.9, 65.5, 35.4.

-Synthesis of: meso-tri(N-methyl-4-pyridyl)mono(N-4-carboxybenzyl-4-pyridyl)porphine tetrachloride

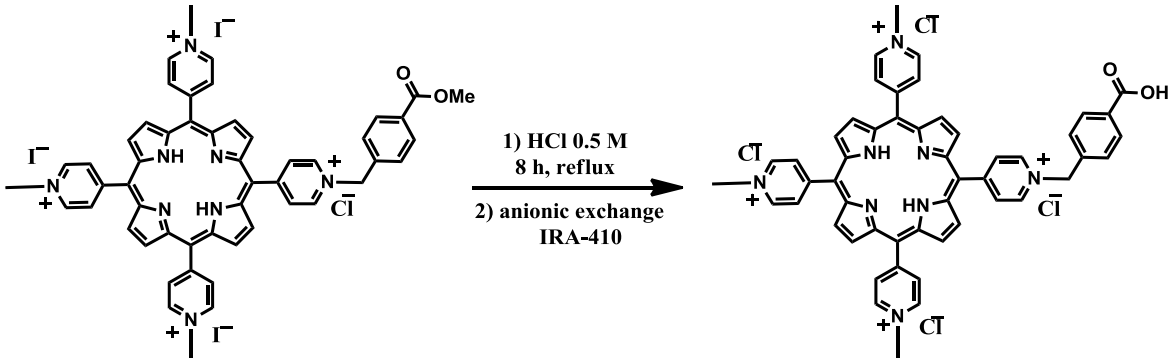

400 mg (330 µmol) of meso-tri(N-methyl-4-pyridyl)mono(N-4-methoxyformylbenzyl-4-pyridyl)porphine were dissolved in 160 ml of HCl 0.5 M and heated under reflux. After 8 h the product was precipitated by adding a 2-propanol:diethyl ether (1:1) solution and the precipitate was washed with a 2-propanol:water (9:1) solution. This procedure was repeated three times to completely remove the acid. Finally the counter anion of the porphyrin was exchanged with chloride by using an anionic exchange resin IRA-410 and dried under vacuum. Yield : 100%, 310 mg. R_f= 0.10 (1:1:8 =$KNO_{3(sat)}$:H_2O: acetonitrile on silica gel).

UV-Vis (H_2O): λ_{max} /nm ($\varepsilon/M^{-1}\,cm^{-1}$) 423.8 ($1.8\cdot10^5$) (Soret bands); 519.6 ($1.3\cdot10^4$), 555.8 ($6.2\cdot10^3$), 585.5 ($6.4\cdot10^3$), 639.6 ($2.4\cdot10^3$) (Q bands).

ESI(+)-MS m/z calcd. for $C_{51}H_{42}N_8O_2^{3+}$ ($M\text{-}H^+$) 265.8, found 265.8 and calcd. for $C_{51}H_{42}N_8O_2^{2+}$ ($M\text{-}2H^+$) 398.2, found 398.1.

^{1}H NMR (500 MHz, DMSO-d_6): δ 9.77 (d, 2H, J = 6.5 Hz), 9.57 (d, 6H, J = 6.0 Hz), 9.27 (s, 2H), 9.19 (s, 6H), 9.07 (d, 2H, J = 6.0 Hz), 9.00 (d, 6H, J = 6.0 Hz), 8.13 (d, 2H, J = 7.5 Hz), 7.95 (d, 2H, J = 7.5 Hz) 6.34 (s, 2H), 4.75 (s, 9H), -3.10 (s, 2H). ^{13}C NMR (300 MHz, CD_3OD): δ (ppm) 166.2, 157.4, 156.5, 156.4, 144.5, 144.0, 139.0, 133.3, 132.4, 130.8, 130.3, 130.0, 116.1, 116.0, 115.8, 63.2, 52.8, 48.3.

-Synthesis of: Mn(III)-meso-tri(N-methyl-4-pyridyl)mono(N-4-carboxybenzyl-4-pyridyl)porphine pentachloride (P2)

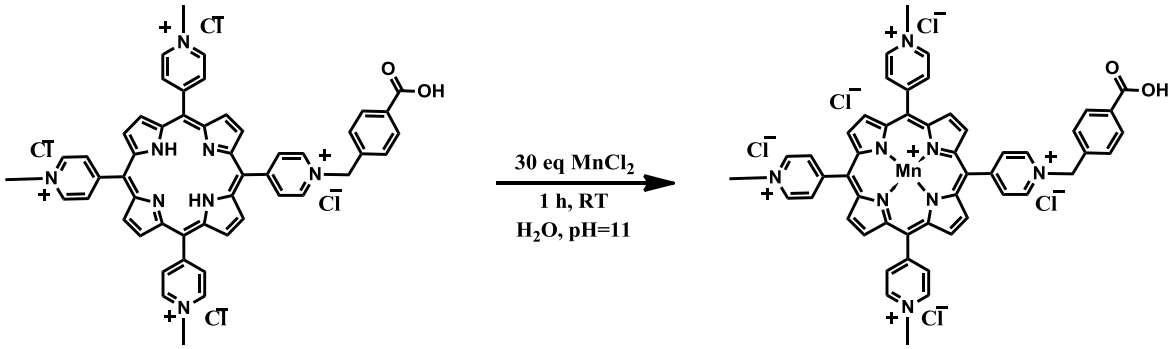

1.26 g (3.5 mmol) of $MnCl_2\cdot6\,H_2O$ were added to 30 ml of a water solution containing meso-tri(N-methyl-4-pyridyl)mono(N-4-carboxybenzyl-4-pyridyl)porphine (200mg, 210 μmol) previously set at pH = 11.5 by adding NaOH 0.5 M solution. Metallation was accomplished in 1 h monitoring the reaction by UV-Vis spectroscopy until disappearing of the Soret band (424 nm) of the metal free porphyrin. Upon completion of metallation the solution was filtered and the product was precipitated as a PF_6^- salt by the addition of an aqueous solution of NH_4PF_6. The precipitate was filtered off and thoroughly washed with water. The dried precipitate was dissolved in acetone and precipitated as a chloride salt by the addition of a saturated acetone solution of tetrabutylammonium chloride and the precipitate was thoroughly washed with acetone. This procedure repeated three times allows a complete removal of the free metal. Finally, the precipitate was dissolved in water and precipitated with 2-propanol:diethyl ether (60:40) solution and thoroughly washed with the same solution to remove the excess tetrabutylammonium chloride arising from the previous step. Yield: 200 mg, 61 %.

UV-Vis (H_2O): λ_{max}/nm (ε/M^{-1} cm^{-1}) 377.3 ($4.0\cdot10^4$), 398.9 ($4.1\cdot10^4$), 462.5 ($1.3\cdot10^5$) (Soret bands), 563.0 ($1.2\cdot10^4$) (Q bands).

FT-IR (KBr): ν (cm^{-1}) 3113(w), 3080(w), 3037(w), 1639(s), 1557(m), 1539(m), 1505(w), 1457(m), 1379(w), 1347(w), 1276(w), 1211(w), 1186(w), 1095(w), 1028(m), 1011(s), 863(w), 807(m), 770(w), 714(w), 559(w), 526(w).

ESI(+)-MS m/z calcd. for $C_{51}H_{40}MnN_8O_2^{3+}$ (M - H^+ + e^-) 283.4, found 283.3, calcd. for $C_{51}H_{40}ClMnN_8O_2^{3+}$ (M - H^+ + Cl^-) 295.2, found 295.4 and for $C_{51}H_{40}ClMnN_8O_2^{2+}$ (M - H^+ + Cl^- + e^-) calcd. 442.8 found 442.6.

Elemental Analysis, calcd. for $C_{51}H_{39}Cl_5MnN_8NaO_2\cdot10\ H_2O$: C = 50.49, H = 4.74, N = 9.24; found C = 50.71, H = 4.85, N = 9.09.

-Synthesis of: [Mn$_2$L$_2$P1)](ClO$_4$)$_5$

12.7 mg (33 µmol) of $Mn(ClO_4)_2\cdot6H_2O$ and ligand 2-{[[di(2-pyridyl)methyl](methyl)amino]methyl}phenol (10.3 mg, 33 µmol), were dissolved under N_2 atmosphere in 2 mL of methanol and the solution was heated until its boiling point. Subsequently, P1 (16.2 mg, 16 µmol) was added. After all solids were dissolved, triethylamine was added (7.0 µL, 50 µmol). After stirring, a solid precipitated so the mixture was let cool down. The precipitate was filtered and thoroughly washed with cold methanol and with ether and finally dried under vacuum. Yield: 19.2 mg, 58 %.

UV-Vis (H_2O): λ_{max}/nm (ε/M^{-1} cm^{-1}) 257.0 ($6.8\cdot10^4$), 379.9 ($4.3\cdot10^4$), 401.9 ($4.6\cdot10^4$), 464.7 ($1.2\cdot10^5$) (Soret bands), 561.7 ($1.2\cdot10^4$) (Q band).

FT-IR (KBr): ν (cm^{-1}) 3120(w), 3079(w), 3055(w), 2976(w), 2952(w), 2881(w), 2858(w), 2808(w), 1640(s), 1599(m), 1568(w), 1541(w), 1479(m), 1451(m), 1402(w), 1373(w), 1345(w), 1280(w), 1144(m), 1108(s), 1090(s), 1011(m), 887(w), 868(w), 806(w), 787(w), 762(m), 628(m), 560(m), 527(m).

Elemental Analysis, calcd. for $C_{83}H_{69}Cl_5Mn_3N_{13}O_{24}$ • 6 H_2O: C = 47.87, H = 3.92, N = 8.74; found C = 47.63, H = 3.94, N = 8.82.

-Synthesis of: [Mn$_2$L$_2$P2]Cl$_2$(ClO$_4$)$_4$

21.6 mg (60 µmol) of $Mn(ClO_4)_2\cdot6H_2O$ and ligand 2-{[[di(2-pyridyl)methyl](methyl)amino]methyl}phenol (18.3 mg, 60 mmol), were dissolved in 2 mL of methanol and the solution was heated until its boiling point. Subsequently, P2 (40.0 mg, 30 µmol) was added. To completely dissolve the porphyrin, 1 ml of H_2O was added.

After all solids were dissolved, triethylamine was added (15 μL, 110 μmol). After 2 h, the solvent was removed under vacuum. The solid obtained was washed three times with small aliquots of water to remove the triethylammonium chloride formed during the reaction. Finally the product was dissolved in methanol, filtered and the solvent was removed under vacuum. Yield: 33.0 mg, 54 %.

UV-Vis (H_2O): λ_{max}/nm ($\varepsilon/M^{-1}\,cm^{-1}$) 257.6 ($6.3\cdot10^4$), 378.2 ($3.9\cdot10^4$), 399.6 ($3.9\cdot10^4$), 462.9 ($1.3\cdot10^5$) (Soret bands), 562.7 ($1.2\cdot10^4$) (Q band).

FT-IR (KBr): ν (cm^{-1}) 3117(w), 3091(w), 3059(w), 2977(w), 2923(w), 2854(w), 2810(w), 1640(s), 1599(s), 1570(w), 1560(w), 1478(s), 1454(m), 1445(m), 1289(m), 1275(m), 1095(vs), 1012(m), 887(w), 865(w), 806(w), 790(w), 762(m), 622(m), 561(w), 528(w).

Elemental Analysis, calcd for $C_{89}H_{75}Cl_6Mn_3N_{12}O_{22} \bullet 2H_2O$: C = 51.54, H = 3.84, N = 9.45; found C = 51.45, H = 3.52, N = 9.15.

-Synthesis of: Cu_2L_2

185 mg (0.5 mmol) of $Cu(ClO_4)_2\cdot6H_2O$ and ligand 2-{[[di(2-pyridyl)methyl](methyl)amino]methyl}phenol (150 mg, 0.5 mmol) were dissolved in 10 mL of methanol. After all solids were dissolved, an excess of triethylamine was added (15 μL, 1.0 mmol) and the solution turned dark green. After stirring, the formation of a green precipitate occurred. The solution was heated until boiling and gradually acetonitrile was added until complete dissolution of the solid. The solution was then let cool down. After a week green crystals were obtained, washed with methanol and ether and finally dried under vacuum. Yield: 153 mg, 56 %.

UV-Vis (H_2O): λ_{max}/nm ($\varepsilon/M^{-1}\,cm^{-1}$) 269 ($2.1\cdot10^4$), 410 ($1.0\cdot10^3$).

FT-IR (KBr): ν (cm^{-1}) 3089(w), 3024(w), 3005(w), 2926(w), 2906(w), 2867(w), 2855(w), 2819(w), 1614(m), 1603(m), 1598(sh), 1574(w), 1480(s), 1453(s), 1448(sh), 1426(w), 1292(m), 1264(m), 1246(m), 1234(m), 1093(s), 984(m), 893(m), 885(m), 781(m), 768(s), 758(s), 623(s), 554(w), 543(w).

ESI(+)-MS m/z calcd. for ($C_{38}H_{36}Cu_2N_6O_2^{2+}$+$HCOO^-$) (M+$HCOO^-$) 779.1, found 779.0 and ($C_{38}H_{36}Cu_2N_6O_2^{2+}$+$ClO_4^-$) (M+ ClO_4^-) 833.1, found 833.0.

Elemental Analysis, calcd. for $C_{38}H_{36}Cl_2Cu_2N_6O_{10}$: C = 48.83, H = 3.88, N = 8.99; found C = 48.65, H = 3.92, N = 8.85.

-Synthesis of: $Cu_2L^1_2$

75 mg (0.2 mmol) of $Cu(ClO_4)_2 \cdot 6H_2O$ and ligand 2-({[di(2-pyridyl)methyl]amino}methyl)phenol (60 mg, 0.2 mmol) were dissolved in 5 mL of ethanol. After all solids were dissolved, an excess of triethylamine was added (6 μL, 0.4 mmol) and the solution turned dark green. After stirring, the formation of a green precipitate occurred. The solution was heated until boiling and gradually DMF was added until complete dissolution of the solid. The solution was then let cool down. After a week green crystals were obtained, washed with methanol and ether and finally dried under vacuum. Yield: 50 mg, 55 %.

UV-Vis (H_2O): λ_{max}/nm (ε/M^{-1} cm^{-1}) 265.1 ($2.3 \cdot 10^4$), 397.4 ($3.6 \cdot 10^3$), 667.5 ($6.2 \cdot 10^2$).
FT-IR (KBr): ν (cm^{-1}) 3239(w), 3094(w), 3070(w), 3034(sh), 2925(w), 2870(w), 1680(sh), 1658(s), 1610(s), 1597(s), 1573(m), 1482(s), 1471(s), 1452(s), 1441(s), 1389(m), 1291(w), 1273(w), 1248(m), 1098(s), 1002(m), 928(w), 882(m), 868(w), 791(w), 778(m), 758(m), 699(w), 640(w), 625(m), 598(w), 551(w), 473 (w).
ESI(+)-MS m/z calcd. for ($C_{36}H_{32}Cu_2N_6O_2^{2+}$-$H^+$) (M-$H^+$) 705.1, found 705.0 ($C_{36}H_{32}Cu_2N_6O_2^{2+}$+$HCOO^-$) (M+$HCOO^-$) 751.1, found 751.0 and ($C_{36}H_{32}Cu_2N_6O_2^{2+}$+$ClO_4^-$) (M+ ClO_4^-) 805.1, found 805.0.
Elemental Analysis, calcd. for $C_{36}H_{32}Cl_2Cu_2N_6O_{10} \cdot$DMF: C = 47.81, H = 4.01, N = 10.01; found C = 47.62, H = 4.23, N = 10.24.

-Synthesis of: $Cu_2L^2_2$

68 mg (0.18 mmol) of $Cu(ClO_4)_2 \cdot 6H_2O$ and ligand 2-({[Di(2-pyridyl)methyl]amino}methyl)-4-nitrophenol (60 mg, 0.18 mmol) were dissolved in 5 mL of ethanol. After all solids were dissolved, an excess of triethylamine was added (6 μL, 0.4 mmol) and the solution turned dark green. After stirring, the formation of a green precipitate occurred. The solid was filtered and washed with ethanol and ether and finally dried under vacuum. Yield: 80 mg, 45 %.

UV-Vis (H_2O): λ_{max}/nm (ε/M^{-1} cm^{-1}) 255.9 ($2.1 \cdot 10^4$), 375.8 ($2.3 \cdot 10^3$), 652.1 ($2.4 \cdot 10^2$).
FT-IR (KBr): ν (cm^{-1}) 3228(w), 3089(w), 2971(w), 2921(w), 1599(s), 1575(m), 1504(sh), 1478(s), 1442(m), 1332(s), 1297(s), 1263(s), 1119(sh), 1096(s), 1056(m), 1006(w), 934(w), 903(w), 840(w), 789(w), 760(w), 652(w), 624(m), 559(w), 467(w).

ESI(+)-MS m/z calcd. for $(C_{36}H_{31}Cu_2N_7O_4^{2+}+HCO_2^-)$ $(M+HCO_2^-)$ 841.1, found 841.1 and $(C_{36}H_{31}Cu_2N_7O_4^{2+}+ClO_4^-)$ $(M+ ClO_4^-)$ 895.1, found 895.0.
Elemental Analysis, calcd. for $C_{36}H_{31}Cl_2Cu_2N_7O_{12}$: C = 43.38, H = 3.03, N = 11.24; found C = 43.09, H = 3.16, N = 10.92.

-Synthesis of: $FeL(Cl)_2$

27 mg (0.1 mmol) of $FeCl_3 \cdot 6H_2O$ and ligand 2-{[[Di(2-pyridyl)methyl](methyl)amino]methyl}phenol (30 mg, 0.1 mmol) were dissolved in 5 mL of methanol. After all solids were dissolved, an excess of triethylamine was added (3 µL, 0.2 mmol) and the solution turned dark blue. After stirring, the formation of a blue precipitate occurred. The solution was heated until boiling and gradually acetonitrile was added until complete dissolution of the solid. The solution was then let cool down. The dark blue crystals obtained upon ether addition were washed with methanol and ether and finally dried under vacuum. Yield: 22 mg, 51 %.

UV-Vis (CH_3CN): λ_{max}/nm ($\varepsilon/M^{-1}\,cm^{-1}$) 261.7 ($1.3\cdot10^4$), 357.8 ($7.0\cdot10^3$), 580.0 ($1.7\cdot10^3$).
FT-IR (KBr): ν (cm^{-1}) 3105(w), 3064(w), 3052(w), 3029(w), 2940(w), 2920(w), 2906(w), 2883(w), 2849(w), 2810(w), 1604(s), 1600(s), 1569(m), 1477(s), 1454(s), 1445(s), 1420(m), 1335(w), 1284(s), 1270(s), 1246(s), 1237(m), 1156(w), 1107(w), 1022(w), 987(w), 889(m), 788(m), 781(m), 765(m), 748(m), 633(m), 558(m), 512(m).
ESI(+)-MS m/z calcd. for $(C_{38}H_{36}Fe_2N_6O_3^{2+}+HCOO^-)$ $(M+HCOO^-)$ 781.1, found 781.0 and $(C_{38}H_{36}Fe_2N_6O_3^{2+}+ClO_4^-)$ $(M+ ClO_4^-)$ 835.1, found 835.0.

-Synthesis of: $Fe_2(L)_2(OH)(H_2O)_2$

45 mg (0.1 mmol) of $Fe(ClO_4)\cdot xH_2O$ and ligand 2-{[[di(2-pyridyl)methyl](methyl)amino]methyl}phenol (30 mg, 0.1 mmol) were dissolved in 5 mL of methanol. After all solids were dissolved, an excess of triethylamine was added (3 µL, 0.2 mmol) and the solution turned dark blue. After stirring, the formation of a blue precipitate occurred. The solution was heated until boiling and gradually acetonitrile was added until complete dissolution of the solid. The solution was then let cool down. The dark blue crystals obtained upon ether addition were washed with methanol and ether and finally dried under vacuum. Yield: 29 mg, 55 %.

UV-Vis (CH_3CN): λ_{max}/nm ($\varepsilon/M^{-1}\,cm^{-1}$) 258.3 ($2.6\cdot10^4$), 345.4 ($7.4\cdot10^3$), 604.2 ($3.4\cdot10^3$)

FT-IR (KBr): ν (cm^{-1}) 3101(w), 3083(w), 3061(w), 3014(w), 2987(w), 2927(w), 2866(w), 2814(w), 1608(s), 1598(m), 1541(s), 1478(s), 1455(s), 1450(s), 1420(w), 1270(s), 1107(s), 1022(m), 982(w), 887(m), 789(m), 779(m), 765(s), 649(w), 635(m), 624(m), 560(w), 525(w), 493(w).

ESI(+)-MS m/z calcd. for ($C_{38}H_{36}Fe_2N_6O_3^{2+}$+$HCOO^-$) (M+$HCOO^-$) 781.1, found 781.0 and ($C_{38}H_{36}Fe_2N_6O_3^{2+}$+$ClO_4^-$) (M+ ClO_4^-) 835.1, found 835.0.

Elemental Analysis, calcd. for $C_{38}H_{36}Cl_2Fe_2N_6O_{11}\cdot 3H_2O$: C = 46.13, H = 4.28, N = 8.49; found C = 46.04, H = 4.31, N = 8.16.

-Synthesis of: Co_2L_2Ac

37 mg (0.1 mmol) of $Co(ClO_4)_2\cdot 6H_2O$ and ligand 2-{[[Di(2-pyridyl)methyl](methyl)amino]methyl}phenol (30 mg, 0.1 mmol) were dissolved in 5 mL of methanol. Subsequently, acetic acid (5 µL, 0.1 mmol) was added. After all solids were dissolved, triethylamine was added (4 µL, 0.3 mmol) and the solution turned pale pink. After stirring for 1 h, the formation of a precipitate occurred. The solution was heated until boiling and gradually acetonitrile was added until complete dissolution of the solid. The solution was then let cool down. After a week dark pink crystals were obtained, washed with methanol and ether and finally dried under vacuum. Yield: 26 mg, 60 %.

UV-Vis (CH_3CN): λ_{max}/nm (ε/M^{-1} cm^{-1}) 245.5 nm ($2.4\cdot 10^4$), 265.8 ($1.6\cdot 10^4$), 289.9 ($8.4\cdot 10^3$).

FT-IR (KBr): ν (cm^{-1}) 3064(w), 3029(w), 3004(w), 2977(w), 2923(w), 2891(w), 2852(w), 2813(w), 1602(s), 1572(s), 1480(s), 1447 (s), 1424(m), 1448(s), 1289(s), 1276(m), 1107(s), 1089(s), 1018(w), 994(w), 889(m), 789(w), 764(m), 729(w), 684(w), 666 (w), 624(m), 572(w), 544(w).

ESI(+)-MS m/z calcd. for $C_{40}H_{38}N_6O_4Co_2^+$ (M) 785.2, found 785.1.

-Synthesis of: Co_2L_2

37 mg (0.1 mmol) of $Co(ClO_4)_2\cdot 6H_2O$ and ligand 2-{[[di(2-pyridyl)methyl](methyl)amino]methyl}phenol (30 mg, 0.1 mmol) were dissolved in 5 mL of methanol. After all solids were dissolved, triethylamine was added (4 µL, 0.3 mmol) and the solution turned pale pink. After stirring for 1 h, the formation of a precipitate occurred. The solution was heated until boiling and gradually acetonitrile was added until complete dissolution of the solid. The solution was then let cool down. After a week dark

pink crystals were obtained, washed with methanol and ether and finally dried under vacuum. Yield: 23 mg, 50 %.

UV-Vis (CH_3CN): λ_{max}/nm ($\varepsilon/M^{-1}\ cm^{-1}$) 242.3 nm ($2.0\cdot10^4$), 266.6 ($1.6\cdot10^4$), 290.3 ($8.9\cdot10^3$).

FT-IR (KBr): ν (cm^{-1}) 3066(w), 3033(w), 3017(w), 2982(w), 2920(w), 2894(w), 2852(w), 2811(w), 1606(s), 1602(s), 1573(m), 1484(s), 1470 (m), 1455(s), 1448(s), 1422(w), 1291(m), 1272(m), 1018(w), 994(w), 888(m), 791(w), 767(m), 756(m), 737 (w), 684(w), 624 (m), 580(w), 542(w).

ESI(+)-MS m/z calcd. for ($C_{38}H_{36}N_6O_4Co_2^+$ + HCOO)(M+HCOO) 771.2, found 771.3 and for (M+ClO_4) 825.1, found 825.2.

-Synthesis of: $K_8[\beta_2\text{-}SiW_{11}O_{39}]$

$$11WO_4^{2-} + SiO_3^{2-} + 16H^+ + 8K^+ + 6H_2O \longrightarrow K_8[\beta_2\text{-}SiW_{11}O_{39}]\cdot14H_2O$$

Sodium metasilicate (3.0g, 24,7mmol) was dissolved in 50 ml of water. In a separated becher sodium tungstate dihydrate (90.9g, 0.276 mol) was dissolved in about 150 ml of water and immersed in an ice/water bath at 5°C. To this solution 40 ml of 4.1 M HCl (0.16mmol) were added dropwise in about 40 minutes under vigorous stirring, in order to dissolve tungstic acid. When the solution returned to room temperature, metasilicate solution was added and pH was adjusted at 5.5 with 4.1 M HCl. The pH was maintained by small addition of 4.1 M HCl for 100 minutes than solid KCl (44.2g, 0.6mol) was added. After 15 minutes of stirring the white precipitate was collected by filtration through a sintered glass filter. Product was dissolved in 420 ml of water filtered and precipitated again with KCl (39.4g, 0.5mol), filtered and washed with 2 M KCl solution (15ml x 2) and dried under vacuum. Yield: 34.0g (11.4mmol, 46%)

FT-IR (KBr, cm^{-1}): 3423 (s, br), 1611 (s), 991 (s), 947 (s), 878 (s), 809 (s), 713 (s), 535 (m).

-Synthesis of: $K_8[\gamma\text{-}SiW_{10}O_{36}]$

$$K_8[\beta_2\text{-}SiW_{11}O_{39}] + 2CO_3^{2-} + 13H_2O \xrightarrow{\text{pH 9.1}} K_8[\gamma\text{-}SiW_{10}O_{36}]\cdot12H_2O + 2HCO_3^- + WO_4^{2-}$$

This synthesis required an accurate control of the pH.

The fresh prepared potassium salt $K_8[\beta\text{-}SiW_{10}O_{36}]$ (34.0 g, 11.4mmol) was dissolved in 530 ml of water and filtered to eliminate impurities. The pH of the solution was quickly adjusted to 9.1 by addition of 2 M aqueous K_2CO_3 solution and kept stable for 15 minutes. KCl (91.0g, 1.2mol) was then added to precipitate the potassium salt of γ-decatungstate. Solution was stirred for 10 minutes maintaining the pH at 9.1 by addition K_2CO_3 solution. The solid was filtered, washed with 1 M KCl solution and dried under vacuum.
Yield: 20.0g (7.6mmol, 66%)
FTIR (KBr, cm^{-1}): 3461 (s, br), 1635 (m), 989 (m), 942 (s), 863 (s), 813 (s), 742 (s), 658 (m), 532 (w).

-Synthesis of: $Na_{10}[Ru_4(\mu\text{-}O_4)(\mu\text{-}OH)_2(H_2O)_4(\gamma\text{-}SiW_{10}O_{36})_2]$

$$2[\gamma\text{-}SiW_{10}O_{36}]^{8-} + 4RuCl_3{\cdot}xH_2O \xrightarrow{70°C} [Ru_4(\mu\text{-}O)_4(\mu\text{-}OH)_2(H_2O)_4(\gamma\text{-}SiW_{10}O_{36})_2]^{10-}$$

In a round bottom flask, $K_8[\gamma\text{-}SiW_{10}O_{36}]{\cdot}12H_2O$ (1.0 g, 0.38 mmol) was dissolved in 16 ml of water, then $RuCl_3{\cdot}xH_2O$ (0.153 g, 0.74 mmol) was added and solution was heated at 70° C for 1 hour (pH drop to 1.6). After cooling excess of CsCl (4.4 g, 25 mmol) was added to precipitate the cesium salt. Product was recovered by centrifugation and washed three time with cold water, then it was dissolved in about 100 ml of water to prepare the sodium salt after cation exchange by eluting it through a cation exchange resin, charged with Na^+. Solvent was evaporated under reduced pressure and the black solid was dissolved in 5ml of water. Product was purified on a size exclusion column charged with Sephadex-G50® resin (10 g). Solvent was evaporated and the purified sodium salt was obtained as a black solid. Yield: 0.8 g (0.28 mmol, 74%).

FT-IR (KBr, cm^{-1}): 3434 (s, br), 2923 (w), 2853 (w), 1622 (m), 1044 (w), 999 (w), 950 (s), 876 (s), 804 (s), 539 (w).
UV-Vis (H_2O) λ_{max}/nm ($\varepsilon/M^{-1}\,cm^{-1}$): 278 ($6.96{\cdot}10^4$), 453 ($1.91{\cdot}10^4$).

-Synthesis of: $DODA_{10}/(Ru_4(SiW_{10})_2$

$DODA_{10}/(Ru_4(SiW_{10})_2$ was synthesized from a biphasic system consisting in DODACl (10 eq) in $CHCl_3$ and $Ru_4(SiW_{10})_2$ (1 eq) in water. The two phases were stirred overnight and the SEP, soluble in the organic phase, was obtained upon solvent removal under vacuum with a yield of 93%.

FT-IR (KBr): ν = 2966 (sh), 2925 (s), 2853 (s), 1467 (m), 1381 (w), 1043 (w), 1001 (m), 950 (m), 919 (sh), 876 (s), 812 (s), 766 (s), 543 (w).
^{1}H-NMR (300 MHz, $CDCl_3$, δ): 3.43 (10H, m), 1.60 (4H, s), 1.26 (60H, s), 0.88 (6H, t). Elemental Analysis, calculated for $C_{38}H_{802}N_{10}O_{78}Ru_4W_{20}Si_2$: C = 42.0%, H = 7.5%, N = 1.5%; found C = 42.43%, H = 7.72%, N = 1.39%.

-Preparation of: PEEK WC membrane

PEEK-WC **2** membrane was prepared from a casting solution made of 10 wt% of PEEK-WC, 4 wt% of 1,4-butanediol, 6 wt% of *i*-propanol, and 0.5 wt% of $DODA_{10}/Ru_4(SiW_{10})_2$ in $CHCl_3$, at room temperature. The blend obtained was let under vigorous stirring for 24 h. The dark solution was then casted on a glass plate with a casting knife of 0.45 mm in glovebox under controlled atmosphere (relative humidity 75%). The membrane characterization was then performed by environmental scanning electron microscopy (ESEM), TGA analysis, and EDX. PEEK-WC **1** membrane was prepared by standard evaporation casting technique.

7.4 Methods

-X-Ray Diffraction Analysis

Crystals of compounds were analyzed by single-crystal X-ray diffraction. Data collection was carried out at the Elettra synchrotron (Trieste, Italy), by using cryo-cooling techniques. Diffraction images were integrated by using the software MOSFLM and scaled by AIMLESS.[288–290] The crystal structure was solved in the $P3_1$ space group by Direct Methods with the SIR2014 software and refined with SHELX-13.[291,292] Thermal parameters of all non-hydrogen atoms were refined anisotropically and hydrogen atoms were placed at the geometrically calculated positions and refined using the riding model.

-FT-IR analysis

FT-IR of KBr pellets were recorded on a Nicolet 5700 FT-IR instrument and FT-IR of thin solutions film were recorded on a Nicolet Nexus 670 using a cell with CaF_2 windows and an optical path of 0.05-1 mm, resolution 2 cm^{-1}, 25 scans. Deuterated solvents were employed to not interfere with the analytes peaks. The residual solvent signals were removed by solvent background subtraction.

-Cyclic Voltammetry

Cyclic voltammetry experiments were performed using a BAS Cell C3 EC-epsilon potentiostat. A standard three-electrode electrochemical cell was used. Glassy carbon electrode (3 mm diameter, geometric surface area = 7 mm^2) from BAS and a Pt wire were used respectively as working and auxiliary electrode. Potentials were referred to an Ag/AgCl/(3 M NaCl) reference electrode. Prior to each experiment, the electrode was polished with 1 μm alumina, rinsed with deionised water and wiped with a paper tissue.

-ESI-MS analysis

ESI-MS measurements were carried out by using an Agilent Technologies MSD SL Trap mass spectrometer with ESI source. Sample solutions in acetonitrile or water were injected into the ion source without the addition of any other solvent at a flow rate of 50 μL/min. For electrospray ionization, the drying gas (nitrogen) was heated at 325 °C. Each species is indicated with the m/z value of the first peak of its isotopic cluster. The peaks in ESI-MS spectra were assigned by comparing the experimental isotopic patterns with the corresponding simulated profiles.

-Hydrogen peroxide dismutation

Screening of the catalase activity was performed according to the following protocol: to a solution of H_2O_2 in BBS 50 mM (pH=7.8) or Krebs-Henseleit (KH) buffer (pH=7.4) (12 ml), 300 μL of a 2-8 mM solution of the selected complex was added with a syringe to start the dismutation reaction. The reactor was maintained at 25 °C by a circulating thermostat, and the progress of reaction was determined by monitoring the pressure developed by molecular oxygen generated from dismutation of hydrogen peroxide into a closed vessel. The amount of O_2 was determined by continuous detection of pressure variation, through a pressure transducer. Initial rates were calculated by linear regression of data within 10 % H_2O_2 conversion. Kinetic runs were performed in triplicate. Control experiments performed without the catalyst, confirmed that no oxygen evolution is detected from the buffer solution in presence of H_2O_2.[135]

-SOD test

Screening of catalysts as SOD-mimicking systems was performed by spectrophotometric analysis of the inhibition of the superoxide-dependent reduction of the cyt c chromophore to ferricytochrome. The superoxide radical anions were generated by the xanthine/xanthine oxidase system. In all experiments, the reaction mixture was prepared with 40 μM

xanthine, 10 μM cyt c, catalase 15 μg/ml, 50 mM phosphate buffer (pH=7.80) and xanthine oxidase 0.0053 U/ml.

Catalyst solutions were prepared upon dilution of a stock solution in water. Possible interference through inhibition of the xanthine/xanthine oxidase reaction by test compounds was examined by following the rate of urate accumulation at 295 nm in the absence of cyt c. The concentration of the stock catalyst solutions was chosen in order to obtain approximately an inhibition interval of the superoxide-dependent reduction of the cyt c between 30-60 %. The inhibition (%) is given by the ration v/v_0, where v_0 is the rate of cyt c reduction without catalyst and v in presence of it. Catalyst solutions were prepared upon dilution of a stock solution in water.

Since IC_{50} values are dependent upon the screening/detection conditions, apparent kinetic rates were calculated by the equation proposed by McCord and Fridovich with $k_{cyt\ c}$= 2.6 x 10^5 $M^{-1}s^{-1}$. The following equation was used for the calculated values of $k_{cat}(O_2^{\bullet-})$:

$$k_{cat}(O_2^{\bullet-}) = k_{cyt\ c} \cdot [\text{cyt c}] / IC_{50}$$

-Michealis-Menten Analysis

To evaluate the Michaelis-Menten parameters, 60 μL of 2 mM solution of catalyst were added to degassed solution of BBS 50 mM (pH=7.8) (12 ml) at different H_2O_2 concentration (0.1-10 mM). The reactor was maintained at 25 °C by a circulating thermostat, and the progress of reaction was determined by monitoring the dissolved oxygen concentration into a closed vessel with a Clark electrode. Initial rates were calculated by linear regression of data within 10 % H_2O_2 conversion. Kinetic runs were performed in triplicate. The initial rates vs substrate concentration were fitted by non-linear curve fit with the Michaelis-Menten equation to determine k_{cat} and K_M.

-Bleaching stability test

The bleaching stability of the porphyrin residue was tested using a commercial tetracationic porphyrin, meso-tetra(N-methyl-4-pyridyl)porphine upon Mn metallation, (Mn(III)-TM-4-PyP^{5+}). Kinetics of the porphyrin degradation were obtained by UV-Vis monitoring of the Soret absorbance (λ_{max}=463 nm, ε = 128825), upon incubation of Mn(III)-TM-4-PyP^{5+} (10 μM, phosphate buffer 50 mM, pH=7.8) with 50-500 H_2O_2 μM (5, 10, 20 or 50 equivalents).[87,111] The porphyrin concentration was estimated from the Lambert-Beer law. Analog experiments were conducted with the $Mn_2L_2P2^{6+}$ di-zyme (10

μM) in phosphate buffer (50 mM, pH=7.8). Pseudo-first-order linear plots of experimental rate constants vs [H_2O_2] were obtained.[87]

- DNA interaction

The test was conducted using calf-thymus DNA (CT-DNA). A stock solution of CT-DNA was prepared dissolving in phosphate buffer by gentle stirring overnight (pH 7.8, 1mM EDTA, stored at 4°C) the DNA. The CT-DNA concentration was obtained from its absorption intensity at 260 nm (ε=1.31·$M^{-1}cm^{-1}$ in base pairs).[89] The ratio from the UV absorbance at 260 and 280 nm, A_{260}/A_{280}>2.0, indicated that the DNA was sufficiently free from proteins.[293] All experiments were run in the phosphate buffer at pH 6.8. The buffer consisted of 10 mM phosphate, 1 mM EDTA and NaCl to obtain ionic strength μ=0.2 M, dissolved in the Milli-Q quality water. The experiments were performed at 25° C by adding to H_2TM-4-PyP^{4+} (DNA intercalator), Mn(III)-TM-4-PyP^{5+} (non-intercalator) or $Mn_2L_2P2^{6+}$ solutions (4-6 μM) aliquots of few microliters of CT-DNA solution.[89]

- In vivo test on H_2O_2 accumulation in Chlamydomonas reinhardtii

The strains used in this study is a wild type and the cell wall deficient strain, $cw15^-$, both derived from the wild-type 137c strain of the green algae Chlamydomonas reinhardtii. Cells were routinely grown at 25°C in a Tris-acetate phosphate medium (TAP) with 50 μmol photons m^{-2} sec^{-1} illumination. Wt and $cw15^-$ strains were incubated with both molecules (Mn_2L_2P2, Mn_2L_2Ac) in different concentrations to assess the cytotoxicity of molecules. Concentrations with no effects on growth when then used for further analyses (0.5 μM for Mn_2L_2Ac and 0.1 μM for Mn_2L_2P2 and P2) and the $cw15^-$ strains used for further analysis. Equal amounts of cells were incubated in presence / absence of Mn_2L_2P2, Mn_2L_2Ac for 48 hours in TAP medium. They were later harvested, washed and incubated in with medium containing 5 mM 3,3-diaminobenzidine-HCl and exposed to strong illumination 800 μE m^{-2} sec^{-1} for 1 hour. Following staining and light treatments, pigments were extracted from the cells using methanol. Oxidized 3,3-diaminobenzidine in reaction with H_2O_2 is a color brown compound that was assessed quantitatively by spectrometric measurement at 465 nm.[294,295]

- Pro-oxidant activity test

Pro-oxidant activity of the complexes was measured by following the oxidative degradation of morin in the presence of hydrogen peroxide by UV-Vis spectroscopy.[186] The reactions were carried out in borate buffer (50 mM, pH 7.8) at 25°C over a period of 3

hours. A freshly prepared morin solution (30 mM) in DMSO was diluted in BBS to obtain a morin solution of 0.12 mM in all the experiments. To this mixture, a stock catalyst solution (1 mM) was added in order to obtain the desired catalyst concentration (50 μM). Finally, a commercial H_2O_2 stock solution (30% w/w) was added to get a concentration between 10-30 mM. The change in the absorption maximum of morin at 390 nm was monitored at intervals of 10 min, to evaluate the peroxidase-like activity of the complexes. Considering the excess of hydrogen peroxide employed in the experiments we can extrapolate a pseudo first order kinetic constant k_{obs}, where $v = k_{app}\cdot[\text{morin}]$. The value of k_{obs} was obtained by linear regression of the initials rate of morin degradation at different hydrogen peroxide concentrations (10-30 mM). Second-order rate constant was determined from linear regression of the observed pseudo-first-order rate constants vs $[H_2O_2]$.

- Oxygen evolution from membrane

A reactor with a differential pressure transducer was employed. The membranes were cut in the shape of disks with a diameter of 22 mm and fixed on the reactor bottom by using a circular gasket. In the reactor, 12 mL of 0.1 M H_2O_2 were added and the variation of pressure was monitored for 24 h keeping constant the temperature at 25 °C.

- Measurement of self cleaning ability

The membrane was incubated with a water solution containing fluorescent beads, at different concentration (0.2 and 0.3 mg mL^{-1}). After solvent evaporation, membrane fouling was verified by surface analysis using a laser scanning confocal microscope (Olympus BX51WI-FV300, λ exc = 488 nm, λ em ≥ 510 nm). Cleaning protocols had been initially attempted through washing cycles with water, including a 24 h immersion in water. The membrane was examined again with CFM and the images, recorded before and after the cleaning protocols, were compared to quantify the removal of the fouling beads. Effective removal of the fluorescent beads was obtained after a 24 h immersion in aqueous H_2O_2 (2.0 M).

- Determination of coverage area

CFM images were elaborated with the image processing program ImageJ for statistically comparing fluorescence spots distributions and intensity. All the images were processed and the results were averaged to obtain the values reported for the self-cleaning tests.

8. Appendix

UV-Vis Spectra

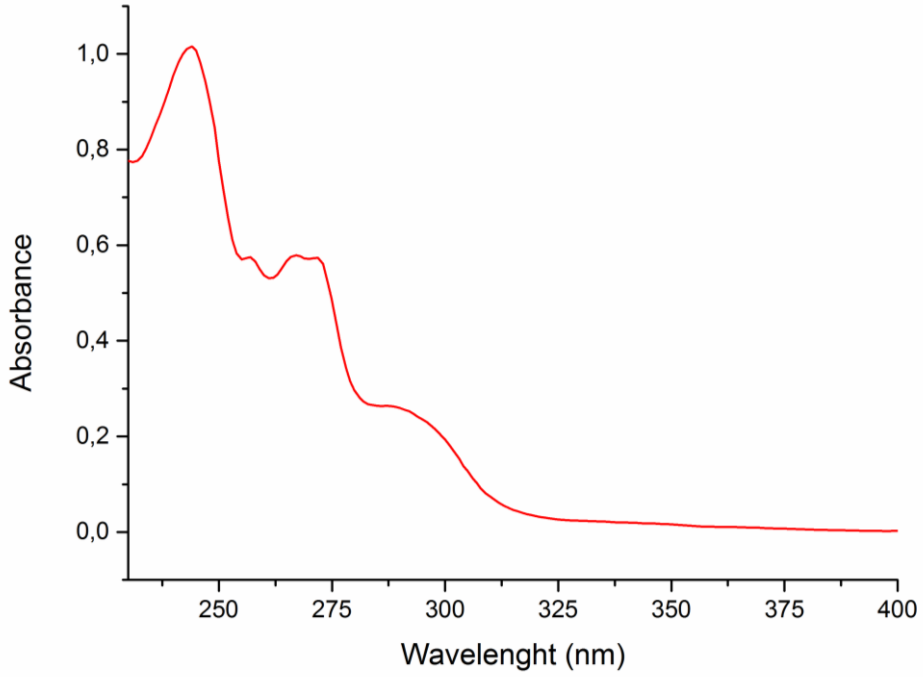

Figure 105. UV-Vis spectrum of $\mathbf{Mn_2L_2Ac}^+$ (10 μM) in acetonitrile, λ_{max}/nm (ε/M^{-1} cm^{-1}) 243.8 ($3.2\cdot10^4$), 256.7 ($2.0\cdot10^4$), 267.0 ($2.1\cdot10^4$) and 271.5 ($2.1\cdot10^4$).

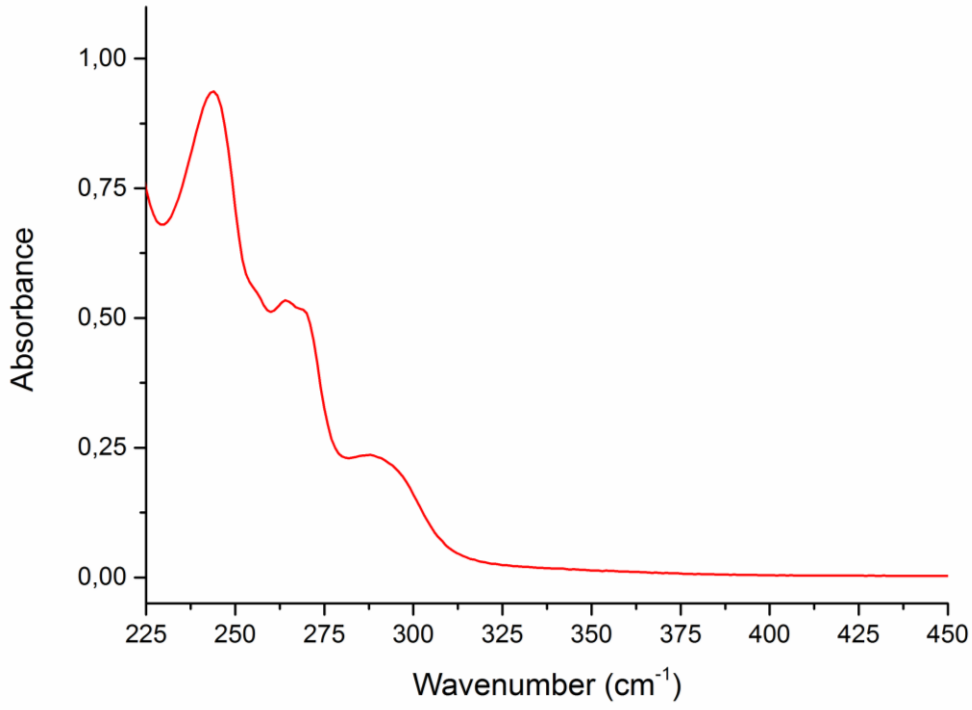

Figure 106. UV-Vis spectrum of $\mathbf{Mn_2L^1{}_2Ac}^+$ (10 μM) in acetonitrile, λ_{max}/nm (ε/M^{-1} cm^{-1}) 243.9 ($2.7\cdot10^4$), 264.2 ($1.5\cdot10^4$), 269.1 ($1.5\cdot10^4$) and 287.9 ($6.7\cdot10^3$).

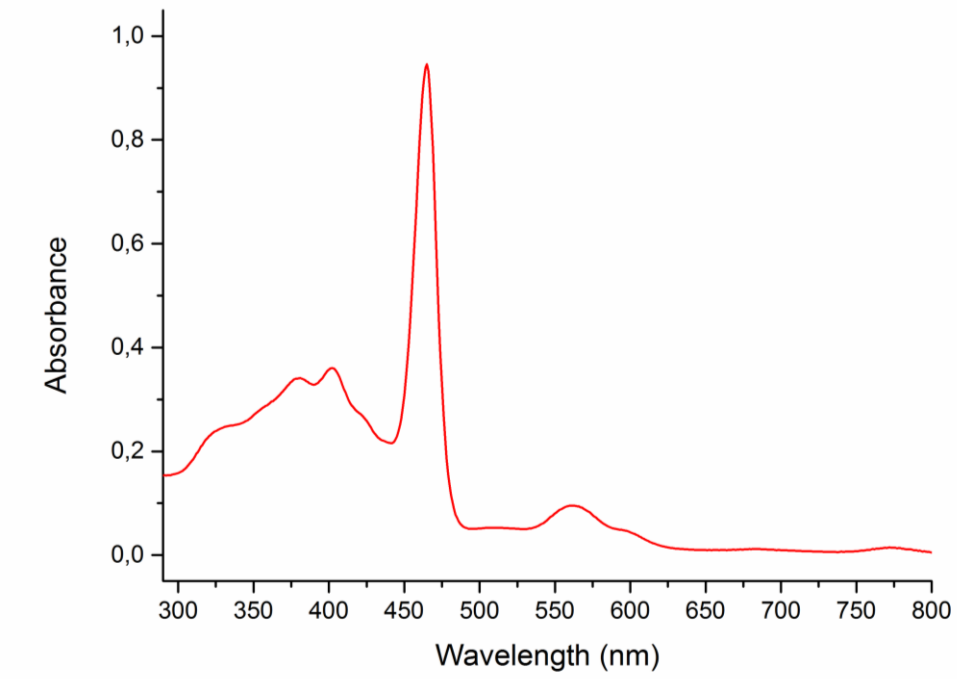

Figure 107. UV-Vis spectrum of Mn(III)-meso-tri(N-methyl-4-pyridyl)mono(4-carboxyphenyl)porphine tetrachloride (P1, 8 μM) in phosphate buffer 50 mM pH = 7.8, λ_{max}/nm (ε/M^{-1} cm^{-1}) 379.7 ($4.3 \cdot 10^4$), 402.1 ($4.6 \cdot 10^4$), 464.9 ($1.2 \cdot 10^5$) (Soret bands), 561.9 ($1.2 \cdot 10^4$) (Q band).

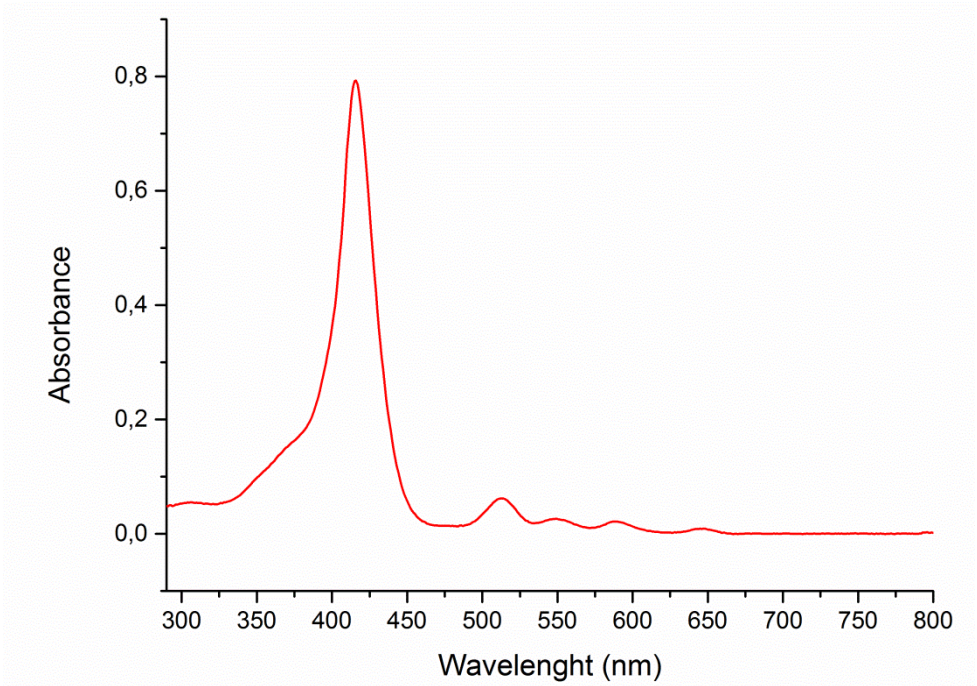

Figure 108. UV-Vis spectrum of meso-tri(4-pyridyl)mono(N-4-methoxyformylbenzyl-4-pyridyl)porphine (5 μM) in methanol, λ_{max}/nm (ε/M^{-1} cm^{-1}) 415.4 ($1.6 \cdot 10^5$) (Soret band); 512.9 ($1.2 \cdot 10^4$), 550.2 ($5.3 \cdot 10^3$), 588.9 ($4.3 \cdot 10^3$), 645.9 ($1.8 \cdot 10^3$) (Q bands).

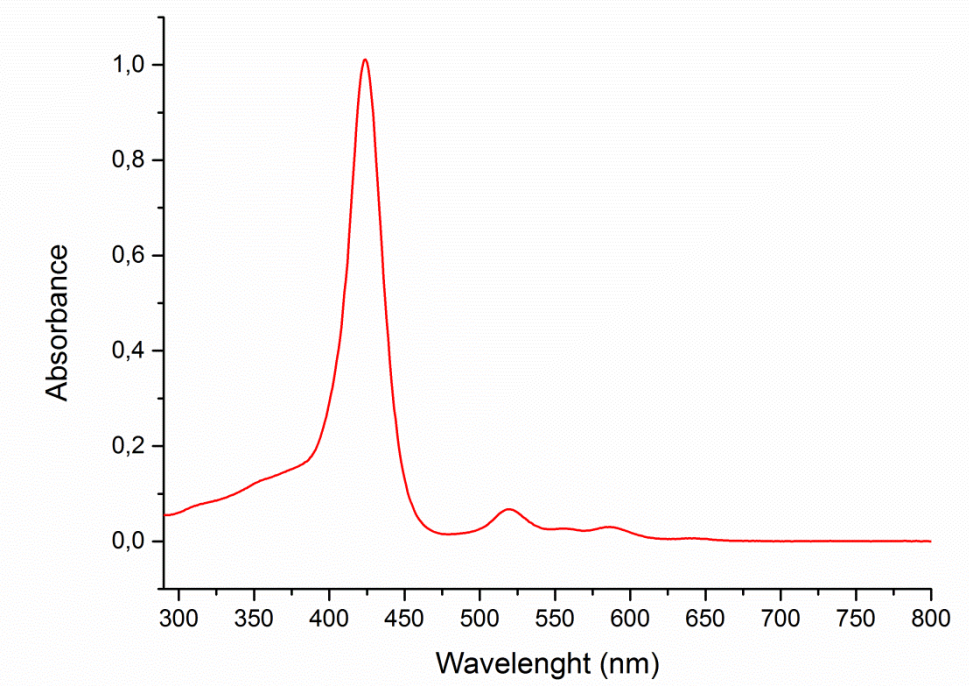

Figure 109. UV-Vis spectrum of meso-tri(N-methyl-4-pyridyl)mono(N-4-methoxyformylbenzyl-4-pyridyl)porphine (5 μM) in phosphate buffer 50 mM pH = 7.8, λ_{max}/nm (ε/M^{-1} cm^{-1}) 423.8 ($2.0 \cdot 10^5$) (Soret band), 519.6 ($1.3 \cdot 10^4$), 555.8 ($5.4 \cdot 10^3$), 585.5 ($6.0 \cdot 10^3$), 639.6 ($1.3 \cdot 10^3$) (Q bands).

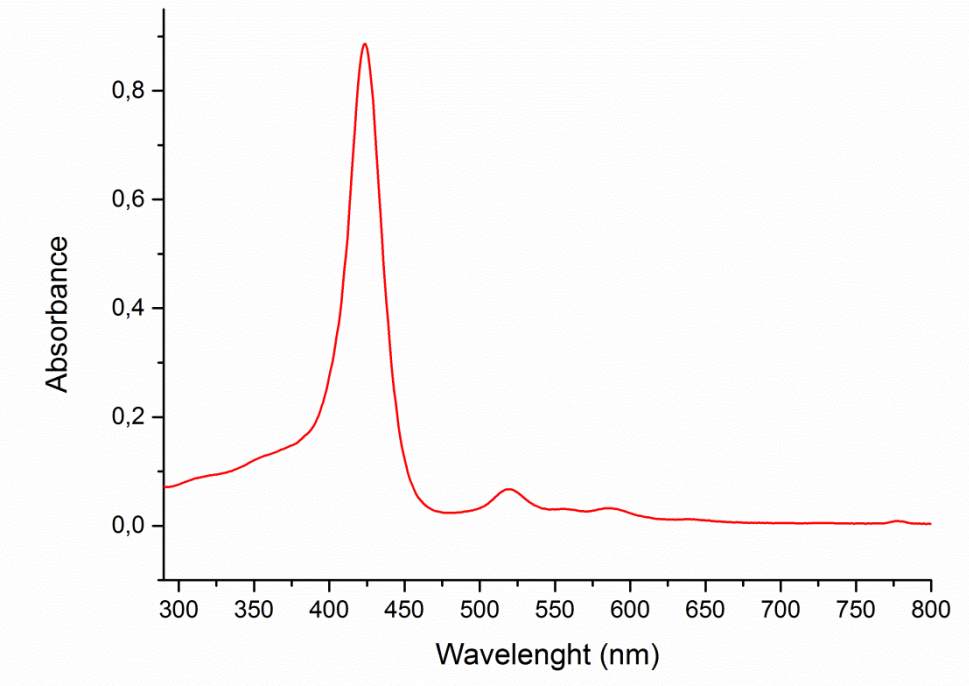

Figure 110. UV-Vis spectrum of meso-tri(N-methyl-4-pyridyl)mono(N-4-carboxybenzyl-4-pyridyl)porphine (5 μM) in phosphate buffer 50 mM pH = 7.8, λ_{max} /nm (ε/M^{-1} cm^{-1}) 423.8 ($1.8 \cdot 10^5$) (Soret band); 519.6 ($1.3 \cdot 10^4$), 555.8 ($6.2 \cdot 10^3$), 585.5 ($6.4 \cdot 10^3$), 639.6 ($2.4 \cdot 10^3$) (Q bands).

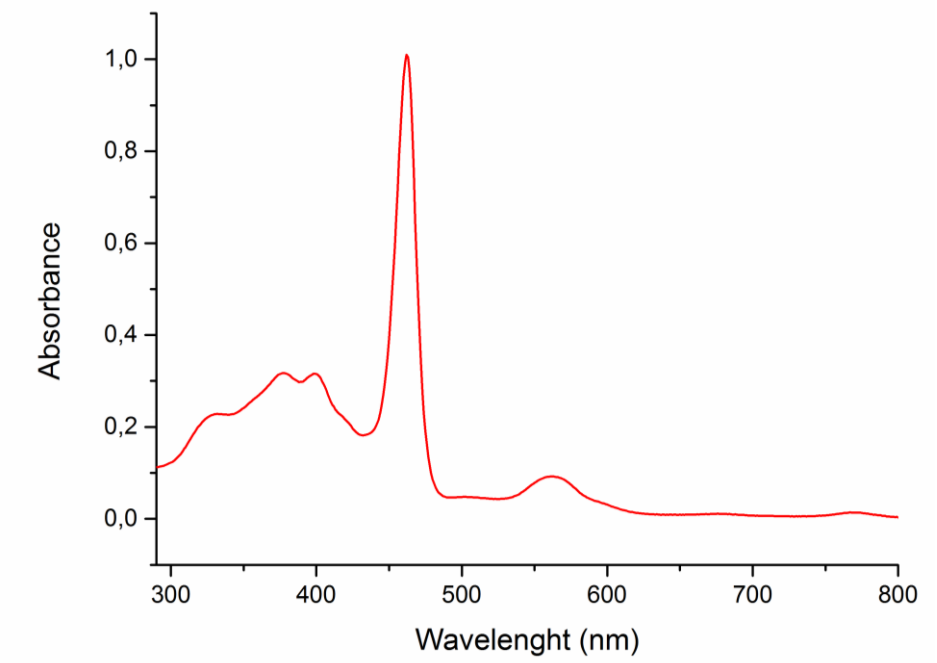

Figure 111. UV-Vis spectrum of Mn(III)-meso-tri(N-methyl-4-pyridyl)mono(N-4-carboxybenzyl-4-pyridyl)porphine (**P2**, 8 μM) in phosphate buffer 50 mM pH = 7.8, λ_{max}/nm (ε/M^{-1} cm^{-1}) 377.3 ($4.0 \cdot 10^4$), 398.9 ($4.1 \cdot 10^4$), 462.5 ($1.3 \cdot 10^5$) (Soret bands), 563.0 ($1.2 \cdot 10^4$) (Q band).

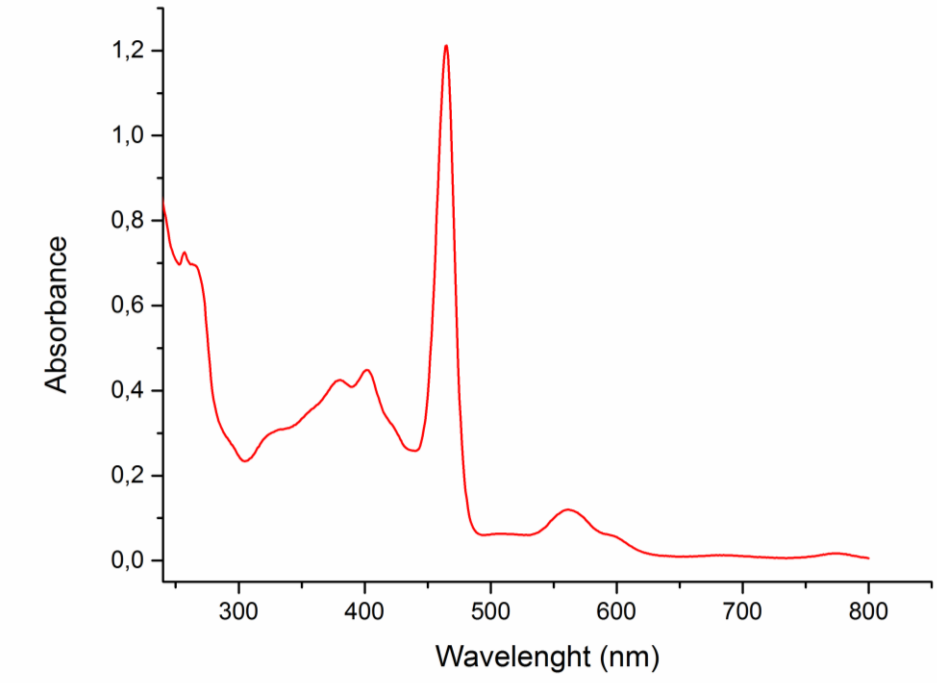

Figure 112. UV-Vis spectrum of $\mathbf{Mn_2L_2P1^{5+}}$ (10 μM) in phosphate buffer 50 mM pH = 7.8, λ_{max}/nm (ε/M^{-1} cm^{-1}) 257.0 ($6.8 \cdot 10^4$), 379.9 ($4.3 \cdot 10^4$), 401.9 ($4.6 \cdot 10^4$), 464.7 ($1.2 \cdot 10^5$) (Soret bands), 561.7 ($1.2 \cdot 10^4$) (Q band).

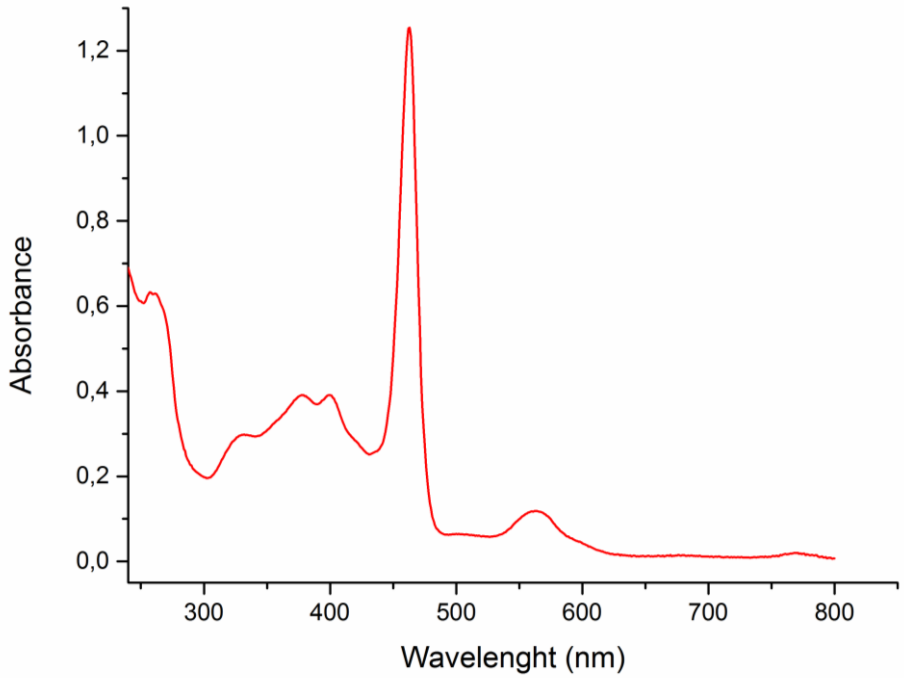

Figure 113. UV-Vis spectrum of $\mathbf{Mn_2L_2P2}^{6+}$ (10 μM) in phosphate buffer 50 mM pH = 7.8, λ_{max}/nm (ε/M^{-1} cm^{-1}) 257.6 ($6.3\cdot10^4$), 378.2 ($3.9\cdot10^4$), 399.6 ($3.9\cdot10^4$), 462.9 ($1.3\cdot10^5$) (Soret bands), 562.7 ($1.2\cdot10^4$) (Q band).

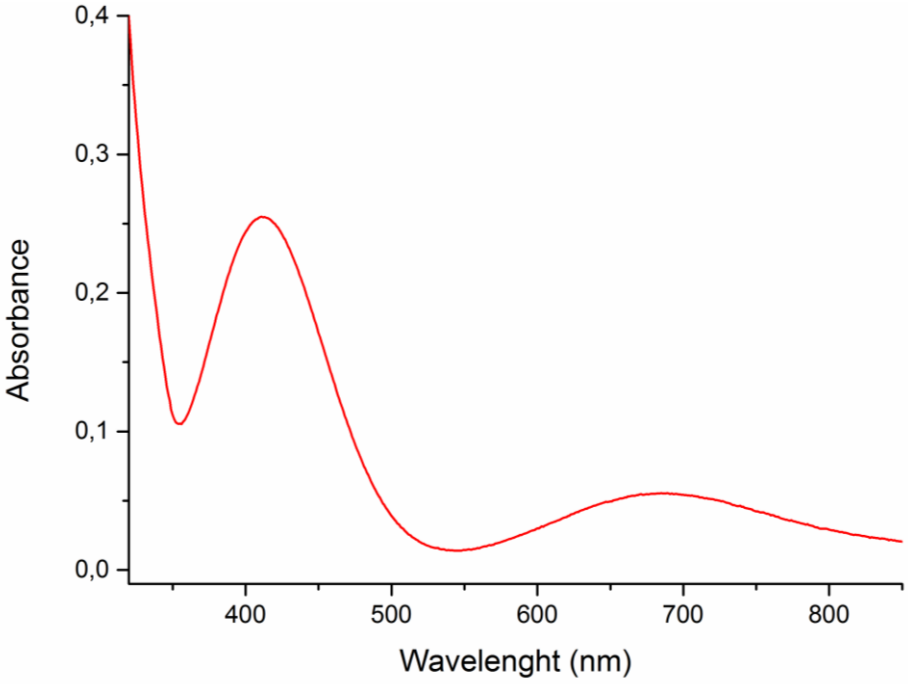

Figure 114. UV-Vis spectrum of $\mathbf{Cu_2L_2}$ (200 μM) in borate buffer 50 mM pH = 7.8, λ_{max}/nm (ε/M^{-1} cm^{-1}) 410 ($2.9\cdot10^3$) (LMCT band) and 675 ($3.8\cdot10^2$) (d-d band).

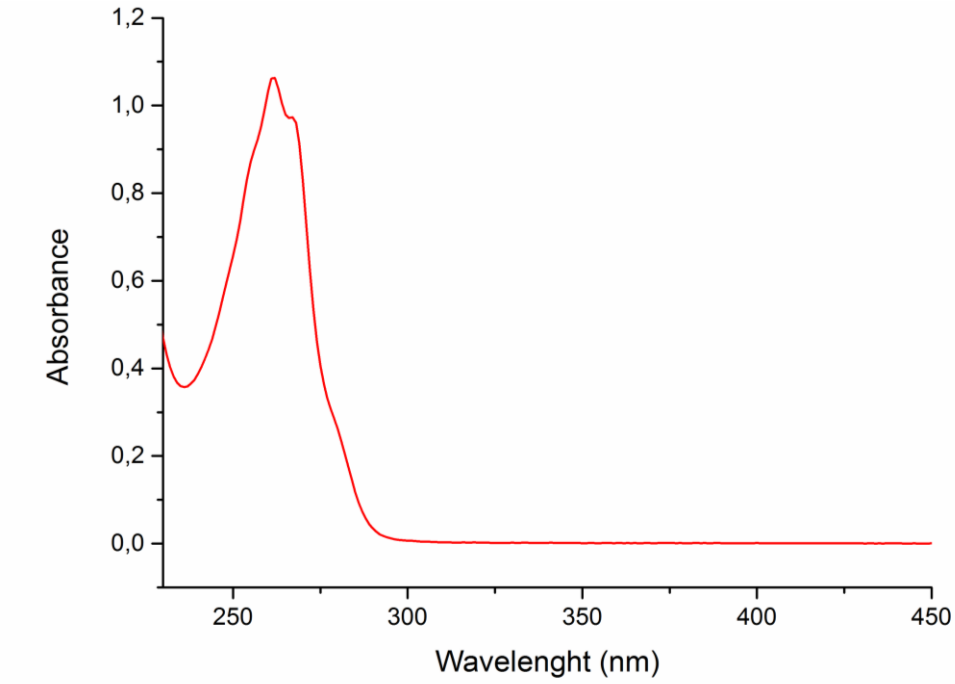

Figure 115. UV-Vis spectrum of $\mathbf{L^1}$ (70 µM) in H_2O, λ_{max}/nm ($\varepsilon/M^{-1}\,cm^{-1}$) 261.5 ($1.5\cdot10^4$), 266.7 ($1.4\cdot10^4$).

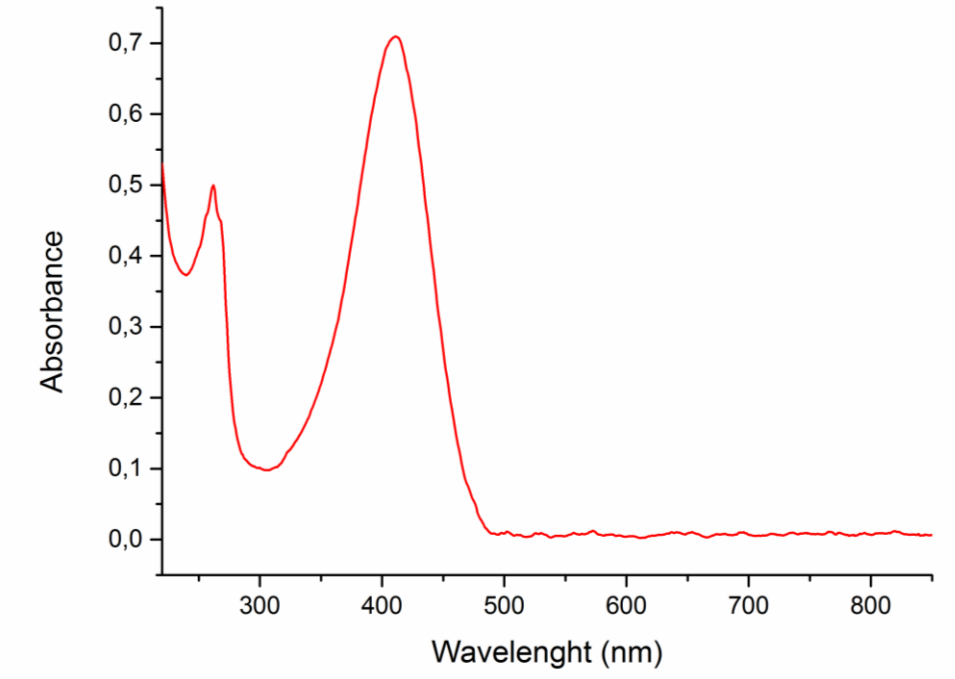

Figure 116. UV-Vis spectrum of $\mathbf{L^2}$ (150 µM) in H_2O, λ_{max}/nm ($\varepsilon/M^{-1}\,cm^{-1}$) 261.9 ($3.3\cdot10^3$), 410.9 ($4.7\cdot10^3$).

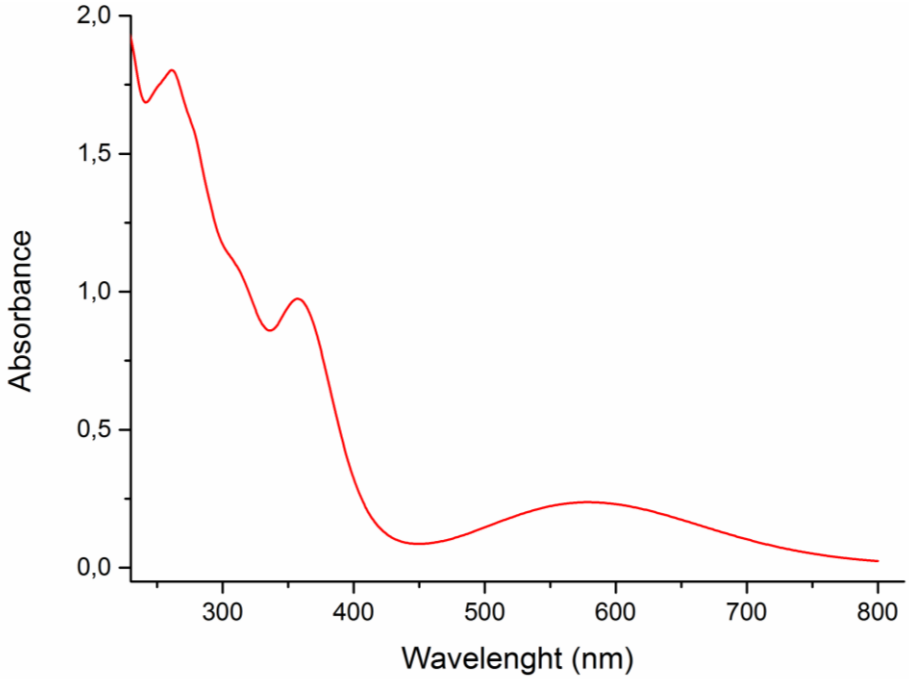

Figure 117. UV-Vis spectrum of **FeL** (140 μM) in acetonitrile, λ_{max}/nm (ε/M^{-1} cm^{-1}) 261.7 ($1.3 \cdot 10^4$), 357.8 ($7.0 \cdot 10^3$), 580.0 ($1.7 \cdot 10^3$).

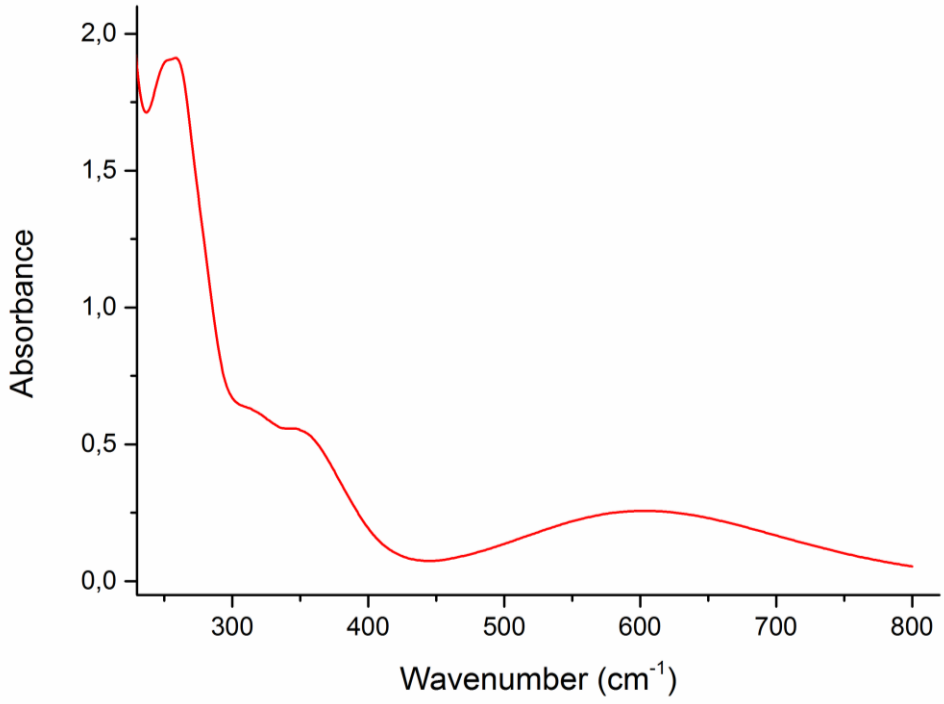

Figure 118. UV-Vis spectrum of **Fe_2L_2** (75 μM) in acetonitrile, λ_{max}/nm (ε/M^{-1} cm^{-1}) 258.3 ($2.6 \cdot 10^4$), 345.4 ($7.4 \cdot 10^3$), 604.2 ($3.4 \cdot 10^3$)

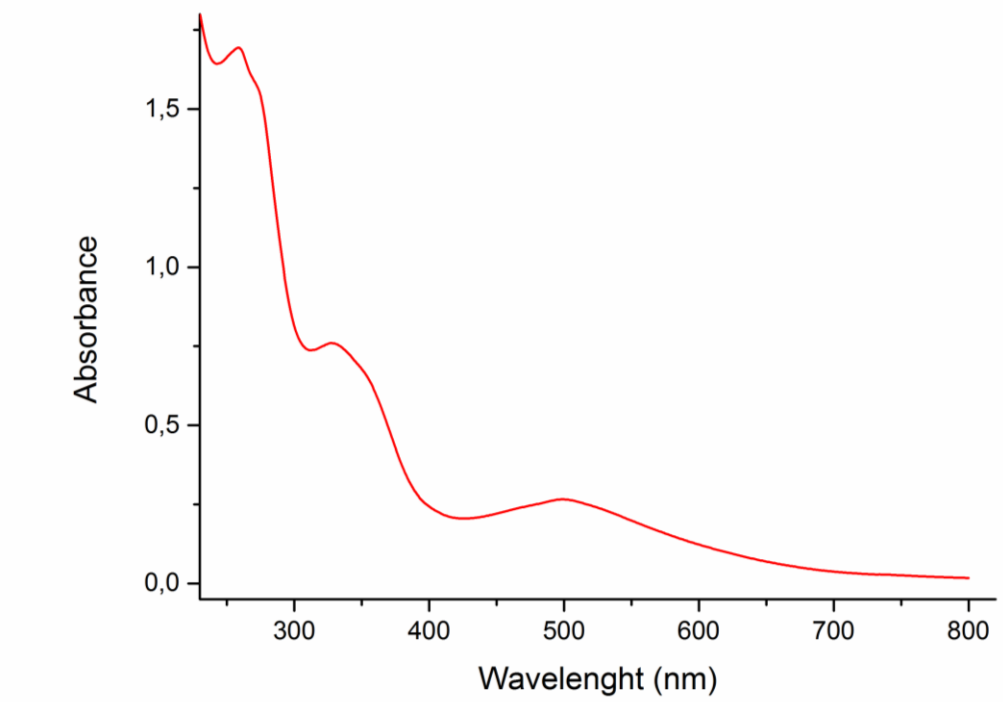

Figure 119. UV-Vis spectrum of $\mathbf{Fe_2L_2}$ (70 μM) in ACN:$H_2O(H^+)$, λ_{max}/nm (ε/M^{-1} cm^{-1}) 258.9 ($2.4\cdot10^4$), 327.8 ($1.1\cdot10^4$), 499.3 ($3.8\cdot10^4$).

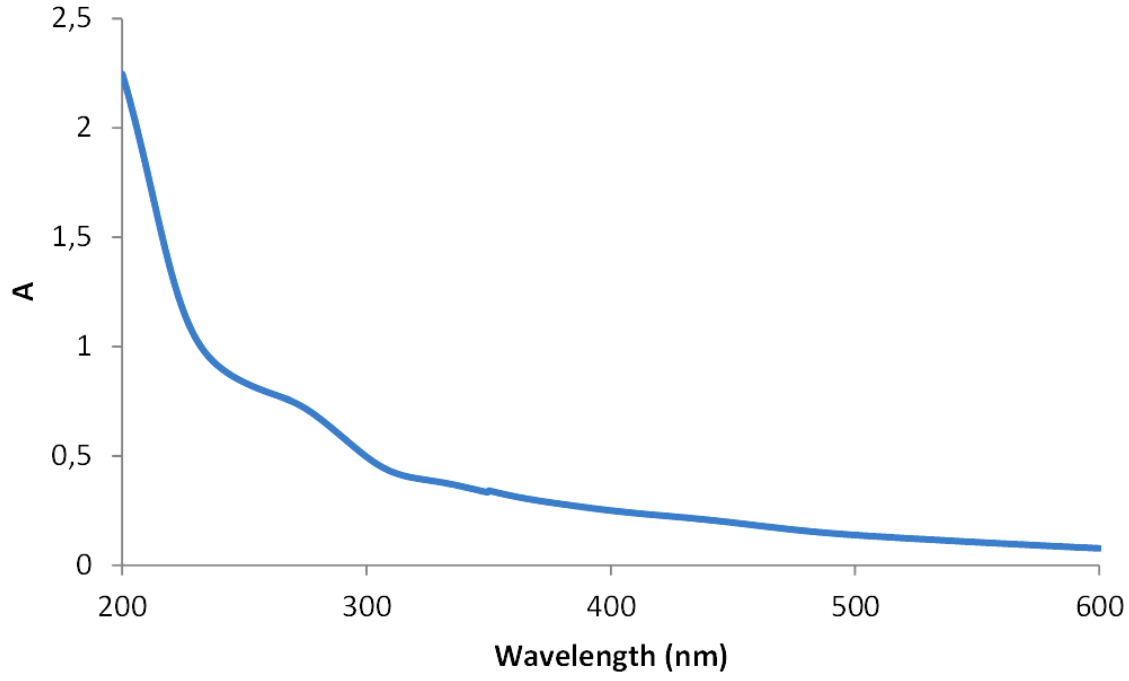

Figure 120. UV-Vis spectrum of $\mathbf{Ru_4(SiW_{10})_2}$ in phosphate buffer 50 mM pH = 7.8

Infrared Spectra

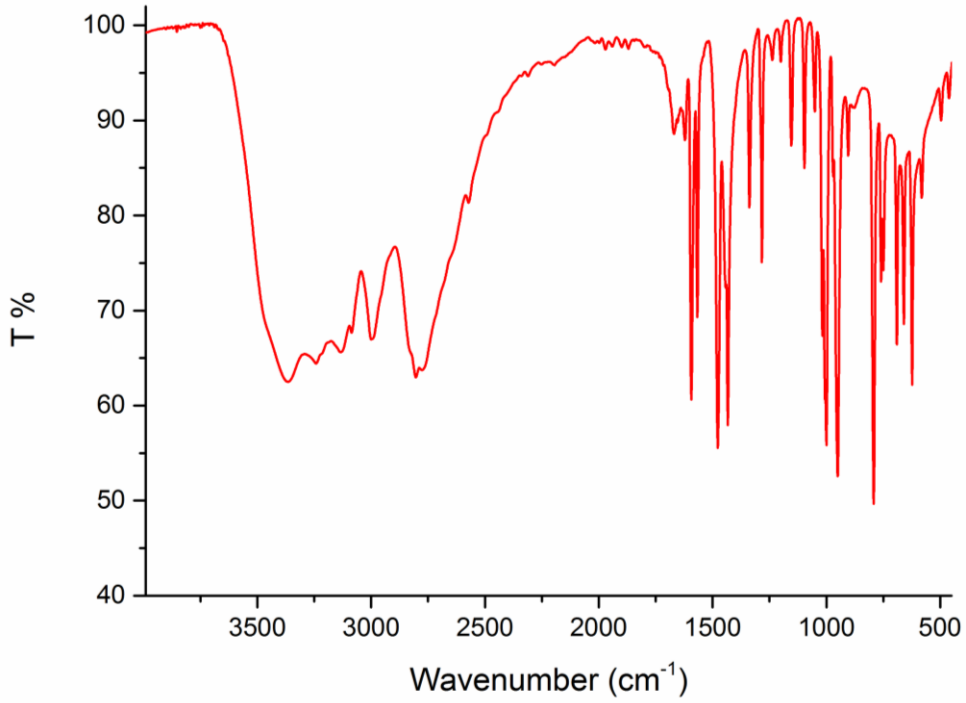

Figure 121. FT-IR spectrum (KBr pellet) of di-2-pyridy-ketoxime.

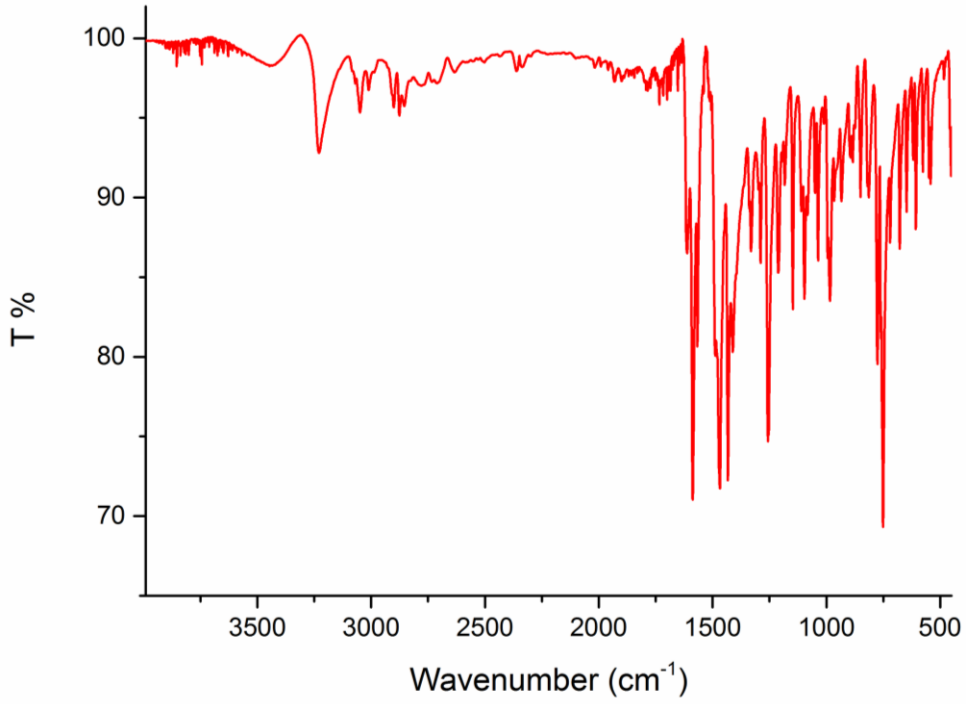

Figure 122. FT-IR spectrum (KBr pellet) of 2-({[Di(2-pyridyl)methyl]amino}methyl)phenol (**L**^{1}).

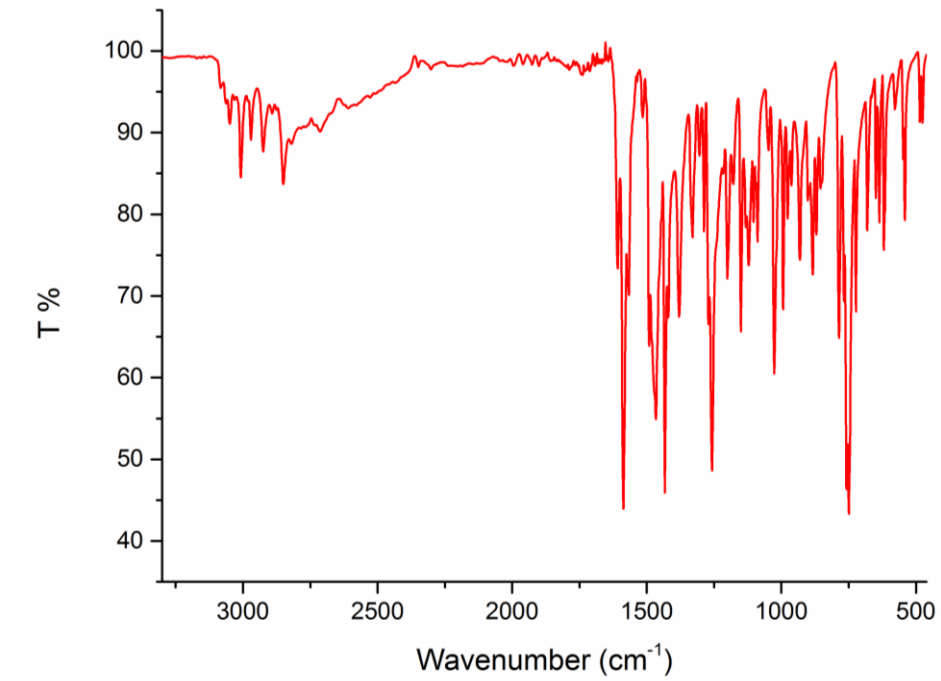

Figure 123. FT-IR spectrum (KBr pellet) of HL= 2-{[[Di(2-pyridyl)methyl](methyl)amino]methyl}phenol.

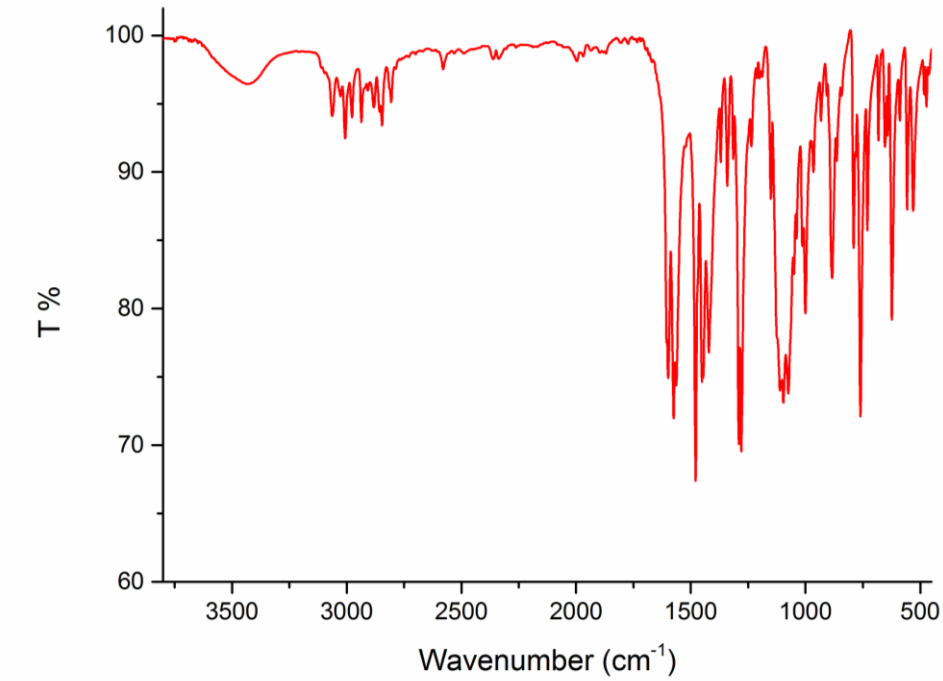

Figure 124. FT-IR spectrum (KBr pellet) of [$\mathbf{Mn_2L_2Ac}$](ClO_4).

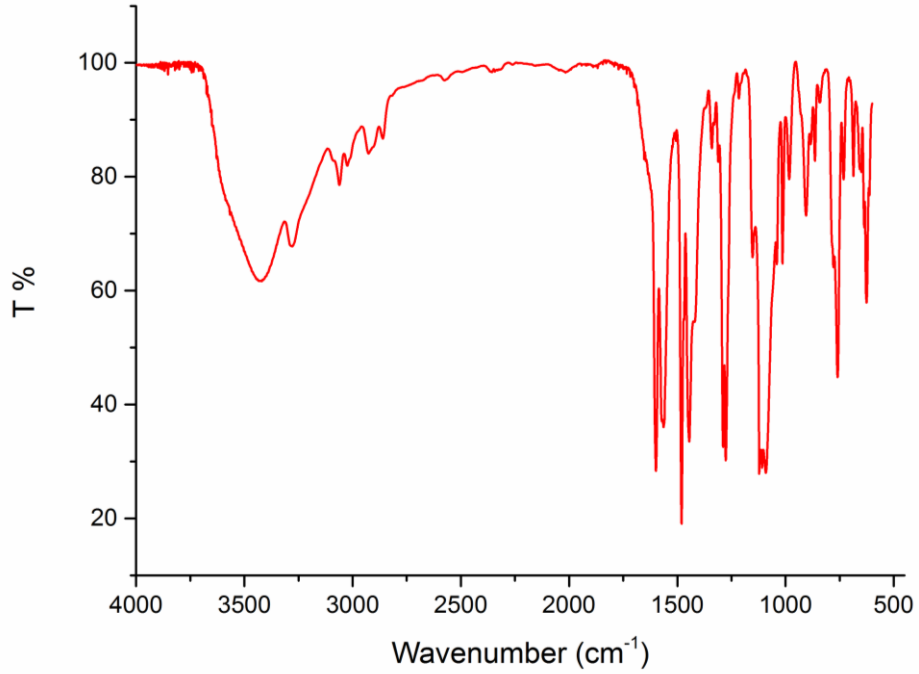

Figure 125. FT-IR spectrum (KBr pellet) of [$\mathbf{Mn_2L^1{}_2Ac}$](ClO_4).

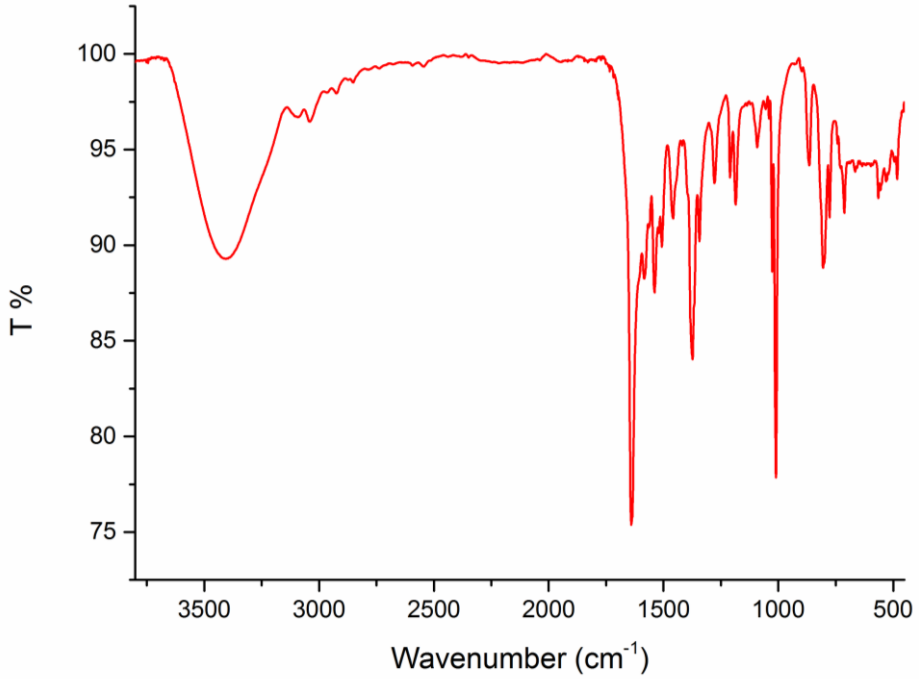

Figure 126. FT-IR spectrum (KBr pellet) of Mn(III)-meso-tri(N-methyl-4-pyridyl)mono(4-carboxyphenyl)porphine tetrachloride (**P1**).

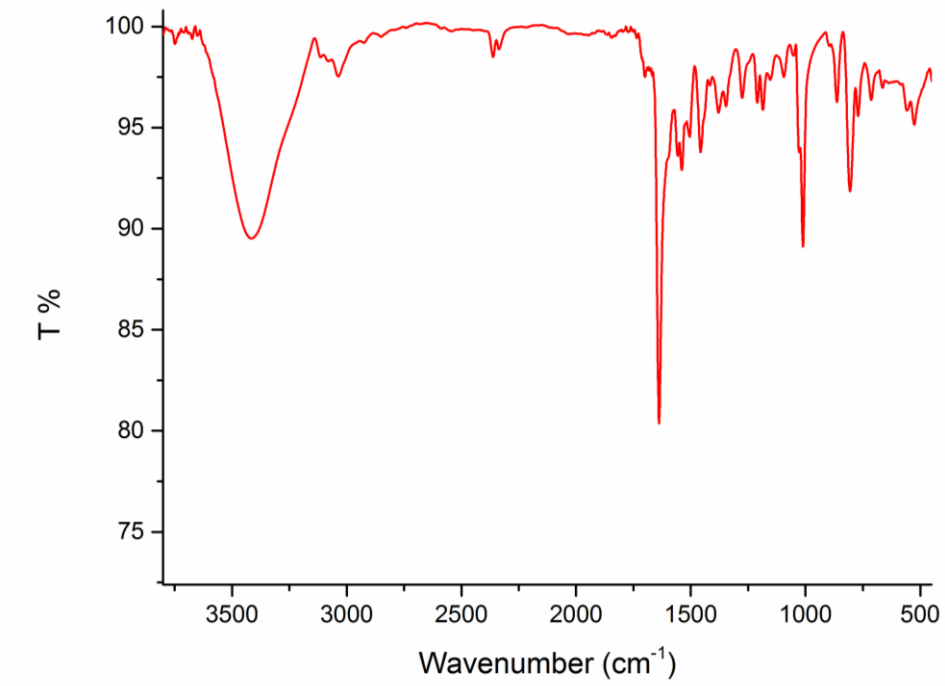

Figure 127. FT-IR spectrum (KBr pellet) of Mn(III)-meso-tri(N-methyl-4-pyridyl)mono(N-4-carboxybenzyl-4-pyridyl)porphine (**P2**) pentachloride.

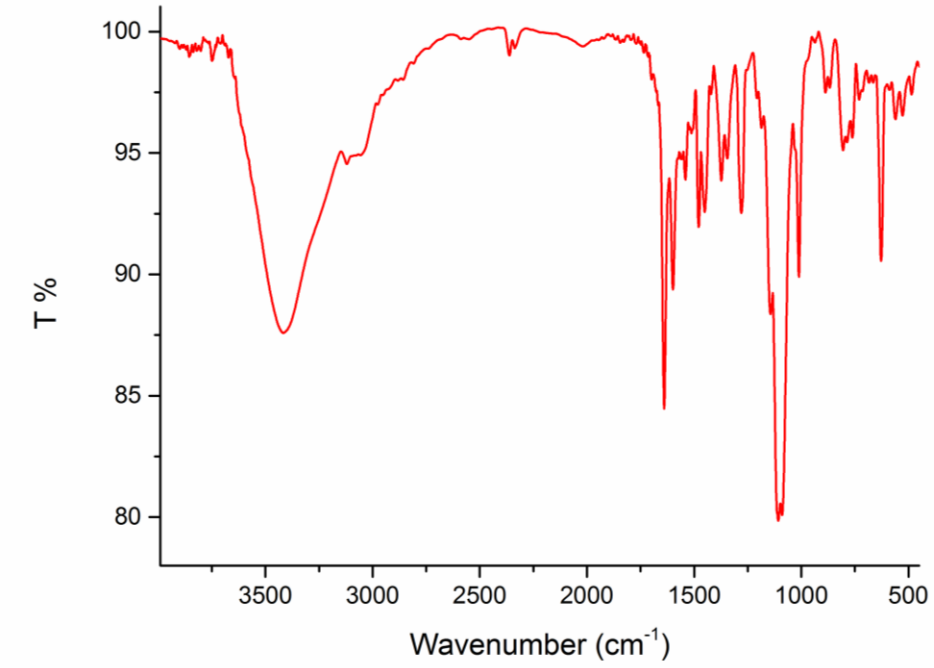

Figure 128. FT-IR spectrum (KBr pellet) of [$\mathbf{Mn_2L_2P1}$]$(ClO_4)_5$.

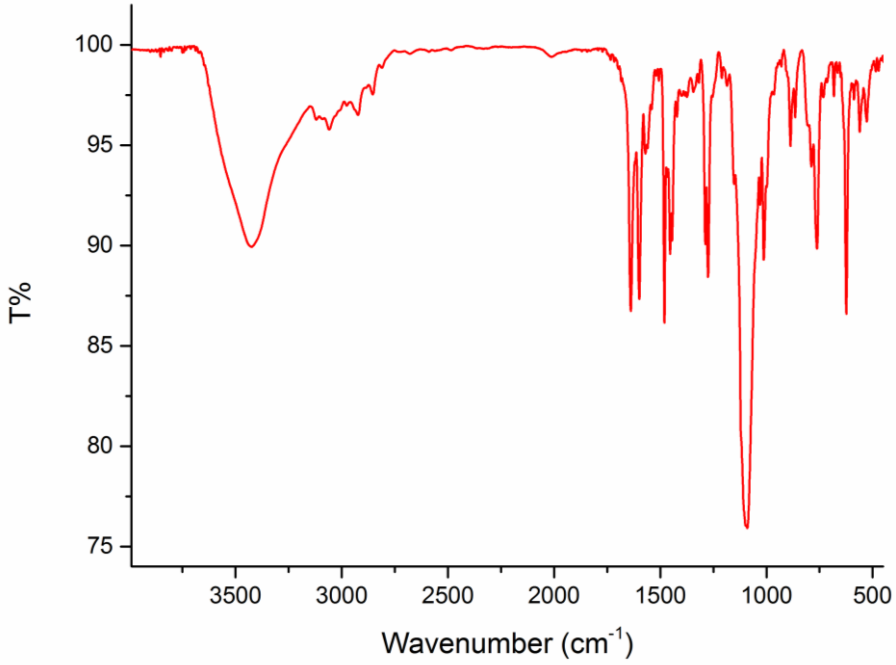

Figure 129. FT-IR spectrum in KBr pellet of the complex [$\mathbf{Mn_2L_2P2}$]$(Cl)_2(ClO_4)_4$.

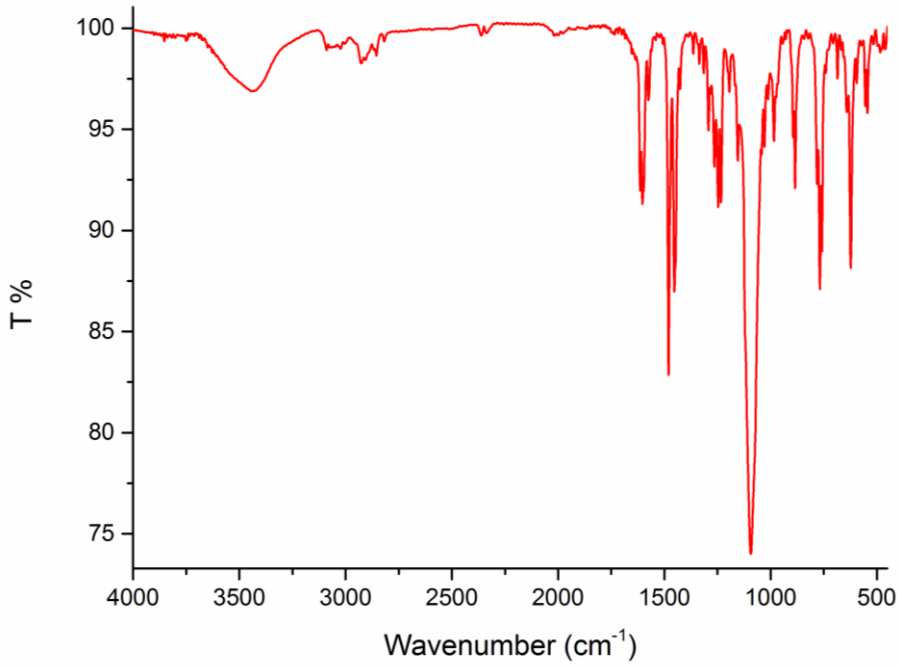

Figure 130. FT-IR spectrum in KBr pellet of the complex [$\mathbf{Cu_2L_2}$]$(ClO_4)_2$.

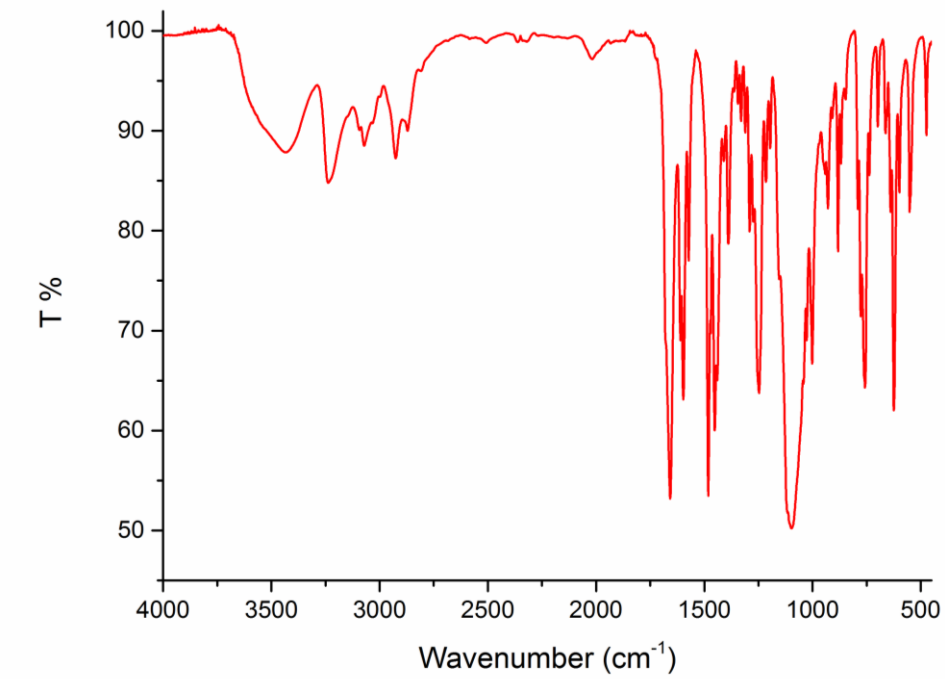

Figure 131. FT-IR spectrum in KBr pellet of the complex $[\mathbf{Cu_2L^1_2}](ClO_4)_2$.

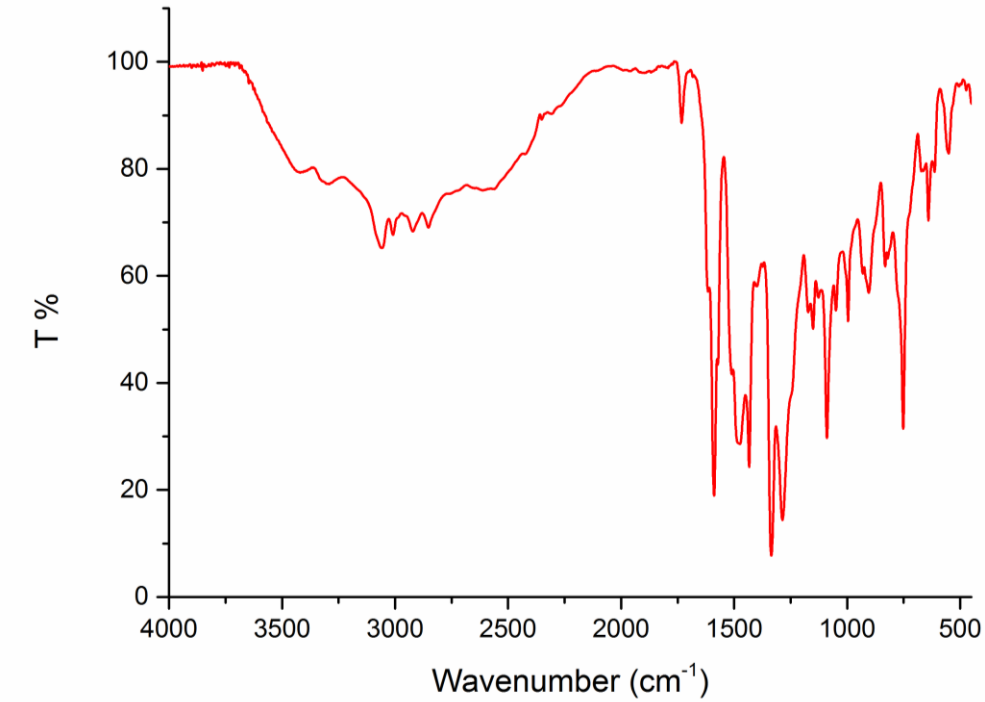

Figure 132. FT-IR spectrum (KBr pellet) of 2-({[Di(2-pyridyl)methyl]amino}methyl)-4-nitrophenol ($\mathbf{L^2}$).

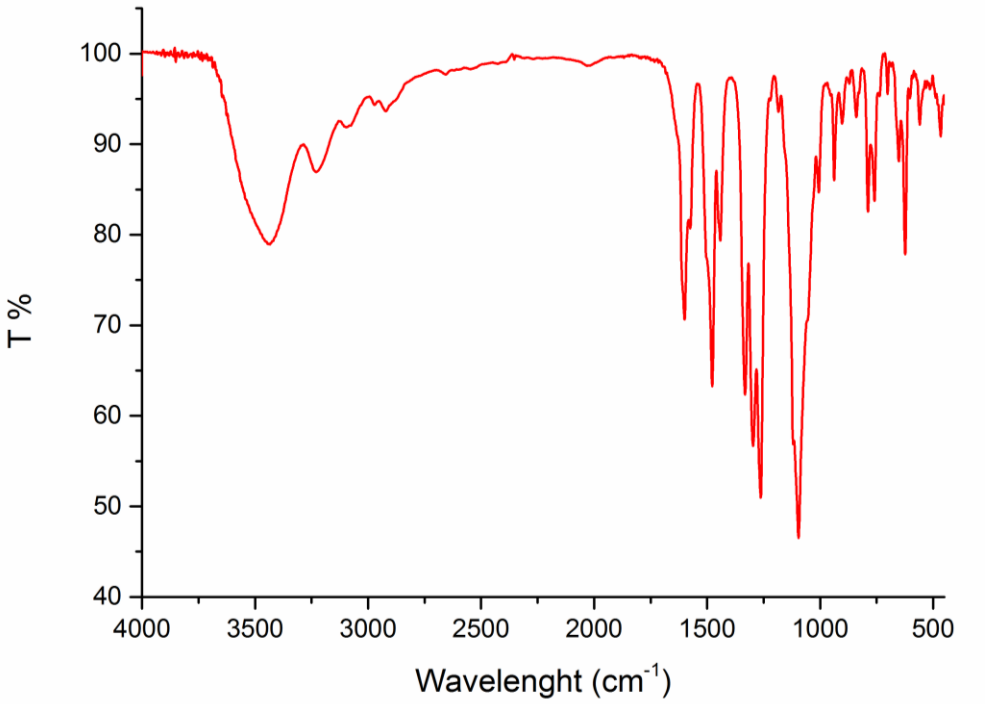

Figure 133. FT-IR spectrum in KBr pellet of the complex $\mathbf{Cu_2L^2_2}$.

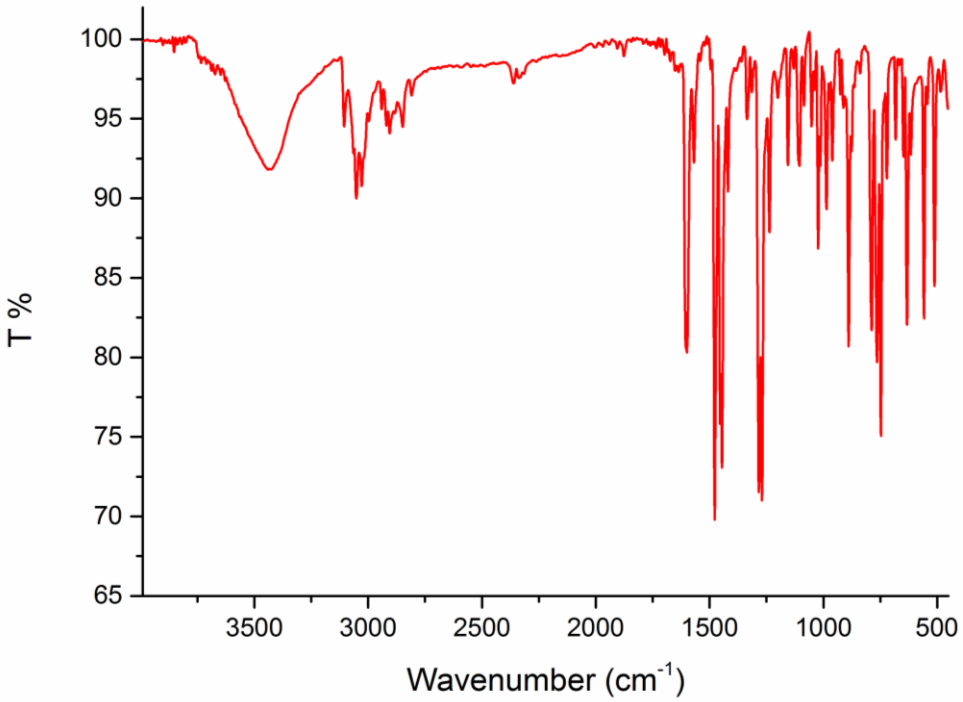

Figure 134. FT-IR spectrum in KBr pellet of the complex $\mathbf{FeL(Cl)_2}$.

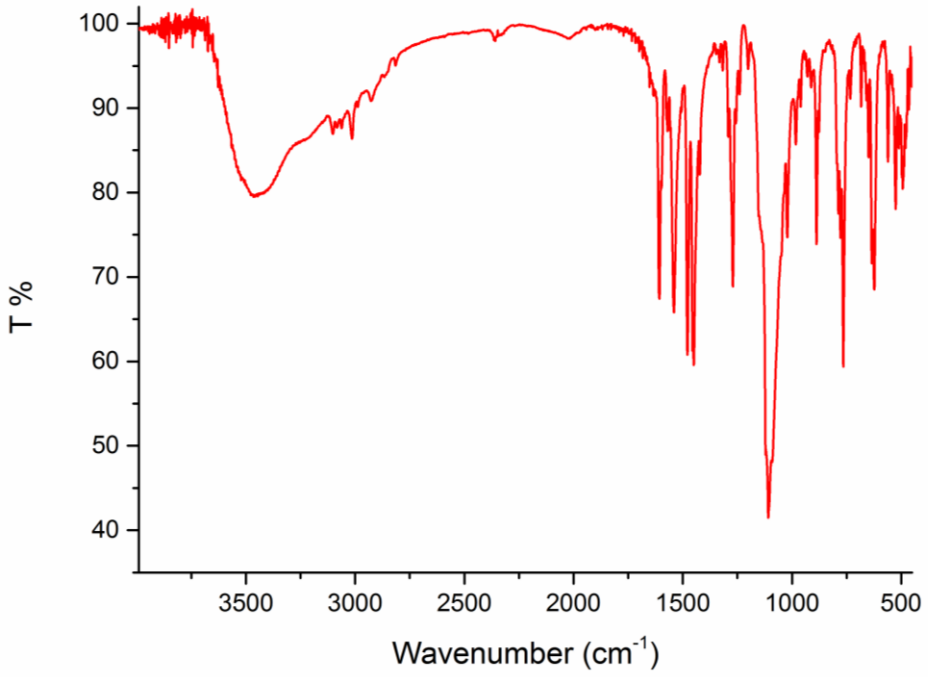

Figure 135. FT-IR spectrum in KBr pellet of the complex $\mathbf{Fe_2(L)_2(OH)(H_2O)_2}$.

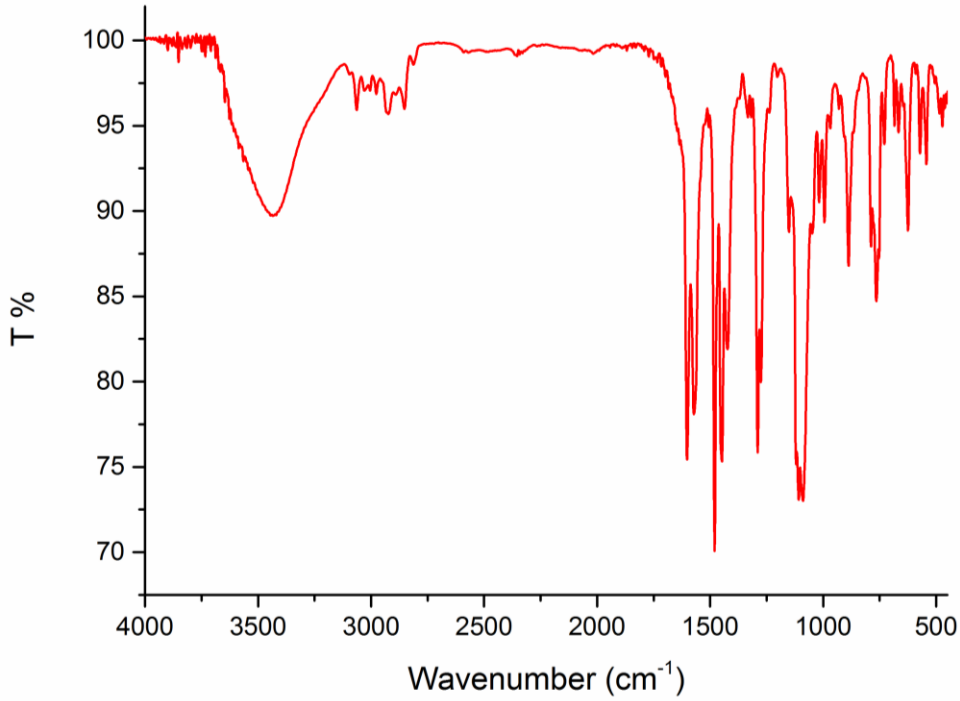

Figure 136. FT-IR spectrum in KBr pellet of the complex $[\mathbf{Co_2L_2Ac}](ClO_4)$.

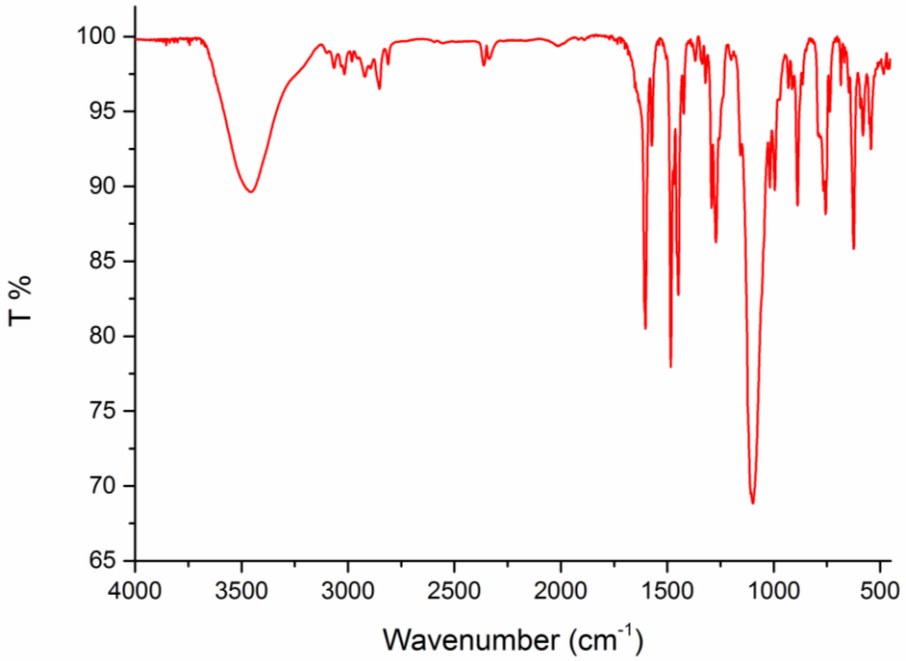

Figure 137. FT-IR spectrum in KBr pellet of the complex $[\mathbf{Co_2L_2}](MeOH)_2(ClO_4)_2$.

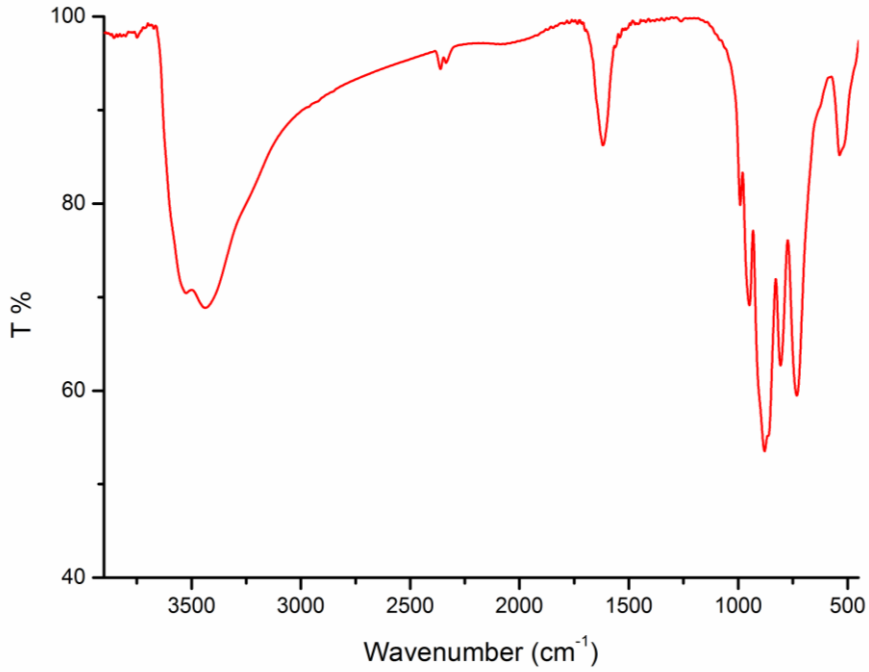

Figure 138. FT-IR spectrum in KBr pellet of β_2-$SiW_{11}O_{39}$.

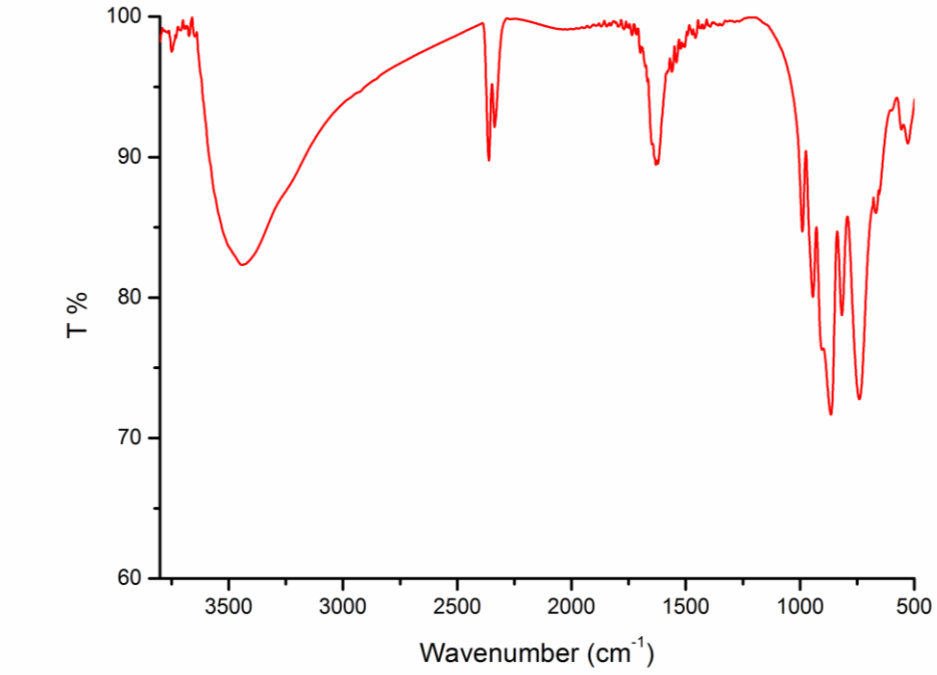

Figure 139. FT-IR spectrum in KBr pellet of $K_8[\gamma\text{-}SiW_{10}O_{36}]$.

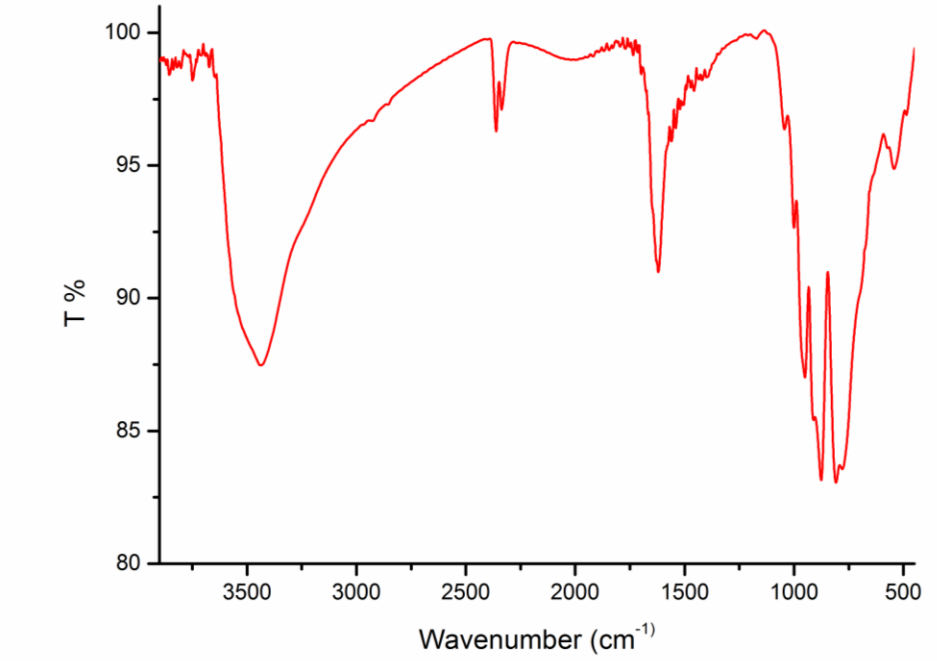

Figure 140. FT-IR spectrum in KBr pellet of $Na_{10}[\mathbf{Ru_4(SiW_{10})_2}]$.

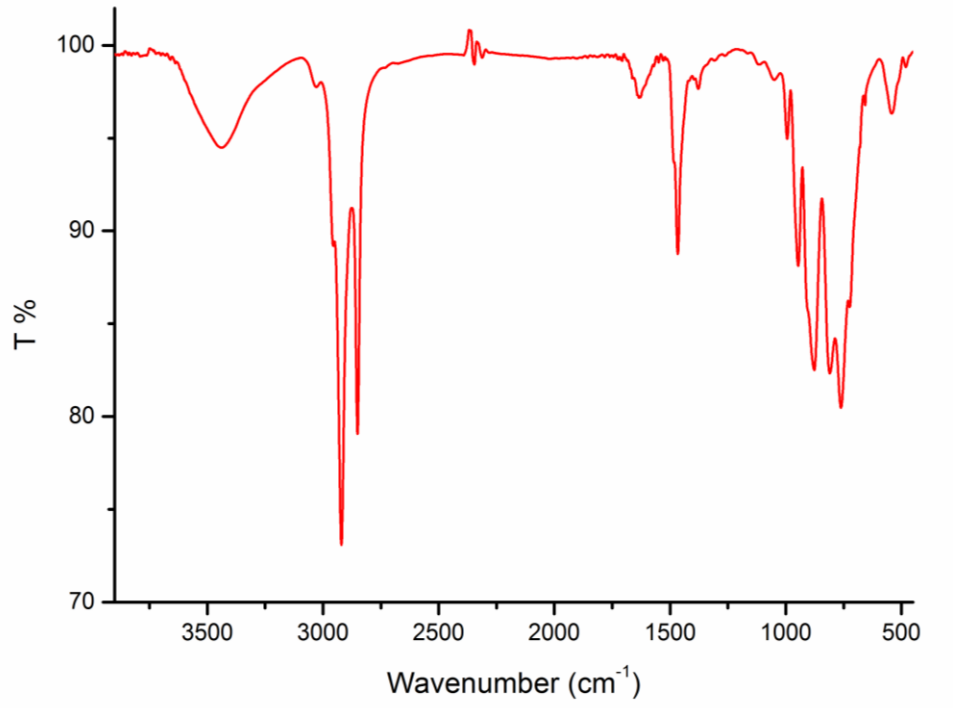

Figure 141. FT-IR spectrum in KBr pellet of $DODA_{10}/Ru_4(SiW_{10})_2$.

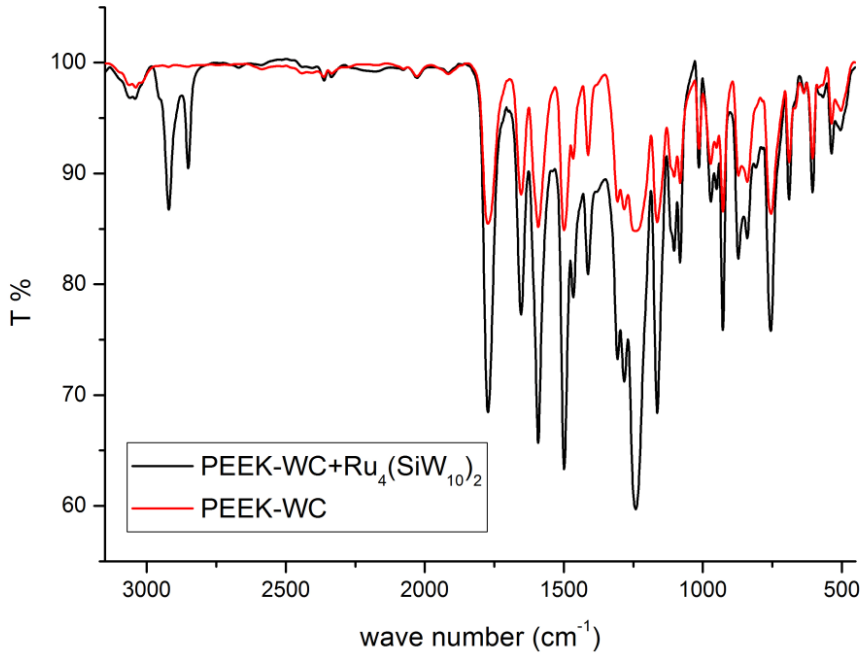

Figure 142. FT-IR spectra in KBr pellet of PEEK-WC (red line) and PEEK-WC+$DODA_{10}$/ $Ru_4(SiW_{10})_2$ (black line), the signal of the $Ru_4(SiW_{10})_2$ are undetectable because are overlapped with the signal of the polymer.

NMR spectra

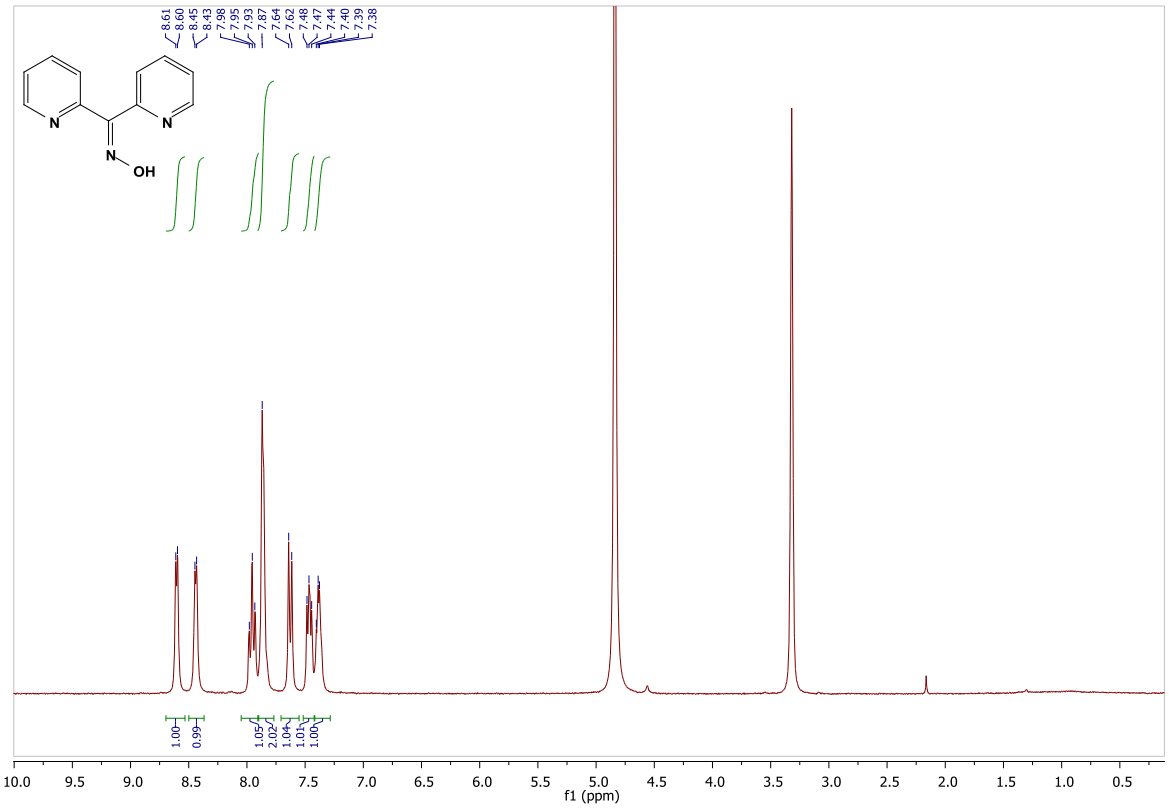

Figure 143. ^{1}H NMR of di-2-pyridyl-methylamine in CD_3OD.

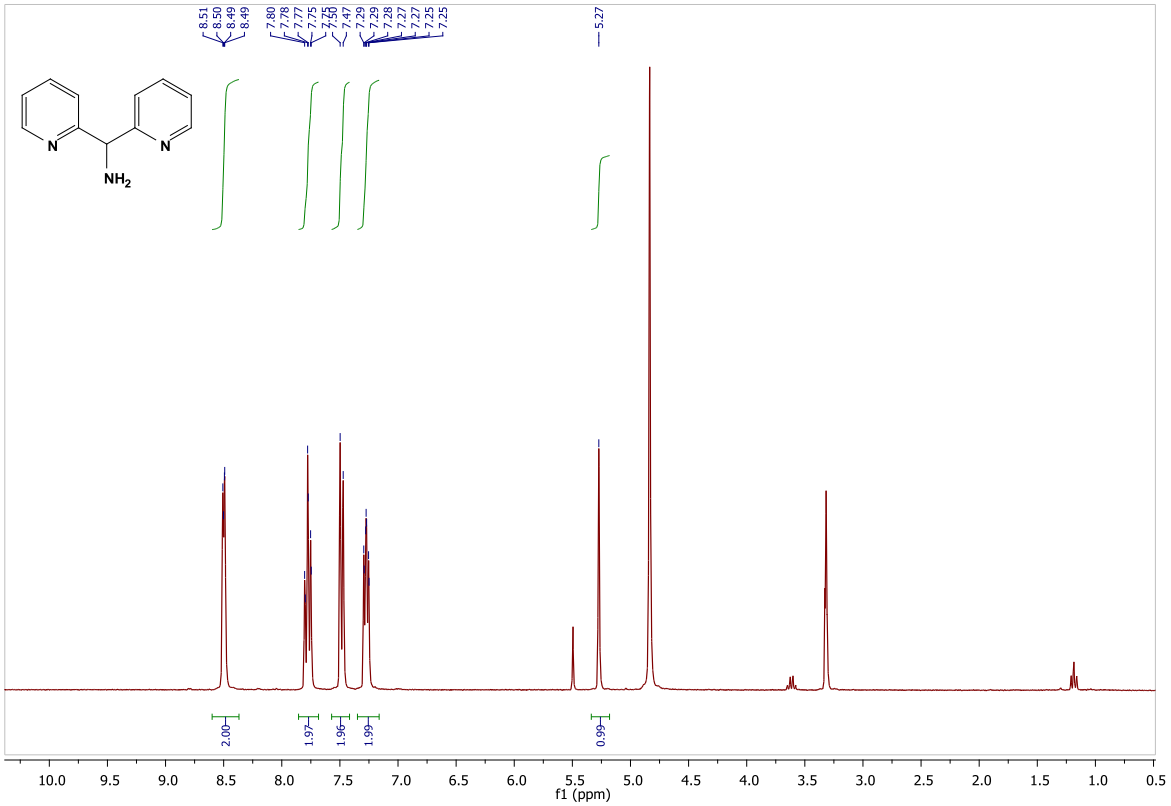

Figure 144. ^{1}H NMR of di-2-pyridyl-methylamine in CD_3OD.

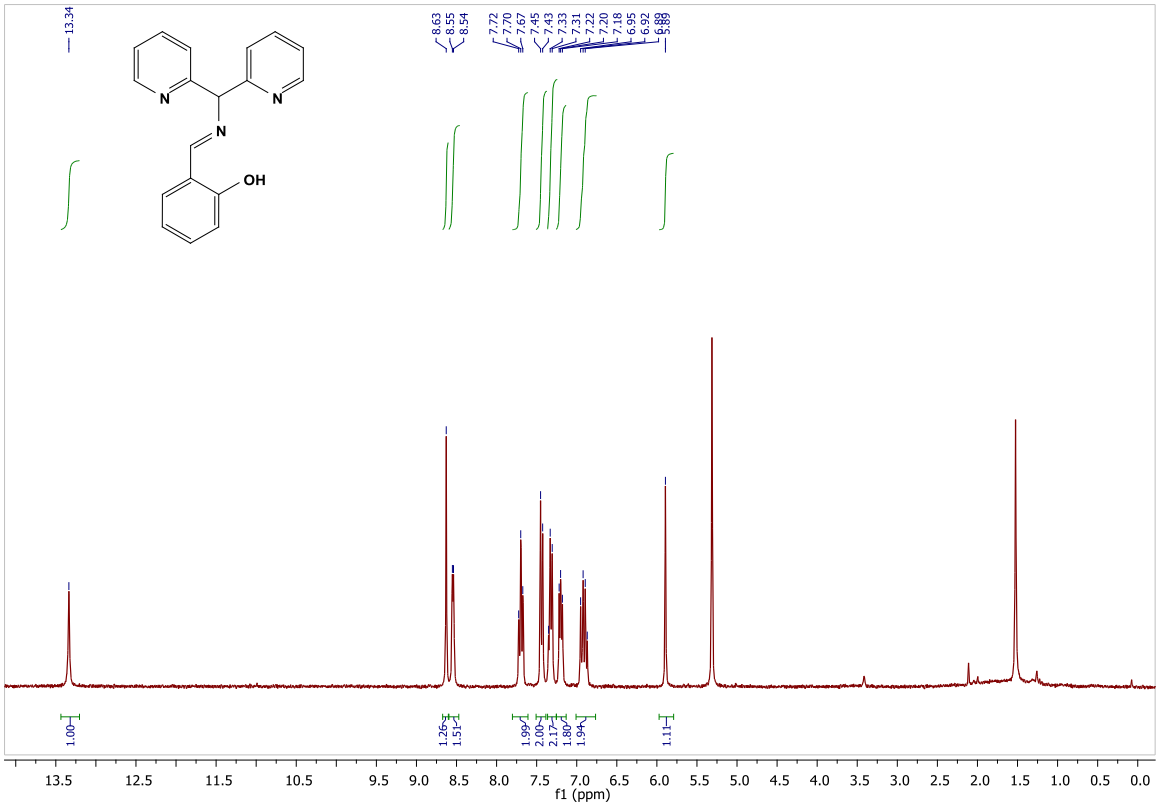

Figure 145. ^{1}H NMR of 2-({[Di(2-pyridyl)methyl]imino}methyl)phenol in CD_2Cl_2.

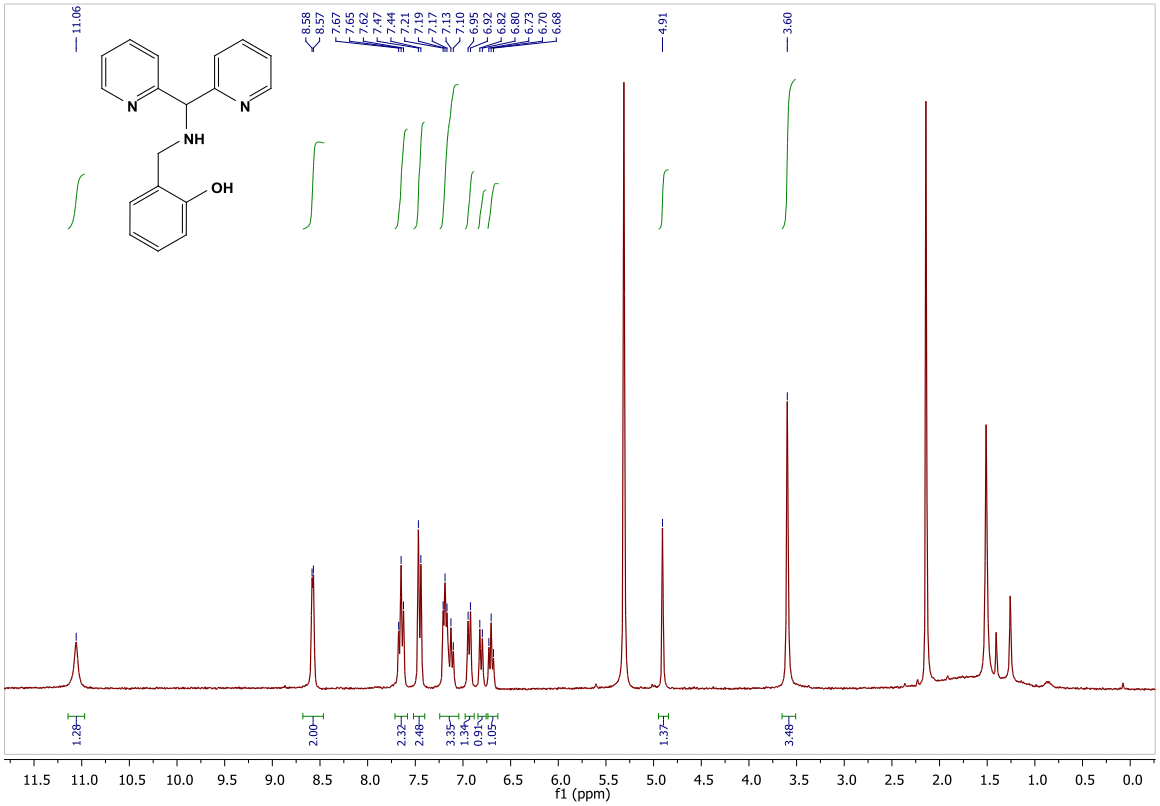

Figure 146. ^{1}H NMR of 2-({[Di(2-pyridyl)methyl]amino}methyl)phenol (L^1) in CD_2Cl_2, peaks under 2.5 ppm are attributable to residual solvents.

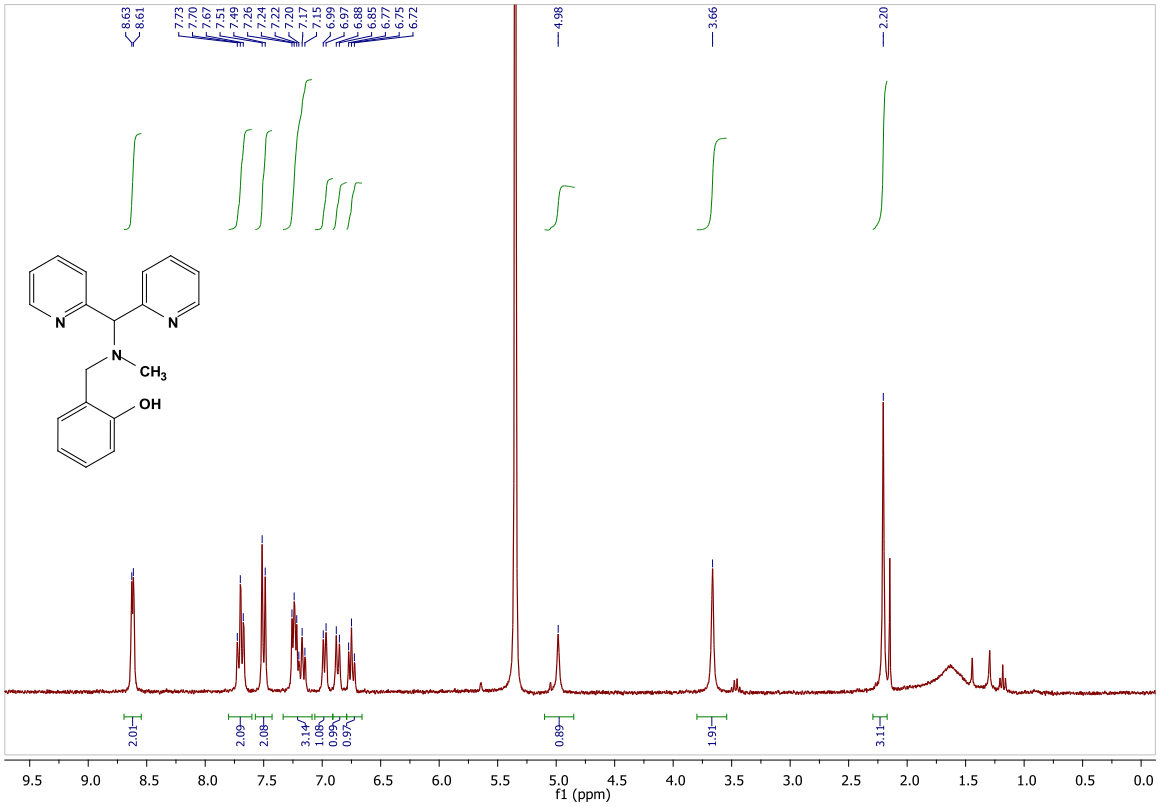

Figure 147. ^{1}H NMR of 2-{[Di(2-pyridyl)methyl](methyl)amino]methyl}phenol (L) in CD_2Cl_2, peaks under 2.5 ppm are attributable to residual solvents.

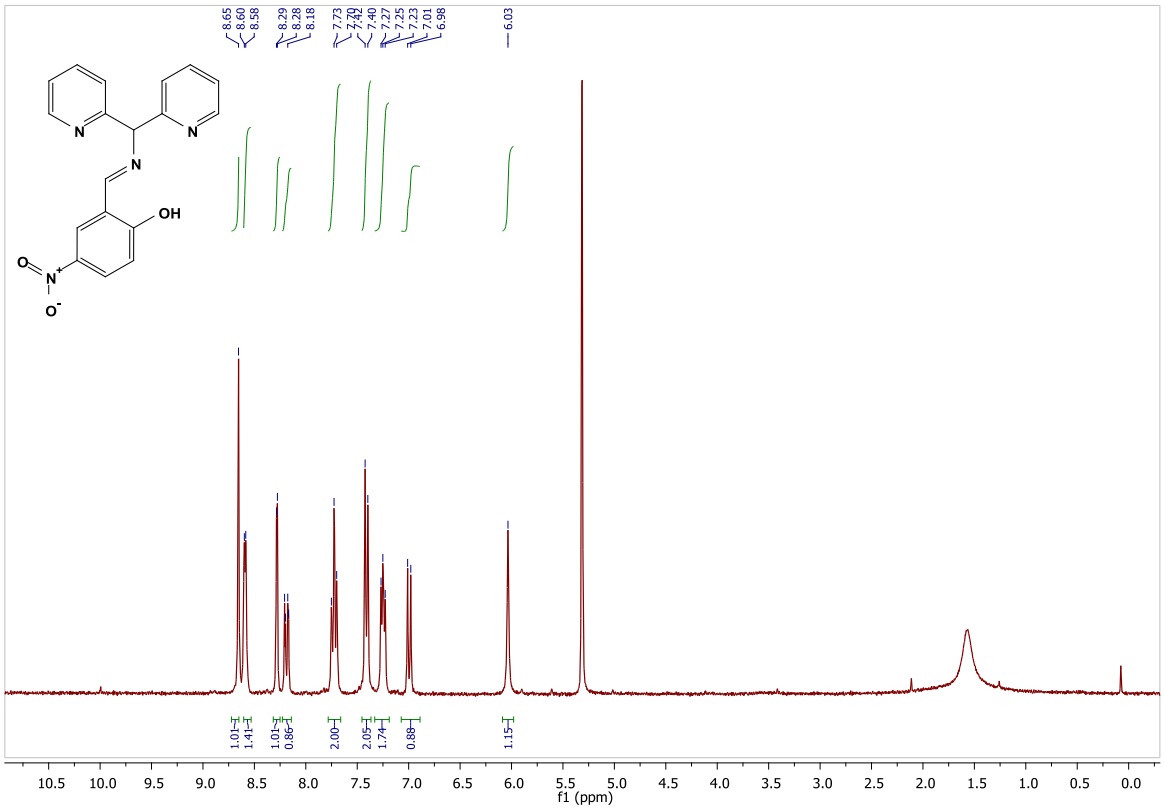

Figure 148. ^{1}H NMR of 2-({[Di(2-pyridyl)methyl]imino}methyl)-4-nitrophenol in CD_2Cl_2.

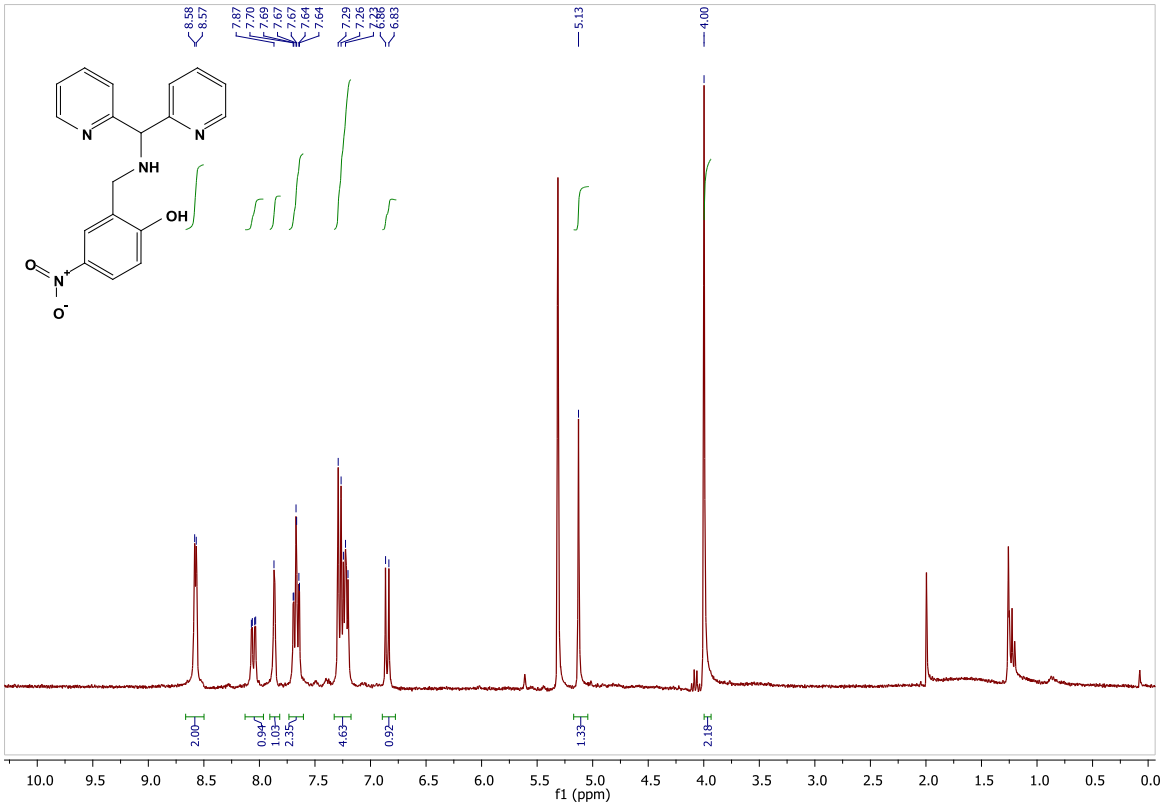

Figure 149. ^{1}H NMR of 2-({[Di(2-pyridyl)methyl]amino}methyl)-4-nitrophenol in CD_2Cl_2.

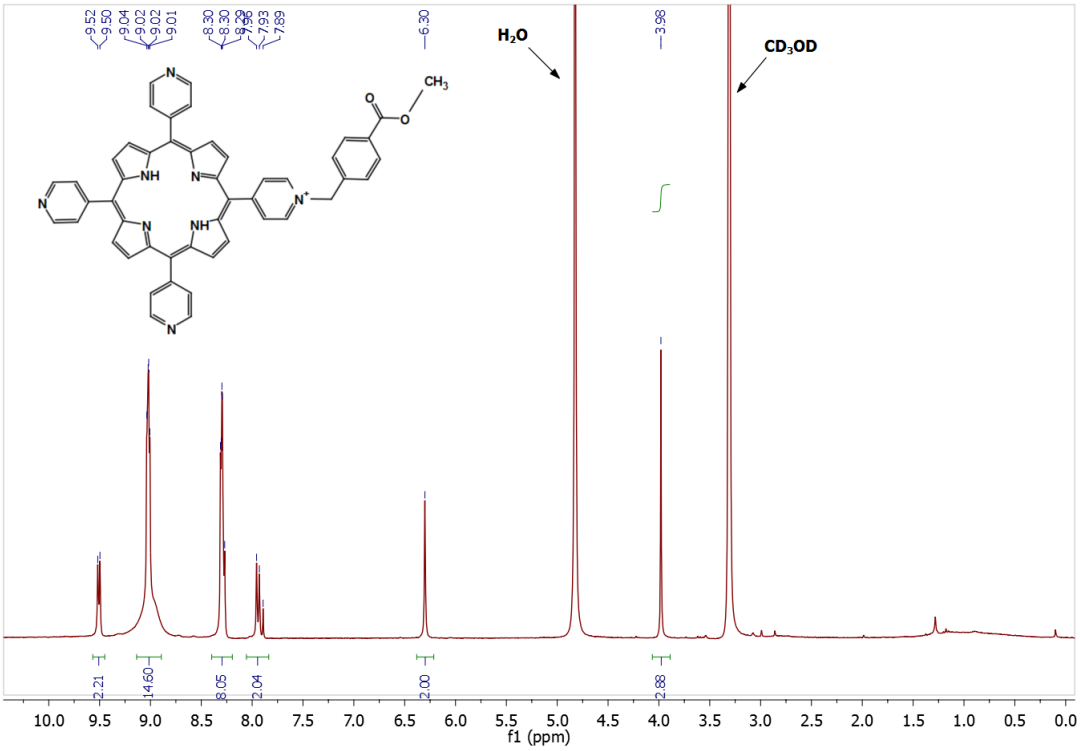

Figure 150. ^{1}H NMR of meso-tri(4-pyridyl)mono(N-4-methoxyformylbenzyl-4-pyridyl)porphine in CD_3OD.

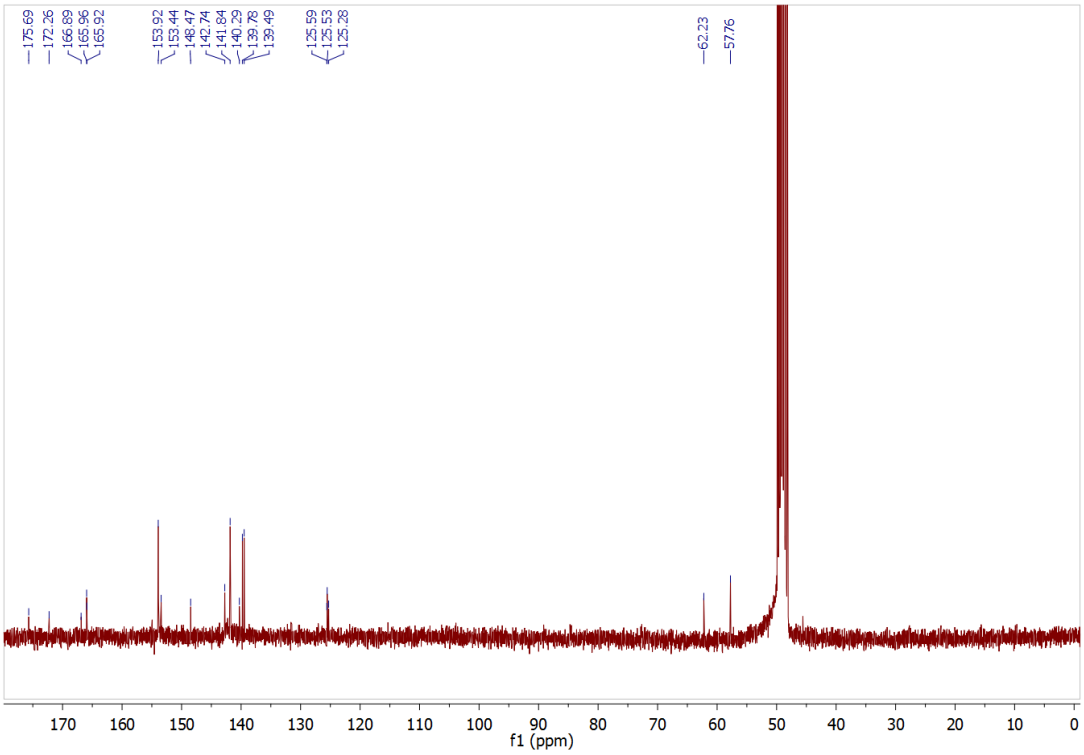

Figure 151. ^{13}C NMR of meso-tri(4-pyridyl)mono(N-4-methoxyformylbenzyl-4-pyridyl)porphine in CD_3OD.

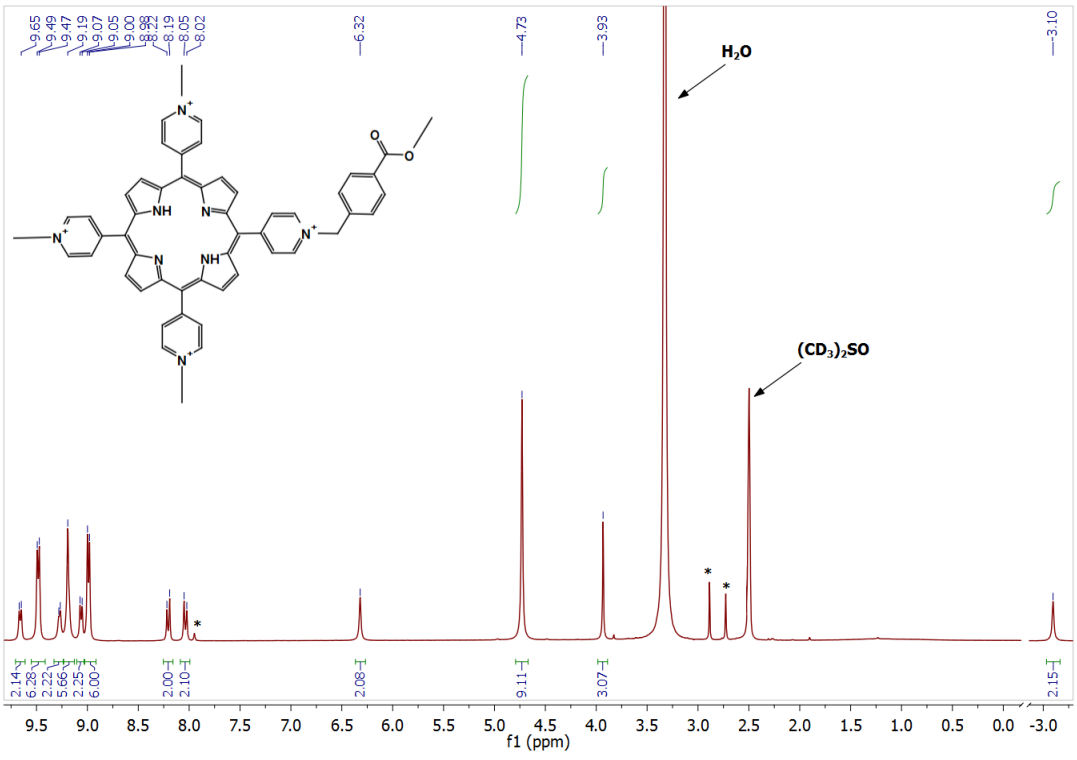

Figure 152. ^{1}H NMR of meso-tri(N-methyl-4-pyridyl)mono(N-4-methoxyformylbenzyl-4-pyridyl)porphine in $(CD_3)_2SO$, (*) indicate DMF residual peaks.

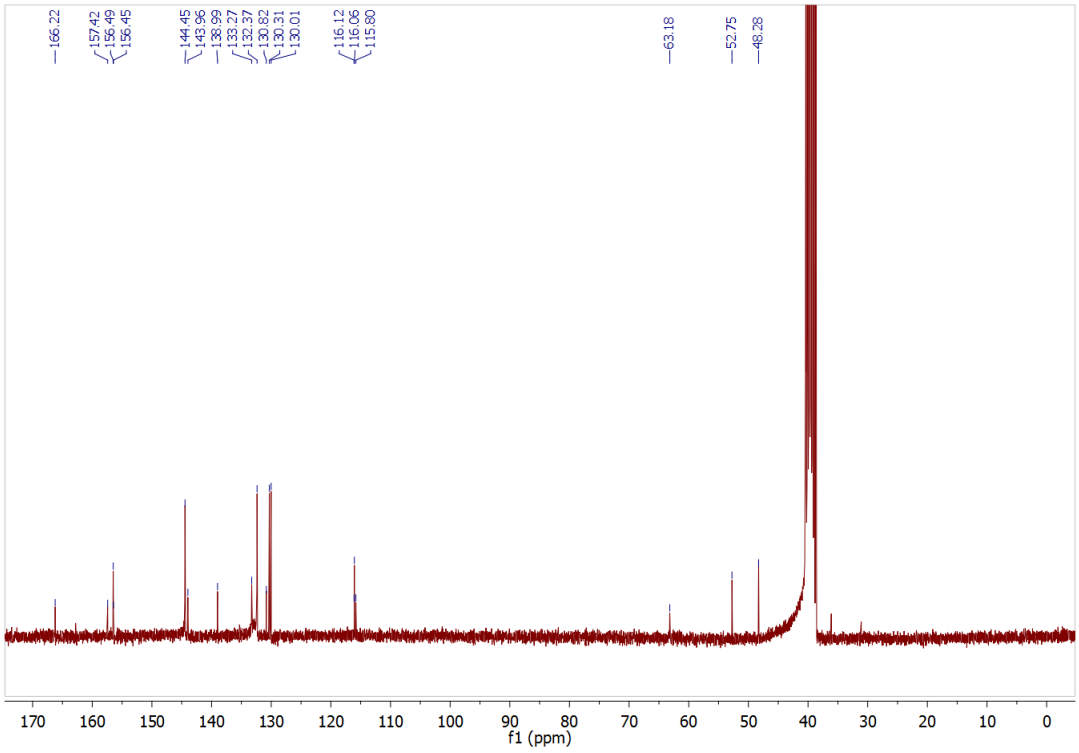

Figure 153. ^{13}C NMR of meso-tri(4-pyridyl)mono(N-4-methoxyformylbenzyl-4-pyridyl)porphine in $(CD_3)_2SO$.

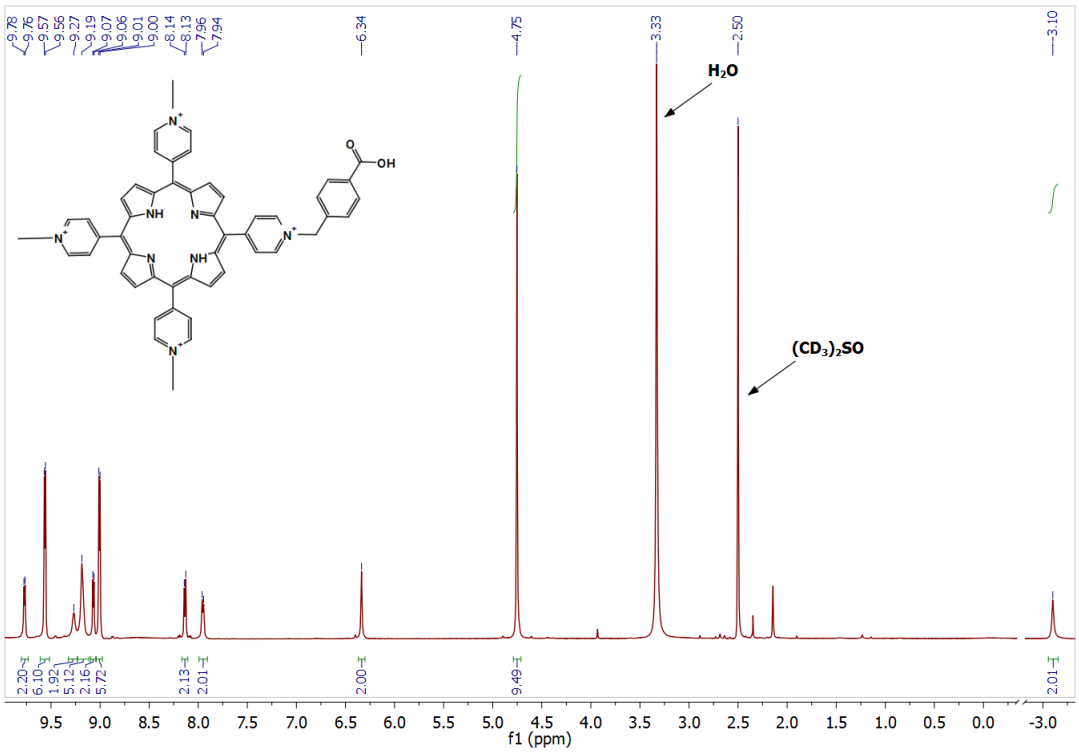

Figure 154. ^{1}H-NMR of meso-tri(N-methyl-4-pyridyl)mono(N-4-carboxybenzyl-4-pyridyl)porphine in $(CD_3)_2SO$.

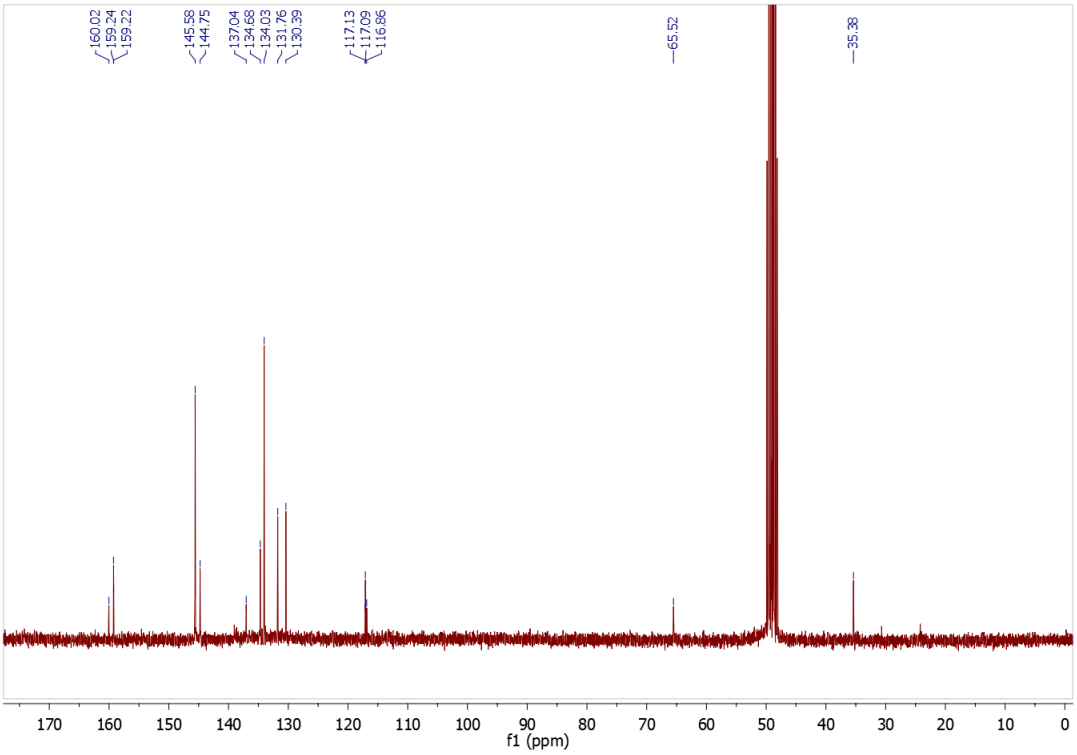

Figure 155. ^{1}H-NMR of meso-tri(N-methyl-4-pyridyl)mono(N-4-carboxybenzyl-4-pyridyl)porphine in CD_3OD.

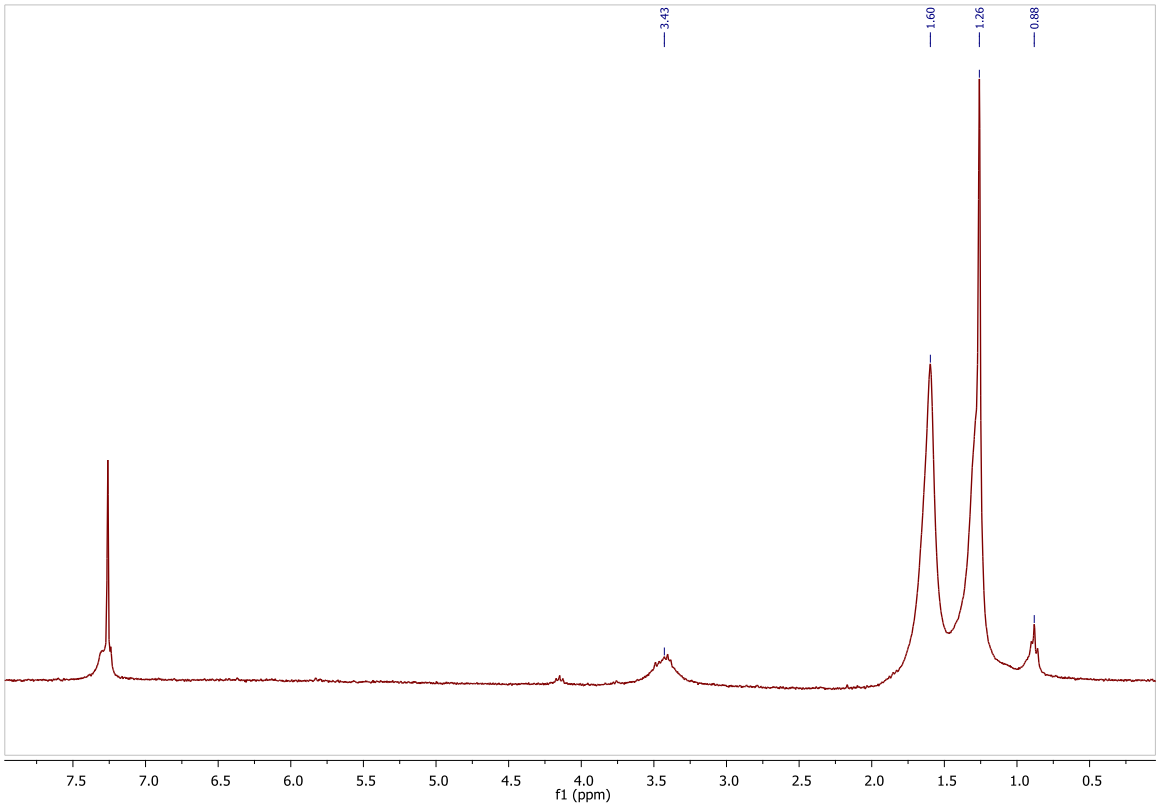

Figure 156. ^{1}H-NMR of $DODA_{10}$/ $Ru_4(SiW_{10})_2$ in $CDCl_3$.

ESI-MS analysis

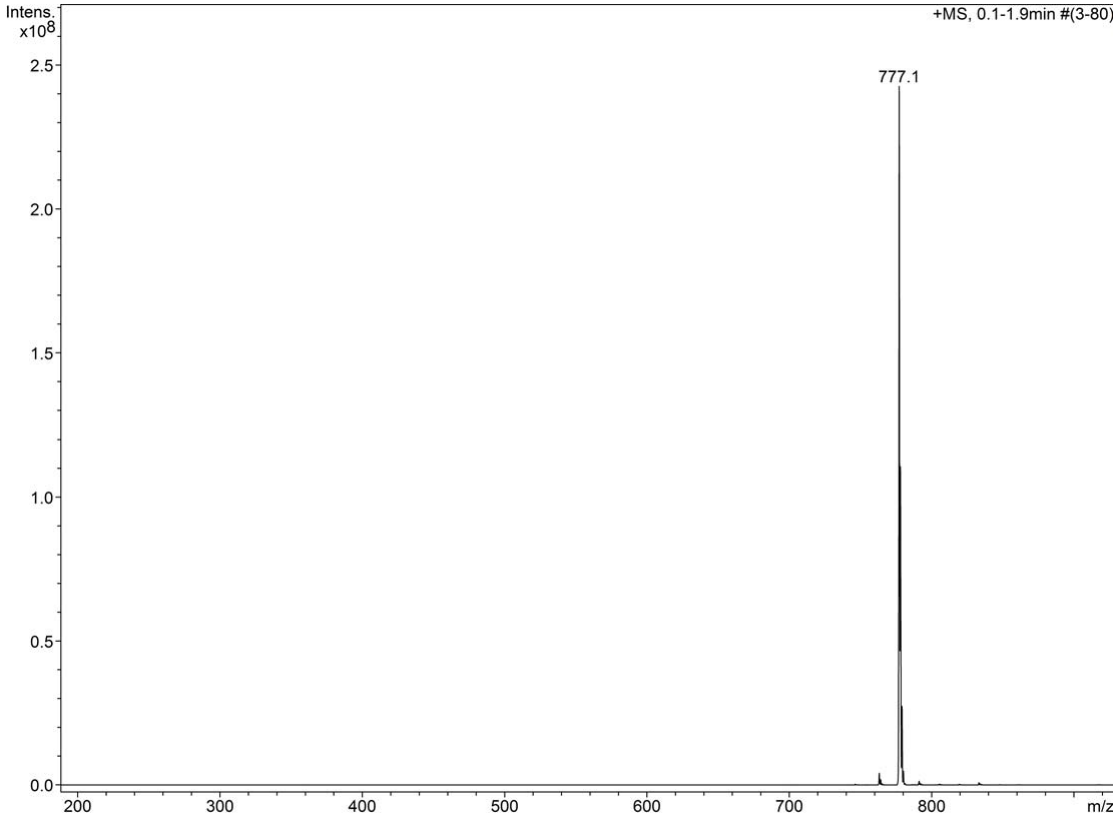

Figure 157. ESI-MS spectrum of **Mn_2L_2Ac** in acetonitrile, where 777.1 m/z correspond to the molecular ion $Mn_2L_2Ac^+$.

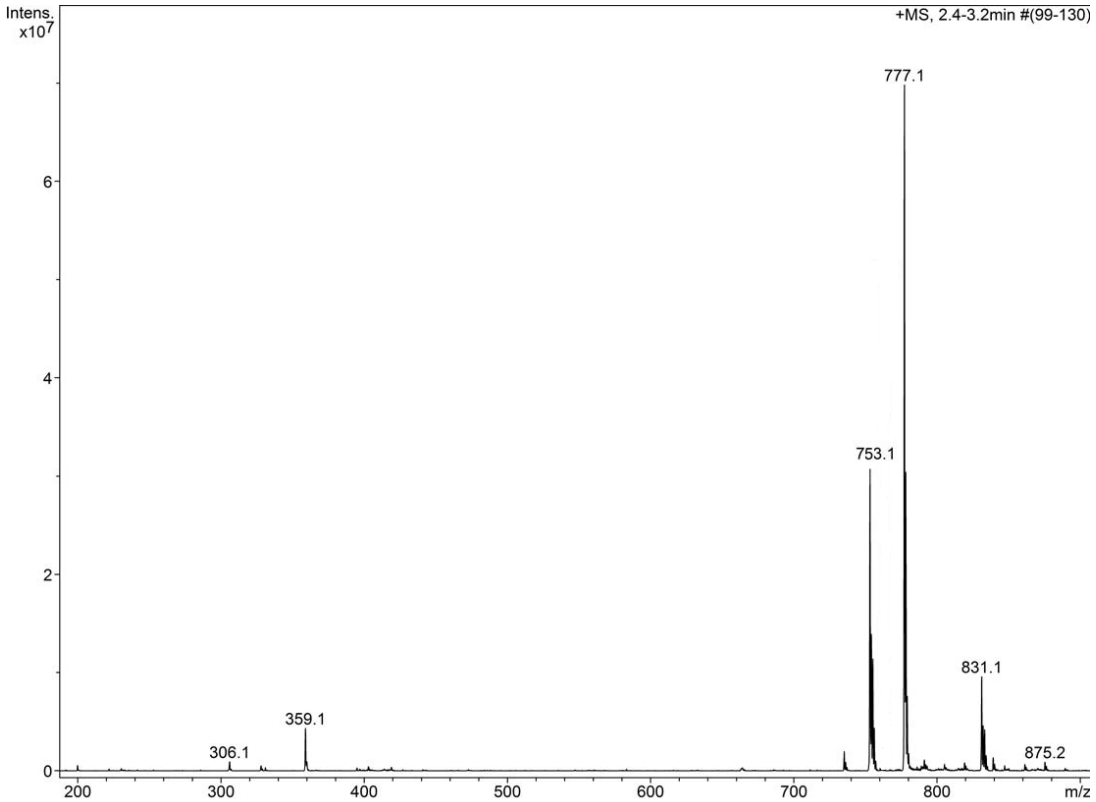

Figure 158. ESI-MS spectrum of **Mn_2L_2Ac** in BBS 50 mM pH = 7.8, where 777.1 m/z correspond to the molecular ion $Mn_2L_2Ac^+$, 753.1 to $[Mn_2L_2(OH)(H_2O)]^+$ and 359.1 m/z to $[Mn_2L_2]^{2+}$.

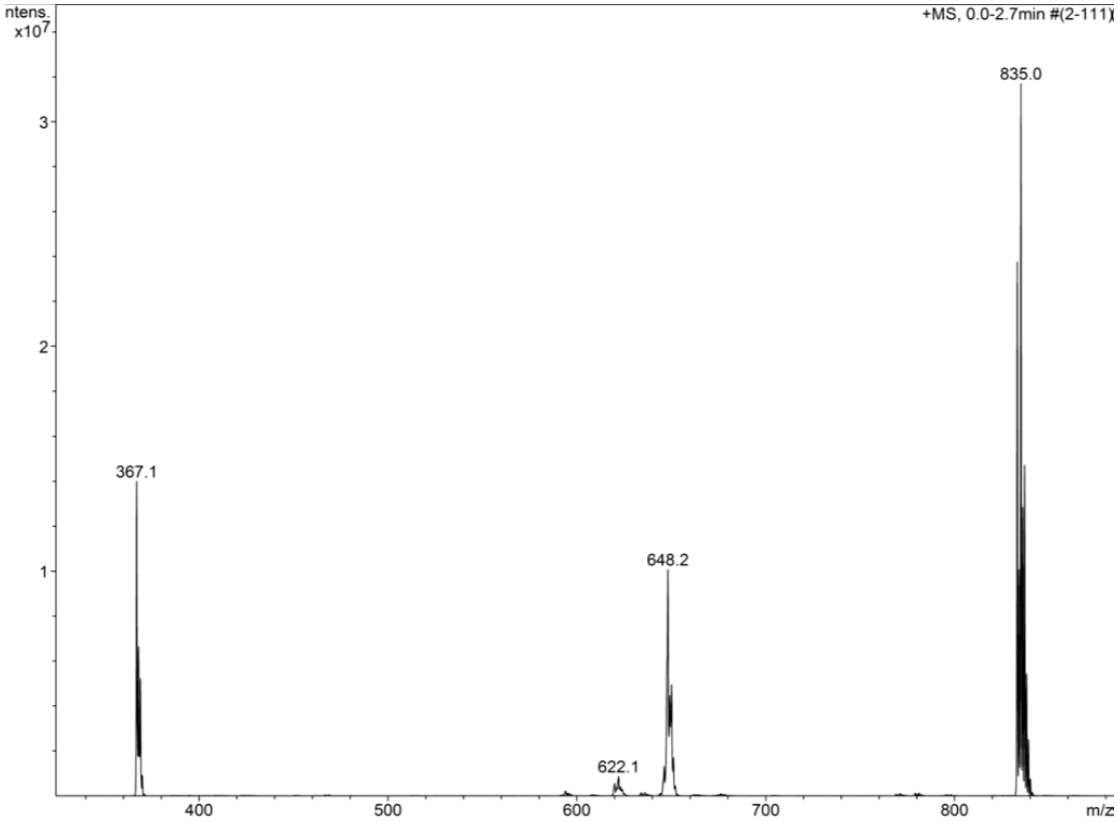

Figure 159. ESI-MS spectrum of $\mathbf{Cu_2L_2}$ in acetonitrile, where 833.0 m/z correspond to the molecular ion $[\mathbf{Cu_2L_2}+ClO_4]^+$ and 367.1 m/z to the fragment $[CuL]^+$.

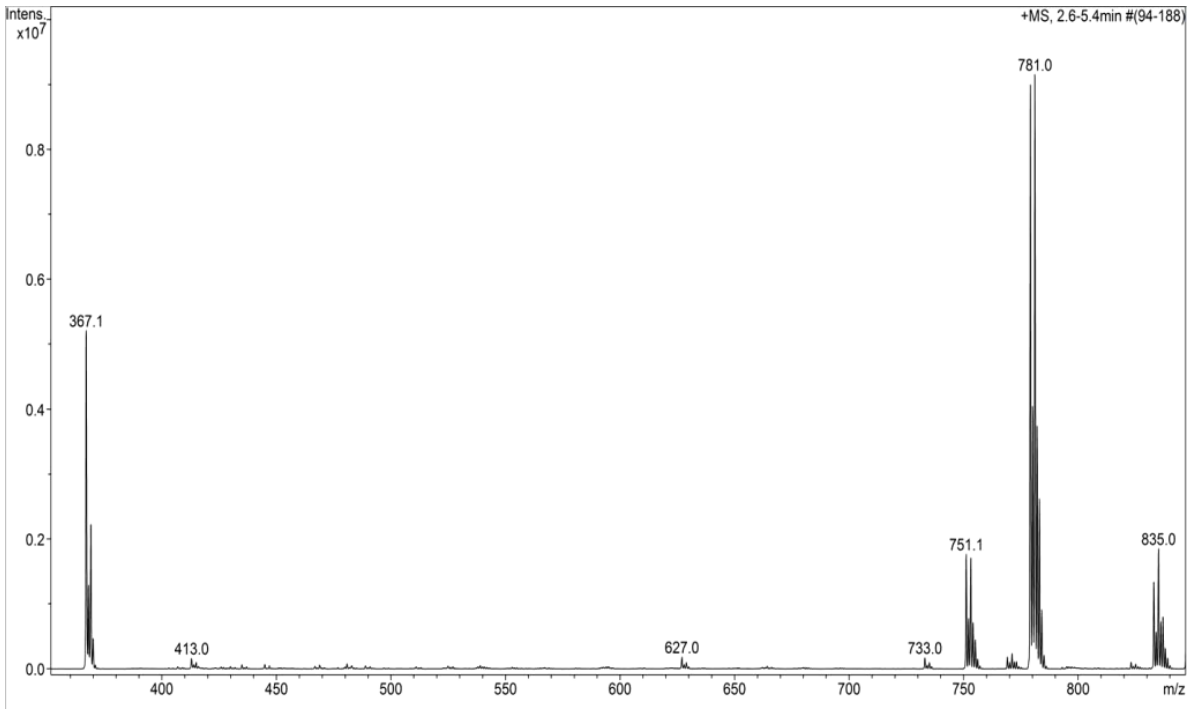

Figure 160. ESI-MS spectrum of $\mathbf{Cu_2L_2}$ in water, where 779.0 correspond to the molecular ion $[\mathbf{Cu_2L_2}+HCO_2]^+$, 751.1 to $[\mathbf{Cu_2L_2}+OH]^+$ and 833.0 m/z $[\mathbf{Cu_2L_2}+ClO_4]^+$ and 367.1 m/z to the fragment $[CuL]^+$.

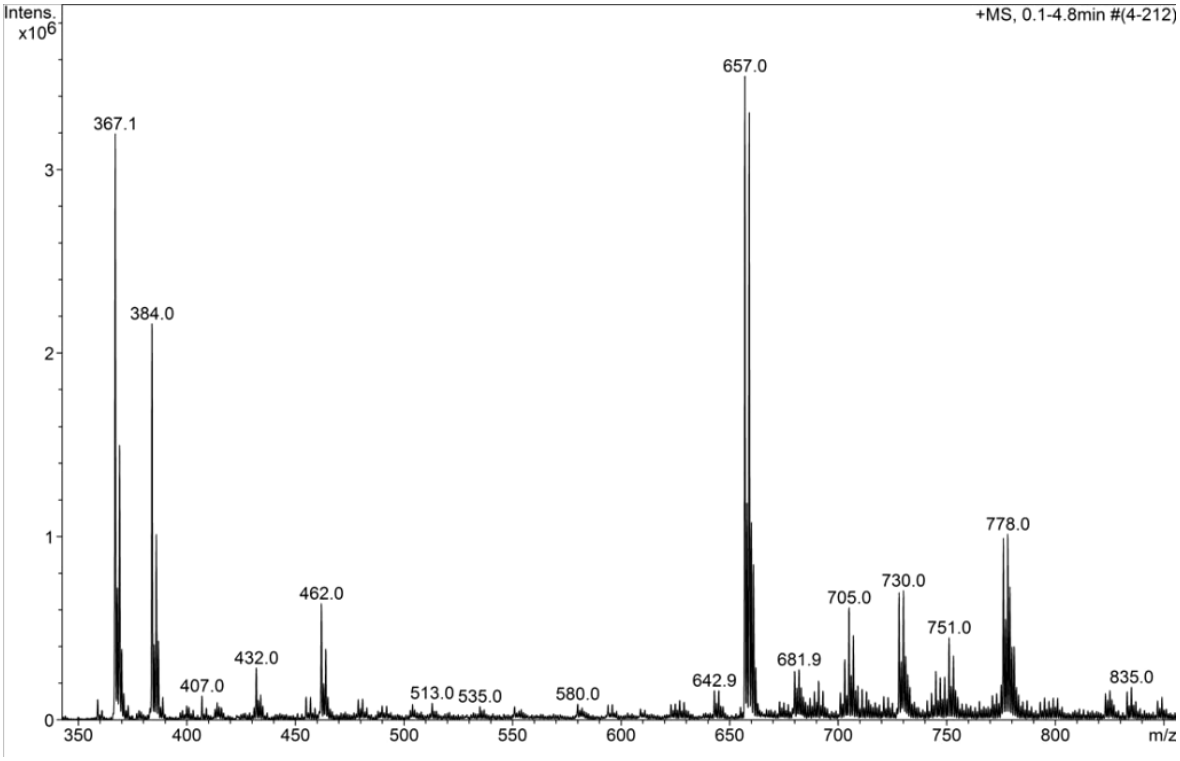

Figure 161. ESI-MS spectrum of $\mathbf{Cu_2L_2}$ + H_2O_2 30 mM in BBS 50 mM after 50 min, where 657.0 m/z correspond to the dinuclear copper specie $[\mathbf{Cu_2L^*_2}]^+$ and 384.0 to the inactive mononuclear copper(III) specie $[CuL]^+$.

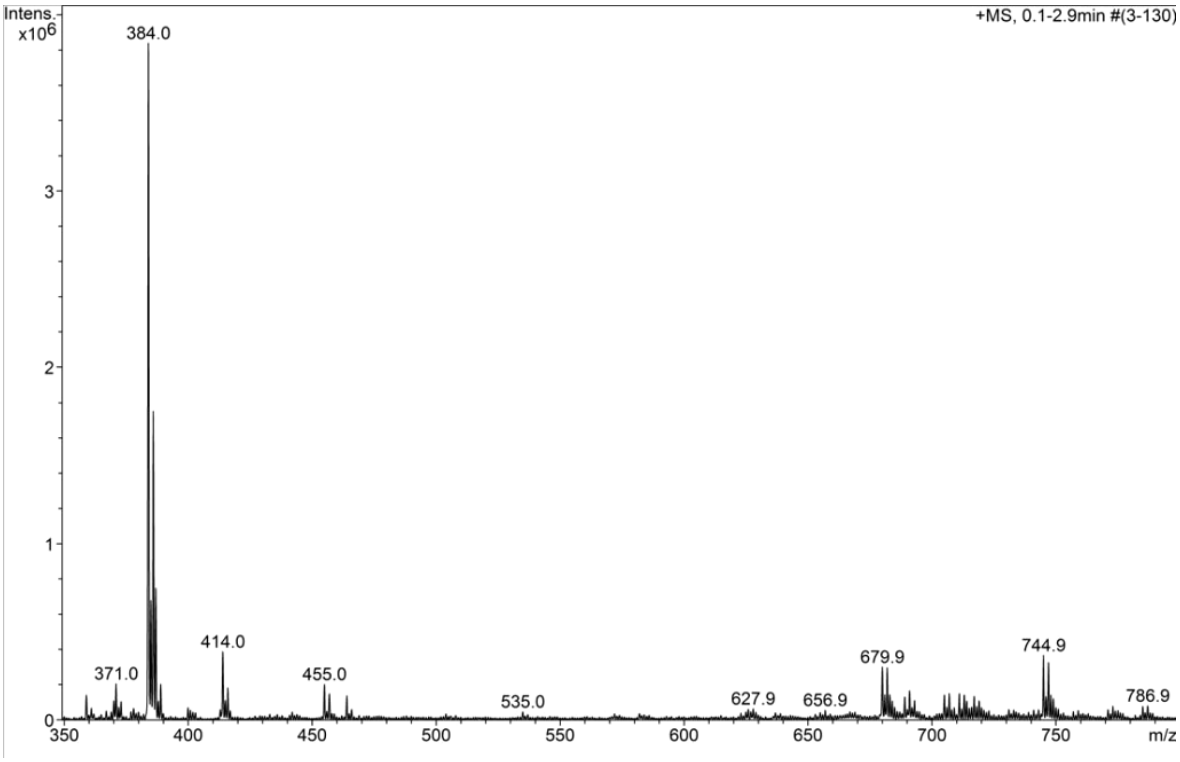

Figure 162. ESI-MS spectrum of $\mathbf{Cu_2L_2}$ + H_2O_2 30 mM in BBS 50 mM after 240 min where 384.0 correspond to the inactive mononuclear copper(III) specie$[CuL]^+$.

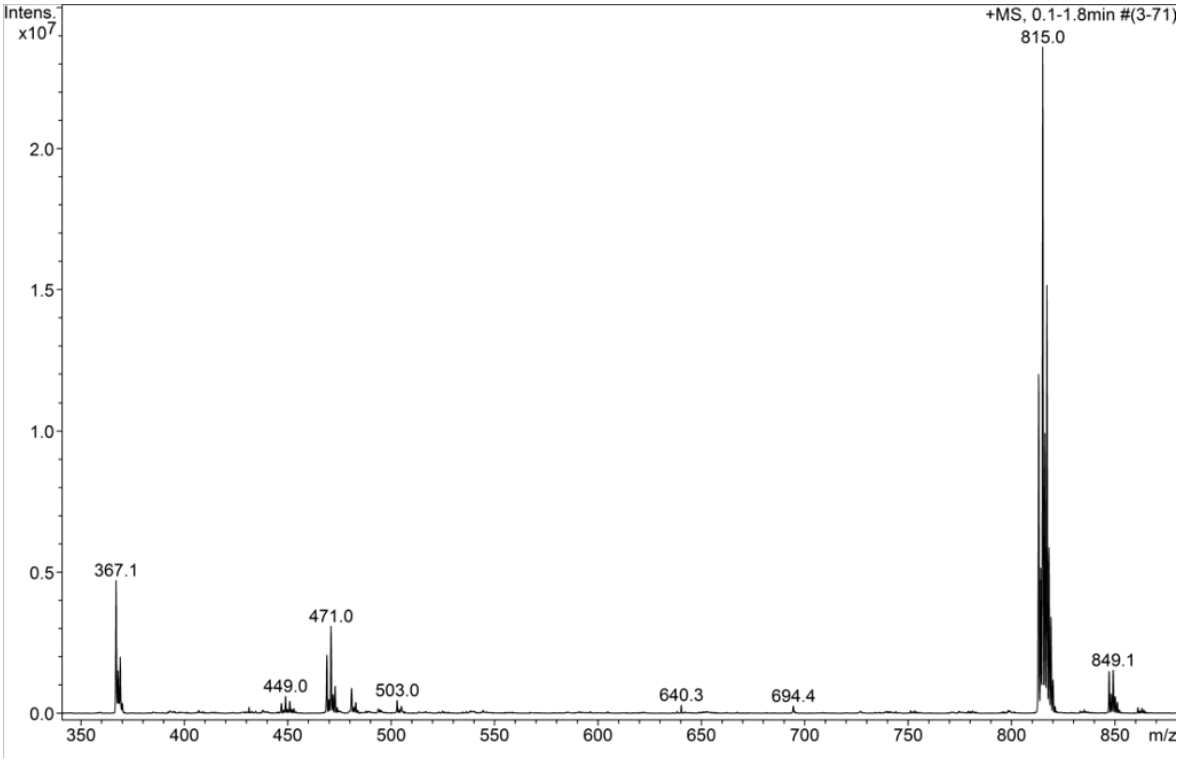

Figure 163. ESI-MS spectrum of $\mathbf{Cu_2L_2}$ + H_2O_2 30 mM + NaBr 50 mM in BBS 50 mM, where 813.0 m/z correspond to the molecular ion $[\mathbf{Cu_2L_2}+Br]^+$ and 367.1 m/z to the fragment $[CuL]^+$.

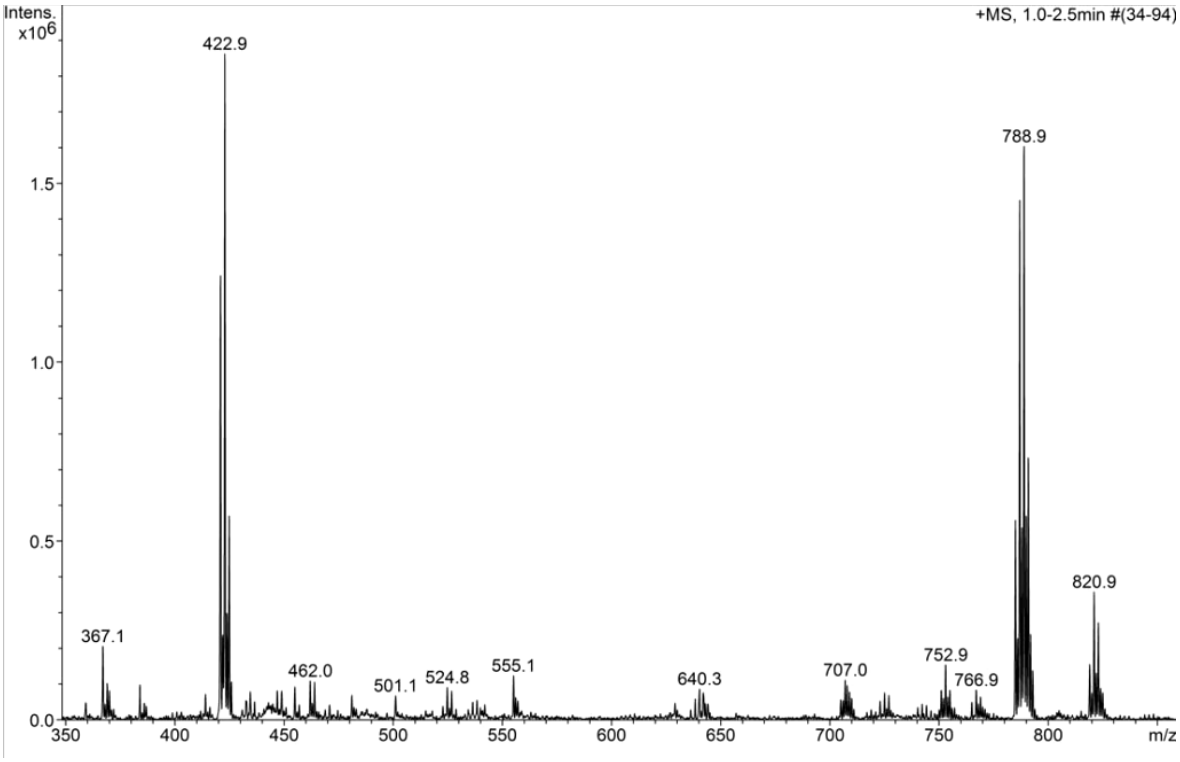

Figure 164. ESI-MS spectrum of $\mathbf{Cu_2L_2}$ + H_2O_2 30 mM + NaBr 50 mM in BBS 50 mM, where 786.9 m/z correspond to the molecular ion $[\mathbf{Cu_2L^*_2}(Br)(H_2O)]^+$ and 420.9 m/z to the inactive specie $[CuL(Br)(H_2O)]^+$.

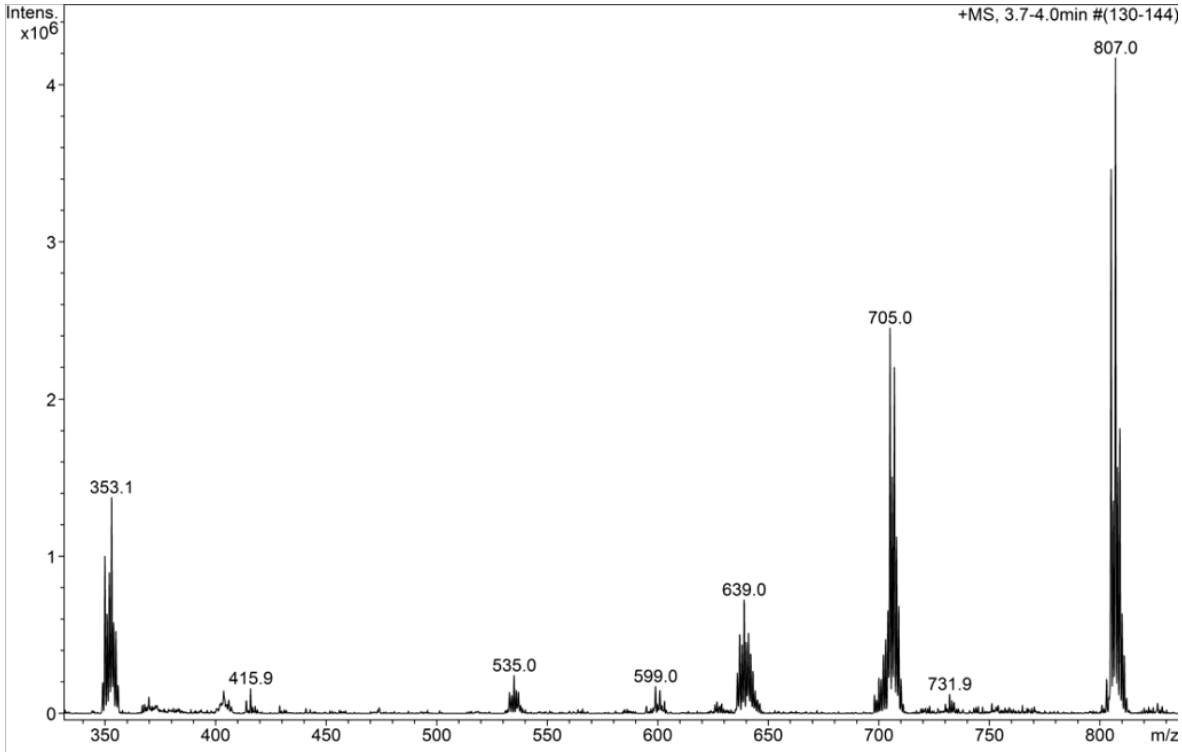

Figure 165. ESI-MS spectrum of $\mathbf{Cu_2L^1_2}$ in acetonitrile, where 805.0 m/z correspond to the molecular ion $[\mathbf{Cu_2L^1_2}+ClO_4]^+$, 705.0 m/z to $[\mathbf{Cu_2L^1_2}-H^+]^+$ and 353.1 m/z to the fragment $[CuL^1]^+$.

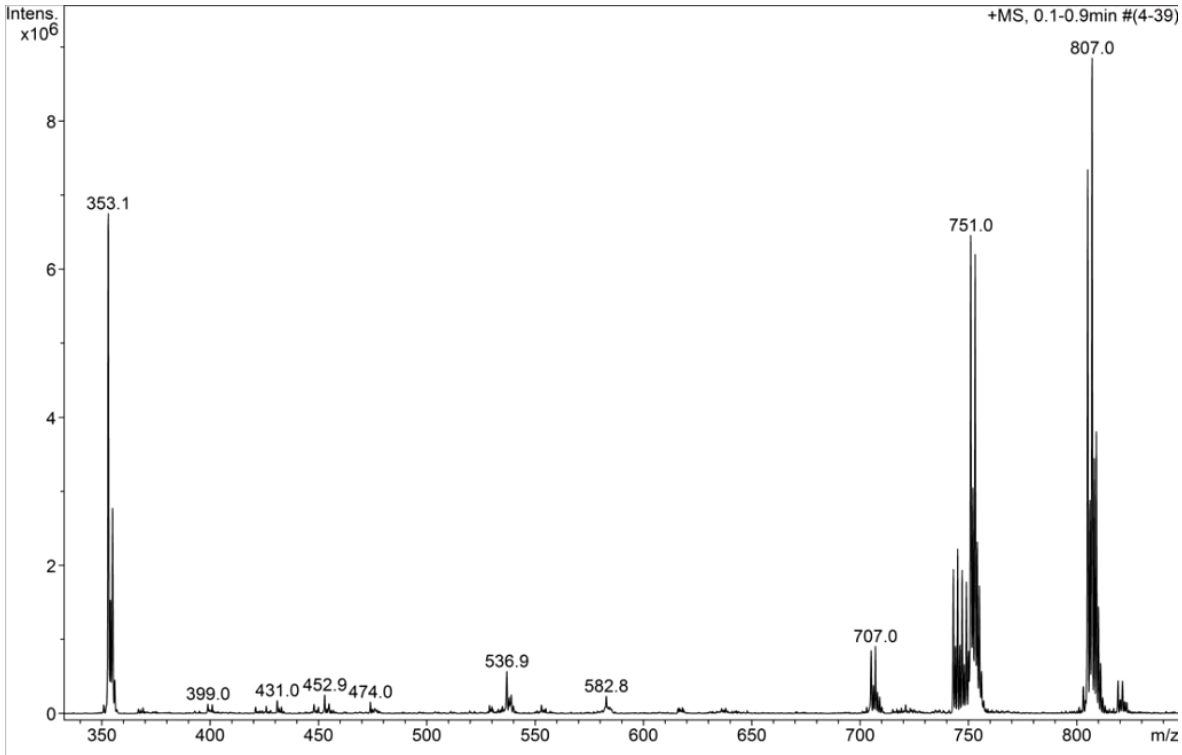

Figure 166. ESI-MS spectrum of $\mathbf{Cu_2L^1_2}$ in water, where 805.0 m/z correspond to the molecular ion $[\mathbf{Cu_2L^1_2}+ClO_4]^+$, 751.0 m/z to $[\mathbf{Cu_2L^1_2}+HCOO]^+$ and 353.1 m/z to the fragment $[CuL^1]^+$.

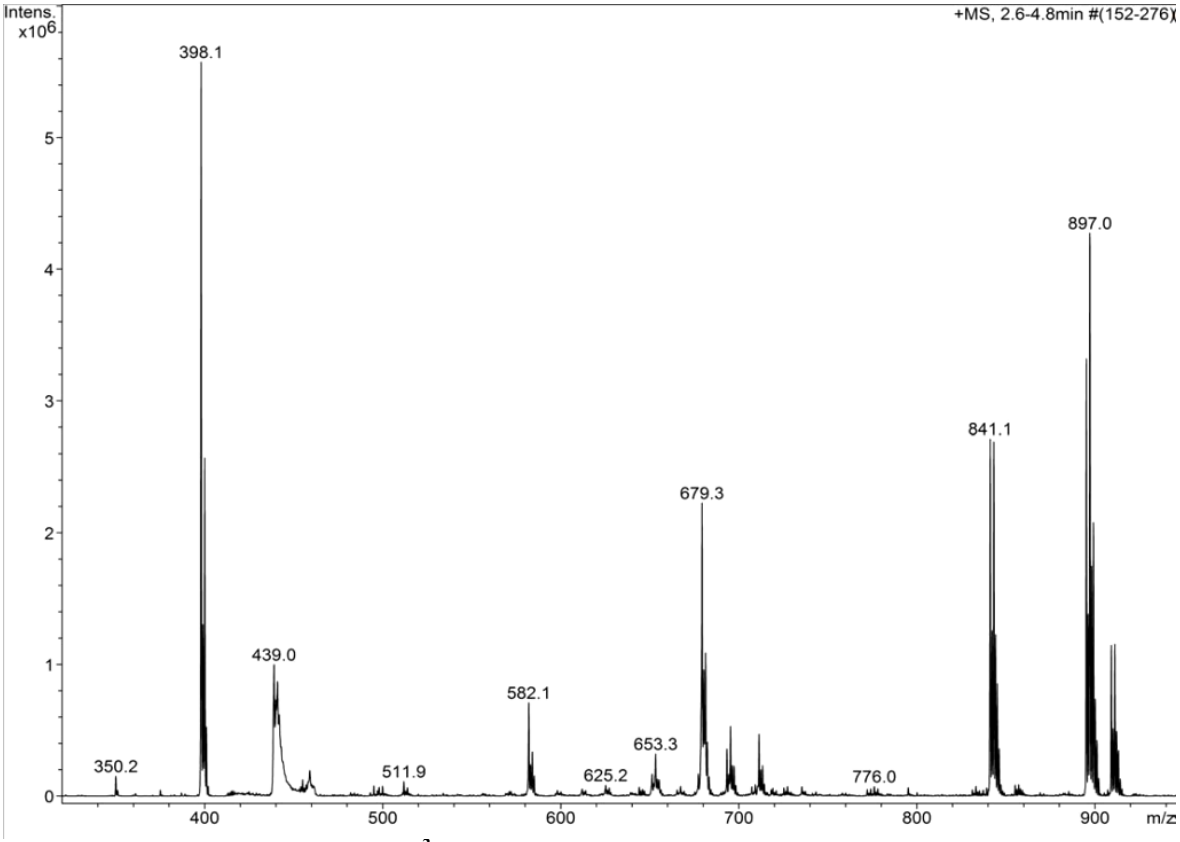

Figure 167. ESI-MS spectrum of $\mathbf{Cu_2L^2_2}$ in acetonitrile, where 895.0 m/z correspond to the molecular ion $[\mathbf{Cu_2L^2_2}+ClO_4]^+$, 841.1 m/z to $[\mathbf{Cu_2L^2_2}+HCO_2]^+$ and 398.1 m/z to the fragment $[CuL^2]^+$.

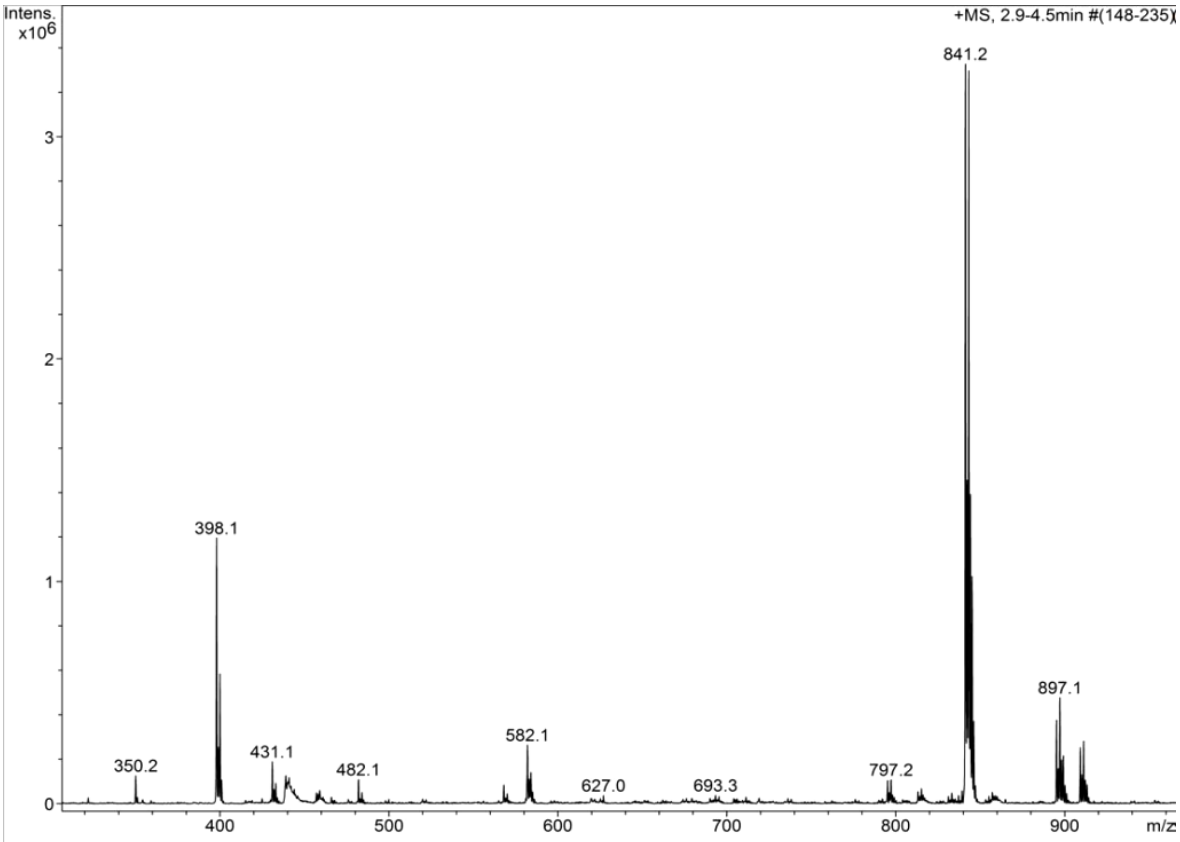

Figure 168. ESI-MS spectrum of $\mathbf{Cu_2L^2_2}$ in water, where 895.0 m/z correspond to the molecular ion $[\mathbf{Cu_2L^2_2}+ClO_4]^+$, 841.1 m/z to $[\mathbf{Cu_2L^2_2}+HCO_2]^+$ and 398.1 m/z to the fragment $[CuL^2]^+$.

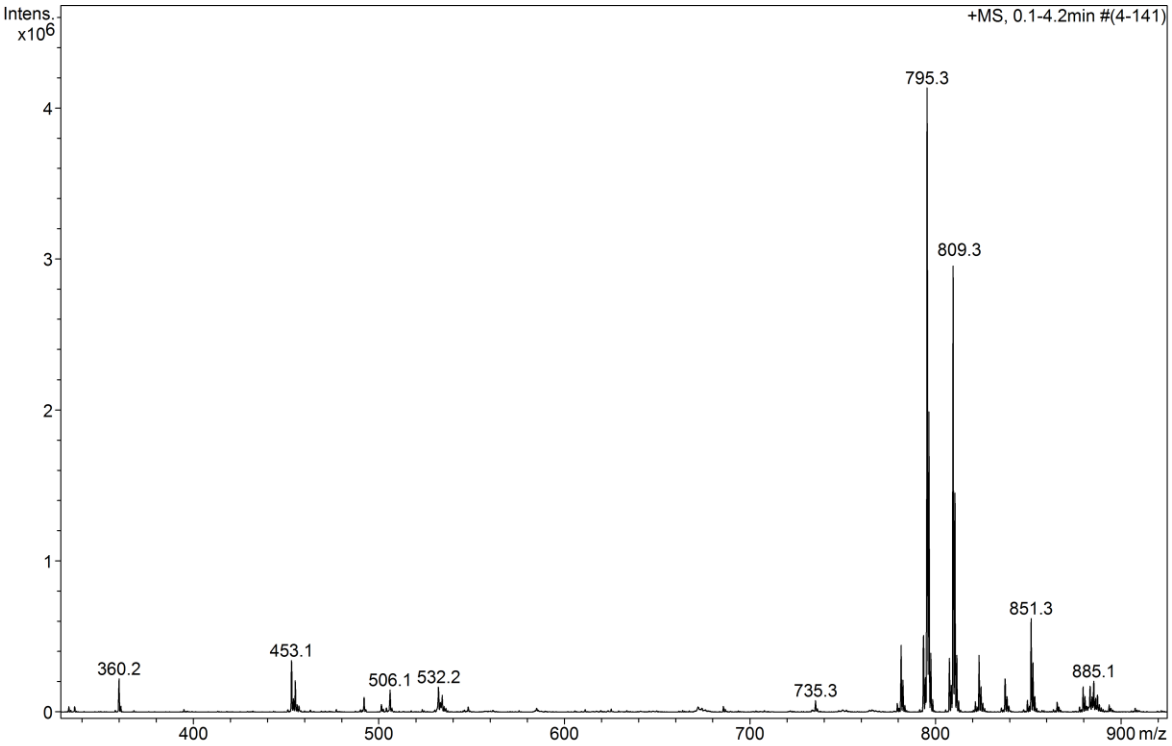

Figure 169. ESI-MS spectrum of **FeL** in acetonitrile where 795 m/z is attributed to $[\mathbf{Fe_2L_2}+H_2O+ACN]^+$ molecular ion.

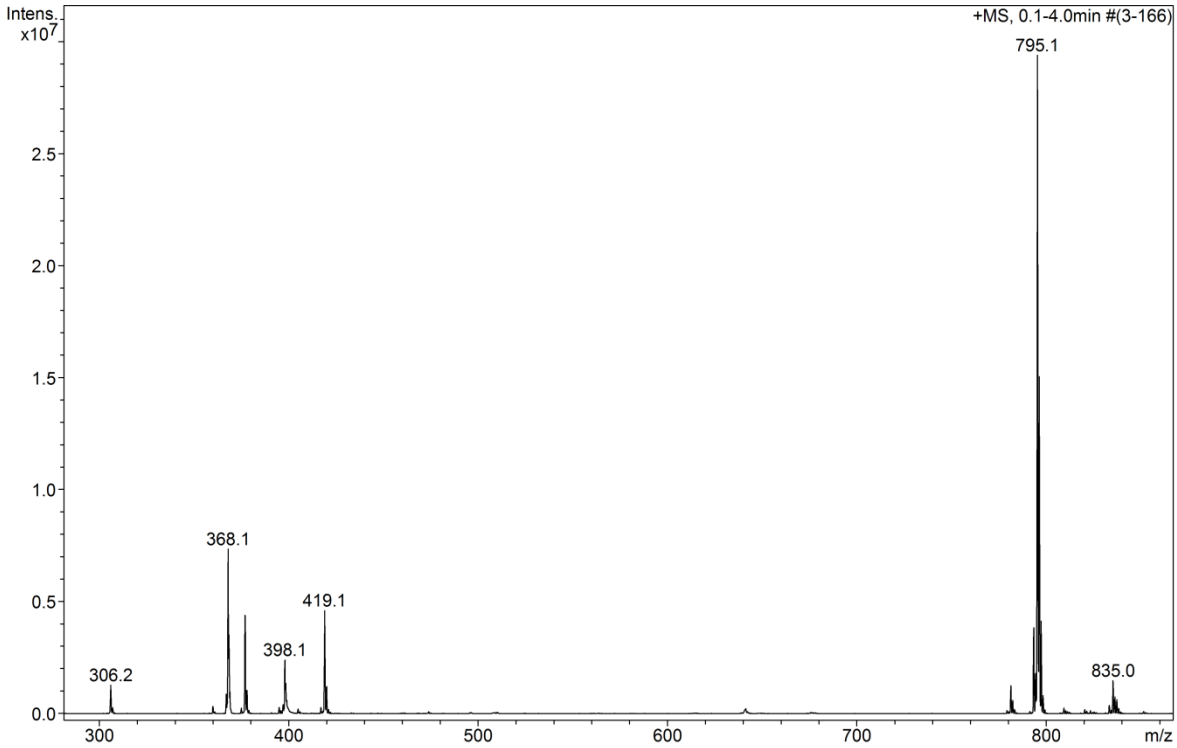

Figure 170. ESI-MS spectrum of $\mathbf{Fe_2L_2}$ in acetonitrile where 795.1 and 835.0 m/z that are respectively attributed to $[\mathbf{Fe_2L_2}+H_2O+ACN]^+$ and $[\mathbf{Fe_2L_2}+ClO_4]^+$, 368.1 and 398.1 m/z attributed to $[\mathbf{Fe_2L_2}]^{2+}$, $[\mathbf{Fe_2L_2}+H^+ +H_2O+ACN]^+$, 377.1 and 419.1 attributed to monomeric fragment $[\mathbf{FeL}+OH^-]^+$ and $[\mathbf{FeL}+H_2O+ACN]^+$.

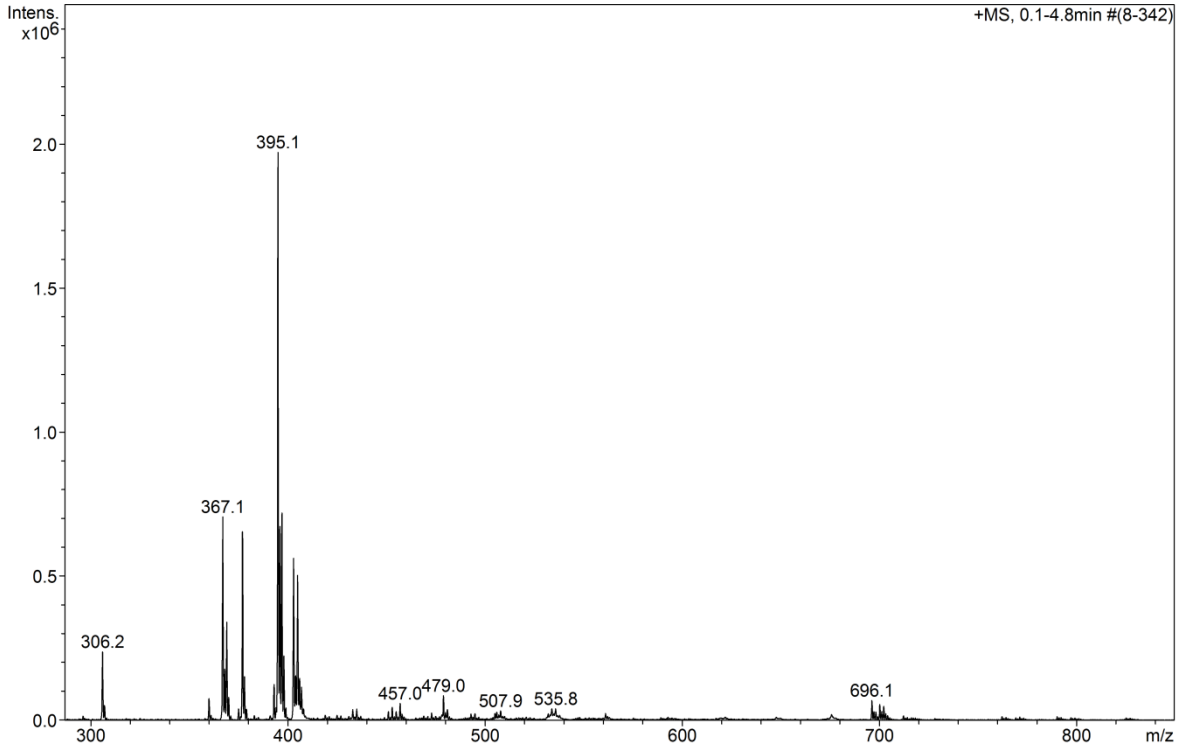

Figure 171. ESI-MS spectrum of **FeL** in water at pH = 3 where 377.1 and 395.1 m/z are attributed respectively to monomers $[\mathbf{FeL}+OH^-]^+$ and $[\mathbf{FeL}+Cl^-]^+$.

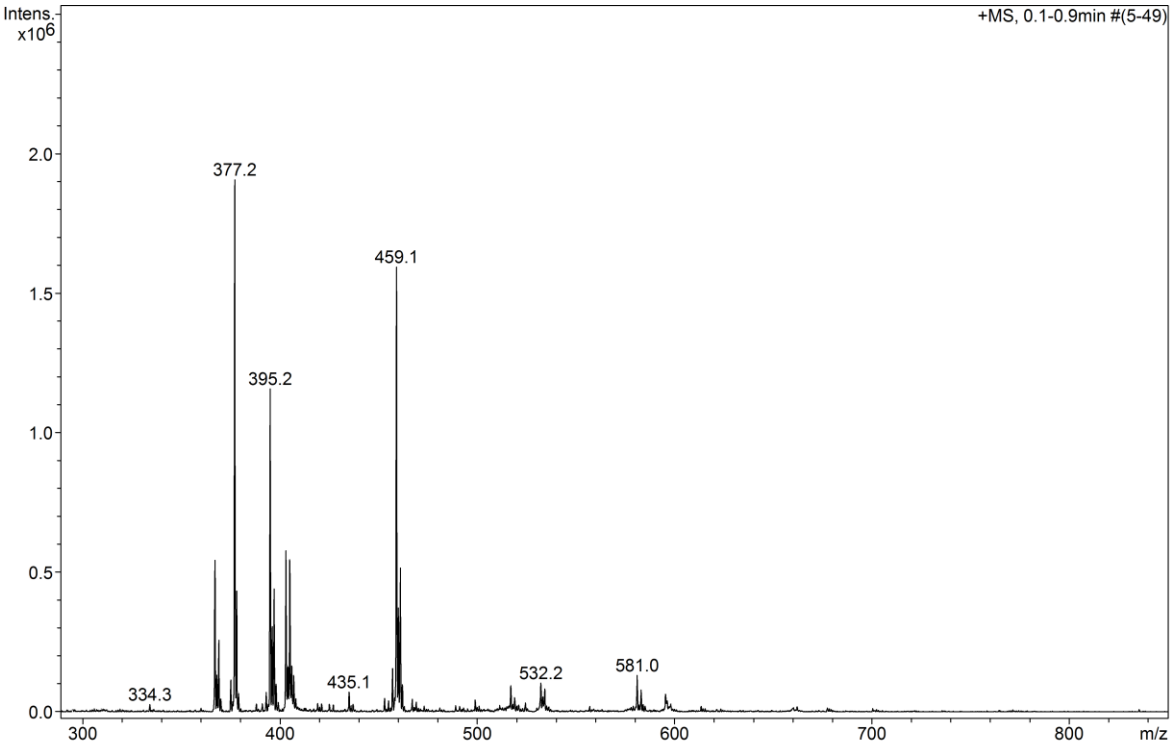

Figure 172. ESI-MS spectrum of $\mathbf{Fe_2L_2}$ in water at pH = 3 where 377.2 and 459.1 m/z are attributed respectively to monomers $[\mathbf{FeL}+OH^-]^+$ and $[\mathbf{FeL}+ClO_4^-]^+$.

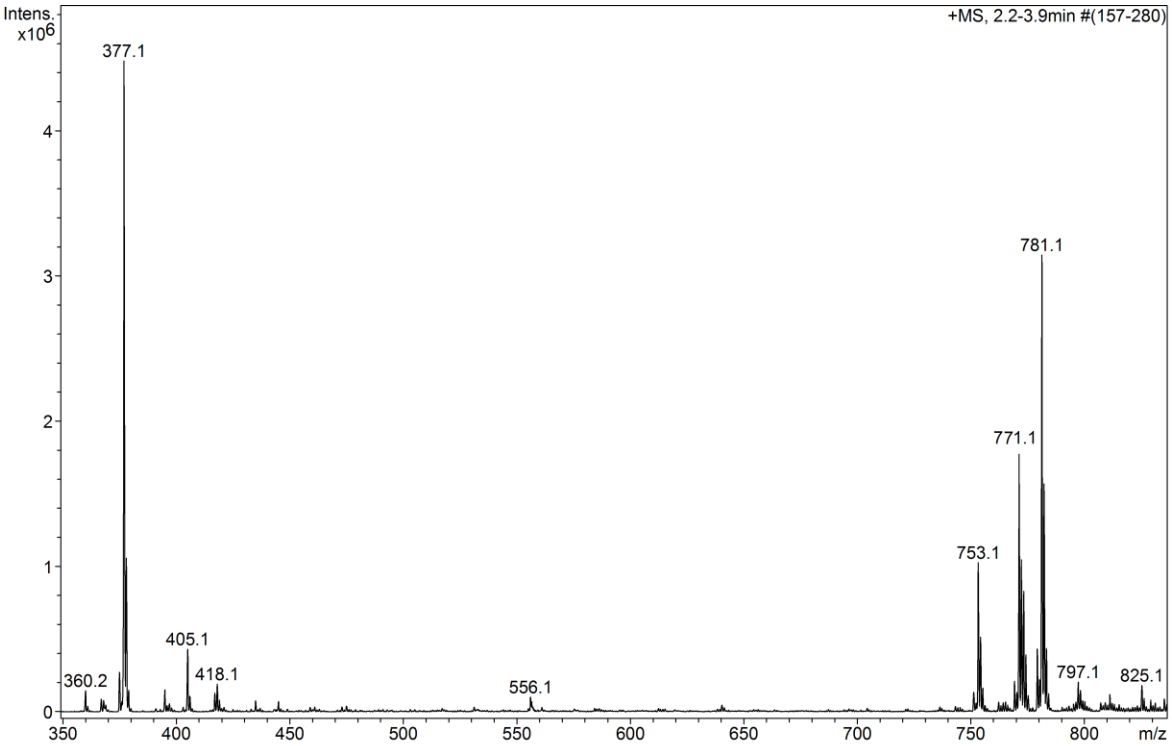

Figure 173. ESI-MS spectrum of **FeL** in water at pH = 5 where 377.1 is attributed to monomer fragment $[\mathbf{FeL}+OH^-]^+$ and 753.1, 771.1 and 781.1 are attributed respectively to dimer $[\mathbf{Fe_2L_2}]^{2+}$ plus OH^-, Cl^- and $HCOO^-$.

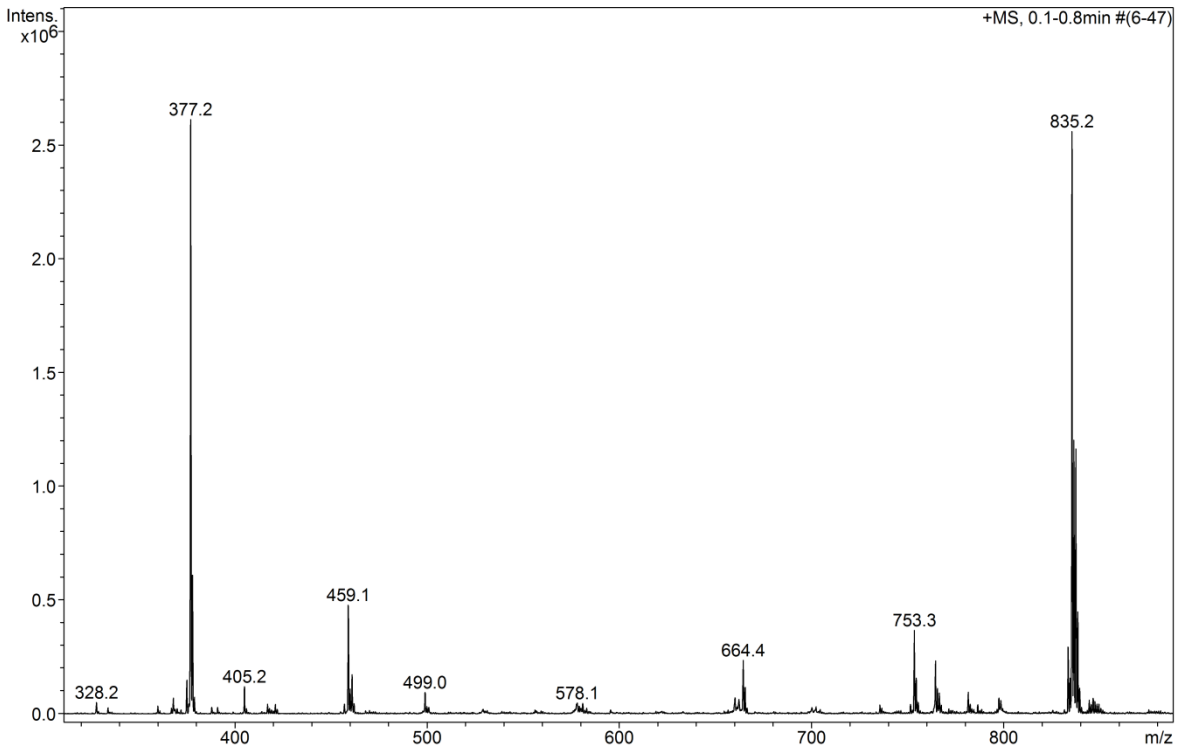

Figure 174. ESI-MS spectrum of $\mathbf{Fe_2L_2}$ in water at pH = 5 where 377.1 and 459.1 m/z are attributed respectively to monomer fragment $[\mathbf{FeL}+OH^-]^+$ and $[\mathbf{FeL}+ClO_4^-]^+$, 753.3 and 835.2 are attributed respectively to dimer $[\mathbf{Fe_2L_2}]^{2+}$ plus OH^- and ClO_4^-.

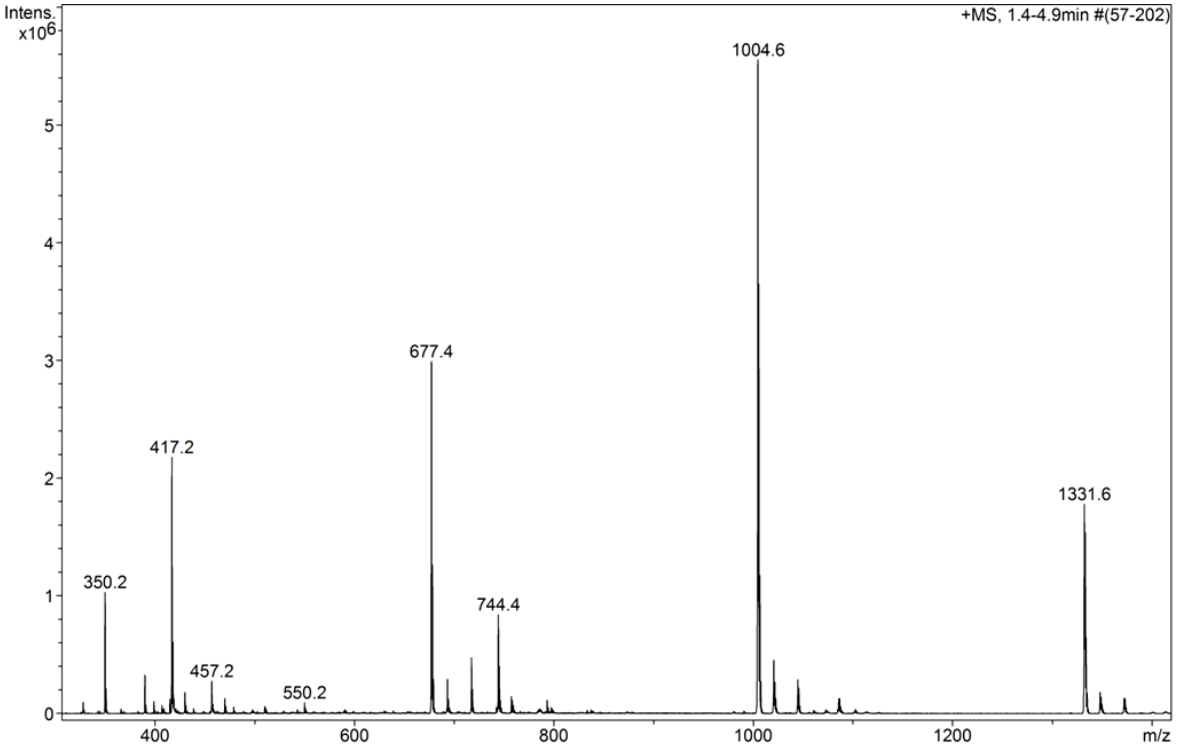

Figure 175. ESI-MS spectrum of $\mathbf{Fe_2L_2}$ in water at pH = 9 where 1331.6, 1004.6, 677.4 and 350.2 m/z are attributed to ligand-sodium cluster $[Na_5L_4]^+$, $[Na_4L_3]^+$, $[Na_3L_2]^+$, $[Na_2L]^+$.

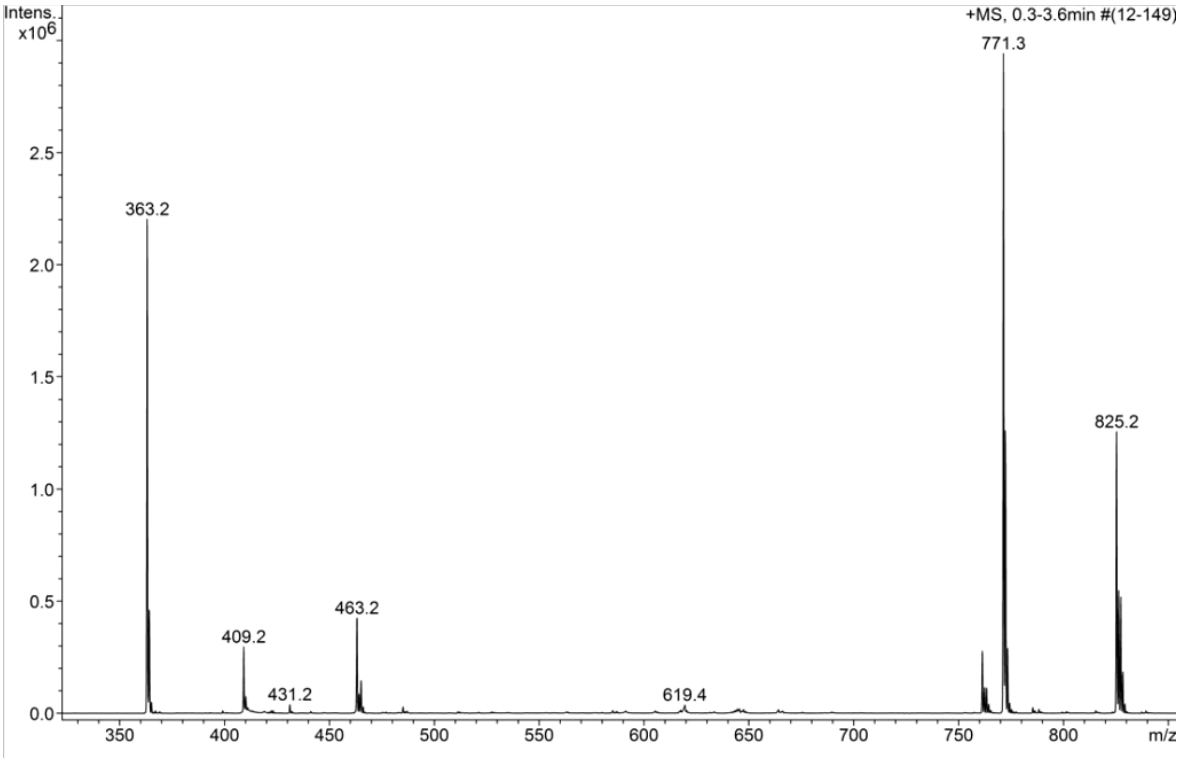

Figure 176. ESI-MS spectrum of $\mathbf{Co_2L_2}$ in acetonitrile, where 771.3 correspond to the molecular ion $[\mathbf{Co_2L_2}+HCOO]^+$, 825.2 m/z to $[\mathbf{Co_2L_2}+ClO_4]^+$ and 363.2 m/z to the fragment $[CoL]^+$.

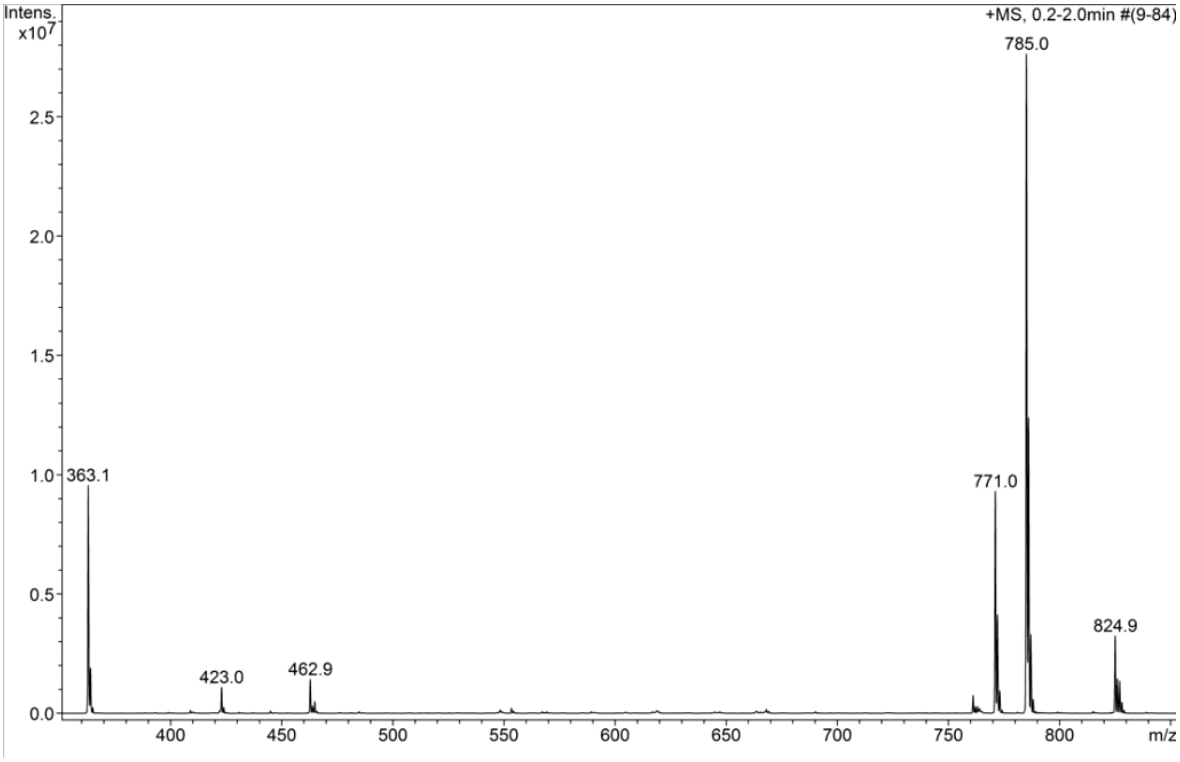

Figure 177. ESI-MS spectrum of $\mathbf{Co_2L_2Ac}$ in acetonitrile, where 785.0 correspond to the molecular ion $[\mathbf{Co_2L_2Ac}]^+$, 825.2 m/z $[\mathbf{Co_2L_2}+ClO_4]^+$ and 363.2 m/z to the fragment $[CoL]^+$.

Cyclic Voltammetry

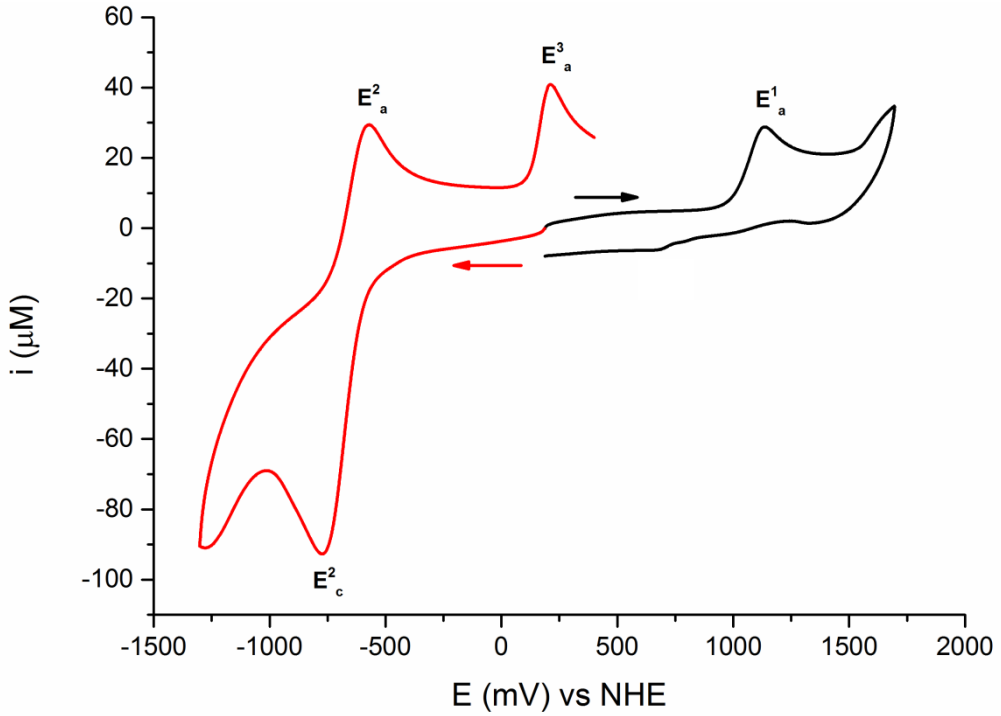

Figure 178. CV of 1 mM 2-{[[Di(2-pyridyl)methyl](methyl)amino]methyl}phenol (L) in CH_3CN ($TBAClO_4$ 0.1 M); E^2_c = -772 mV, E^2_a = -599 mV, E^3_a = 197 mV and E^1_a = 1133 mV.

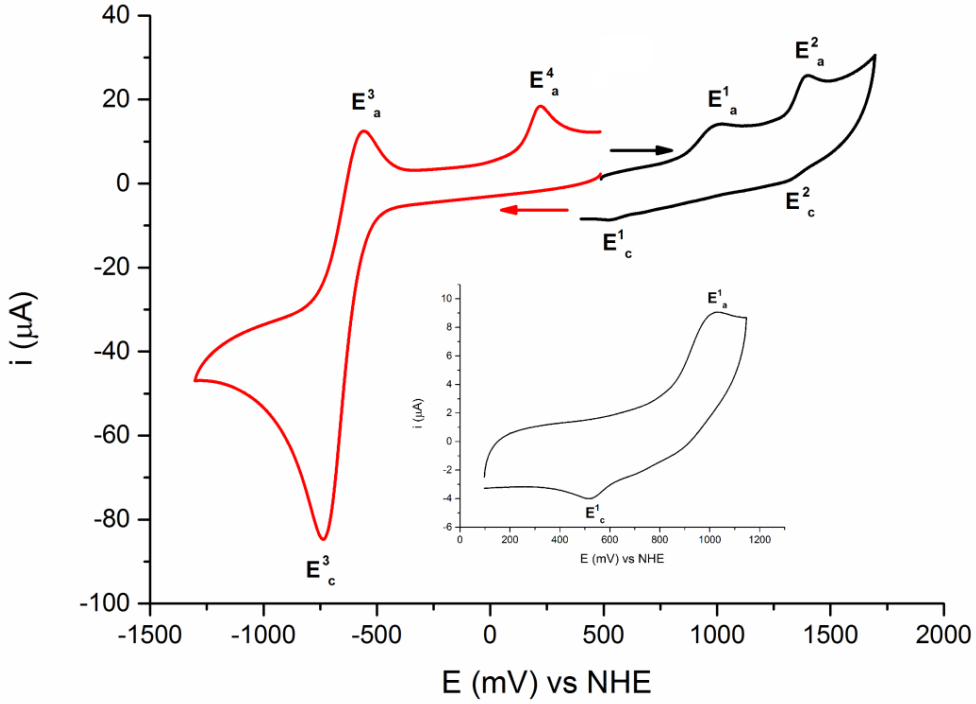

Figure 179. CV of 0.5 mM $\mathbf{Mn_2L_2Ac^+}$ in CH_3CN (TBAClO_4 0.1 M); The anodic peak E^1_a is ascribed to monoelectronic $Mn_2^{II,II} \rightarrow Mn_2^{II,III}$ oxidation. The second $Mn_2^{II,III} \rightarrow Mn_2^{III,III}$ oxidation overlaps with the ligand features.[S6] The reduction waves in red are attributed to the ligand. E^1_a = 1022 mV, E^2_a = 1402 mV, E^2_c = 1299 mV, E^1_c = 516 mV, E^3_c = -749 mV and E^3_a = -563 mV and E^4_a = 220 mV. The inset show the wave of the the $Mn_2^{II,III}$/ $Mn_2^{II,II}$ couple. Addition of water results in a steady shift of the $Mn_2^{II,III}$/ $Mn_2^{II,II}$ redox potentials.

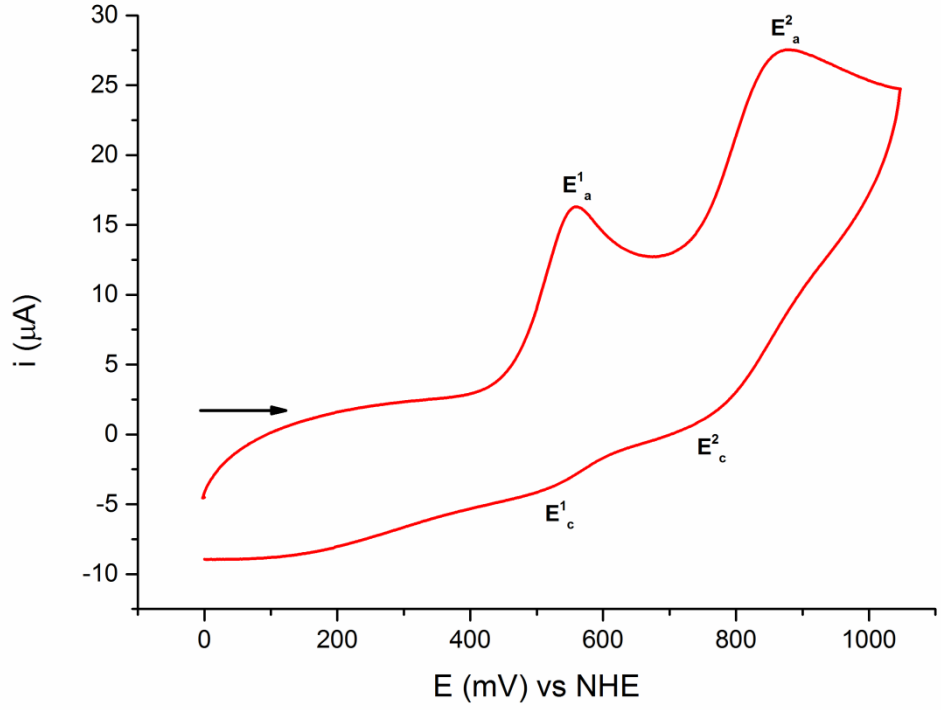

Figure 180. CV of 0.5 mM $\mathbf{Mn_2L_2Ac^+}$ in 50 mM phosphate buffer (pH = 7.8, NaCl 0.1 M); E^1_a = 559 mV, E^2_a = 879 mV, E^2_c = 747 mV and E^1_c = 515 mV.

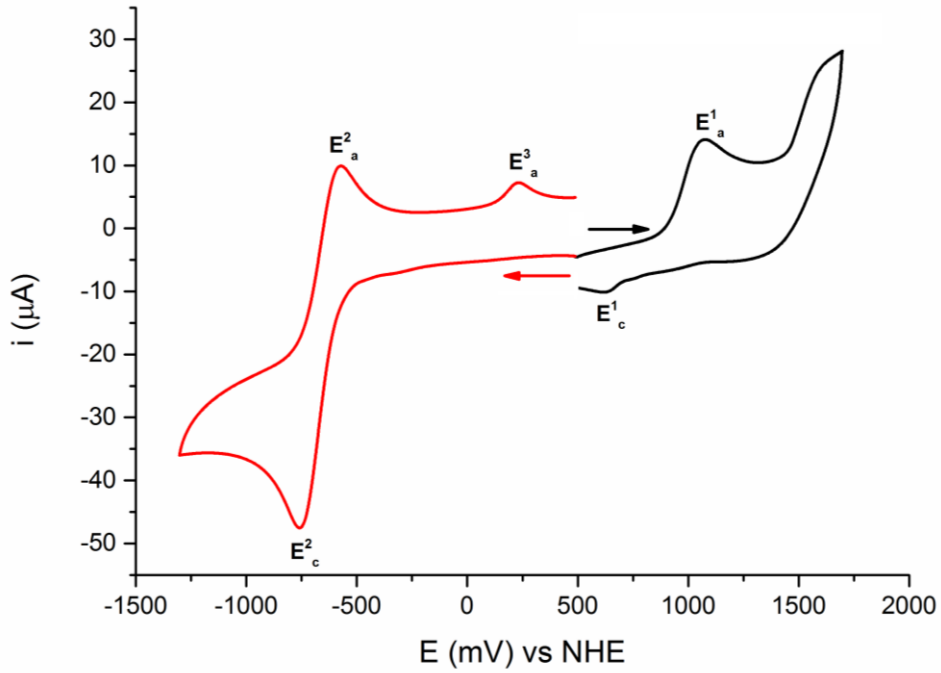

Figure 181. CV of 1 mM 2-({[Di(2-pyridyl)methyl]amino}methyl)phenol (L^1) in CH_3CN ($TBAClO_4$ 0.1 M); E^2_c = -758 mV, E^2_a = -573 mV, E^3_a = 231 mV, E^1_a = 1079 mV and E^1_c = 621 mV.

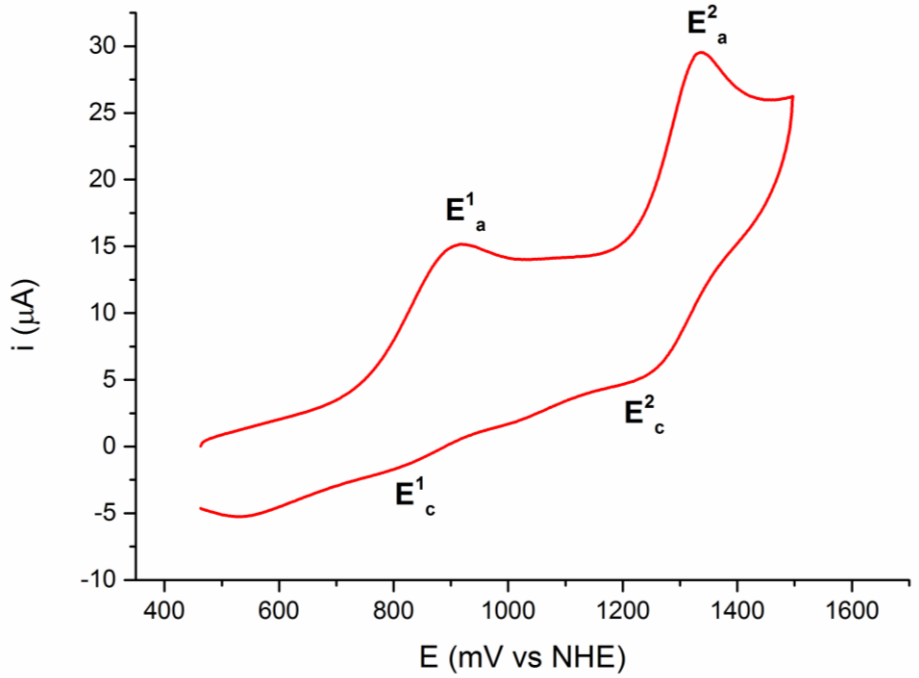

Figure 182. CV of 0.5 mM $\mathbf{Mn_2L^1{}_2Ac^+}$ in acetonitrile ($TBAClO_4$ 0.1 M); E^1_a = 920 mV, E^2_a = 1335 mV, E^2_c = 1220 mV and E^1_c = 820 mV.

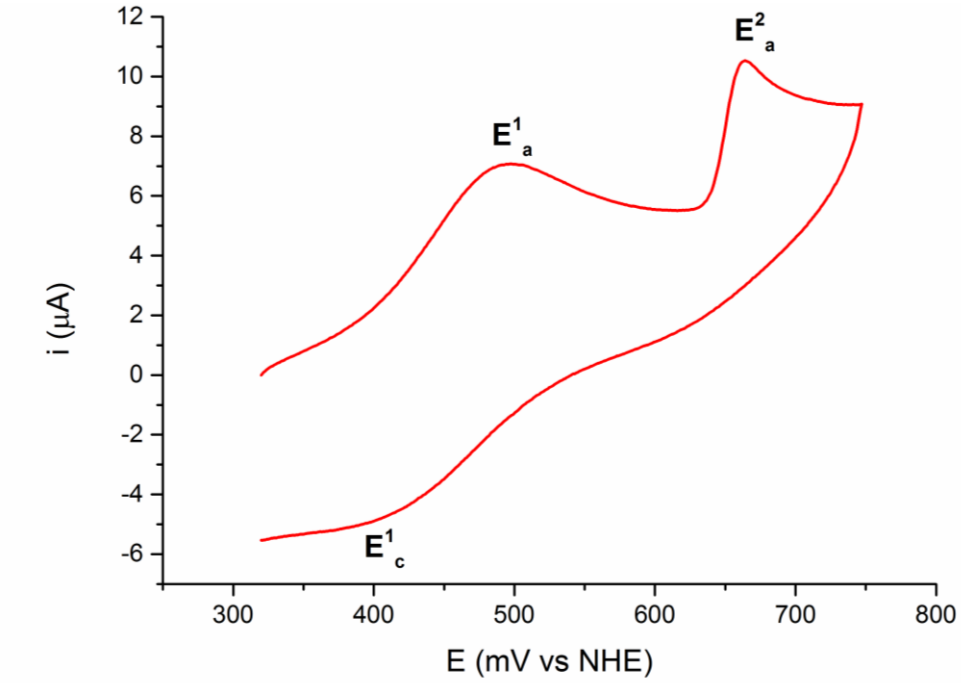

Figure 183. CV of 0.5 mM $\mathbf{Mn_2L^1_2Ac^+}$ in 50 mM borate buffer (pH = 7.8, NaCl 0.1 M); E^1_a = 498 mV, E^2_a = 664 mV and E^1_c = 392 mV.

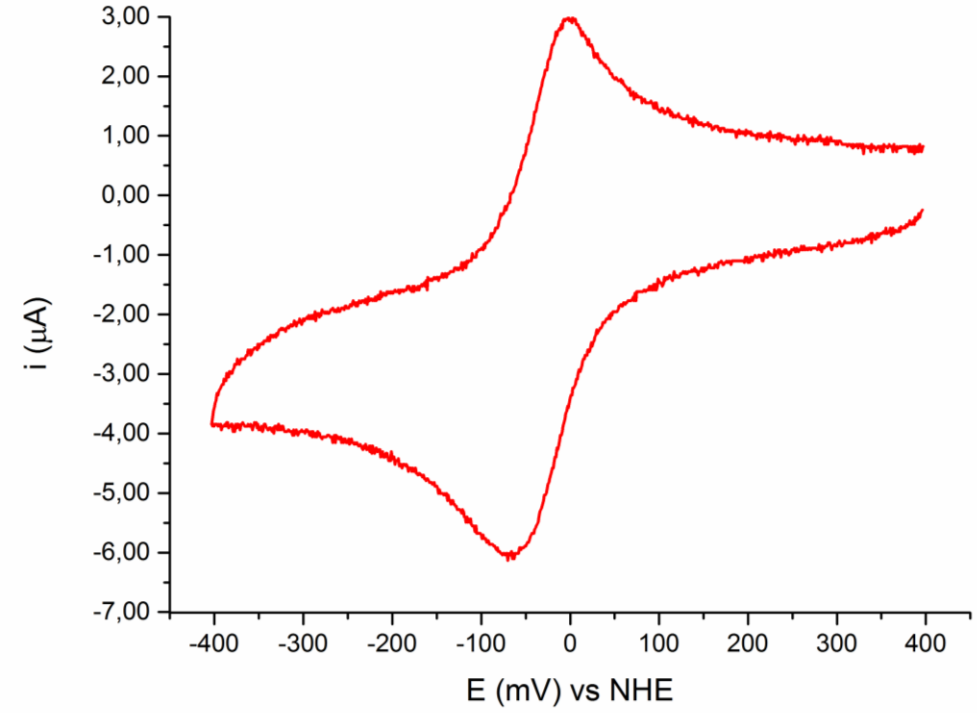

Figure 184. CV of 0.5 mM Mn(III)-meso-tri(N-methyl-4-pyridyl)mono(4-carboxyphenyl)porphine (**P1**) in 50 mM phosphate buffer (pH = 7.8, NaCl 0.1 M); for Mn^{III}/Mn^{II} couple $E_{1/2}$ = -32 mV, ΔE = 65 mV.

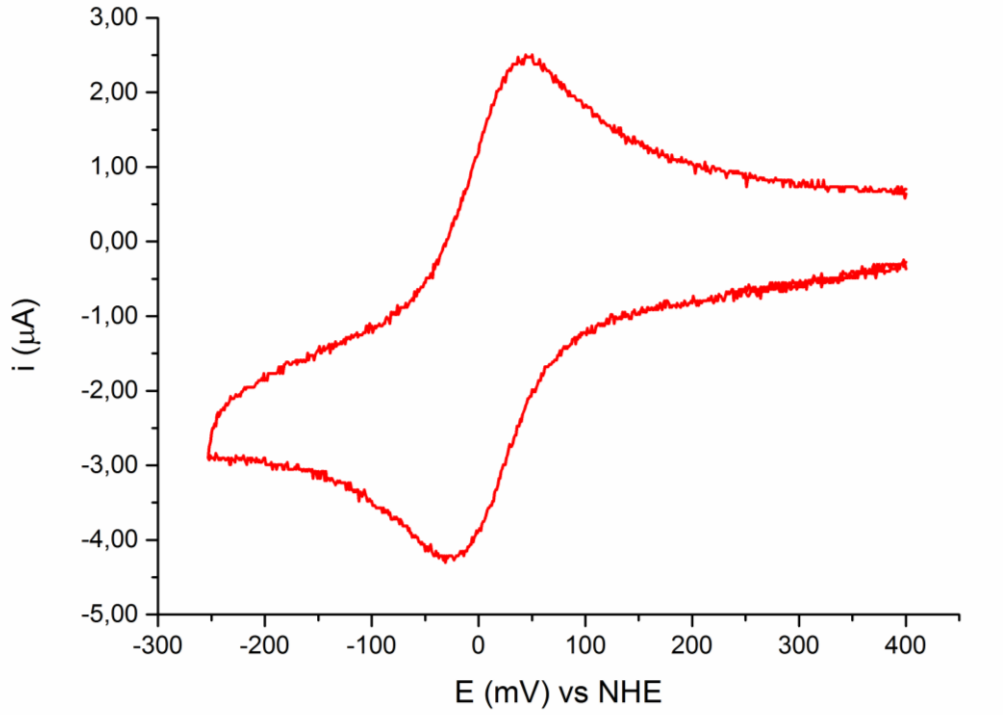

Figure 185. CV of 0.5 mM Mn(III)-meso-tri(N-methyl-4-pyridyl)mono(N-4-carboxybenzyl-4-pyridyl)porphine (**P2**) in 50 mM phosphate buffer (pH = 7.8, NaCl 0.1 M); for Mn^{III}/Mn^{II} couple $E_{1/2}$ = 10 mV, ΔE = 76 mV.

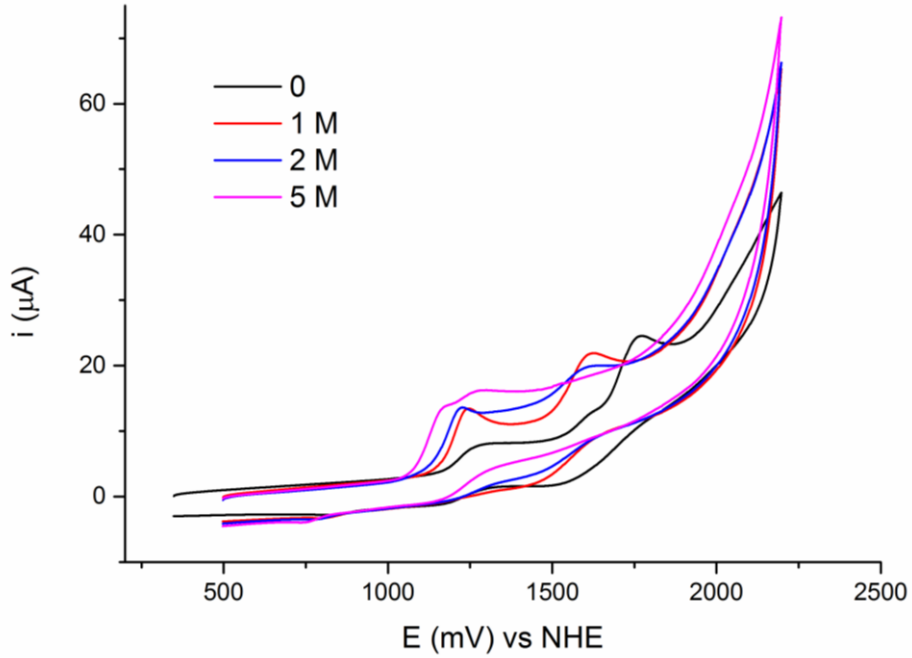

Figure 186. CV of the oxidation of $\mathbf{Cu_2L^1_2}$ (0.5 mM) in CH_3CN ($TEABF_4$ 0.1 M) with increasing aliquots of water.

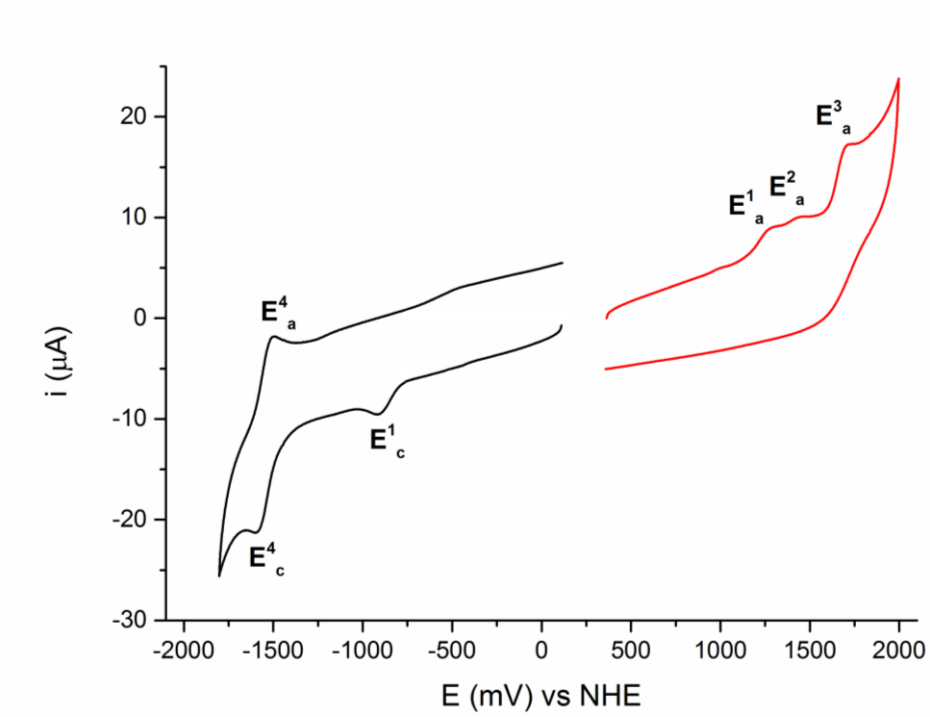

Figure 187. CV of 1 mM 2-({[Di(2-pyridyl)methyl]amino}methyl)-4-nitrophenol (L^2) in CH_3CN ($TEABF_4$ 0.1 M); E^4_c = -1600 mV, E^4_a = -1499 mV, E^1_c = -916 mV, E^1_a = 1299 mV, E^2_a = 1452 mV and E^3_a = 1727 mV.

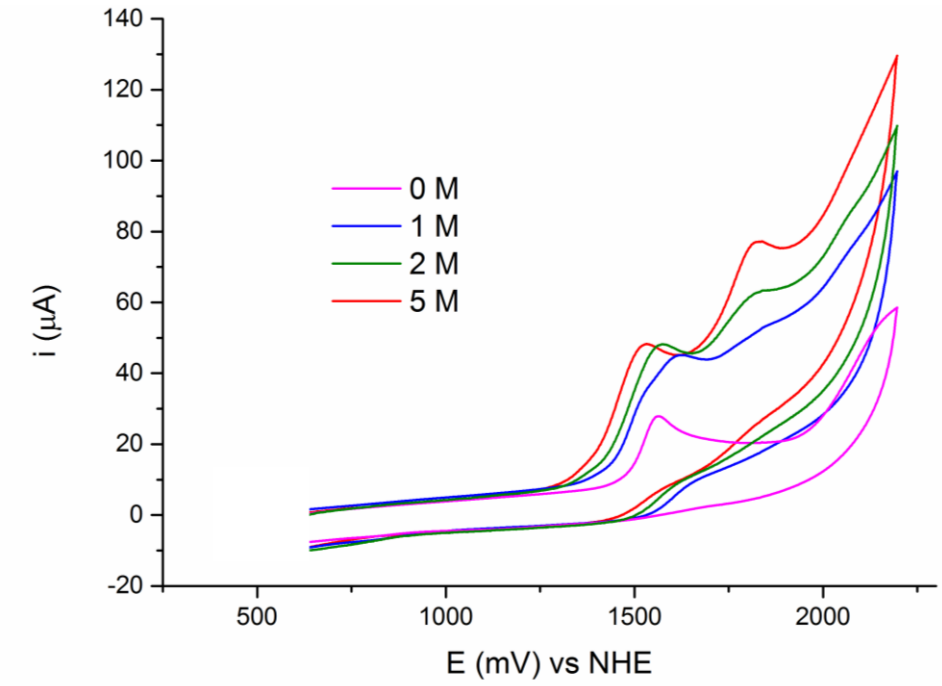

Figure 188. CV of the oxidation of $Cu_2L^2_2$ (0.5 mM) in CH_3CN ($TEABF_4$ 0.1 M) with increasing aliquots of water.

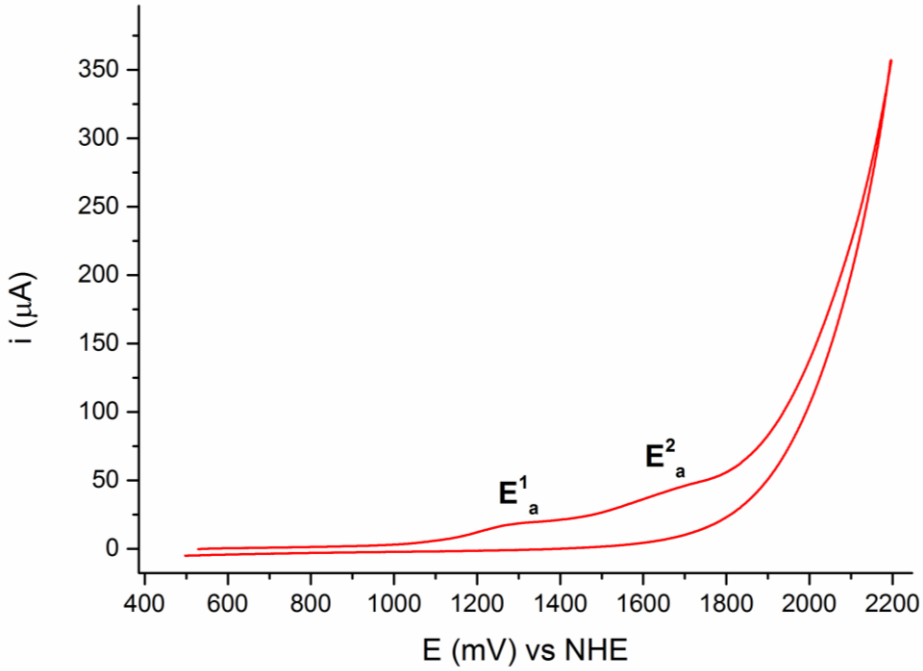

Figure 189. CV of the oxidation of $\mathbf{Cu_2L^2_2}$ (0.5 mM) in PBS 50 mM (pH 7.8, $TEABF_4$ 0.1 M), E^1_a = 1.31 V and E^2_a = 1.71 V (vs NHE).

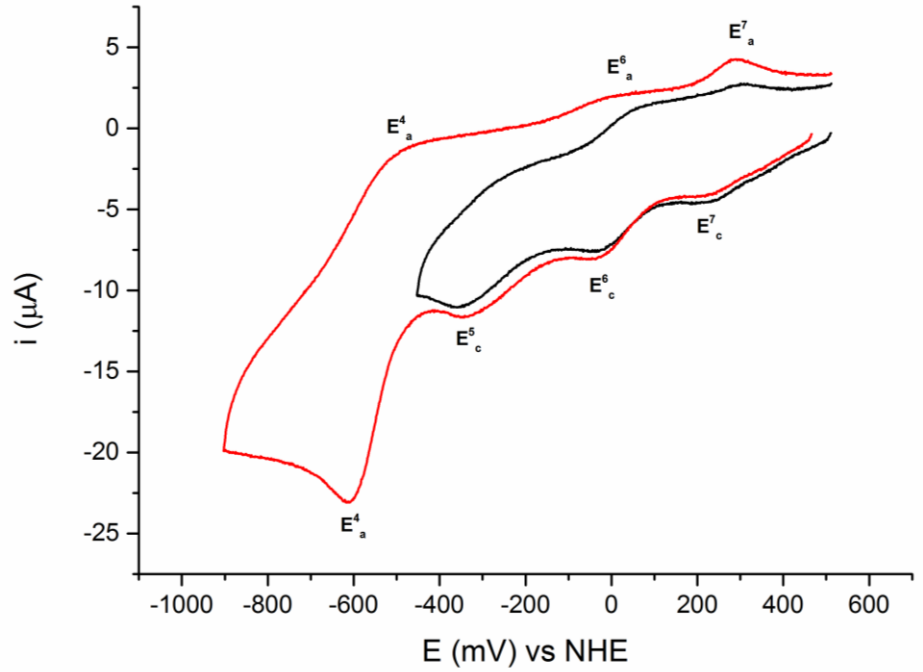

Figure 190. CV of the reduction of $\mathbf{Fe_2L_2}$ (0.5 mM) in CH_3CN ($TBAClO_4$ 0.1 M). In black are reported the metal based processes $E_{1/2}$ = 257 is ascribed to monoelectronic $Fe_2^{III,III} \rightarrow Fe_2^{III,II}$ reduction, the second $E_{1/2}$ = -28 mV to $Fe_2^{III/II}$-$Fe_2^{II,II}$ reduction and peak E_c^5 = -360 mV ascribed to the complex reduction to the $Fe_2^{II/II}$-$Fe_2^{II,I}$ redox state. In red is reported the full reduction CV including the ligand based processes.

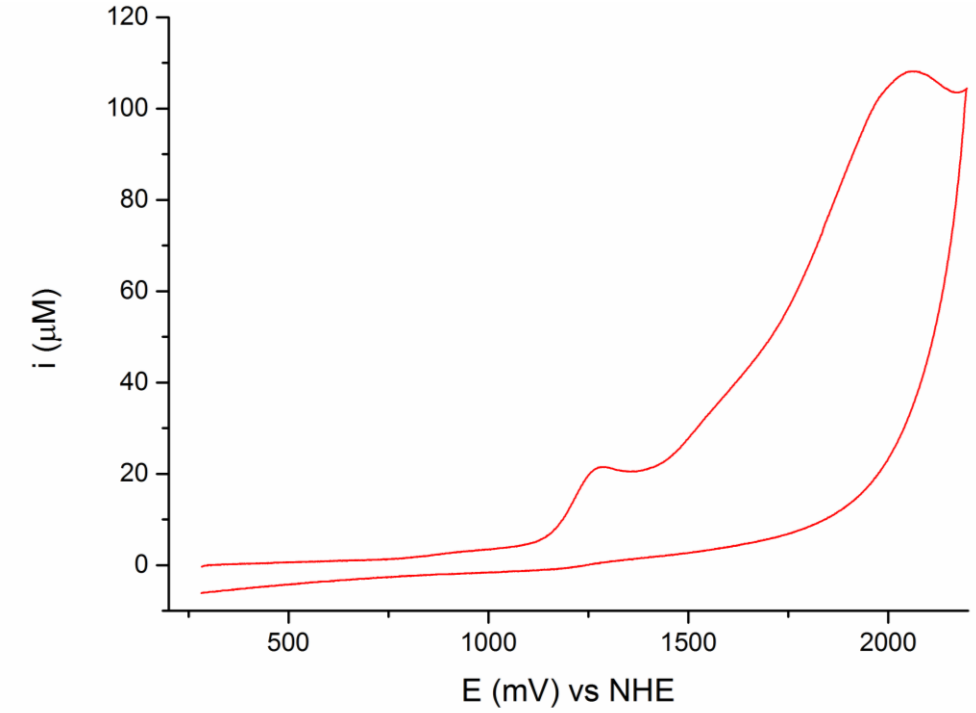

Figure 191. CV of **FeL** (0.5 mM) in ACN:PBS (0.1 M, pH = 7) 50:50.

Bleaching Stability

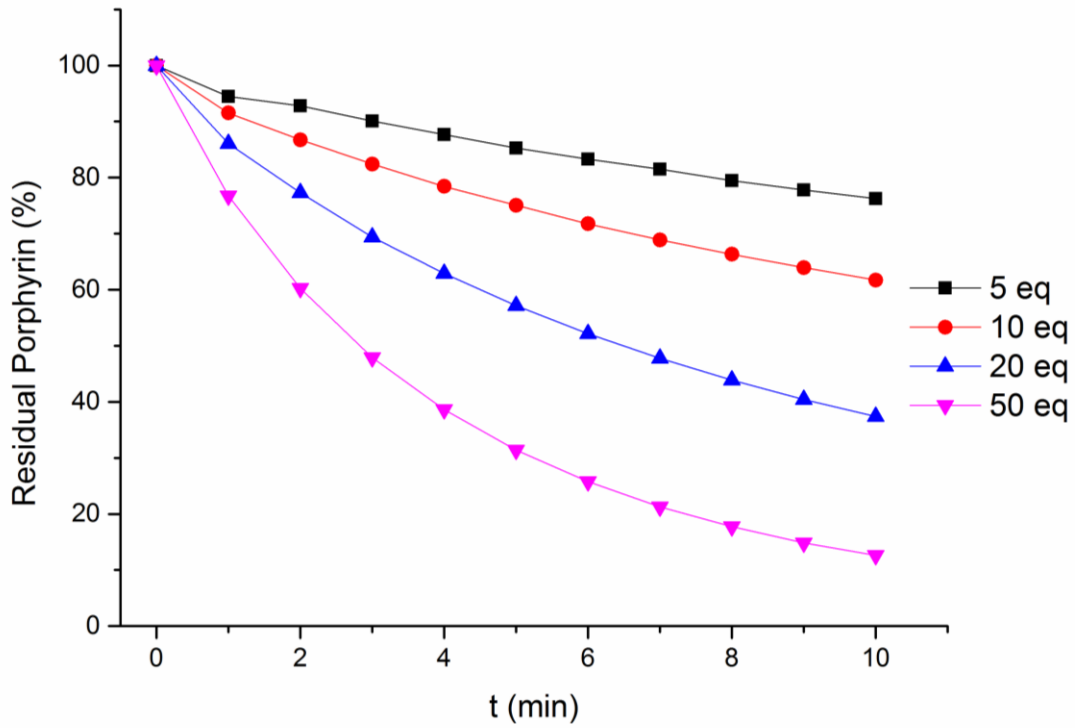

Figure 192. Bleaching kinetics of Mn(III)-meso-tetra(N-methyl-4-pyridyl)porphine (Mn(III)-TM-4-PyP^{5+}, 10 μM), obtained by plotting the residual porphyrin amount (%) over a time window of 10 minutes, in the presence of increasing H_2O_2 equivalents: 5 eq (black), 10 eq (red), 20 eq (blue) and 50 eq (purple) in phosphate buffer solution (50 mM, pH=7.8).

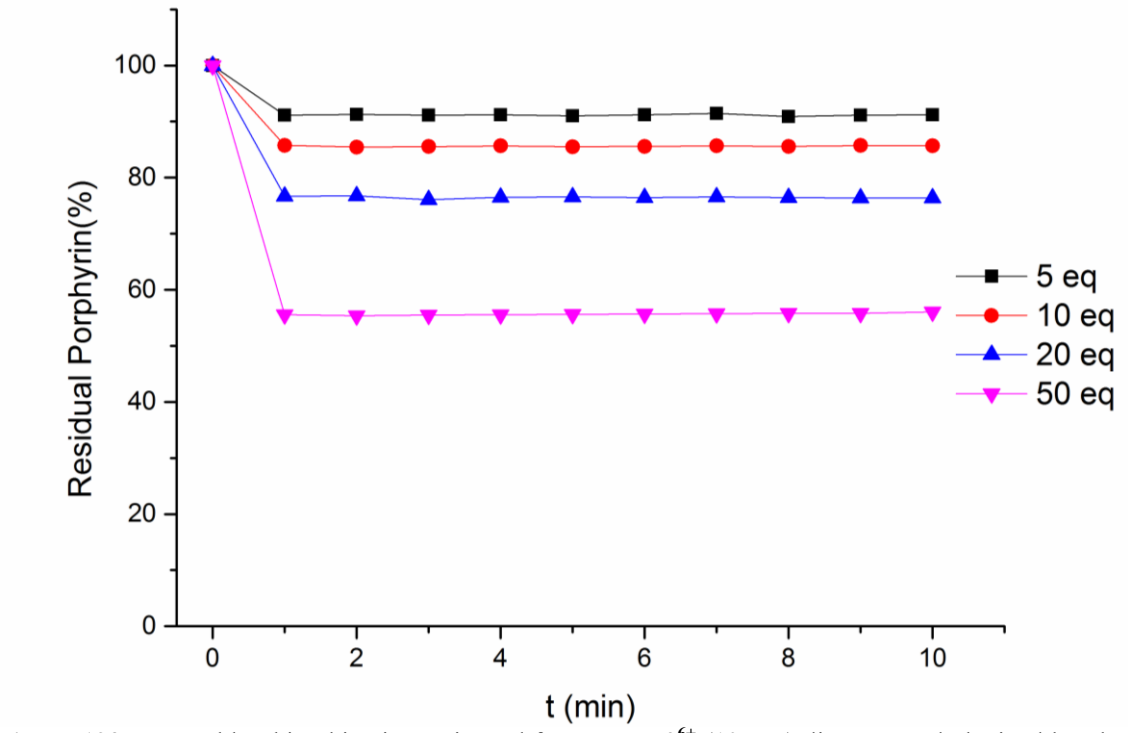

Figure 193. Heme bleaching kinetics registered for $\mathbf{Mn_2L_2P2^{6+}}$ (10 μM) di-zyme, and obtained by plotting the residual heme absorbance (%) over a time window of 10 minutes, in the presence of increasing H_2O_2 equivalents: 5 eq (black), 10 eq (red), 20 eq (blue) and 50 eq (purple) in phosphate buffer solution (50 mM, pH=7.8).

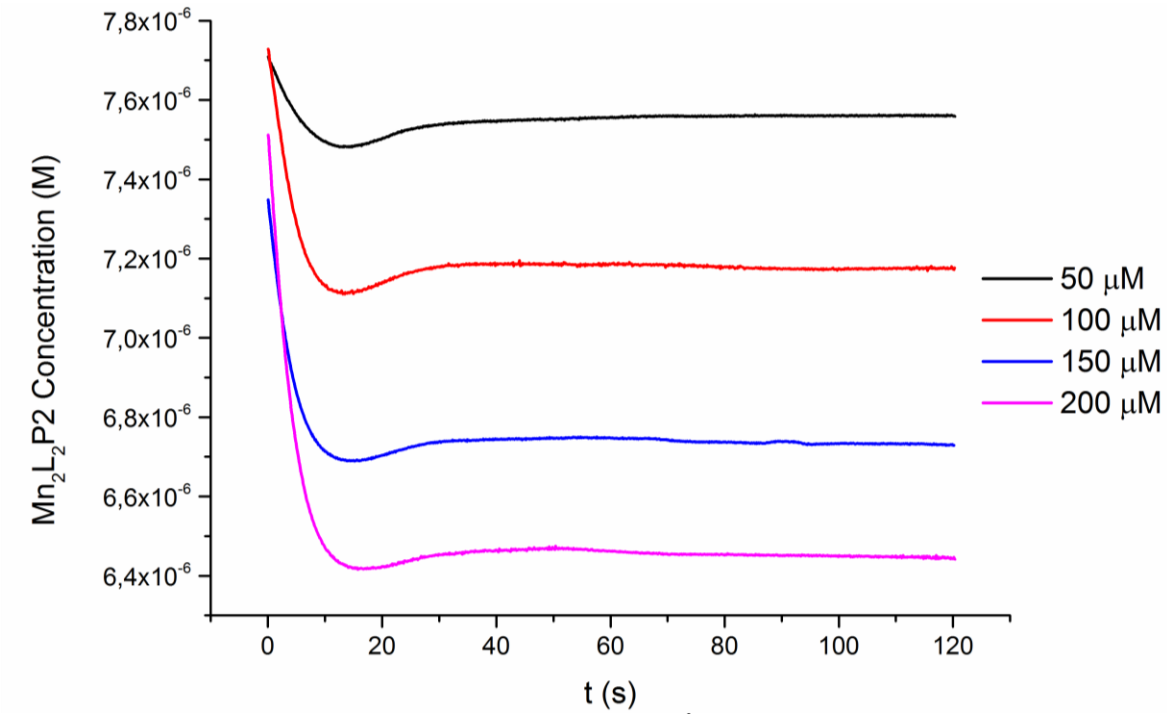

Figure 194. Heme bleaching kinetics registered for $\mathbf{Mn_2L_2P2^{6+}}$ (8 μM) di-zyme, obtained by plotting the residual heme concentration (over a time window of 120 s), in the presence of increasing [H_2O_2]: 50 μM (black), 100 μM (red), 150 μM (blue) and 200 μM (purple) in phosphate buffer solution (50 mM, pH 7.8).

DNA interaction

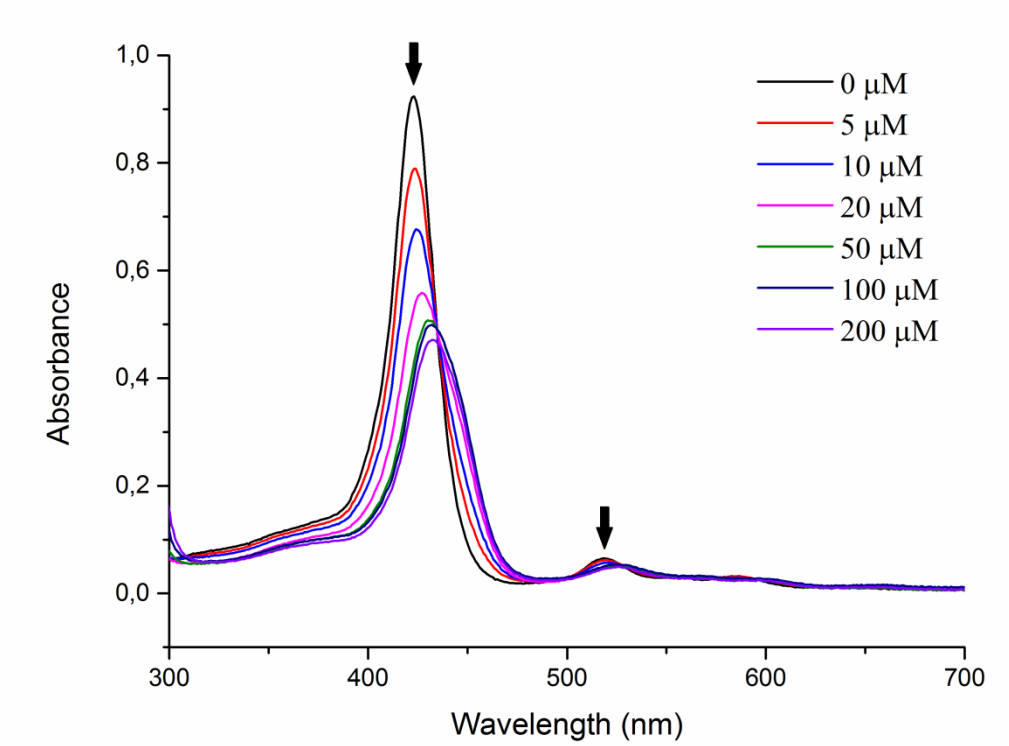

Figure 195. Spectrophotometric titration of H_2TM-4-PyP^{4+} (4 µM) with nucleic acids (CT-DNA): phosphate buffer 10 mM pH 6.8, 1 mM EDTA **,** μ = 0.2 M, 25 °C.

Hydrogen peroxide dismutation

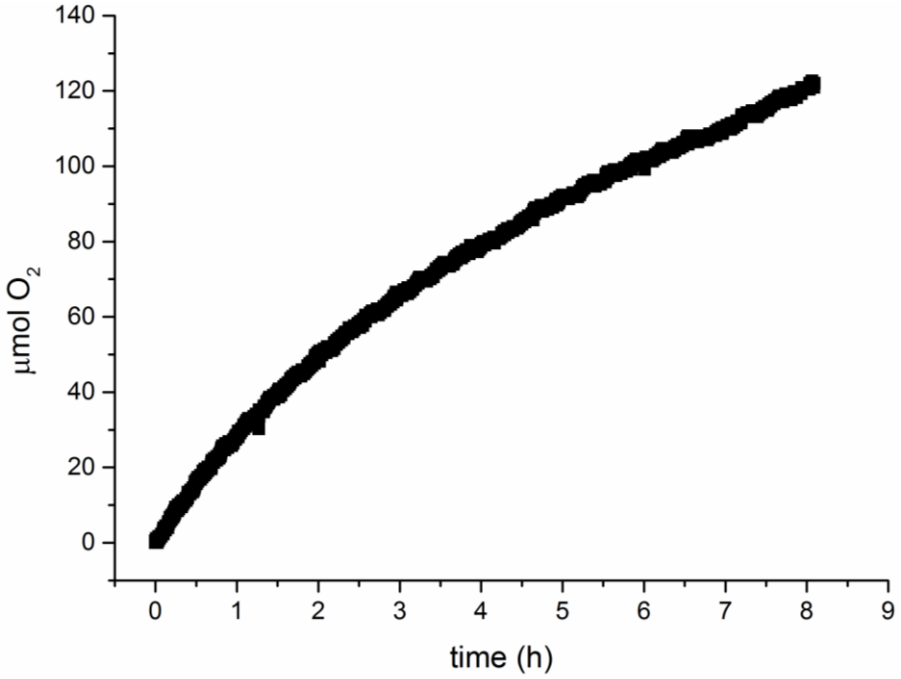

Figure 196. O_2 evolution kinetics by Cu^{2+} (400 µM) upon incubation with H_2O_2 (30 mM) at 25°C in BBS (50 mM pH=7.8).

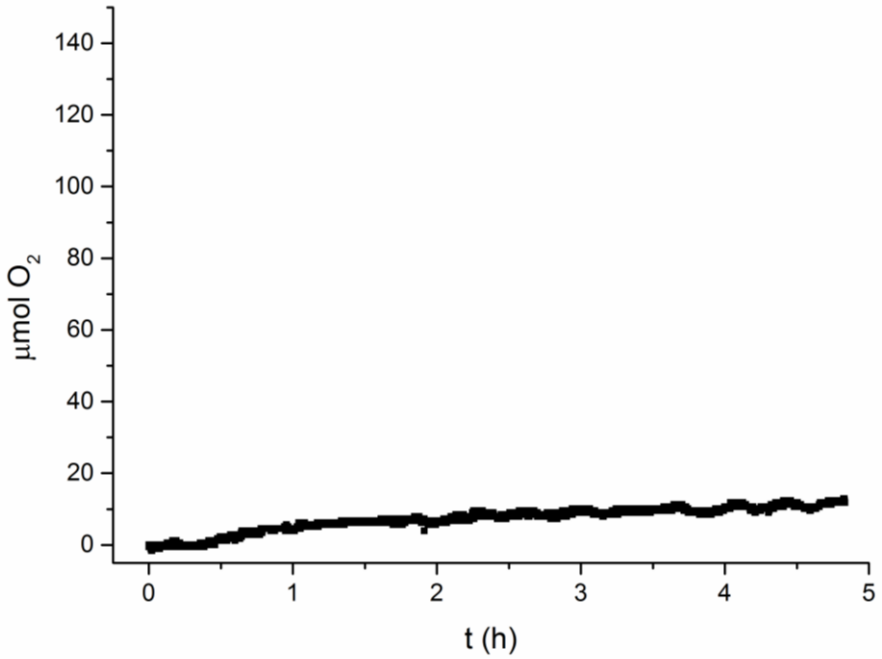

Figure 197. O_2 evolution kinetics by **Cu_2L_2** (240 µM) upon incubation with H_2O_2 (30 mM) at 25°C in acetonitrile.

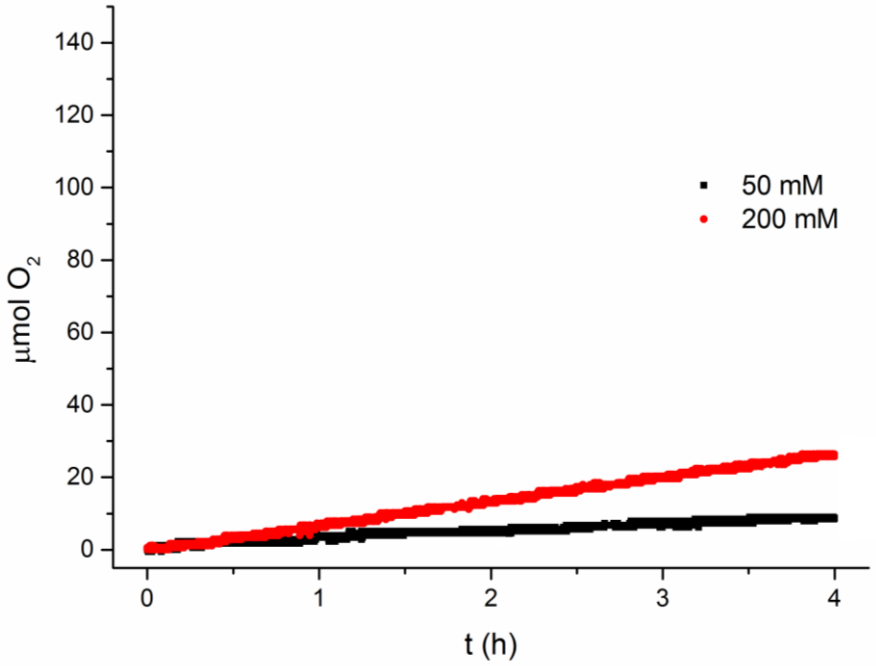

Figure 198. O_2 evolution kinetics by incubation of H_2O_2 (30 mM) at 25°C in BBS (50 mM pH=7.8) with different concentration of NaBr.

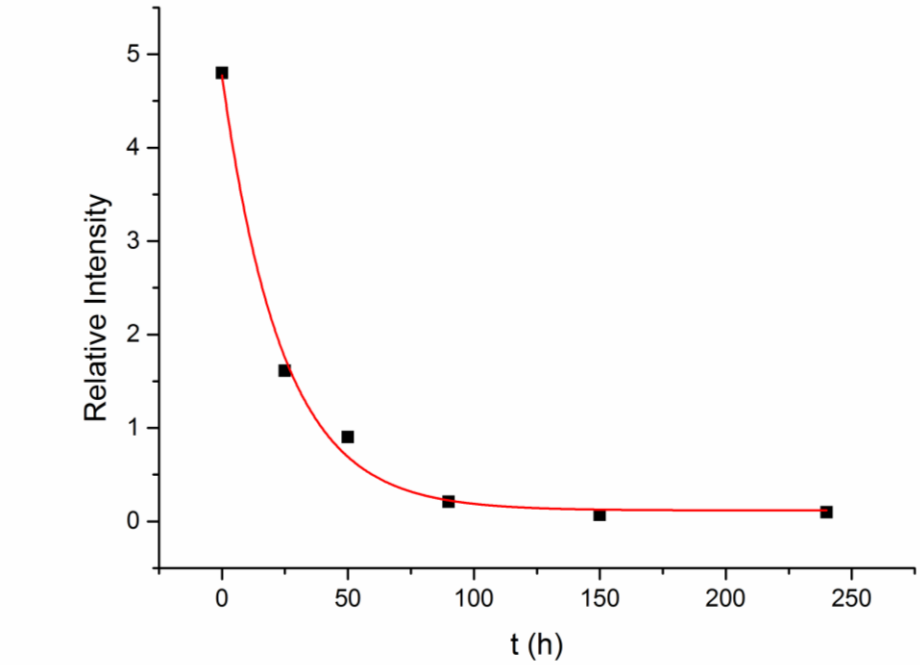

Figure 199. Kinetics profile of **Cu_2L_2** degradation with 30 mM H_2O_2 in BBS 50 mM pH = 7.8.

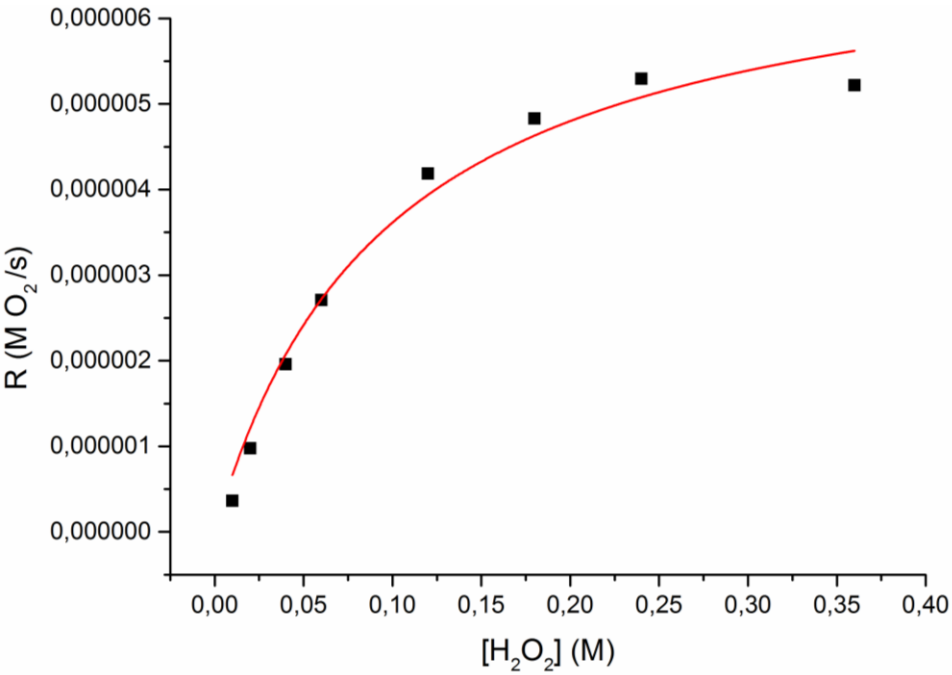

Figure 200. Effect of the H_2O_2 concentration on the rate of H_2O_2 disproportionation at 25 °C in a BBS buffer pH=7.8, [**Cu_2L_2**]= 200 μM.

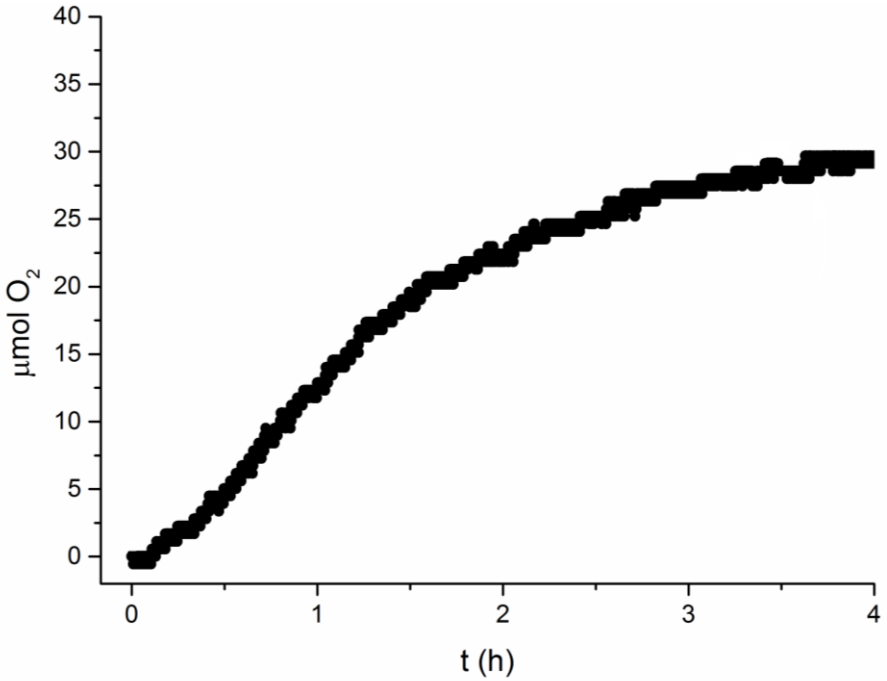

Figure 201. O_2 evolution kinetics by **Cu_2L_2** (200 µM) upon incubation with H_2O_2 (10 mM) at 25°C in BBS (50 mM pH=7.8).

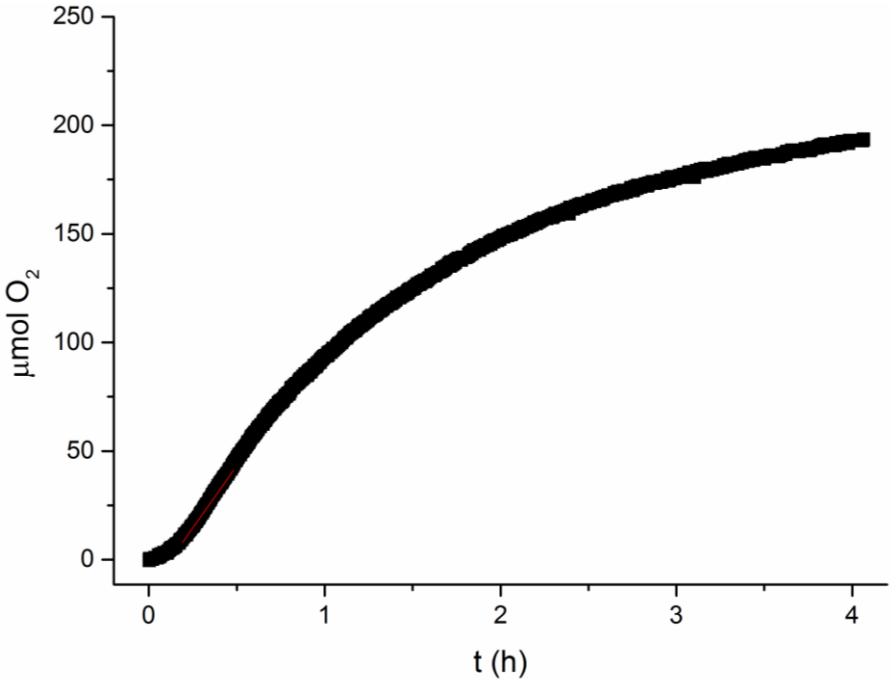

Figure 202. O_2 evolution kinetics by **Cu_2L_2** (200 µM) upon incubation with H_2O_2 (60 mM) at 25°C in BBS (50 mM pH=7.8).

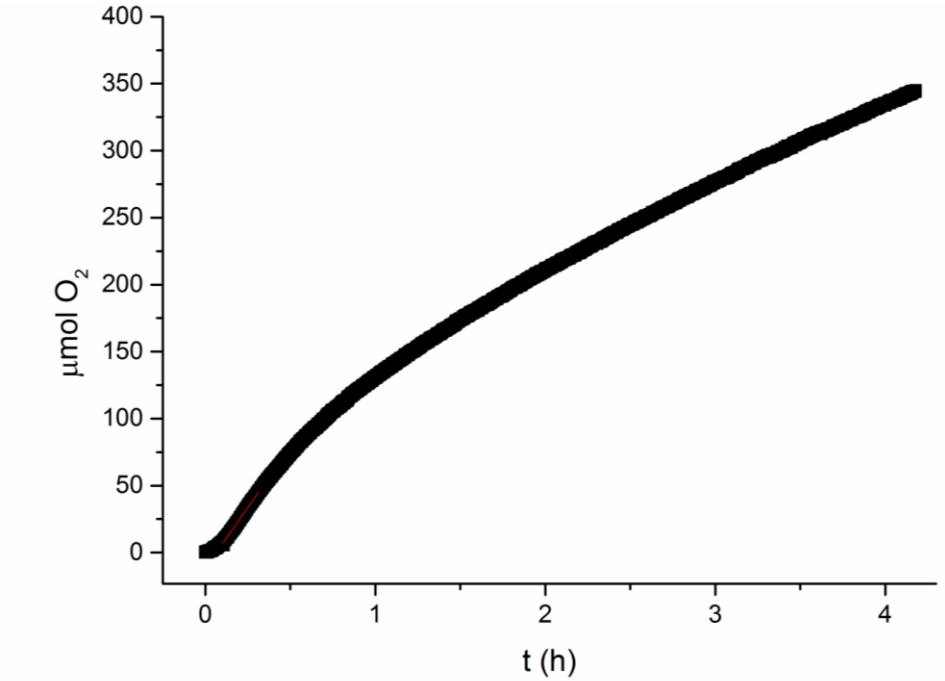

Figure 203. O_2 evolution kinetics by **Cu_2L_2** (200 µM) upon incubation with H_2O_2 (120 mM) at 25°C in BBS (50 mM pH=7.8).

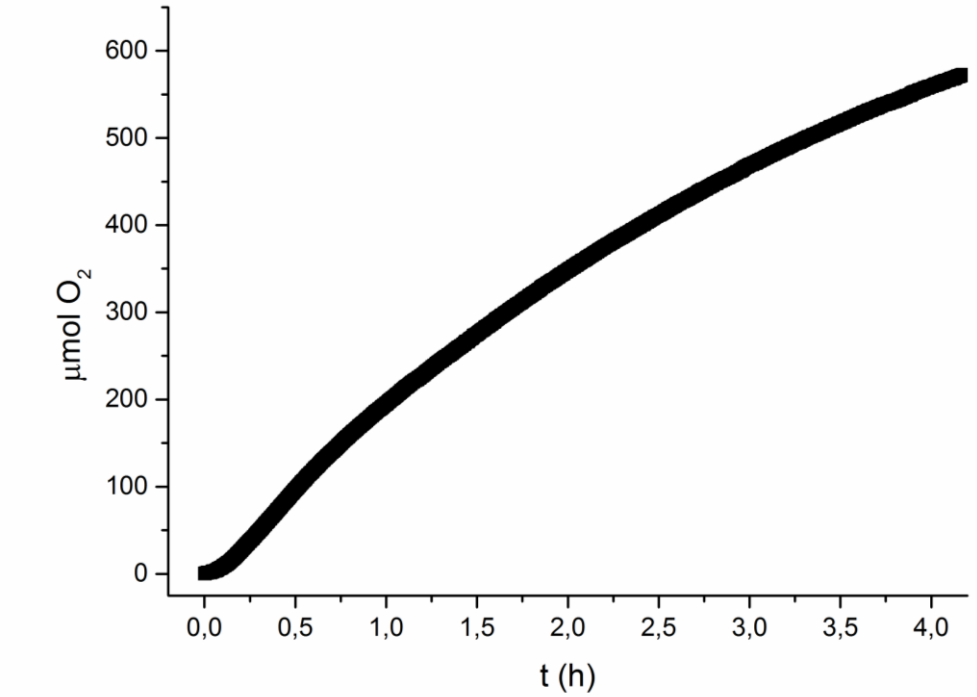

Figure 204. O_2 evolution kinetics by **Cu_2L_2** (200 µM) upon incubation with H_2O_2 (360 mM) at 25°C in BBS (50 mM pH=7.8).

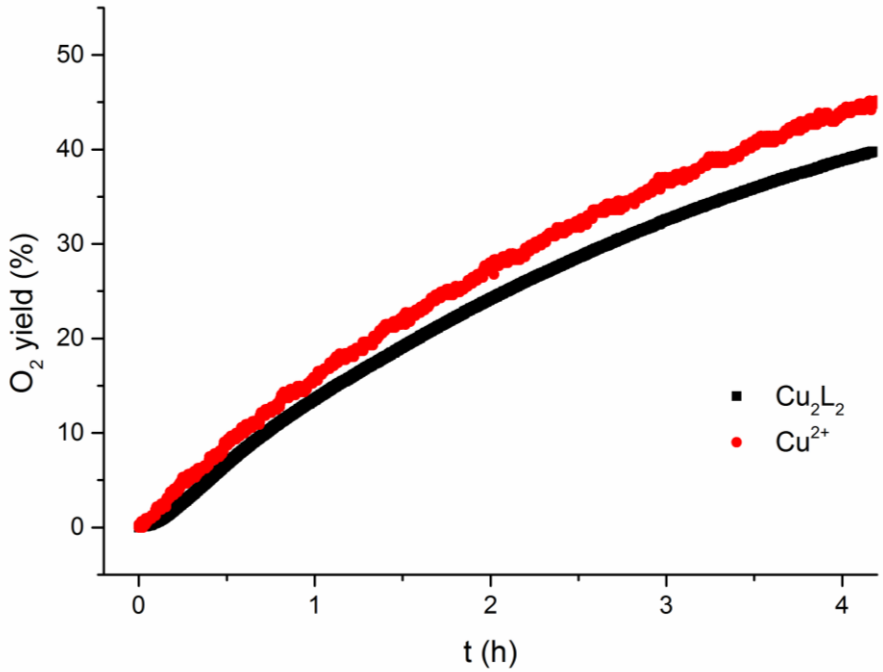

Figure 205. Comparison between the O_2 evolution kinetics by $\mathbf{Cu_2L_2}$ (200 μM) upon incubation with H_2O_2 (360 mM) (black) and free copper (400 μM) upon incubation with H_2O_2 (30 mM) (red) at 25°C in BBS (50 mM pH=7.8).

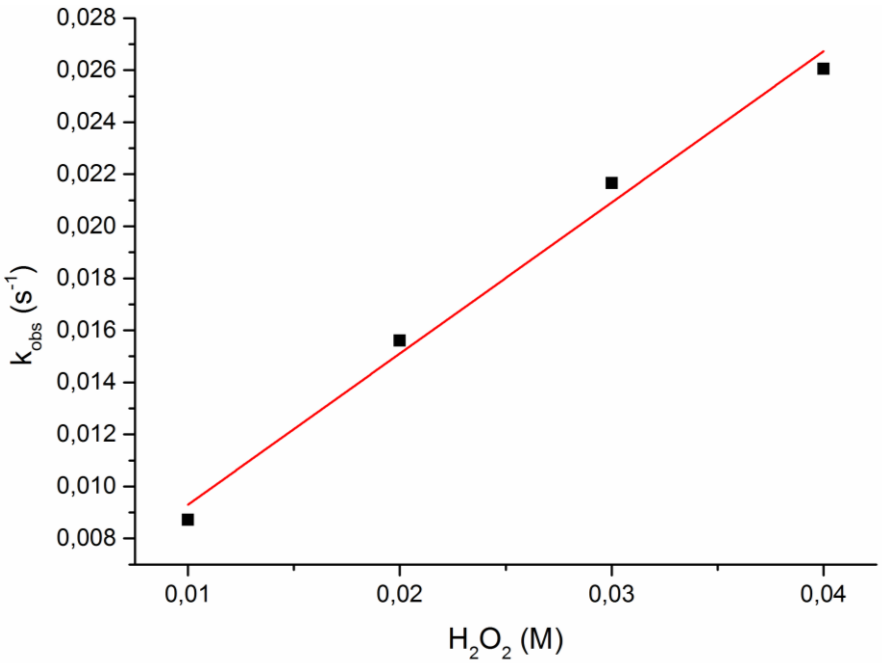

Figure 206. Linear dependence of pseudo-first-order rate constants k_{obs} on $[H_2O_2]$, determined for hydrogen peroxide dismutation by $\mathbf{Cu_2L^1_2}$ (200 μM) at 25°C in borate buffer (50 mM, pH 7.8). The second-order rate constants were determined from linear plots of the observed k_{obs} vs $[H_2O_2]$, $k_{obs} = k[H_2O_2]$.

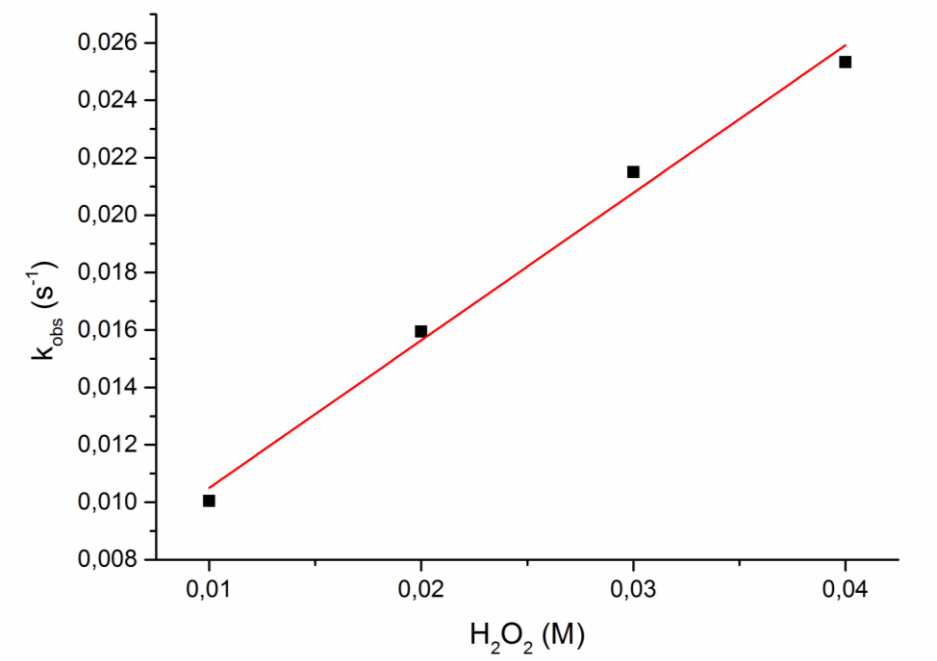

Figure 207. Linear dependence of pseudo-first-order rate constants k_{obs} on $[H_2O_2]$, determined for hydrogen peroxide dismutation by $\mathbf{Cu_2L^2_2}$ (200 µM) at 25°C in borate buffer (50 mM, pH 7.8). The second-order rate constants were determined from linear plots of the observed k_{obs} vs $[H_2O_2]$, $k_{obs} = k[H_2O_2]$.

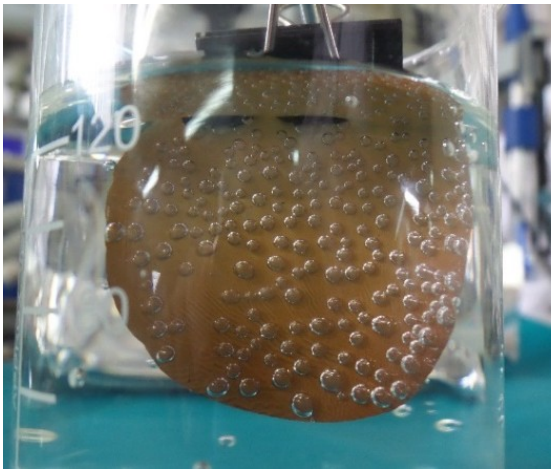

Figure 208. Pictures showing the oxygen evolved for the membrane **PEEK-WC 2** incubated in 0.1 M H_2O_2.

TGA analysis

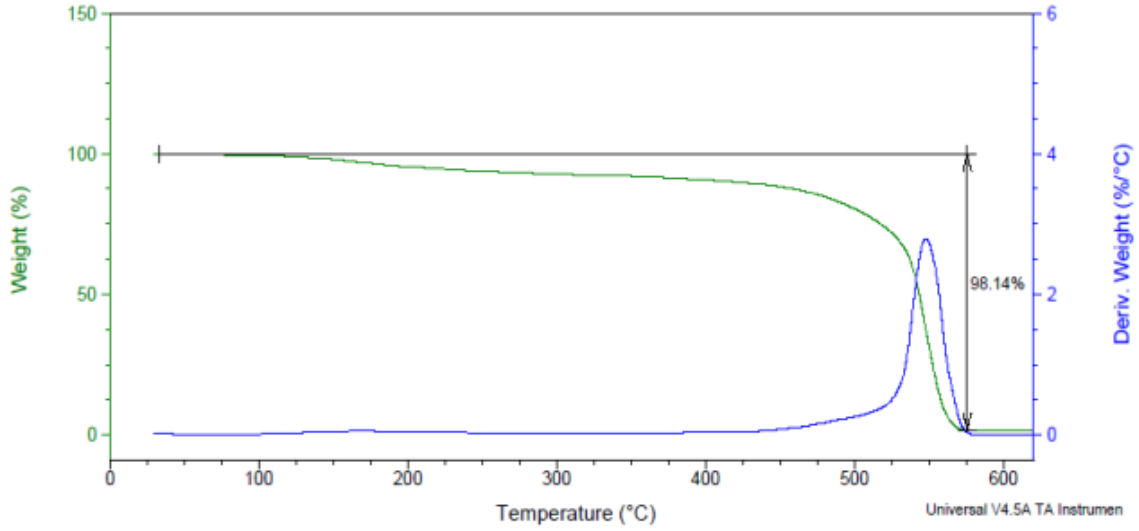

Figure 209. TGA analysis in air of the membrane **PEEK-WC 2**, the green line represent the weight profile (%) and the blue line the first derivate of weight (%).

EDX analysis

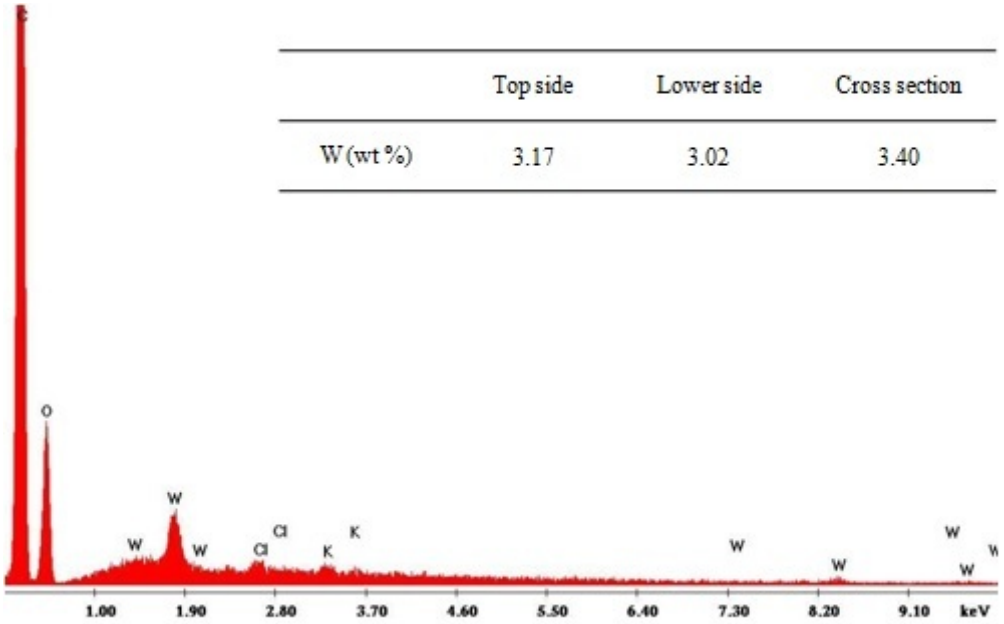

	Top side	Lower side	Cross section
W (wt %)	3.17	3.02	3.40

Figure 210. EDX analysis of the membrane **PEEK-WC 2**. In the table are reported the %wt of tungsten obtained on different areas of the membrane.

Fluorescence spectra

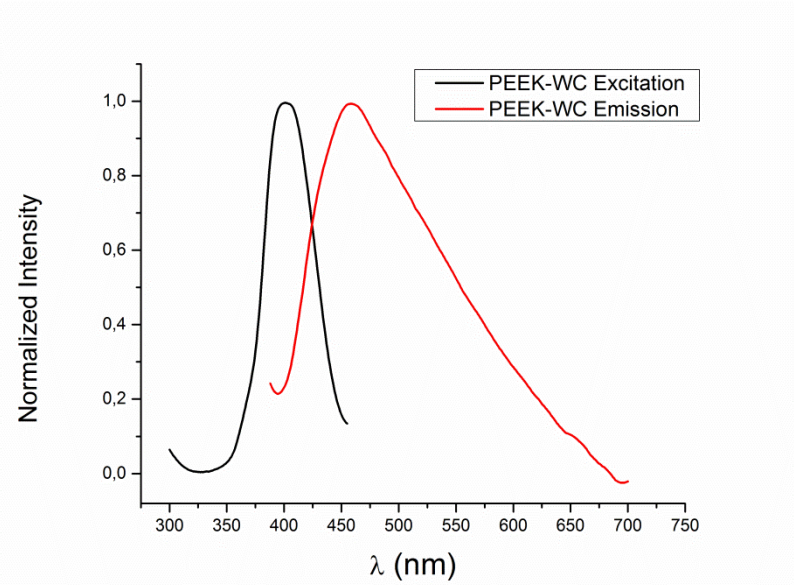

Figure 211. Excitation and emission spectra of PEEK-WC membrane, λ_{max}(exc) = 400 nm and λ_{max}(em) = 460 nm.

References

(1) Finkel, T.; Holbrook, N. J. *Nature* **2000**, *408*, 239.

(2) Ježek, P.; Hlavatá, L. *Int. J. Biochem. Cell Biol.* **2005**, *37* (12), 2478.

(3) Venditti, P.; Di Stefano, L.; Di Meo, S. *Mitochondrion* **2013**, *13* (2), 71.

(4) Fukui, H.; Moraes, C. T. *Trends Neurosci.* **2008**, *31* (5), 251.

(5) Sayre, L. M.; Perry, G.; Smith, M. A. *Chem. Res. Toxicol.* **2008**, *21* (1), 172.

(6) Signorelli, S. S.; Neri, S.; Di Pino, L.; Costa, M. P.; Pennisi, G.; Digrandi, D.; Ierna, D. *Clin. Exp. Med.* **2001**, *1* (1), 9.

(7) Runge-Morris, M.; Frank, P.; Novak, R. F. *Chem. Res. Toxicol.* **1989**, *2* (2), 76.

(8) Valko, M.; Rhodes, C. J.; Moncol, J.; Izakovic, M.; Mazur, M. *Chem. Biol. Interact.* **2006**, *160* (1), 1.

(9) Pospíšil, P. *Plant Cell Physiol.* **2014**, *55* (7), 1224.

(10) Nakano, Y.; Asada, K. *Photochem. Photobiol.* **1978**, *28* (1975), 5.

(11) Asada, K. *Phil. Trans. R. Soc. Lond. B* **2000**, *355*, 1419.

(12) Badger, M. R.; von Caemmerer, S.; Ruuska, S.; Nakano, H. *Philos. Trans. R. Soc. B Biol. Sci.* **2000**, *355* (1402), 1433.

(13) Frankel, L. K.; Sallans, L.; Limbach, P. A.; Bricker, T. M. **2012**.

(14) Zorov, D. B.; Juhaszova, M.; Sollott, S. J. *Physiol. Rev.* **2014**, *94* (3), 909.

(15) Signorella, S.; Hureau, C. *Coord. Chem. Rev.* **2012**, *256* (11–12), 1229.

(16) Cadenas, E.; Davies, K. J. a. *Free Radic. Biol. Med.* **2000**, *29* (3–4), 222.

(17) Zhou, Y. H.; Tao, J.; Lv, Q. C.; Jia, W. G.; Yun, R. R.; Cheng, Y. *Inorganica Chim. Acta* **2015**, *426*, 211.

(18) Iranzo, O. *Bioorg. Chem.* **2011**, *39* (2), 73.

(19) Batinic-Haberle, I.; Rajic, Z.; Tovmasyan, A.; Reboucas, J. S.; Ye, X.; Leong, K. W.; Dewhirst, M. W.; Vujaskovic, Z.; Benov, L.; Spasojevic, I. *Free Radic. Biol. Med.* **2011**, *51* (5), 1035.

(20) Weisiger, R. A.; Fridovicn, I. *J. Biol. Chem.* **1973**, *486* (13), 4793.

(21) Marklund, S. L. *Biochem. J.* **1984**, *222* (3), 649.

(22) Crapo, J. D.; Oury, T.; Rabouille, C.; Slot, J. W.; Chang, L. Y. *Proc. Natl. Acad. Sci. U. S. A.* **1992**, *89* (21), 10405.

(23) Keller, G. A.; Warner, T. G.; Steimer, K. S.; Hallewell, R. A. *Proc. Natl. Acad. Sci. U. S. A.* **1991**, *88* (16), 7381.

(24) Barondeau, D. P.; Kassmann, C. J.; Bruns, C. K.; Tainer, J. A.; Getzoff, E. D.

Biochemistry **2004**, *43* (25), 8038.

(25) Alfonso-Prieto, M.; Biarnés, X.; Vidossich, P.; Rovira, C. *J. Am. Chem. Soc.* **2009**, *131* (33), 11751.

(26) Whittaker, M. M.; Barynin, V. V.; Igarashi, T.; Whittaker, J. W. *Eur. J. Biochem.* **2003**, *270* (6), 1102.

(27) Waldo, G. S.; Penner-Hahn, J. E. *Biochemistry* **1995**, *34* (5), 1507.

(28) Khangulov, S. V.; Barynin, V. V.; Antonyuk-Barynina, S. V. *BBA - Bioenerg.* **1990**, *1020* (1), 25.

(29) Wu, A. J.; Penner-Hahn, J. E.; Pecoraro, V. L. *Chem. Rev.* **2004**, *104* (2), 903.

(30) Boelrijk, A. E. M.; Dismukes, G. C. *Inorg. Chem.* **2000**, *39* (14), 3020.

(31) Demidchik, V. *Environ. Exp. Bot.* **2015**, *109*, 212.

(32) Weissig, V.; Cheng, S. M.; D'Souza, G. G. M. *Mitochondrion* **2004**, *3* (4), 229.

(33) Lippard, S. J.; Berg, J. M. *Principle of Bioinorganic Chemistry*; 1994.

(34) Pordea, A. *Curr. Opin. Chem. Biol.* **2015**, *25*, 124.

(35) Liu, J.; Meier, K. K.; Tian, S.; Zhang, J. L.; Guo, H.; Schulz, C. E.; Robinson, H.; Nilges, M. J.; Münck, E.; Lu, Y. *J. Am. Chem. Soc.* **2014**, *136* (35), 12337.

(36) Onoda, A.; Fukumoto, K.; Arlt, M.; Bocola, M.; Schwaneberg, U.; Hayashi, T. *Chem. Commun.* **2012**, *48* (78), 9756.

(37) Weber, P. C.; Ohlendorf, D. H.; Wendoloski, J. J.; Salemme, F. R. *Science* **1989**, *243* (4887), 85.

(38) Mann, S. I.; Heinisch, T.; Weitz, A. C.; Hendrich, M. P.; Ward, T. R.; Borovik, A. S. *J. Am. Chem. Soc.* **2016**, *138* (29), 9073.

(39) Okamoto, Y.; Köhler, V.; Ward, T. R. *J. Am. Chem. Soc.* **2016**, *138* (18), 5781.

(40) Tebo, A. G.; Pecoraro, V. L. *Curr. Opin. Chem. Biol.* **2015**, *25*, 65.

(41) Yu, F.; Cangelosi, V. M.; Zastrow, M. L.; Tegoni, M.; Plegaria, J. S.; Tebo, a. G.; Mocny, C. S.; Ruckthong, L.; Qayyum, H.; Pecoraro, V. L. *Chem. Rev.* **2014**, *114* (7), 3495.

(42) Rufo, C. M.; Moroz, Y. S.; Moroz, O. V.; Stöhr, J.; Smith, T. a.; Hu, X.; DeGrado, W. F.; Korendovych, I. V. *Nat. Chem.* **2014**, *6* (4), 303.

(43) Rioz-Martínez, A.; Roelfes, G. *Curr. Opin. Chem. Biol.* **2015**, *25*, 80.

(44) Wang, J.; Benedetti, E.; Bethge, L.; Vonhoff, S.; Klussmann, S.; Vasseur, J. J.; Cossy, J.; Smietana, M.; Arseniyadis, S. *Angew. Chemie - Int. Ed.* **2013**, *52* (44), 11546.

(45) Park, S.; Zheng, L.; Kumakiri, S.; Sakashita, S.; Otomo, H.; Ikehata, K.; Sugiyama,

H. *ACS Catal.* **2014**, *4* (11), 4070.

(46) Batinić-Haberle, I.; Rebouças, J. S.; Spasojević, I. *Antioxid. Redox Signal.* **2010**, *13* (6), 877.

(47) Slosky, L. M.; Vanderah, T. W. *Expert Opin. Ther. Pat.* **2015**, *25* (4), 443.

(48) Appel, A. M.; Bercaw, J. E.; Bocarsly, A. B.; Dobbek, H.; Dubois, D. L.; Dupuis, M.; Ferry, J. G.; Fujita, E.; Hille, R.; Kenis, P. J. A.; Kerfeld, C. A.; Morris, R. H.; Peden, C. H. F.; Portis, A. R.; Ragsdale, S. W.; Rauchfuss, T. B.; Reek, J. N. H.; Seefeldt, L. C.; Thauer, R. K.; Waldrop, G. L. *Chem. Rev.* **2013**, *113* (8), 6621.

(49) Artero, V.; Chavarot-Kerlidou, M.; Fontecave, M. *Angew. Chemie - Int. Ed.* **2011**, *50* (32), 7238.

(50) Kanady, J. S.; Tsui, E. Y.; Day, M. W.; Agapie, T. *Science (80-.).* **2011**, *333* (6043), 733.

(51) Umena, Y.; Kawakami, K.; Shen, J.-R.; Kamiya, N. *Nature* **2011**, *473* (7345), 55.

(52) Oosterom, G. E.; Reek, J. N. H.; Kamer, P. C. J.; van Leeuwen, P. W. N. M. *Angew. Chem. Int. Ed. Engl.* **2001**, *40* (10), 1828.

(53) Jang, B. Bin; Lee, K. P.; Min, D. H.; Suh, J. *J. Am. Chem. Soc.* **1998**, *120* (46), 12008.

(54) Mancin, F.; Prins, L. J.; Pengo, P.; Pasquato, L.; Tecilla, P.; Scrimin, P. *Molecules* **2016**, *21* (8).

(55) Stock, C.; Heureux, N.; Browne, W. R.; Feringa, B. L. *Chem. - A Eur. J.* **2008**, *14* (10), 3146.

(56) Diez-Castellnou, M.; Mancin, F.; Scrimin, P. *J. Am. Chem. Soc.* **2014**, *136* (4), 1158.

(57) Hubert-Pfalzgraf, L. G. *Coord. Chem. Rev.* **1998**, *178–180*, 967.

(58) Long, D. L.; Kögerler, P.; Farrugia, L. J.; Cronin, L. *Chem. - An Asian J.* **2006**, *1* (3), 352.

(59) Faccioli, F.; Bauer, M.; Pedron, D.; Sorarù, A.; Carraro, M.; Gross, S. *Eur. J. Inorg. Chem.* **2015**, *2015* (2), 210.

(60) Pope, M. T.; Muller, A. *Heteropoly and Isopoly Oxometalate*; 1983.

(61) Stracke, J. J.; Finke, R. G. *J. Am. Chem. Soc.* **2011**, *133*, 14872.

(62) Zhang, L.; Clérac, R.; Heijboer, P.; Schmitt, W. *Angew. Chemie - Int. Ed.* **2012**, *51* (12), 3007.

(63) Al-Oweini, R.; Sartorel, A.; Bassil, B. S.; Natali, M.; Berardi, S.; Scandola, F.; Kortz, U.; Bonchio, M. *Angew. Chemie - Int. Ed.* **2014**, *53* (42), 11182.

(64) Sartorel, A.; Truccolo, M.; Berardi, S.; Gardan, M.; Carraro, M.; Toma, F. M.; Scorrano, G.; Prato, M.; Bonchio, M. *Chem. Commun. (Camb).* **2011**, *47* (6), 1716.

(65) Zheng, L.; Ma, Y.; Zhang, G.; Yao, J.; Keita, B.; Nadjo, L. *Phys. Chem. Chem. Phys.* **2010**, *12* (6), 1299.

(66) Zhang, H.; Watanabe, T.; Okumura, M.; Haruta, M.; Toshima, N. *Nat. Mater.* **2012**, *11* (1), 49.

(67) Comotti, M.; Della Pina, C.; Matarrese, R.; Rossi, M. *Angew. Chemie - Int. Ed.* **2004**, *43* (43), 5812.

(68) Chen, J.; Patil, S.; Seal, S.; McGinnis, J. F. *Nat. Nanotechnol.* **2006**, *1* (2), 142.

(69) Gao, L.; Zhuang, J.; Nie, L.; Zhang, J.; Zhang, Y.; Gu, N.; Wang, T.; Feng, J.; Yang, D.; Perrett, S.; Yan, X. *Nat. Nanotechnol.* **2007**, *2* (9), 577.

(70) Natalio, F.; André, R.; Hartog, A. F.; Stoll, B.; Jochum, K. P.; Wever, R.; Tremel, W. *Nat. Nanotechnol.* **2012**, *7* (8), 530.

(71) Herring, C. J.; Qin, J.; Korn, E. D.; Du, C.; Lobner, D.; Wheeler, M.; Almli, C. R.; Shen, C. K.; Luh, T.; Choi, D. W. **1997**, *65* (24).

(72) Manea, F.; Houillon, F. B.; Pasquato, L.; Scrimin, P. *Angew. Chemie - Int. Ed.* **2004**, *43* (45), 6165.

(73) Kotov, N. A. *Science* **2010**, *330*, 188.

(74) Tarnuzzer, R. W.; Colon, J.; Patil, S.; Seal, S. *Nano Lett.* **2005**, *5* (12), 2573.

(75) Kajita, M.; Hikosaka, K.; Iitsuka, M.; Kanayama, A.; Toshima, N.; Miyamoto, Y. *Free Radic. Res.* **2007**, *41* (6), 615.

(76) Asati, M. A.; Santra, D. S.; Kaittanis, M. C.; Nath, D. S.; Perez, P. J. M. *Angew. Chemie* **2010**, *48* (13), 2308.

(77) Luo, W.; Zhu, C.; Su, S.; Li, D.; He, Y.; Huang, Q.; Fan, C. *ACS Nano* **2010**, *4* (12), 7451.

(78) Wan, Y.; Qi, P.; Zhang, D.; Wu, J.; Wang, Y. *Biosens. Bioelectron.* **2012**, *33* (1), 69.

(79) Liu, S.; Lu, F.; Xing, R.; Zhu, J. J. *Chemistry* **2011**, *17* (2), 620.

(80) Celardo, I.; De Nicola, M.; Mandoli, C.; Pedersen, J. Z.; Traversa, E.; Ghibelli, L. *ACS Nano* **2011**, *5* (6), 4537.

(81) Zhu, A.; Sun, K.; Petty, H. R. *Inorg. Chem. Commun.* **2012**, *15*, 235.

(82) Pasquato, L.; Rancan, F.; Scrimin, P.; Mancin, F.; Frigeri, C. *Chem. Commun.* **2000**, *2* (22), 2253.

(83) Mahmoudi, M.; Azadmanesh, K.; Shokrgozar, M. A.; Journeay, W. S.; Laurent, S. *Chem. Rev.* **2011**, *111*, 3407.

(84) Horie, M.; Kato, H.; Fujita, K.; Endoh, S.; Iwahashi, H. *Chem. Res. Toxicol.* **2012**, *25* (3), 605.

(85) McCord, J. M.; Fridovich, I. *J. Biol. Chem.* **1969**, *244* (December), 6049.

(86) Miriyala, S.; Spasojevic, I.; Tovmasyan, A.; Salvemini, D.; Vujaskovic, Z.; St. Clair, D.; Batinic-Haberle, I. *Biochim. Biophys. Acta - Mol. Basis Dis.* **2012**, *1822* (5), 794.

(87) Batinić-Haberle, I.; Spasojevic, I.; Hambright, P.; Benov, L.; Crumbliss, a L.; Fridovich, I. *Inorg. Chem.* **1999**, *38* (18), 4011.

(88) Spasojevi, I.; Batini-Haberle, I. *Inorganica Chim. Acta* **2001**, *317* (1–2), 230.

(89) Pasternack, R. F.; Gibbs, E. J.; Villafranca, J. J. *Biochemistry* **1983**, *22* (23), 2406.

(90) Pasternack, R. F.; Gibbs, E. J.; Villafranca, J. J. *Biochemistry* **1983**, *22* (23), 5409.

(91) Tovmasyan, A. G.; Rajic, Z.; Spasojevic, I.; Reboucas, J. S.; Chen, X.; Salvemini, D.; Sheng, H.; Warner, D. S.; Benov, L.; Batinic-Haberle, I. *Dalton Trans.* **2011**, *40* (16), 4111.

(92) Pollard, J. M.; Reboucas, J. S.; Durazo, A.; Kos, I.; Fike, F.; Panni, M.; Gralla, E. B.; Valentine, J. S.; Batinic-Haberle, I.; Gatti, R. A. *Free Radic. Biol. Med.* **2009**, *47* (3), 250.

(93) Baudry, M.; Etienne, S.; Bruce, A.; Palucki, M.; Jacobsen, E.; Malfroy, B. *Biochem. Biophys. Res. Commun.* 1993, pp 964–968.

(94) Fucassi, F.; Lowe, J. E.; Pavey, K. D.; Shah, S.; Faragher, R. G. A.; Green, M. H. L.; Paul, F.; O'Hare, D.; Cragg, P. J. *J. Inorg. Biochem.* **2007**, *101* (2), 225.

(95) Noritake, Y.; Umezawa, N.; Kato, N.; Higuchi, T. *Inorg. Chem.* **2013**, *52*, 3653.

(96) Bayne, A. C. V; Sohal, R. S. *Free Radic. Biol. Med.* **2002**, *32* (11), 1229.

(97) van Empel, V. P. M.; Bertrand, A. T.; van Oort, R. J.; van der Nagel, R.; Engelen, M.; van Rijen, H. V.; Doevendans, P. A.; Crijns, H. J.; Ackerman, S. L.; Sluiter, W.; De Windt, L. J. *J. Am. Coll. Cardiol.* **2006**, *48* (4), 824.

(98) Brazier, M. W.; Doctrow, S. R.; Masters, C. L.; Collins, S. J. *Free Radic. Biol. Med.* **2008**, *45* (2), 184.

(99) Riley, D. P. *Chem. Rev.* **1999**, *99*, 2573.

(100) Riley, D. P.; Schall, O. F. *Adv. Inorg. Chem.* **2006**, *59* (6), 233.

(101) Riley, D. P.; Lennon, P. J.; Neumann, W. L.; Weiss, R. H. *J. Am. Chem. Soc.* **1997**, *119* (28), 6522.

(102) Muscoli, C.; Cuzzocrea, S.; Riley, D. P.; Zweier, J. L.; Thiemermann, C.; Wang, Z.-Q.; Salvemini, D. *Br. J. Pharmacol.* **2003**, *140* (3), 445.

(103) Policar, C.; Durot, S.; Lambert, F.; Cesario, M.; Ramiandrasoa, F.; Morgenstern-Badarau, I. *Eur. J. Inorg. Chem.* **2001**, 1807.

(104) Durot, S.; Policar, C.; Cisnetti, F.; Lambert, F.; Renault, J. P.; Pelosi, G.; Blain, G.; Korri-Youssoufi, H.; Mahy, J. P. *Eur. J. Inorg. Chem.* **2005**, No. 17, 3513.

(105) Korsvik, C.; Patil, S.; Seal, S.; Self, W. T. *Chem. Commun.* **2007**, No. 10, 1056.

(106) Heckert, E. G.; Karakoti, A. S.; Seal, S.; Self, W. T. *Biomaterials* **2008**, *29* (18), 2705.

(107) Celardo, I.; Pedersen, J. Z.; Traversa, E.; Ghibelli, L. *Nanoscale* **2011**, *3* (4), 1411.

(108) Malterer, M. B.; Glass, S. J.; Newman, J. P. *Biomaterials* **2008**, *44* (3), 735.

(109) Lévêque, V.; Vance, C. C. K.; Nick, H. H. S.; Silverman, D. N. D.; Leveque, V. J. P.; Vance, C. C. K.; Nick, H. H. S.; Silverman, D. N. D. *Biochemistry* **2001**, *40* (35), 10586.

(110) Zheng, J.; Domsic, J. F.; Cabelli, D.; McKenna, R.; Silverman, D. N. *Biochemistry* **2007**, *46* (51), 14830.

(111) Batinić-Haberle, I.; Benov, L.; Spasojević, I.; Fridovich, I. *J. Biol. Chem.* **1998**, *273* (38), 24521.

(112) Batinić-haberle, I.; Spasojević, I.; Stevens, R. D.; Hambright, P. *Dalt. Trans.* **2004**, 1696.

(113) Batinić-Haberle, I.; Spasojević, I.; Stevens, R. D.; Hambright, P.; Fridovich, I. *J. Chem. Soc. Dalt. Trans.* **2002**, No. 13, 2689.

(114) DeFreitas-Silva, G.; Rebouças, J. S.; Spasojević, I.; Benov, L.; Idemori, Y. M.; Batinić-Haberle, I. *Arch. Biochem. Biophys.* **2008**, *477* (1), 105.

(115) Ghosh, K.; Tyagi, N.; Kumar, P.; Singh, U. P.; Goel, N. *J. Inorg. Biochem.* **2010**, *104* (1), 9.

(116) Liu, G. F.; Filipović, M.; Heinemann, F. W.; Ivanović-Burmazović, I. *Inorg. Chem.* **2007**, *46* (21), 8825.

(117) Ali, S. S.; Hardt, J. I.; Quick, K. L.; Sook Kim-Han, J.; Erlanger, B. F.; Huang, T. T.; Epstein, C. J.; Dugan, L. L. *Free Radic. Biol. Med.* **2004**, *37* (8), 1191.

(118) Shank, M.; Barynin, V.; Dismukes, G. C. *Biochemistry* **1994**, *33*, 15433.

(119) de Boer, J. W.; Browne, W. R.; Feringa, B. L.; Hage, R. *Comptes Rendus Chim.* **2007**, *10* (4–5), 341.

(120) Abdolahzadeh, S.; De Boer, J. W.; Browne, W. R. *Eur. J. Inorg. Chem.* **2015**, *2015* (21), 3432.

(121) Pessiki, P. J.; Dismukes, G. C. *J. Am. Chem. Soc.* **1994**, *116* (4), 898.

(122) Blondin, G.; Hureau, C.; Anxolabehere-Mallart, E.; Nierlich, M.; Gonnet, F.; Riviere, E. *Eur. J. Inorg. Chem.* **2002**, No. 10, 2710.

(123) Huang, P.; Magnuson, A.; Lomoth, R.; Abrahamsson, M.; Tamm, M.; Sun, L.; van Rotterdam, B.; Park, J.; Hammarstrom, L.; Akermark, B.; Styring, S. *J. Inorg. Biochem.* **2002**, *91* (1), 159.

(124) Sabater, L.; Hureau, C.; Blain, G.; Guillot, R.; Thuéry, P.; Rivière, E.; Aukauloo, A. *Eur. J. Inorg. Chem.* **2006**, No. 21, 4324.

(125) Reddig, N.; Pursche, D.; Kloskowski, M.; Slinn, C.; Baldeau, S. M.; Rompel, A. *Eur. J. Inorg. Chem.* **2004**, No. 4, 879.

(126) Collomb, M. N.; Deronzier, A. *Eur. J. Inorg. Chem.* **2009**, No. 14, 2025.

(127) Romero, I.; Dubois, L.; Deronzier, A.; Chimie, L. De; Cea-cnrs-ujf, U. M. R. *System* **2002**, *41* (7), 1795.

(128) Vázquez-Fernández, M. Á.; Bermejo, M. R.; Fernández-García, M. I.; González-Riopedre, G.; Rodríguez-Doutón, M. J.; Maneiro, M. *J. Inorg. Biochem.* **2011**, *105* (12), 1538.

(129) Doctrow, S. R.; Huffman, K.; Marcus, C. B.; Tocco, G.; Malfroy, E.; Adinolfi, C. A.; Kruk, H.; Baker, K.; Lazarowych, N.; Mascarenhas, J.; Malfroy, B. *J. Med. Chem.* **2002**, *45* (20), 4549.

(130) Watanabe, Y.; Namba, A.; Umezawa, N.; Kawahata, M.; Yamaguchi, K.; Higuchi, T. *Chem. Commun.* **2006**, 4958.

(131) Yang, J. Y.; Nocera, D. G. *J. Am. Chem. Soc.* **2007**, *129* (26), 8192.

(132) Maneiro, M.; Bermejo, M. R.; Fernandez, M. I.; Gomez-Forneas, E.; Gonzalez-Noya, A. M.; Tyryshkin, A. M. *New J. Chem.* **2003**, *27* (4), 727.

(133) Moreno, D.; Daier, V.; Palopoli, C.; Tuchagues, J.-P.; Signorella, S. *J. Inorg. Biochem.* **2010**, *104* (5), 496.

(134) Palopoli, C.; Bruzzo, N.; Hureau, C.; Ladeira, S.; Murgida, D.; Signorella, S. *Inorg. Chem.* **2011**, *50* (18), 8973.

(135) Grau, M.; Rigodanza, F.; White, a J.; Soraru, a; Carraro, M.; Bonchio, M.; Britovsek, G. J. *Chem Commun* **2014**, *50* (35), 4607.

(136) Sartorel, A.; Truccolo, M.; Berardi, S.; Gardan, M.; Carraro, M.; Toma, F. M.; Scorrano, G.; Prato, M.; Bonchio, M. *Chem. Commun.* **2011**, *47* (6), 1716.

(137) Pirmohamed, T.; Dowding, J. M.; Singh, S.; Wasserman, B.; Heckert, E.; Karakoti, A. S.; King, J. E. S.; Seal, S.; Self, W. T. *Chem. Commun. (Camb).* **2010**, *46* (16), 2736.

(138) Mu, J.; Wang, Y.; Zhao, M.; Zhang, L. *Chem. Commun.* **2012**, *48* (19), 2540.

(139) Chen, Z.; Yin, J. J.; Zhou, Y. T.; Zhang, Y.; Song, L.; Song, M.; Hu, S.; Gu, N. *ACS Nano* **2012**, *6* (5), 4001.

(140) Najafpour, M. M.; Ehrenberg, T.; Wiechen, M.; Kurz, P. *Angew. Chemie - Int. Ed.* **2010**, *49* (12), 2233.

(141) Dismukes, G. C. *Chem. Rev.* **1996**, *96* (7), 2909.

(142) Triller, M. U.; Hsieh, W. Y.; Pecoraro, V. L.; Rompel, A.; Krebs, B. *Inorg. Chem.* **2002**, *41* (21), 5544.

(143) Kloskowski, M.; Pursche, D.; Hoffmann, R.-D.; Pöttgen, R.; Läge, M.; Hammerschmidt, A.; Glaser, T.; Krebs, B. *Zeitschrift für Anorg. und Allg. Chemie* **2007**, *633* (1), 106.

(144) Larson, E. J.; Pecoraro, V. L. *J. Am. Chem. Soc.* **1991**, *113* (8), 3810.

(145) Huang, Y.; Liu, Z.; Liu, C.; Ju, E.; Zhang, Y.; Ren, J.; Qu, X. *Angew. Chemie - Int. Ed.* **2016**, *55* (23), 6646.

(146) Sartorel, A.; Carraro, M.; Toma, F. M.; Prato, M.; Bonchio, M. *Energy Environ. Sci.* **2012**, *5* (2), 5592.

(147) Sheng, Y.; Stich, T. A.; Barnese, K.; Gralla, E. B.; Cascio, D.; Britt, R. D.; Cabelli, D. E.; Valentine, J. S. *J. Am. Chem. Soc.* **2011**, *133* (51), 20878.

(148) Zheng, M.; Khangulov, S. V.; Dismukes, G. C.; Barynin, V. V. *Inorg. Chem.* **1994**, *33* (5), 382.

(149) Vicario, J.; Eelkema, R.; Browne, W. R.; Meetsma, A.; La Crois, R. M.; Feringa, B. L. *Chem. Comms.* **2005**, No. 31, 3936.

(150) Abdolahzadeh, S.; Boyle, N. M.; Hoogendijk, M. L.; Hage, R.; de Boer, J. W.; Browne, W. R. *Dalton Trans.* **2014**, *43* (17), 6322.

(151) Kurz, P.; Anderlund, M. F.; Shaikh, N.; Styring, S.; Huang, P. *Eur. J. Inorg. Chem.* **2008**, No. 5, 762.

(152) Krebs, H. A.; Henseleit, K. *Z. Physiol. Chem* **1932**, *210* (52), 33.

(153) Jitsukawa, K.; Harata, M.; Arii, H.; Sakurai, H.; Masuda, H. *Inorganica Chim. Acta* **2001**, *324* (1–2), 108.

(154) Batinic-Haberle, I.; Tovmasyan, A.; Spasojevic, I. *Redox Biol.* **2015**, *5*, 43.

(155) Shi, D. F.; Wheelhouse, R. T.; Sun, D.; Hurley, L. H. *J. Med. Chem.* **2001**, *44* (26), 4509.

(156) Habdas, J.; Boduszek, B. *J. Pept. Sci.* **2009**, *15* (4), 305.

(157) Stoyanovsky, D. A.; Huang, Z.; Jiang, J.; Belikova, N. A.; Tyurin, V.; Epperly, M.

W.; Greenberger, J. S.; Bayir, H.; Kagan, V. E. *ACS Med. Chem. Lett.* **2011**, *2* (11), 814.

(158) Mohamed, E. A.; Iwaki, T.; Munir, I.; Tamoi, M.; Shigeoka, S.; Wadano, A. *Plant, Cell Environ.* **2003**, *26* (12), 2037.

(159) Singhal, A.; Morris, V. B.; Labhasetwar, V.; Ghorpade, A. *Cell Death Dis.* **2013**, *4* (11), 1.

(160) Schiavon, M. A.; Iwamoto, L. S.; Ferreira, A. G.; Iamamoto, Y.; Zanoni, M. V. B.; Assis, M. D. D. *J. Braz. Chem. Soc.* **2000**, *11* (5), 458.

(161) Liang, H. L.; Hilton, G.; Mortensen, J.; Regner, K.; Christopher, P.; Nilakantan, V. *Am J Physiol Ren. Physiol* **2012**, *53226* (December 2008), 266.

(162) Sharma, S. S.; Gupta, S. *Eur. J. Pharmacol.* **2007**, *561* (1–3), 72.

(163) Moriscot, C.; Candel, S.; Sauret, V.; Kerr-Conte, J.; Richard, M. J.; Favrot, M. C.; Benhamou, P. Y. *Diabetes Metab.* **2007**, *33* (1), 44.

(164) Sari, M. A.; Battioni, J. P.; Dupre, D.; Mansuy, D.; Le Pecq, J. B. *Biochemistry* **1990**, *29* (17), 4205.

(165) Ďuračková, Z.; Mendiola, M. A.; Sevilla, M. T.; Valent, A. *Bioelectrochemistry Bioenerg.* **1999**, *48* (1), 109.

(166) Abreu, I. A.; Cabelli, D. E. *Biochim. Biophys. Acta - Proteins Proteomics* **2010**, *1804* (2), 263.

(167) Pierre, J.-L. *Chem. Soc. Rev.* **2000**, *29* (4), 251.

(168) Ellerby, L. M.; Cabelli, D. E.; Graden, J. A.; Valentine, J. S. **1996**, No. 11, 6556.

(169) Rosenzweig, A. C.; Sazinsky, M. H. *Curr. Opin. Struct. Biol.* **2006**, *16* (6), 729.

(170) Mirica, L. M.; Ottenwaelder, X.; Stack, T. D. P. *Chem. Rev.* **2004**, *104* (I), 1013.

(171) Itoh, S.; Fukuzumi, S. *Acc. Chem. Res.* **2007**, *40* (7), 592.

(172) Kozlowski, H.; Bal, W.; Dyba, M.; Kowalik-Jankowska, T.; Koval, I. a; Gamez, P.; Belle, C.; Selmeczi, K.; Reedijk, J.; Jancsó, a; Paksi, Z.; Jakab, N.; Gyurcsik, B.; Rockenbauer, a; Gajda, T.; Hamley, I. W.; Faller, P.; Hureau, C.; Dorlet, P.; Hellwig, P.; Coppel, Y.; Collin, F.; Alies, B.; Berthoumieu, O. *Coord. Chem. Rev.* **2012**, *256* (19–20), 2381.

(173) Saczewski, F.; Dziemidowicz-Borys, E.; Bednarski, P. J.; Grünert, R.; Gdaniec, M.; Tabin, P. *J. Inorg. Biochem.* **2006**, *100* (8), 1389.

(174) Ďuračková, Z.; Labuda, J. *J. Inorg. Biochem.* **1995**, *58* (4), 297.

(175) Cejudo-Marìn, R.; Alzuet, G.; Ferrer, S.; Borràs, J. *Inorg. Chem.* **2004**, *43* (21), 6805.

(176) Tabbì, G.; Driessen, W. L.; Reedijk, J.; Bonomo, R. P.; Veldman, N.; Spek, A. L. *Inorg. Chem.* **1997**, *36* (Ii), 1168.

(177) Ohtsu, H.; Shimazaki, Y.; Odani, A.; Yamauchi, O.; Mori, W.; Itoh, S.; Fukuzumi, S. *J. Am. Chem. Soc.* **2000**, *122* (24), 5733.

(178) Devereux, M.; O'Shea, D.; O'Connor, M.; Grehan, H.; Connor, G.; McCann, M.; Rosair, G.; Lyng, F.; Kellett, A.; Walsh, M.; Egan, D.; Thati, B. *Polyhedron* **2007**, *26* (15), 4073.

(179) Weder, J. E.; Dillon, C. T.; Hambley, T. W.; Kennedy, B. J.; Lay, P. A.; Biffin, J. R.; Regtop, H. L.; Davies, N. M. *Copper complexes of non-steroidal anti-inflammatory drugs: An opportunity yet to be realized*; 2002; Vol. 232.

(180) Dillon, C. T.; Hambley, T. W.; Kennedy, B. J.; Lay, P. a; Zhou, Q.; Davies, N. M.; Biffin, J. R.; Regtop, H. L. *Chem. Res. Toxicol.* **2003**, *16* (1), 28.

(181) Kovala-Demertzi, D.; Galani, A.; Demertzis, M. A.; Skoulika, S.; Kotoglou, C. *J. Inorg. Biochem.* **2004**, *98* (2), 358.

(182) Abuhijleh, A. L.; Khalaf, J. *Eur. J. Med. Chem.* **2010**, *45* (9), 3811.

(183) Latif Abuhijleh, A.; Woods, C. *Inorg. Chem. Commun.* **2002**, *5* (4), 269.

(184) Ohtsu, H.; Shimazaki, Y.; Yamauchi, O. *Chem. Commun.* **1999**, *84* (7), 2393.

(185) Ramadan, A. E.-M. M. *J. Coord. Chem.* **2012**, *65* (8), 1417.

(186) Pap, J. S.; Kripli, B.; Bors, I.; Bogáth, D.; Giorgi, M.; Kaizer, J.; Speier, G. *J. Inorg. Biochem.* **2012**, *117*, 60.

(187) Gao, J.; Martell, A. E.; Reibenspies, J. H. *Inorganica Chim. Acta* **2003**, *346* (March), 32.

(188) Caglar, S.; Adigüzel, E.; Caglar, B.; Saykal, T.; Sahin, E.; Büyükgüngör, O. *Inorganica Chim. Acta* **2013**, *397*, 101.

(189) Kaizer, J.; Csonka, R.; Speier, G.; Giorgi, M.; Réglier, M. *J. Mol. Catal. A Chem.* **2005**, *236* (1–2), 12.

(190) Deacon, G. B.; PHILLIPS, R. J. *Coord. Chem. Rev.* 1980, pp 227–250.

(191) Oliveri, V.; Puglisi, A.; Viale, M.; Aiello, C.; Sgarlata, C.; Vecchio, G.; Clarke, J.; Milton, J.; Spencer, J. *Chem. - A Eur. J.* **2013**, *19* (41), 13946.

(192) Amundsen, A. R.; Whelan, J.; Bosnich, B. *J. Am. Chem. Soc.* **1977**, *99* (20), 6730.

(193) Draksharapu, A.; Li, Q.; Roelfes, G.; Browne, W. R. *Dalt. Trans.* **2012**, *41* (42), 13180.

(194) Noël, S.; Perez, F.; Pedersen, J. T.; Alies, B.; Ladeira, S.; Sayen, S.; Guillon, E.; Gras, E.; Hureau, C. *J. Inorg. Biochem.* **2012**, *117*, 322.

(195) Faller, P.; Hureau, C.; Berthoumieu, O. *Inorg. Chem.* **2013**, *52* (21), 12193.

(196) Viles, J. H. *Coord. Chem. Rev.* **2012**, *256* (19–20), 2271.

(197) Goldstein, S.; Fridovich, I.; Czapski, G. *Free Radic. Biol. Med.* **2006**, *41* (6), 937.

(198) Higuchi, C.; Sakiyama, H.; Okawa, H.; Isobe, R.; Fenton, D. E. *J. Chem. Soc. Dalt. Trans.* **1994**, No. 7, 1097.

(199) Vikse, K. L.; Ahmadi, Z.; Scott McIndoe, J. *Coord. Chem. Rev.* **2014**, *279*, 96.

(200) De La Lande, A.; Parisel, O.; Gérard, H.; Moliner, V.; Reinaud, O. *Chem. - A Eur. J.* **2008**, *14* (21), 6465.

(201) Deville, C.; Padamati, S. K.; Sundberg, J.; McKee, V.; Browne, W. R.; McKenzie, C. J. *Angew. Chemie - Int. Ed.* **2016**, *55* (2), 545.

(202) Pirovano, P.; Magherusan, A. M.; McGlynn, C.; Ure, A.; Lynes, A.; McDonald, A. R. *Angew. Chemie - Int. Ed.* **2014**, *53* (23), 5946.

(203) Fei, B. L.; Yan, Q. L.; Wang, J. H.; Liu, Q. B.; Long, J. Y.; Li, Y. G.; Shao, K. Z.; Su, Z. M.; Sun, W. Y. *Zeitschrift fur Anorg. und Allg. Chemie* **2014**, *640* (10), 2035.

(204) Ao, Y.; Tang, H.; Wang, P.; Wang, C.; Hou, J.; Qian, J. *J. Mol. Catal. A Chem.* **2011**, *344*, 138.

(205) Sustmann, R.; Korth, H.; Kobus, D.; Seiffert, K.; Verheggen, E.; Bill, E.; Kirsch, M.; Groot, H. De. *Inorg. Chem.* **2007**, *46* (26), 270.

(206) Pelletier, H.; Kraut, J. *Science (80-.).* **1992**, *258* (5089), 1748.

(207) Wieprecht, T.; Xia, J.; Heinz, U.; Dannacher, J.; Schlingloff, G. *J. Mol. Catal. A Chem.* **2003**, *203* (1–2), 113.

(208) Polzer, F.; Wunder, S.; Lu, Y.; Ballauff, M. *J. Catal.* **2012**, *289*, 80.

(209) Wieprecht, T.; Heinz, U.; Xia, J.; Schlingloff, G.; Dannacher, J. *J. Surfactants Deterg.* **2004**, *7* (1), 59.

(210) Tovmasyan, A.; Maia, C. G. C.; Weitner, T.; Carballal, S.; Sampaio, R. S.; Lieb, D.; Ghazaryan, R.; Ivanovic-Burmazovic, I.; Ferrer-Sueta, G.; Radi, R.; Reboucas, J. S.; Spasojevic, I.; Benov, L.; Batinic-Haberle, I. *Free Radic. Biol. Med.* **2015**, *86*, 308.

(211) Prushan, M. J.; Tomezsko, D. M.; Lofland, S.; Zeller, M.; Hunter, A. D. *Inorganica Chim. Acta* **2007**, *360* (7), 2245.

(212) Fernandes, C.; Oliveira Moreira, R.; Lube, L. M.; Horn Jr, A.; Szpoganicz, B.; Sherrod, S.; Russell, D. H. *Dalt. Trans.* **2010**, *39* (21), 5094.

(213) Horn, A.; Parrilha, G. L.; Melo, K. V.; Fernandes, C.; Horner, M.; Visentin, L. D. C.; Santos, J. A. S.; Santos, M. S.; Eleutherio, E. C. A.; Pereira, M. D. *Inorg. Chem.* **2010**, *49* (4), 1274.

(214) Parrilha, G. L.; Fernandes, C.; Bortoluzzi, A. J.; Szpoganicz, B.; Silva, M. de S.; Pich, C. T.; Terenzi, H.; Horn, A. *Inorg. Chem. Commun.* **2008**, *11* (6), 643.

(215) Ligtenbarg, A. G. J.; Oosting, P.; Roelfes, G.; La Crois, R. M.; Lutz, M.; Spek, A. L.; Hage, R.; Feringa, B. L. *Chem. Commun.* **2001**, No. 4, 385.

(216) Kurtz, D. M. *Chem. Rev.* **1990**, *90*, 585.

(217) Hartley, C. L.; DiRisio, R. J.; Screen, M. E.; Mayer, K. J.; McNamara, W. R. *Inorg. Chem.* **2016**, *55* (17), 8865.

(218) Imbert, C.; Hratchian, H. P.; Lanznaster, M.; Heeg, M. J.; Hryhorczuk, L. M.; McGarvey, B. R.; Schlegel, H. B.; Verani, C. N. *Inorg. Chem.* **2005**, *44* (21), 7414.

(219) Lanznaster, M.; Neves, A.; Bortoluzzi, A. J.; Assumpção, A. M. C.; Vencato, I.; Machado, S. P.; Drechsel, S. M. *Inorg. Chem.* **2006**, *45* (3), 1005.

(220) Ito, S.; Okuno, T.; Matsushima, H.; Tokii, T.; Nishida, Y. **1996**, No. m, 4037.

(221) Coggins, M. K.; Zhang, M. T.; Vannucci, A. K.; Dares, C. J.; Meyer, T. J. *J. Am. Chem. Soc.* **2014**, *136* (15), 5531.

(222) Wickramasinghe, L. D.; Zhou, R.; Zong, R.; Vo, P.; Gagnon, K. J.; Thummel, R. P. *J. Am. Chem. Soc.* **2015**, *137* (41), 13260.

(223) Zhang, B.; Li, F.; Yu, F.; Cui, H.; Zhou, X.; Li, H.; Wang, Y.; Sun, L. *Chem. - An Asian J.* **2014**, *9* (6), 1515.

(224) Okamura, M.; Kondo, M.; Kuga, R.; Kurashige, Y.; Yanai, T.; Hayami, S.; Praneeth, V. K.; Yoshida, M.; Yoneda, K.; Kawata, S.; Masaoka, S. *Nature* **2016**, *530* (7591), 465.

(225) Evans, D. J.; Pickett, C. J. *Chem. Soc. Rev.* **2003**, *32* (5), 268.

(226) Gao, W.; Sun, J.; Åkermark, T.; Li, M.; Eriksson, L.; Sun, L.; Åkermark, B. *Chem. - A Eur. J.* **2010**, *16* (8), 2537.

(227) Wang, Z.; Liu, J.; He, C.; Jiang, S.; Åkermark, B.; Sun, L. *Inorganica Chim. Acta* **2007**, *360* (7), 2411.

(228) Mejia-Rodriguez, R.; Chong, D.; Reibenspies, J. H.; Soriaga, M. P.; Darensbourg, M. Y. *J. Am. Chem. Soc.* **2004**, *126* (38), 12004.

(229) Quentel, F.; Passard, G.; Gloaguen, F. *Energy Environ. Sci.* **2012**, *5* (7), 7757.

(230) Parent, A. R.; Sakai, K. *ChemSusChem* **2014**, *7* (8), 2070.

(231) Singh, A.; Spiccia, L. *Coord. Chem. Rev.* **2013**, *257* (17–18), 2419.

(232) Kanan, M. W.; Nocera, D. G. *Science (80-.).* **2008**, *321*, 1072.

(233) Thoi, V. S.; Sun, Y.; Long, J. R.; Chang, C. J. *Chem. Soc. Rev.* **2013**, *42* (6), 2388.

(234) Dempsey, J. L.; Brunschwig, B. S.; Winkler, J. R.; Gray, H. B. *Acc. Chem. Res.*

2009, *42* (12), 1995.

(235) Fisher, B.; Eisenberg, R. *J. Am. Chem. Soc.* **1980**, *102* (24), 7361.

(236) Bernhardt, P. V; Jones, L. a. *Inorg. Chem.* **1999**, *38* (22), 5086.

(237) Anxolabéhère-Mallart, E.; Costentin, C.; Fournier, M.; Nowak, S.; Robert, M.; Savéant, J. M. *J. Am. Chem. Soc.* **2012**, *134* (14), 6104.

(238) Sun, Y.; Bigi, J. P.; Piro, N. A.; Tang, M. L.; Long, J. R.; Chang, C. J. *J. Am. Chem. Soc.* **2011**, *133* (24), 9212.

(239) Singh, W. M.; Baine, T.; Kudo, S.; Tian, S.; Ma, X. A. N.; Zhou, H.; Deyonker, N. J.; Pham, T. C.; Bollinger, J. C.; Baker, D. L.; Yan, B.; Webster, C. E.; Zhao, X. **2012**, *8* (Figure 1), 5941.

(240) Ventresque, C.; Turner, G.; Bablon, G. *J. Am. WATER Work. Assoc.* **1997**, *89* (10), 65.

(241) Vrijenhoek, E. M.; Waypa, J. J. *Desalination* **2000**, *130* (3), 265.

(242) Shivapooja, P.; Wang, Q.; Orihuela, B.; Rittschof, D.; Lõpez, G. P.; Zhao, X. *Adv. Mater.* **2013**, *25* (10), 1430.

(243) Kuroki, H.; Tokarev, I.; Nykypanchuk, D.; Zhulina, E.; Minko, S. *Adv. Funct. Mater.* **2013**, *23* (36), 4593.

(244) Tasso, M.; Conlan, S. L.; Clare, A. S.; Werner, C. *Adv. Funct. Mater.* **2012**, *22* (1), 39.

(245) Tsai, M. Y.; Chen, Y. C.; Lin, T. J.; Hsu, Y. C.; Lin, C. Y.; Yuan, R. H.; Yu, J.; Teng, M. S.; Hirtz, M.; Chen, M. H. C.; Chang, C. H.; Chen, H. Y. *Adv. Funct. Mater.* **2014**, *24* (16), 2281.

(246) Banerjee, I.; Pangule, R. C.; Kane, R. S. *Adv. Mater.* **2011**, *23* (6), 690.

(247) Tyagi, P.; Deratani, A.; Bouyer, D.; Cot, D.; Gence, V.; Barboiu, M.; Phan, T. N. T.; Bertin, D.; Gigmes, D.; Quemener, D. *Angew. Chemie - Int. Ed.* **2012**, *51* (29), 7166.

(248) Qin, Y.; Wu, L. *Polym. Int.* **2008**, *58*, 171.

(249) Hiskia, A.; Mylonas, A.; Papaconstantinou, E. *Chem. Soc. Rev.* **2001**, *30* (1), 62.

(250) Pope, M. T.; Müller, A. *Angew. Chem. Int. Ed. Engl.* **1991**, *30*, 34.

(251) Rhule, J. T.; Hill, C. L.; Judd, D. a.; Schinazi, R. F. *Chem. Rev.* **1998**, *98* (1), 327.

(252) Lipscomb, W. N. *Inorg. Chem.* **1965**, *4* (1), 132.

(253) Usón, R.; Laguna, A.; Laguna, M.; Briggs, D. A.; Murray, H. H.; Fackler John P, J. *Inorganic Syntheses*; 1990; Vol. 27.

(254) Hill, C. L.; Prosser-McCartha, C. M. *Coord. Chem. Rev.* **1995**, *143* (C), 407.

(255) Bartis, J.; Dankova, M.; Lessmann, J. J.; Luo, Q.; Horrocks, W. D.; Francesconi, L. C. *Inorg. Chem.* **1999**, *38* (6), 1042.

(256) Zhang, C.; Howell, R. C.; Luo, Q. H.; Fieselmann, H. L.; Todaro, L. J.; Francesconi, L. C. *Inorg. Chem.* **2005**, *44* (10), 3569.

(257) Müller, A.; Kögerler, P. *Coord. Chem. Rev.* **1999**, *182*, 3.

(258) Long, D. L.; Tsunashima, R.; Cronin, L. *Angew. Chemie - Int. Ed.* **2010**, *49* (10), 1736.

(259) Rare, N.; Germanotungstates, E.; Hybrid, O. *Growth (Lakeland)* **2006**, *949* (m), 9.

(260) Wang, J.; Yan, Q.; Du, X.; Duan, X.; Niu, J. *Inorganica Chim. Acta* **2008**, *361* (9–10), 2701.

(261) Aureliano, M.; Crans, D. C. *J. Inorg. Biochem.* **2009**, *103* (4), 536.

(262) Zheng, L.; Ma, Y.; Zhang, G.; Yao, J.; Bassil, B. S.; Kortz, U.; Keita, B.; de Oliveira, P.; Nadjo, L.; Craescu, C. T.; Miron, S. *Eur. J. Inorg. Chem.* **2009**, No. 34, 5189.

(263) Sarafianos, S. G.; Kortz, U.; Pope, M. T.; Modak, M. J. *Reactions* **1996**, *626*, 619.

(264) Wu, K. H.; Yu, P. Y.; Yang, C. C.; Wang, G. P.; Chao, C. M. *Polym. Degrad. Stab.* **2009**, *94* (9), 1411.

(265) Stroobants, K.; Absillis, G.; Moelants, E.; Proost, P.; Parac-Vogt, T. N. *Chemistry* **2014**, *20* (14), 3894.

(266) Zhang, G.; Keita, B.; Craescu, C. T.; Miron, S.; De Oliveira, P.; Nadjo, L. *J. Phys. Chem. B* **2007**, *111* (38), 11253.

(267) Sartorel, A.; Miró, P.; Salvadori, E.; Romain, S.; Carraro, M.; Scorrano, G.; Di Valentin, M.; Llobet, A.; Bo, C.; Bonchio, M. *J. Am. Chem. Soc.* **2009**, *131* (44), 16051.

(268) Sartorel, A.; Carraro, M.; Scorrano, G.; De Zorzi, R.; Geremia, S.; McDaniel, N. D.; Bernhard, S.; Bonchio, M. *J. Am. Chem. Soc.* **2008**, *130* (15), 5006.

(269) Toma, F. M.; Sartorel, A.; Iurlo, M.; Carraro, M.; Parisse, P.; Maccato, C.; Rapino, S.; Gonzalez, B. R.; Amenitsch, H.; Da Ros, T.; Casalis, L.; Goldoni, A.; Marcaccio, M.; Scorrano, G.; Scoles, G.; Paolucci, F.; Prato, M.; Bonchio, M. *Nat. Chem.* **2010**, *2* (10), 826.

(270) Pérez-Ramírez, J. *Adv. Funct. Mater.* **2014**, *24* (2), 180.

(271) Jackson, E. A.; Hillmyer, M. A. *ACS Nano* **2010**, *4* (7), 3548.

(272) Del Mercato, L. L.; Carraro, M.; Zizzari, A.; Bianco, M.; Miglietta, R.; Arima, V.; Viola, I.; Nobile, C.; Sorarù, A.; Vilona, D.; Gigli, G.; Bonchio, M.; Rinaldi, R.

Chem. - A Eur. J. **2014**, *20* (35), 10910.

(273) Zizzari, A.; Bianco, M.; Miglietta, R.; Del Mercato, L. L.; Carraro, M.; Sorarù, A.; Bonchio, M.; Gigli, G.; Rinaldi, R.; Viola, I.; Arima, V. *Lab a Chip - Miniaturisation Chem. Biol.* **2014**, *14* (22), 4391.

(274) Carraro, M.; Gardan, M.; Scorrano, G.; Drioli, E.; Fontananova, E.; Bonchio, M. *Chem. Commun.* **2006**, No. 43, 4533.

(275) Bonchio, M.; Carraro, M.; Scorrano, G.; Fontananova, E.; Drioli, E. *Adv. Synth. Catal.* **2003**, *345* (9–10), 1119.

(276) Bonchio, M.; Carraro, M.; Gardan, M.; Scorrano, G.; Drioli, E.; Fontananova, E. *Top. Catal.* **2006**, *40* (1–4), 133.

(277) Jansen, J. C.; Drioli, E. *Polym. Sci. - Ser. A* **2009**, *51* (11–12), 1355.

(278) Srinivasarao, M.; Collings, D.; Philips, A.; Patel, S. *Science (80-.).* **2001**, *292* (5514), 79.

(279) Shojaie, S. S.; Krantz, W. B.; Greenberg, A. R. *J. Memb. Sci.* **1994**, *94* (1), 281.

(280) Zeman, L.; Fraser, T. *J. Memb. Sci.* **1994**, *87* (3), 267.

(281) Urban, J.; Jandera, P.; Schoenmakers, P. *J. Chromatogr. A* **2007**, *1150* (1–2), 279.

(282) Bunz, U. H. F. *Adv. Mater.* **2006**, *18* (8), 973.

(283) Sun, H.; Li, H.; Bu, W.; Xu, M.; Wu, L. *J. Phys. Chem. B* **2006**, *110* (49), 24847.

(284) Quintana, M.; López, A. M.; Rapino, S.; Toma, F. M.; Iurlo, M.; Carraro, M.; Sartorel, A.; MacCato, C.; Ke, X.; Bittencourt, C.; Da Ros, T.; Van Tendeloo, G.; Marcaccio, M.; Paolucci, F.; Prato, M.; Bonchio, M. *ACS Nano* **2013**, *7* (1), 811.

(285) Di Crescenzo, A.; Bardini, L.; Sinjari, B.; Traini, T.; Marinelli, L.; Carraro, M.; Germani, R.; Di Profio, P.; Caputi, S.; Di Stefano, A.; Bonchio, M.; Paolucci, F.; Fontana, A. *Chem. - A Eur. J.* **2013**, *19* (48), 16415.

(286) Niemers, E.; Hiltmann, R. *Synthesis (Stuttg).* **1976**, 593.

(287) Renz, M.; Hemmert, C.; Meunier, B. *European J. Org. Chem.* **1998**, 1271.

(288) Battye, T. G. G.; Kontogiannis, L.; Johnson, O.; Powell, H. R.; Leslie, A. G. W. *Acta Crystallogr. Sect. D Biol. Crystallogr.* **2011**, *67* (4), 271.

(289) Evans, P. *Acta Crystallogr. Sect. D Biol. Crystallogr.* **2006**, *62* (1), 72.

(290) Winn, M. D.; Ballard, C. C.; Cowtan, K. D.; Dodson, E. J.; Emsley, P.; Evans, P. R.; Keegan, R. M.; Krissinel, E. B.; Leslie, A. G. W.; McCoy, A.; McNicholas, S. J.; Murshudov, G. N.; Pannu, N. S.; Potterton, E. A.; Powell, H. R.; Read, R. J.; Vagin, A.; Wilson, K. S. *Acta Crystallogr. Sect. D Biol. Crystallogr.* **2011**, *67* (4), 235.

(291) Burla, M. C.; Caliandro, R.; Carrozzini, B.; Cascarano, G. L.; Cuocci, C.;

Giacovazzo, C.; Mallamo, M.; Mazzone, A.; Polidori, G. *J. Appl. Crystallogr.* **2015**, *48* (1), 306.

(292) Sheldrick, G. M. *Acta Crystallogr. Sect. A Found. Crystallogr.* **2007**, *64* (1), 112.

(293) Zhang, Y.; Wen, J.; Wang, X.; Mahmood, M. H.; Liu, Z.-Y.; Wang, H.; Ji, L.; Liu, H. *Appl. Organomet. Chem.* **2014**, *28* (7), 559.

(294) Campbell, A. *Harv. Bus. Rev.* **1992**, *15* (October), 1106.

(295) Larosa, V. .; Coosemans, N.; Motte, P.; Bonnefoy, N.; Remacle, C. *Plant J.* **2012**, *70* (5), 759.